

Single-cell lipidomics reveals a role for cell-to-cell sphingolipid heterogeneity in fibroblast activation

Présentée le 27 janvier 2021

à la Faculté des sciences de la vie
Unité du Prof. D'Angelo
Programme doctoral en biotechnologie et génie biologique

pour l'obtention du grade de Docteur ès Sciences

par

Laura CAPOLUPO

Acceptée sur proposition du jury

Prof. B. E. Ferreira De Sousa Correia, président du jury
Prof. G. D'Angelo, directeur de thèse
Prof. H. Riezman, rapporteur
Prof. P. Liberali, rapporteuse
Prof. B. Deplancke, rapporteur

ACKNOWLEDGMENTS

This PhD was the best and at the same time the hardest journey of my life till now. It is thanks to all the people I met and that supported me during these years that I could make it.

First, I would like to express my immense gratitude to my supervisor Giovanni. Words will never be enough to explain how grateful I am for the opportunity you gave me 4 years ago to work in your lab. Thanks for your advice, feedback, help, support, great scientific and non-scientific chats, and thanks for the freedom you gave me that allow me to become the scientist I am now. Having a supportive supervisor is one of the most important factor for the success of a PhD and I am therefore particularly grateful. Moreover, I want to thank you because when you moved to Lausanne, I found the courage to follow my scientific dream and start a new adventure that helped me to become a better scientist and a more mature person. Thanks for reminding me to concentrate on my personal and scientific growth despite the bad moments I had during my PhD.

Going to the place where I studied, EPFL has been a wonderful place where I had the chance to meet new friends and great scientists who helped to pursue my PhD. Among them, I firstly want to thank Gioele La Manno and Irina Khven for their fruitful collaboration that helped me to build up my research story. Thanks to Jessica and Gianni, for their help with histology and for fruitful discussions. Thanks to every member of the BIOP, for their help and immense patience. Thanks to every member of Prof. Gisou van der Goot's lab that I met in these years, with a special thanks to Sylvia, now part of our lab. Thanks for the discussions in the lab meetings and thanks for sharing materials and knowledge.

A special thanks goes to Prof. Paolo Dotto from UNIL for sharing his expertise with me. It was a pleasure to meet him and receive his precious suggestions.

I would also like to acknowledge Max, Christian and Dhaka from Prof. Bernhard Spengler's lab. I cannot find the right words to thank you for your constant help with MALDI during these 4 years.

Moving on, none of my work would have been possible without the people that in Napoli, at the IBP-CNR, helped me to work like a scientist and to approach cell biology when I started this adventure. They taught me the basics which were very important for the future of my PhD. It is thanks to Advait, Domenico, Lucia, Rosaria and Serena that now I can make my cells survive! Amazing colleagues but also good friends.

Thanks to my great friend, Fede. We met the first time during the university, but it is thanks to PhD that we became friends. Despite at some point our scientific paths diverged, I am so grateful that we could start together this journey and share our first two years together. You are a great scientist and an amazing friend and I was really lucky to have you right next to my lab. Distance will never change anything!

A special thanks goes to my Pulcelle, the family I choose. Regardless of where in the globe, we stay truly united and we are always counting on each other for everything.

I would like to express my deepest gratitude to my PhD partner, Jai. Any struggles encountered during the PhD life were always manageable because they could be shared with you. I consider myself very fortunate for having the chance to learn, grow and mature with you. I think you have been one of the most crucial elements for my mental health survival! Thanks for your moral and emotional support and thank you for being part of my family.

Grazie a voi, i migliori genitori del mondo, per il vostro infinito supporto e illimitato amore, nonostante la distanza. Non c'è stato un giorno in cui non sono stata orgogliosa di avere genitori come voi. È grazie a voi se oggi sono la donna di cui vado fiera. Vi ringrazio perché i vostri sacrifici mi hanno permesso di inseguire i miei sogni e perché non avete mai smesso di credere in me. Grazie di essere stati testimoni di ogni mio traguardo scientifico e personale, non sarei qui senza di voi.

E grazie a mio fratello per tutti gli anni di università in cui, nonostante non ci capissi nulla, hai ascoltato le mie presentazioni e mi hai aiutata a prepararmi per ogni esame. Inoltre, grazie per esserti preso cura di mamma e papà quando non ci sono stata.

Finally, thanks to my endless love. Words will never be sufficient to thank you for your support every day of my life. I want to express my deep appreciation for you because you were always standing beside me throughout all my ups and downs, happy and not so happy moments. Thank you for your support when I decided to follow my dream and thank you for still being here with me after so long. I couldn't make it without you. I am waiting to start any new adventure with you.

I love you.

*Dedicated to my brother who taught me how obstacles should never stop you
from following your dreams ...*

I am so proud of you...

*To my grandparents who have always been encouraging me to do whatever
made me happy.*

I love you all...

ABSTRACT

Cell-to-cell variability plays a key role in tissue patterning by setting initial asymmetry that primes cell fate decisions. Fluctuations in the activity of regulatory molecules can commit individual cells to divergent differentiation pathways, and cell-to-cell variability can diversify the response of an otherwise homogeneous cell community to its environment. Recent advances have provided scientists with tools to study the variability associated with individual cells. However, while single-cell data are available for genomes, transcriptomes and proteomes, they are scarce for metabolic products, such as lipids.

Eukaryotic cells produce thousands of lipids – each potentially contributing to specific biological functions. Furthermore, a number of metabolic switches involving lipids have been described to occur in development and cell differentiation.

Few studies have directly addressed cell-to-cell lipid variations in syngeneic cell populations suggesting that lipid heterogeneity contributes to the emergence of multicellular patterns. Nonetheless, lipid biologists have so far addressed lipidomes in bulk cell extracts or selected lipids at the single-cell level. Thus, how lipidomes vary from one cell to another and which cell-to-cell lipid variations have biological meaning remains to be defined.

Recent developments have provided mass spectrometry with sufficient sensitivity to reveal molecules in few hundred copies, making single-cell lipidomics possible. A rapidly emerging technique with a potential use in single-cell lipidomics is imaging mass spectrometry.

Here, we devised a high-resolution MALDI imaging mass spectrometry pipeline to study cell-to-cell variability of the lipidome of hundreds of primary dermal human fibroblasts.

We found that sphingolipid metabolism shows high cell-to-cell heterogeneity and that specific sphingolipids mark distinct cell sub-populations: coined herein as “*lipotypes*”.

Furthermore, we found that fibroblast *lipotypes* correspond to cell states endowed with proliferative, inflammatory or fibrogenic properties.

Finally, we asked whether *lipotypes* participate in the specification of cell states and find that specific glycosphingolipids modulate signalling pathways (i.e., the FGF and TGF- β) to shape the transcriptional cell landscape.

In summary, through the use of single-cell omics techniques, we found that: (i) specific lipid metabolic segments (i.e., the sphingolipid pathways) have cell-to-cell variation; (ii) given lipid

configurations mark discrete cell states; and (iii) sphingolipids modulate dermal fibroblast activation involved in wound healing and skin homeostasis.

Altogether, this study is among the first to demonstrate the potential of MALDI-IMS for single-cell lipidomics and to reveal cell-to-cell lipidome heterogeneity. It also demonstrates a role for lipids in the determination of cell states and in tissue patterning and reveals a new regulatory component to the self-organization of multicellular systems.

Keywords

MALDI-IMS | glycosphingolipids | sphingolipids | *lipotypes* | CholeraToxinB | ShigaToxinB1a
| ShigaToxinB2e | FGF | TGF- β | dHFs | single-cell | heterogeneity | cell fate

RÉSUMÉ

La variabilité intercellulaire joue un rôle déterminant dans l'établissement de motifs tissulaires en définissant la symétrie initiale qui amorce les décisions du sort cellulaire. Des fluctuations dans l'activité de molécules régulatrices peuvent engager des cellules individuelles dans des voies de différenciation choisies, alors que la variabilité intercellulaire peut diversifier la réponse à l'environnement de ce qui serait autrement une population cellulaire homogène. Des progrès récents ont offert aux chercheurs des outils pour étudier la variabilité associée aux cellules individuelles. Cependant, malgré la disponibilité de données de cellules uniques aux niveaux génomes, transcriptomes et protéomes, celles-ci demeurent rares au niveau des produits métaboliques, comme par exemple les lipides.

Les cellules eucaryotes produisent des milliers de lipides, dont chacun contribue potentiellement à une fonction biologique spécifique. En effet, un certain nombre de commutateurs métaboliques impliquant des lipides ont bien été décrits dans le développement et la différenciation cellulaire.

Quelques études ayant directement abordé les variations intercellulaires des lipides dans des populations cellulaires syngéniques et homogènes suggèrent que l'hétérogénéité lipidique contribue à l'émergence de motifs multicellulaires. A présent, les chercheurs en biologie des lipides ont abordé soit des lipidomes à partir d'extraits de masses cellulaires, ou bien certains lipides choisis au niveau de la cellule unique. Il reste donc à définir comment les lipidomes varient d'une cellule à l'autre et quelle variation intercellulaire de lipides revêt un sens biologique.

Les progrès récents en spectrométrie de masse ont conduit à une sensibilité adéquate pour révéler des molécules présentes en seulement quelques centaines d'exemplaires, ce qui concrétise la faisabilité de la lipidomique au niveau de la cellule unique. Une technique en plein essor ayant un potentiel d'utilisation dans la lipidomique à cette échelle est l'imagerie par spectrométrie de masse.

Ici, nous avons conçu un mode opératoire basé sur l'imagerie par spectrométrie de masse de type MALDI à haute résolution afin d'étudier la variabilité intercellulaire de lipidomes de centaines de fibroblastes primaires du derme humain.

Nous avons ainsi trouvé que les sphingolipides ont remarquablement une grande

hétérogénéité intercellulaire. Ces lipides caractérisent des sous-populations distinctes parmi les fibroblastes humains syngéniques, définies ici comme *lipotypes*.

De plus, nous avons trouvé que chez les fibroblastes les *lipotypes* distincts correspondent à des états cellulaires pourvus de propriétés prolifératives, inflammatoires ou fibrotiques.

En dernier lieu, nous voulions savoir si les lipotypes participent à la spécification des états cellulaires et nous avons conclu que des glycosphingolipides spécifiques modulaient des voies de signalisation, précisément celles de FGF et TGF- β , pour façonner le paysage transcriptionnel de la cellule unique.

Pour résumer, l'application de méthodes omiques aux cellules uniques m'a permis de découvrir que: (i) des segments spécifiques du métabolisme des lipides, c'est-à-dire les voies des sphingolipides, sont variables de cellule en cellule ; (ii) certaines configurations de lipides sont la marque d'états cellulaires discrets ; (iii) et que les sphingolipides modulent chez les fibroblastes dermiques l'activation impliquée dans la guérison des plaies et le microenvironnement tumoral.

En tout, cette étude est parmi les premières à démontrer le potentiel du MALDI-IMS pour la lipidomique des cellules uniques, et à révéler l'hétérogénéité des lipidomes intercellulaires. Elle démontre également un rôle des lipides dans la détermination des états cellulaires et dans l'homéostasie tissulaire, et dévoile une nouvelle composante régulatrice dans l'auto-organisation des systèmes multicellulaires.

Mots clés

MALDI-IMS | glycosphingolipides | sphingolipides | *lipotypes* | CholeraToxinB | ShigaToxinB1a | ShigaToxinB2e | FGF | TGF- β | dHFs | cellule unique | hétérogénéité | sort cellulaire

TABLE OF CONTENTS

ACKNOWLEDGMENTS	i
ABSTRACT	iv
RÉSUMÉ	vi
TABLE OF CONTENTS	viii
LIST OF FIGURES AND TABLES	xii
LIST OF ABBREVIATION.....	xv
CHAPTER 1. INTRODUCTION.....	1
1.1 Membrane lipid synthesis and membrane composition	1
1.1.1 Bioactive lipids.....	6
1.2 Cellular Heterogeneity.....	10
1.2.1 Biological Noise vs. deterministic variability	12
1.3 Cell-to-cell lipid variability	15
1.4 Single-cell techniques to investigate cellular heterogeneity	16
1.4.1 Single-cell sequencing	17
1.4.1.1 Single-cell genomics	18
1.4.1.2 Single-cell epigenomics.....	18
1.4.1.3 Single-cell transcriptomics	19
1.4.2 Single-cell temporal omics approach	20
1.4.3 Single-cell proteomics and metabolomics.....	21
1.4.3.1 Proteomics.....	22
1.4.3.2 Metabolomics	23
1.5 Imaging Mass Spectrometry (MSI)	25
1.5.1 SIMS-IMS.....	28
1.5.2 MALDI-IMS	29
1.6. Goal of the project.....	31
CHAPTER 2. SINGLE-CELL LIPIDOMICS OF DERMAL HUMAN FIBROBLASTS.....	33

2.1 Single-Cell Lipidomics by MALDI-IMS	33
2.2 Single-pixel analysis on MALDI-IMS images	39
2.3 Conclusions	42
CHAPTER 3. INVESTIGATION OF CELL-TO-CELL LIPID VARIABILITY	44
3.1 Cell-to-cell lipid variability	44
3.2 Conclusions	50
CHAPTER 4. CORRELATIVE VIDEO/ MASS MICROSCOPY OF SINGLE dHFs REVEALS THE EXISTENCE OF CELL ‘LIPOTYPES’	52
4. 1 Development of Correlative video/ mass microscopy of dHFs	52
4.2 Conclusions	58
CHAPTER 5. MS-INDEPENDENT VALIDATION OF CELL-TO-CELL LIPID VARIABILITY	60
5.1 Validation of single-cell lipid heterogeneity by using bacterial toxins.....	60
5.2 Conclusions	69
CHAPTER 6. THE ORIGIN OF CELL-TO-CELL LIPID VARIABILITY: <i>LIPOTYPES</i> MARK SPECIFIC CELL STATES	71
6.1 Transcriptomic analysis of dHFs.....	71
6. 2 Conclusions	76
CHAPTER 7. HIGHLY VARIABLE LIPIDS PARTICIPATE IN THE MAINTENANCE OF FIBROBLASTS TRANSCRIPTIONAL STATES	78
7.1 Transcriptomic analysis of dHFs after sphingolipids depletion	78
7.2 GSLs participate in the activation of FGF and TGF- β signalling pathways	81
7.3 Which lipid participates in the modulation of FGF signalling pathway?	87
7.4 Conclusions	91
CHAPTER 8. CROSSTALKING BETWEEN dHFs AND <i>LIPOTYPES</i>	93
8.1 Do <i>lipotypes</i> and fibroblasts signalling pathways crosstalk?.....	93
8.2 Conclusions	96
CHAPTER 9. DISCUSSION	98
CHAPTER 10. MATERIALS AND METHODS.....	107
10.1 Cell lines and cell growth conditions	107
10.2 Generation of stable cell line over-expressing GSLs synthesizing enzymes.....	107
10.3 Single-cell MALDI Imaging Mass Spectrometry (MALDI-IMS) workflow	108

10.3.1 Sample preparation	108
10.3.2 MALDI-IMS analysis.....	108
10.3.3 MALDI-IMS images reconstruction and annotation.....	109
10.3.4 Single pixel analysis.....	109
10.3.5 Image Processing and Batch Correction.....	110
10.3.6 Single-cell lipids data analysis (lipid and cell network).....	110
10.4 Lipid analysis	111
10.4.1 Lipid extraction	111
10.4.2 MALDI-TOF untargeted lipidomics.....	111
10.4.3 LC-MS untargeted lipidomics.....	112
10.4.4 TSQ ANALYSIS (Multi Reaction Monitoring)	113
10.4.5 HPTLC	113
10.5 Immunofluorescence analysis.....	114
10.5.1 Immunofluorescence staining with toxins.....	114
10.6 Flow cytometry analysis	115
10.6.1 Isolation of lipids population by FACS	115
10.7 siRNA treatment and transfection.....	115
10.8 Cell manipulation	116
10.8.1 Drug treatments	116
10.8.2 FGF2/TGF- β 1 treatment.....	116
10.9 Fluorescence In Situ Hybridization (FISH)	116
10.10 Correlative video-confocal microscopy.....	117
10.10.1 Time-lapse and lineage analysis.....	117
10.11 Bulk RNA-sequencing of FACS sorted dHFs population	118
10.12 scRNA-seq experiment.....	119
10.12.1 scRNA-seq: Treatment-Control comparison.....	120
10.13 Real Time qPCR	120
10.14 SDS-PAGE and western blotting.....	121
10.14.1 SDS-PAGE.....	121

10.14.2 Western blotting.....	122
Annex 1.....	123
Annex 2.....	124
Annex 3.....	125
Annex 4.....	126
Annex 5.....	126
TABLES.....	128
REFERENCES.....	138
CURRICULUM VITAE.....	164

LIST OF FIGURES AND TABLES

Figure 1. Lipids Structure.

Figure 2. Membrane lipid biosynthesis.

Figure 3. Stage-specific changes of GSLs expression during mouse embryogenesis.

Figure 4. Regulatory circuits for GSL expression and metabolism.

Figure 5. Cell-to-cell heterogeneity.

Figure 6. Stochastic vs. deterministic variability.

Figure 7. Main single-cell omics techniques.

Figure 8. Imaging mass spectrometry.

Figure 9. dHFs analysis workflow by MALDI-IMS

Figure 10. MALDI-TOF mass spectra of GSLs standards.

Figure 11. LC-MS/MS mass spectrum of Gb3 and Gb4.

Figure 12. IMS images gallery of dHFs lipids identified with high accuracy.

Figure 13. Comparison between LC/MS and MALDI-IMS lipidomics analysis of dHFs.

Figure 14. Single pixel analysis.

Figure 15. Principal Component Analysis of lipids based on single-pixel analysis.

Figure 16. Single-cell IMS analysis workflow.

Figure 17. Single ROI mass spectra from individual cells.

Figure 18. Batch correction analysis of single-cell lipid data.

Figure 19. Lipids cell-to-cell variability.

Figure 20. Single-cell lipid co-variation network.

Figure 21. Mass Images of highly variable lipids.

Figure 22. Cell-to-cell co-variation network.

Figure 23. Correlative video/ mass microscopy of dHFs.

Figure 24. t-SNE dimensionality reduction analysis on dHFs based on single-cell lipid count values.

Figure 25. Lineage analysis of dHFs.

Figure 26. Lipid-based family separability analysis.

Figure 27. Lipid analysed based on family separability analysis.

Figure 28. Bacterial toxin staining of dHFs.

Figure 29. Cytofluorometric analysis of dHFs using bacterial toxins

Figure 30. Chemical inhibition of sphingolipid biosynthetic pathway.

Figure 31. Cytofluorometric analysis of dHFs after siRNA-KD of the main GSLs synthesizing enzymes.

- Figure 32.** Correlative IMS-confocal analysis of dHFs.
- Figure 33.** Cytofluorometric assessment of lipids heterogeneity in dHFs from healthy donors.
- Figure 34.** Correlative video/ confocal microscopy of dHFs.
- Figure 35.** Dendrograms of single-cell lipid composition across cell generation.
- Figure 36.** Fluorescence in situ hybridization (FISH) analysis of GSL synthesizing enzymes.
- Figure 37.** Characterization of skin tissue sections by bacterial toxins.
- Figure 38.** UMAP analysis after scRNA-seq analysis.
- Figure 39.** Bulk RNA-seq analysis of dHFs FACS sorted according to their lipotypes.
- Figure 40.** Over-represented gene ontology analysis (ORA)
- Figure 41.** Lipotype signatures mapped in the UMAP space.
- Figure 42.** IF staining of dHFs with specific markers belonging to distinct transcriptional state.
- Figure 43.** UMAP analysis of control and FB1 treated dHFs after scRNAseq analysis.
- Figure 44.** UMAP and cell density map of control and FB1 treated dHFs after scRNAseq.
- Figure 45.** Integrated UMAP map of key marker genes for pro-fibrotic or stressed genes
- Figure 46.** Lipotypes signatures mapped in the integrated UMAP space.
- Figure 47.** Integrated UMAP projections of FGF and TGF- β signatures.
- Figure 48.** qRT-PCR, WB and IF analysis of FGF and TGF- β genes after SLs depletion
- Figure 49.** FGF2 and TGF- β 1 dose response analysis after SLs depletion by FB1.
- Figure 50.** qRT-PCR and WB analysis of FGF and TGF- β key markers after FB1 treatment on DNTGFR2 and DNFGFR1 dHFs.
- Figure 51.** IF analysis of stable dHFs lines OE GSLs synthesizing enzymes.
- Figure 52.** Cytofluorometric and fluorescence analysis of dHFs OE GSLs synthesizing enzymes.
- Figure 53.** WB and IF analysis of FGF and TGF- β markers in dHFs OE GSLs synthesizing enzymes
- Figure 54.** Cytofluorimetric and fluorescence analysis of dHFs expressing dominant negative form of TGFBR and FGFR after toxin staining.
- Figure 55.** De novo sphingolipids synthesis in DNTGFR2 and DNFGFR1 dHFs.
- Figure 56.** Fluorescence in situ hybridization (FISH) analysis of GSLs synthesizing enzymes in DNTGFR2 and DNFGFR1 dHFs.
- Figure 57.** Fluorescence in situ hybridization (FISH) analysis of GSLs synthesizing enzymes in dHFs treated with FGF2 or TGF- β 1.
- Figure 58.** Simplified scheme of dHFs activation for tissue repair and cancer progression.
- Figure 59.** Hypothetical molecular model.
- Figure 60.** The asialo- to ganglio-GSL switch during EMT.

Table 1. List of identified compounds.

Table 2. Lipotypes gene signatures.

Table 3. FGF and TGF- β gene signatures.

LIST OF ABBREVIATIONS

2,5-DHB	2,5- dihydroxybenzoic acid
ACS	Attribution Confidence Score
<i>A4GALT</i>	alpha 1,4-galactosyltransferase
<i>B3GALNT1</i>	beta-1,3-N-Acetylgalactosaminyltransferase1
BSA	Bovine Serum Albumin
ChTxB	Cholera Toxin B Subunit
dHFs	Dermal human fibroblasts
ESI-LC-MS	Electrospray Ionization – Liquid Chromatography – Mass Spectrometry
FACS	Fluorescence Activated Cell Sorting
FB1	Fumonisin B1
FGF	Fibroblast Growth Factor
FGFR	FGF receptor
FISH	Fluorescence In Situ Hybridization
GO	Gene Ontology
GPLs	Glycerophospholipids
GSLs	Glycosphingolipids
HPTLC	High Performance Thin Layer Chromatography
IHC	Immunohistochemistry
IMS	Imaging Mass Spectrometry
imzML	Imaging Mass Spectrometry Markup Language
IoD	Index of Dispersion
MALDI	Matrix Assisted Laser Desorption Ionization
MRM	Multiple Reaction Monitoring
NGS	Next Generation Sequencing
OCT	Optimal Cutting Temperature
ORA	Over-represented gene ontology analysis
PCA	Principal Component Analysis
PCC	Pearson Correlation Coefficient

PDMP	DL-threo-1-Phenyl-2-decanoylamino-3-morpholino-1-propanol
ROI	Region of Interest
scRNA-seq	Single-cell RNA sequencing
ShTxB	Shiga Toxin B Subunit
SLs	Sphingolipids
SMA	Smooth Muscle Actin
<i>ST3GAL5</i>	ST3 beta-galactoside alpha-2,3-sialyltransferase 5
TGF- β	Transforming Growth Factor beta
TGFR	TGF Receptor
TIC	Total Ion Current
UMAP	Uniform Manifold Approximation and Projection

CHAPTER 1. INTRODUCTION

1.1 Membrane lipid synthesis and membrane composition

Lipids are among the most abundant and functionally relevant cell metabolites. They play fundamental roles in several biological functions, including the regulation of signal transduction, gene expression, apoptosis, membrane trafficking, cell division, cell polarity, cell motility, acting as energy stores, precursor of hormones and being the main constituents of cell membranes (Eyster KM, 2007). Lipids comprise a vast group of hydrophobic molecules that can be classified into three main categories: glycerophospholipids (GPLs), sphingolipids (SLs), and sterols (**Figure 1**).

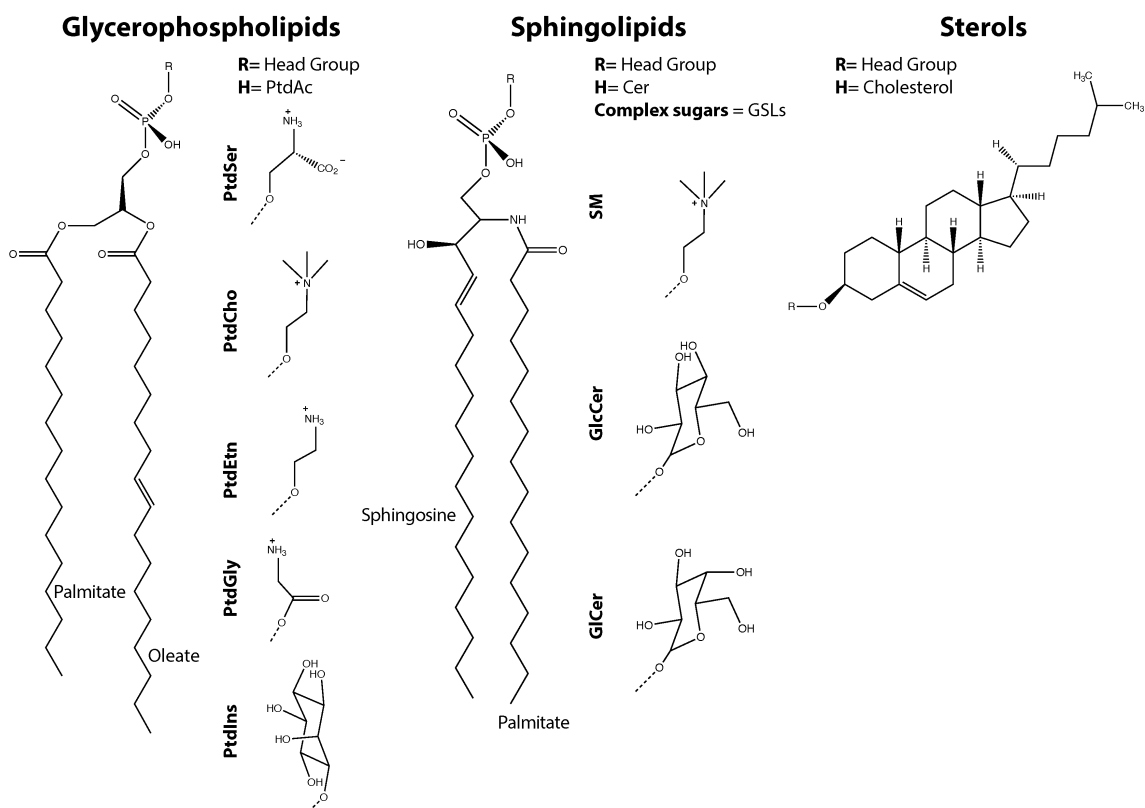


Figure 1. Lipids structure. Structure of the three main lipids categories: Glycerophospholipids (GPLs), Sphingolipids (SLs) and sterols. Depending on the head group attached to the fatty acid acyl chains several lipids exist. PtdCho, phosphatidylcholine; PtdSer, phosphatidylserine; PtdEtn, phosphatidylethanolamine; PtdGly, phosphatidylglycine; PtdAc, phosphatidic acid; SM,

sphingomyelin; Cer, Ceramide; GlcCer, Glucosyl Ceramide; GalCer, Galactosyl Ceramide; GSLs, glycosphingolipids.

GPLs are the most abundant membrane lipids in mammalian cells. They are composed of a hydrophobic core of fatty acids attached to a hydrophilic headgroup facing the aqueous phase. GPLs consist of a glycerol-3-phosphate (G3P) backbone, linked to a head group via a phosphodiester bond and to fatty acid chains, with different lengths, through ester, ether or vinyl ether bonds (Hermansson M et al., 2011). GPLs are subdivided into different classes according to the nature of their headgroup: phosphatidylcholine (PtdCho), phosphatidylethanolamine (PtdEtn), phosphatidylinositol (PtdIns), phosphatidylserine (PtdSer), phosphatidic acid (PtdAc) and phosphatidylglycerol (PtdGly) (van Meer G, 2005). The synthesis of GPLs starts in the Endoplasmic Reticulum (ER) with acylation of G3P by glycerol-3-phosphate acyltransferase (GPAT), and lysophosphatidic acid acyltransferase (LPPAT), to form PtdAc that can be either dephosphorylated into diacylglycerol (DAG) – the precursor of PtdCho, PtdEtn and PtdSer – or converted into CDP-diacylglycerol (CDP-DG) – the precursor of the anionic PtdIns, PtdGly and cardiolipin (CL) (**Figure 2A**). Other minor classes of GPLs also exist. They can be derived from existing GPLs (phosphoinositides, lysophospholipids) or result from a different biosynthetic pathway (ether-phospholipids).

Phosphoinositides are derivatives of PtdIns, obtained by successive phosphorylation and dephosphorylation of the inositol ring in position D-3, D-4 or D-5, in different combinations. These phosphorylation reactions are reversible thanks to the action of PtdIns phosphatases (**Figure 2A**). Seven distinct PtdIns species have been identified with a non-homogeneous distribution among cell organelles that is due to the balance of kinases vs phosphatases. For instance, the Plasma Membrane (PM) is enriched in PtdIns(4,5)P₂, PtdIns(4)P and PtdIns(3,4,5)P₃; Early Endosomes (EE) are enriched in PtdIns(3)P; Late Endosomes (LE) in PtdIns(3,5)P₂; and, the Golgi in PtdIns(4)P (De Matteis MA and Godi A, 2004).

Lysophospholipids are GPLs in which one of the fatty acyl chains is replaced by a hydroxyl group in position 1 or 2 of their glycerol backbone. Unlike other GPLs, they are low abundant in biological cell membranes. Lysophospholipids are synthesized either by *de novo* synthesis

from G3P or by hydrolysis of GPLs via the action of phospholipases and acyltransferases (D'Arrigo P and Servi S, 2010).

In mammalian cells, ether-phospholipids represent derivatives of GPLs in which the fatty acyl chain at the sn-1 position is linked to the glycerol backbone by an ether bond, as opposed to an ester bond. Ether lipids synthesis starts in the peroxisomes where G3P is dehydrogenated to dihydroxyacetone phosphate (DHAP). DHAP is then acylated with a long-chain fatty acyl by the glycerone phosphate O-acyltransferase (GNPAT) before that the enzyme alkyl-glycerone phosphate synthase (AGPS) replaces the acyl-chain by a fatty alcohol. The final peroxisomal step in ether lipid synthesis is carried out by acyl/alkyl-DHAP reductase, which reduces alkyl-DHAP into the ether lipid precursor 1-O-alkyl-glycerol-3-phosphate (AGP). The DHAP reductase can also reduce acyl-DHAP to generate the diacyl phospholipid precursor lysophosphatidic acid (LysoPtdAc) (Brites P et al., 2004).

Sterols are made of a sterane nucleus with four rings and one hydroxylation on carbon 3. In mammalian cells, sterols mainly consist of free cholesterol whose biosynthesis starts in the ER with the synthesis of 3-hydroxy-3-methylglutaryl-CoA (HMG-CoA) from Acetyl-CoA, which is then irreversibly reduced into mevalonate by the HMG-CoA reductase (HMGCR). Then, mevalonate is converted into 3-isopentenyl pyrophosphate, and six molecules of isopentenyl pyrophosphate are added to synthesize squalene. Finally, squalene is cyclized to form cholesterol (**Figure 2A**) (Schroepfer GJ, 1981).

Lastly, SLs are another class of structural lipids whose synthesis begins in the ER with the condensation of serine and palmitoyl CoA into 3-ketodihydrosphingosine by serine palmitoyltransferase (SPT). This product is then reduced to generate sphinganine, the precursor of Long-Chain Bases (LCBs). LCBs can be phosphorylated by a kinase or condensed with fatty acids by one of the 6 different ceramide synthases (CerS 1-6), giving dihydroceramides that can be desaturated to form ceramide (Cer) (Mullen TD et al., 2012). Cer can be then galactosylated in the ER to produce galactosylceramide (GalCer) (Holthuis JCM et al., 2001) or it can be transported to the Golgi complex through vesicular or non-vesicular transport routes (Gault CR et al., 2010; Hanada K et al., 2003). The subsequent fate of Cer is highly dependent on the mode of transport: either conversion to glucosylceramide

(GlcCer) or sphingomyelin (SM) (Funakoshi T et al., 2000; Hannun YA and Obeid LM, 2018; Hanada K et al., 2003).

GlcCer has to be transported, through vesicular transport or by the lipid-transfer protein FAPP2 (D'Angelo G et al., 2007; D'Angelo G et al., 2013) to the Trans Golgi Network (TGN), where it serves as precursor for the production of complex GSLs through the action of TGN-specific glycosylating enzymes (Merrill AH, 2011). In particular, the first step is the production of lactosylceramide (LacCer), via β 4-galactosyltransferases V and VI, represents the metabolic branch point for the formation of the different classes of complex GSLs: asialo, ganglio, globo/iso-globo and lacto/neo-lacto series (Kumagai T et al., 2010; Nishie T et al., 2010). Indeed, LacCer is the substrate of: β 1,4-N-acetylgalactosylaminyltransferase B4GALNT1 to produce GA2 (Nagata Y et al., 1992); α -2,3-sialyltransferase ST3GAL5 to produce GM3 (Ishii A et al., 1998); α 1-4 galactosyltransferase A4GALT to produce Gb3 (Kojima Y et al., 2000); and, β -1,3-N-acetylglucosaminyltransferase B3GNT5 to produce Lc3 (Biellmann F et al., 2008) (**Figure 2A,B**).

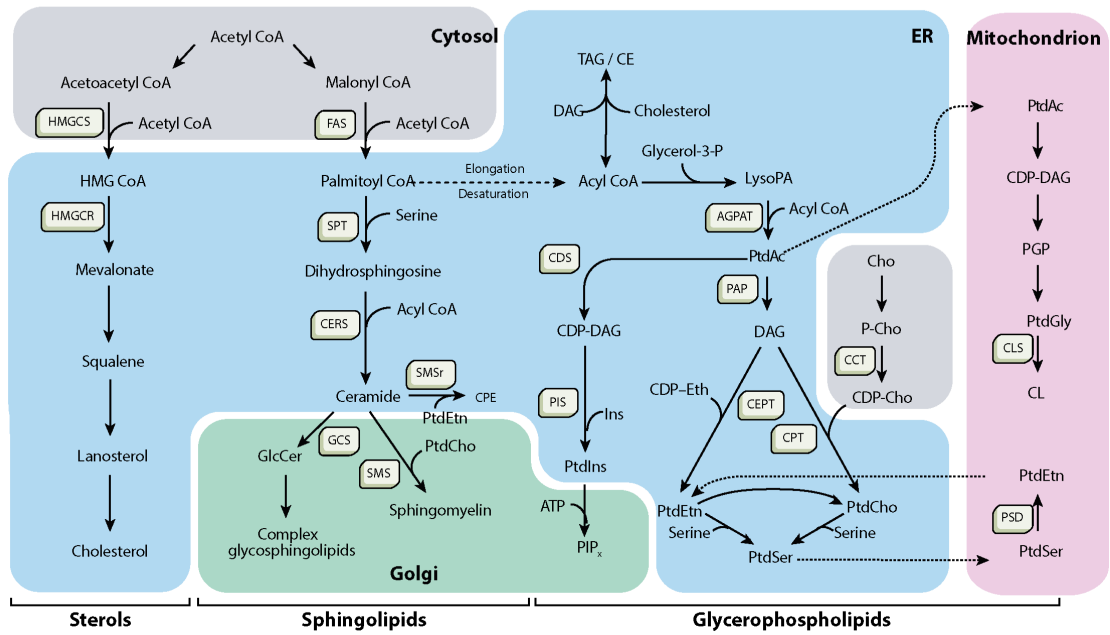
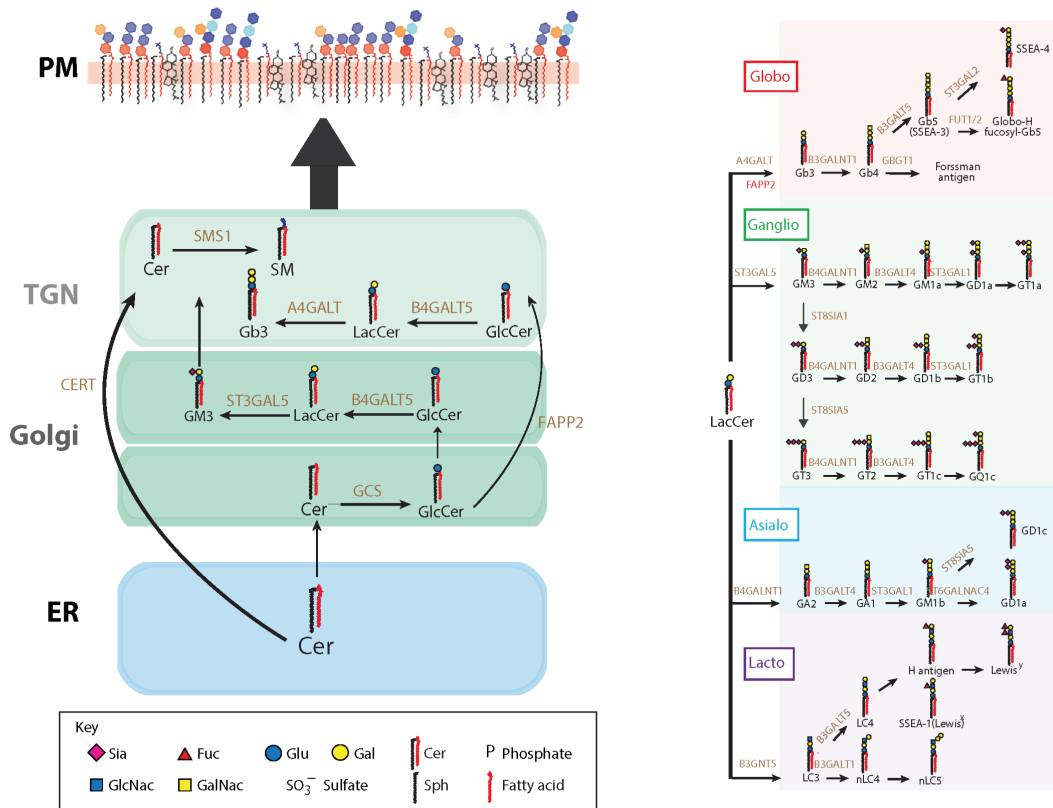
A**B**

Figure 2. Membrane lipid biosynthesis. A) Principal pathways for the production of sterols, sphingolipids and glycerophospholipids in mammals, and the key biosynthetic enzymes involved. (Adapted from Holthuis JCM and Menon AK, 2014). **B)** GSLs synthesis and classification and schematic representation of the GSL synthetic pathways. Cer can be conveyed by CERT to the TGN for the

synthesis of SM. Alternatively, Cer is glycosylated for the synthesis of the GSL precursors, GlcCer. GlcCer is galactosylated to LacCer, which serves as a common precursor for the different GSL series (left panel): globo (red), ganglio (green), asialo (blue) and lacto (purple). Glycosphingolipid-synthetizing enzymes (GSEs) catalyzing the major synthetic reactions are shown in dark orange. (Adapted from Russo D et al., 2018).

1.1.1 Bioactive lipids

Apart from being major structural components of cell membranes, lipids are signalling molecules and precursors of bioactive compounds.

For instance, each of the seven different phosphoinositides that decorate the cytosolic membrane leaflet of specific cell compartments determines the recruitment of a number of effector proteins operating at the membrane-cytosol interface (Balla T, 2013). Thus, at the plasma membrane, phosphatidylinositol 4,5-bisphosphate [PtdIns(4,5)P₂] and phosphatidylinositol 3,4,5-trisphosphate [PtdIns(3,4,5)P₃] have fundamental roles in key signalling pathways (i.e., the PI3K, PLA2, and PLC pathways) where their malfunction is at the basis of common diseases (Skwarek LC and Boulianne GL, 2009). Phosphoinositides associated with intracellular organelles [i.e., phosphatidylinositol 3-phosphate (PtdIns(3)P) and phosphatidylinositol 4-phosphate (PtdIns(4)P)] are direct regulators of membrane trafficking at the endosomal compartment and Golgi complex, and a key controllers of the intracellular protein and lipid fluxes (De Matteis MA et al., 2005; D'Angelo G et al., 2008).

Another important class of bioactive lipids are SLs, which are ubiquitous components of eukaryotic Plasma Membranes (PM) (Hannun YA and Obeid LM, 2008, 2018; Bartke N and Hannun YA, 2009). Their hydrophobic structure allows establishment of lateral interactions to yield a tightly-packed and thick membrane structure (Hannun YA and Obeid LM, 2018; Holthuis JCM et al., 2001) that works at the plasma membrane as a 'barrier' towards the extracellular environment (Holthuis JCM and Menon AK, 2014).

Simple SL species have been shown to act as second messengers and to be produced upon cell stimulation. These include:

- 1) Sphingosine: it is produced by ceramidase-dependent ceramide hydrolysis (Kitatani K et al., 2008). Sphingosine production can be stimulated under several stress conditions and it has roles in regulating actin cytoskeleton, endocytosis, cell cycle and apoptosis by modulation of protein kinases (Smith ER et al., 2000).
- 2) Ceramide (Cer): it is produced either by acylation of long chain bases by ceramide synthases (CerS1-6) or by hydrolysis of complex sphingolipids (Bartke N and Hannun YA, 2009). Sphingomyelinases, specifically, can produce Cer from sphingomyelin upon cell stimulation (Kitatani K et al., 2008). Cer is involved in the regulation of senescence (Modrak DE et al., 2009), necrosis (Hetz CA et al., 2002), proliferation (Mesicek J et al., 2010), and apoptosis (Hartmann D et al., 2012; Kroesen BJ et al., 2001; Seumois G et al., 2007; Senkal CE et al., 2011).
- 3) Sphingosine-1-phosphate (S1P): sphingosine phosphorylation by sphingosine kinases (SPHK1 and 2) leads to the production of S1P. S1P is the ligand for a family of G-protein coupled receptors at the PM (Pyne S and Pyne N, 2000) and shows antagonizing effects to those of ceramide. S1P is involved in the regulation of cell migration (Adada MM et al., 2015), inflammation and proliferation (Spiegel S and Milstein S, 2011), cell growth, cell survival and resistance to apoptotic cell death (Osawa Y et al., 2005).
- 4) Ceramide-1-phosphate (C1P): it is produced by ceramide phosphorylation catalysed by Ceramide Kinase (CERK) and has roles in inflammation and vesicular trafficking (Gomez-Muñoz A et al., 2016).
- 5) Glucosylceramide (GlcCer): at the Golgi complex, glucosyl ceramide transferase (GCS) glycosylates ceramide to produce GlcCer (Ichikawa S and Hirabayashi Y, 1998). GlcCer has roles in post-Golgi trafficking and in drug resistance (Liu YY et al., 2013).

A further layer of signalling diversification is found in the structural variability of SL backbones with different acyl chains and in the modifications of the hydrophobic SL portion. This is the case for dihydroceramide (dhCer) – which has a role in apoptosis, autophagy and inhibition of cell growth (Kravetska JM et al., 2007) – and deoxy-sphingolipids, whose role is still not clear but they have been shown as the mediators of neurotoxicity in hereditary sensory neuropathy (HSAN1), cell death and diabetes (Hammad SM et al., 2017; Penno A et al., 2010; Hannich TJ et al., 2019).

Complex sphingolipids (i.e., SM and GSLs) at the PM participate in signalling events by segregating signalling molecules into membrane microdomains for the modulation of their activities and for their endocytosis (Holthuis JCM and Menon AK, 2014; Holthuis JCM et al., 2001; Simons K and Ikonen E, 1997). Among complex SLs, glycosphingolipids (GSLs) are essential components of the PM that consist of a ceramide backbone linked to a glycan moiety. Their complexity is mainly due to the heterogeneous elongation of glycan chains. Indeed, GSL-associated glycans have between one and more than 20 sugar residues, with 11 different monosaccharide types existing in vertebrates (D'Angelo G et al., 2013b). Importantly, the elongation of glycans in GSLs is not driven by a template; instead, it entirely depends on the relative expression and organization of their specific synthetic enzymes (Bieberich E et al., 2002; Giraudo CG and Maccioni HJF, 2003). Still, GSLs production is tightly controlled during differentiation programs; as a result, specific GSLs are used as differentiation stage or cell-type-specific markers (D'Angelo G et al., 2013b). Accordingly, numerous studies have reported that the GSL membrane composition is remodeled during embryonic development (Cochran FB et al., 1982; Handa K and Hakomori S, 2017; Kannagi R et al., 1983; Yamashita T et al., 1999).

Mice KO for the genes encoding the first two enzymes initiating GSLs production (i.e., GlcCer and LacCer synthases) are unable to synthesize GSLs downstream GlcCer and die embryonically. In both these cases, the embryos are able to progress through the pre-implantation phase but not beyond the formation of the three germ layers (Yamashita T et al., 2002; Nishie T et al., 2010; Allende ML and Proia RL, 2014). According to these studies the preimplantation phase is dominated by globosides (Handa K and Hakomori S, 2017; Sato B et al., 2007), while during gastrulation, the ganglioside production is induced in both neuronal and glial cell precursors (Goldman JE et al., 1984) (**Figure 3**).

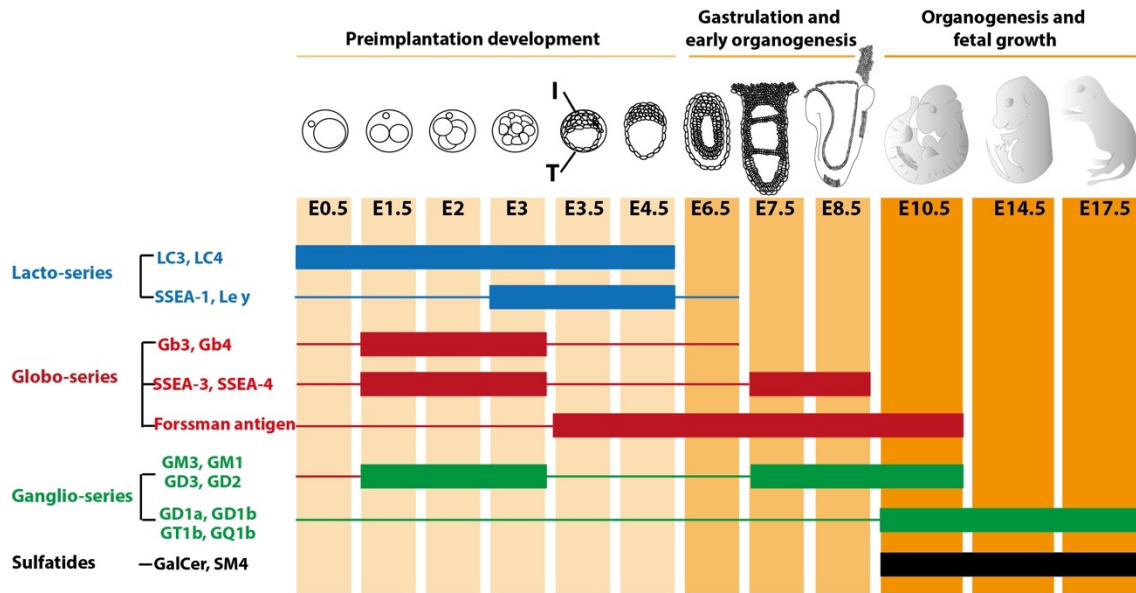


Figure 3. Stage-specific changes of GSLs expression during mouse embryogenesis. Globo- and lacto-series GSLs are expressed predominantly during the preimplantation phase and gastrulation. Ganglio-series GSLs and sulfatides, start to be synthesized during late gastrulation until the prenatal phase and concomitantly to embryonic brain development. The three phases of embryonic development are indicated by three different shades of orange. The colour-coded rectangles represent lipid species expressed at that specific stage. (Adapted from Russo D et al., 2018).

Similar GSL changes have been measured during in vitro differentiation of pluripotent stem cells to neuronal cells (Liang YJ et al., 2010, 2011; Russo D et al., 2018a; Breimer ME et al., 2017) (**Figure 4**).

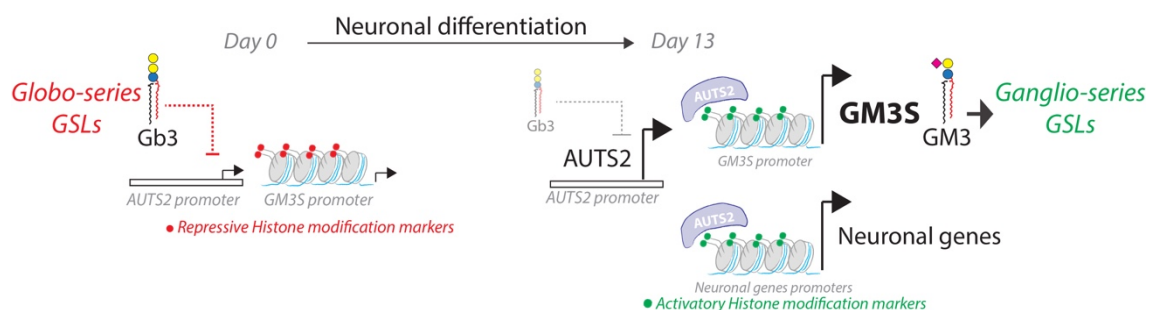


Figure 4. Regulatory circuits for GSL expression and metabolism. The globo- to ganglio-GSL switch during neuronal differentiation. In parallel with the decrease in the globo-series GSL, the epigenetic regulator AUTS2 is induced. AUTS2, in turn, binds and activates the promoters

of neuronal genes – and of GM3S – inducing GM3S gene expression and favouring neuronal differentiation.

The globo-to-ganglio metabolic switch is specifically required for proper brain development as mice KO of genes involved in this process yield a wide range of neurological phenotypes. In addition, loss-of-function mutations in the three genes that encode enzymes involved in the synthesis of ganglio-series GSLs cause neuronal diseases in humans (Boccuto et al., 2014; Boukhris et al., 2013; Fragaki et al., 2013; Harlalka et al., 2013; Simpson et al., 2004). Aberrations in GSL metabolism have also been linked to cancer. In fact, for cells during oncogenic transformation, changes in GSL composition contribute to cellular transformation, metastasis and the emergence of multi-drug resistance (Gouaze-Andersson V and Cabot MC, 2006; Morad SAF and Cabot MC, 2013; Ogretmen B, 2018; Jacob F et al., 2014; Kovbasnjuk O et al., 2005). Finally, GSLs can be used as tumour-associated antigens (TAAs) since specific GSL overproduction has been reported in several tumours (Geyer PE et al., 2016).

1.2 Cellular Heterogeneity

Cells do not live in isolation. They are part of communities where individual components can contribute to collective phenotypes. For years, in biology, cell phenotypes have been explained by genetic variations. However, even populations of monoclonal cells cultured under identical conditions can show cell-to-cell variability (Pelkmans L, 2012). Cellular heterogeneity, is induced by one or more parameters ranging from genetic and epigenetic to metabolic, proteomic and environmental factors, and it can reflect phenotypic differences in cell morphology and physiology (Altschuler SJ et al., 2010; Symmons O and Raj A, 2016; Junker JP and van Oudenaarden A, 2014) (**Figure 5**).

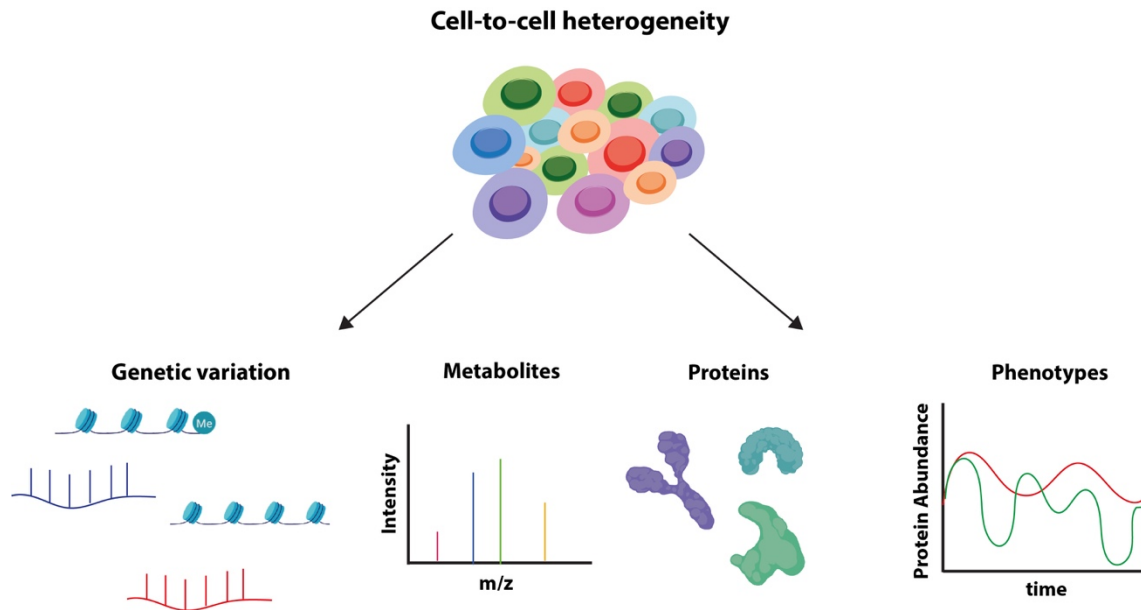


Figure 5. Cell-to-cell heterogeneity. Cell-to-cell variability is a phenomenon caused by various genetic, epigenetic and environmental factors and is reflected by differences in morphology, physiology and pathology. Cell variability can be reflected in genetic variation, metabolites and proteins heterogeneity but also in diverse cellular phenotypes.

The experimental observation of heterogeneity in clonal population of bacteria was reported long ago (Balaban NQ et al., 2004; Spudich JL and Koshland DE, 1976; Takhaveev V and Heinemann M, 2018). Already in 1957, Novick and Weiner showed that the production of β -galactosidase in individual cells was highly variable and random (Novick A and Weiner M, 1957). In the last 10-15 years, the biological significance of non-genetic variability has been described in the context of stem cell development, embryogenesis and cell fate decision (Chang HH et al., 2008; Krieger T and Simons BD, 2015; Graf T and Stadtfeld M, 2008; Xenopoulos P et al. 2012). A prototypical example of functionally significant cell-to-cell variability is that of Nanog, a key transcription factor in the maintenance of pluripotency, that exhibits heterogeneous expression in the early mouse embryo and in undifferentiated embryonic stem cells (Dietrich JE and Hiiragi T, 2007; Chambers I et al., 2007).

Biologists have interrogated cell systems using technologies that often rely on population-averaged assays, deriving from pooling thousands to millions of cells. These technologies are powerful tools that enable the identification of components and interactions within

metabolic complexes, signalling pathways, and transcriptional networks. These characteristics of given cell states are able to reveal how these states change in response to perturbations. However, averaged population behaviours do not always reflect the complexity of biological mechanisms and often even obscure the presence of rare or small subpopulations with key roles. This highlights the necessity to study cells as individual objects since cell-to-cell variability may affect a wide range of cellular processes causing phenotypic variations including in the lipid composition of cell membranes (Snijder B et al., 2009).

1.2.1 Biological noise vs. deterministic variability

Cell-to-cell variability both in populations of unicellular organisms and in complex tissues is a widely reported phenomenon. Where this heterogeneity arises is the focus of intense research. There are two main reasons why cells could vary from one another: deterministic, which means that cells can receive different instructions, leading to different outcomes (Pelkmans L, 2012; St-Pierre F and Endy D, 2008; Snijder B et al., 2009), and stochastic (or probabilistic), in which cells receiving the same instructions can have different outcomes (Raj A and van Oudenaarden A, 2008; Eldar A and Elowitz MB, 2010; Maheshri N and O'Shea EK, 2007; Losick R and Despaln C, 2008) (**Figure 6**). Cell-to-cell variability, is often coupled with the term “cellular noise”, because it may arise from the inherently probabilistic nature of intracellular reactions. Indeed, it is true that many biochemical processes involve low molecule numbers, especially when looking at gene expression where the low copy number of most genes is highly susceptible to noise.

The lack of reliable single-cell assays has precluded prior detection of noise in living cells. The main open question was: is cell-to-cell variation set by the intrinsic noise in expression of a particular gene itself or by extrinsic fluctuations in the amounts of other cellular components? The first to introduce the concepts of intrinsic and extrinsic noise and explore stochastic gene expression was Elowitz in 2002 (Elowitz MB et al. 2002). In their experiments, Elowitz and coworkers quantified the variability associated with gene expression in *E. coli*, by introducing two copies of the same promoter, one upstream of the cyan fluorescent protein (CFP) and the other upstream of the yellow fluorescent protein (YFP). In this setup, they could study both extrinsic and intrinsic fluctuations in gene expression. The former can be derived from

general variations in the efficiency of the transcriptional and translational machineries that should similarly affect the expression of both reporters in a given cell. The latter is due to the randomness inherent to transcription and translation and should affect each copy of the gene independently, giving rise to uncorrelated variations in the CFP and YFP levels. With this study they demonstrated that fluctuations in the expression of a single gene can propagate in a clonal population through metabolic pathways or networks, eventually inducing other changes that can affect the entire cellular metabolism.

The existence of extrinsic biological noise does not, however, mean that biological systems are themselves stochastic. Such upstream sources of variability, could indeed be programmed features of wider deterministic circuits. The two extrinsic factors that determine cell-to-cell variability in syngeneic and homogeneous cell populations are the microenvironment (cell-cell contacts and cell crowding) and the cell cycle. Even in the same culture conditions, cells continuously experience variability as a consequence of an increase in cell number together with cell adhesion and migration (Snijder B et al., 2009) or because they are in different cell cycle phases (Liu P et al., 2014).

Given that most cellular activities are highly complex and still not totally understood, it is complicated to separate stochasticity from determinism. Indeed, while numerous studies, both experimental and theoretical, has been devoted to understanding the implications of intrinsic or extrinsic stochastic variability (Hilfinger A and Paulsson J, 2011; Fu AQ and Pachter L, 2016; Wang DG et al., 2019; Lynch MD and Watt FM, 2018; Kiviet DJ et al., 2014; Locke JCW and Elowitz MB, 2009; Kobayashi Tet al., 2009), there are many examples where heterogeneity in apoptosis (Spencer SL et al., 2009), cancer (Cohen AA et al., 2008; Roesch A et al., 2010) and stem-cell differentiation (Ungrin MD et al., 2008) is induced by deterministic factors.

Although, it is now accepted that single-cell variability can be either stochastic or deterministic, understanding the way cells acquire their fates is still a major challenge in developmental biology. Noise alone is indeed insufficient to explain why cells break population symmetry, creating binary switches between alternative cell fates. One largely unexplored role for stochastic behaviour can be to ensure deterministic outcomes in the

multicellular context. As consequence, the choice to adopt a particular fate can occur with an apparent stochasticity, even if all the events are influenced by precisely programmed and regulated signals that induce symmetry breaking events and stabilize cell fate decision.

An illustration of this, is the case of stem cells differentiation or embryo development. Stem cells often exhibit variable levels of expression of key regulators and genes. Are these different subpopulations of cells in a probabilistic and transient state in which they are exploring potential trajectories, or are they intermediate states influenced by previous deterministic factors (Kalmar T et al., 2009; Singer ZS et al., 2014; Biase FH et al., 2014; White MD et al., 2016)? Another example are tissue-specific stem cells; their correct balance between stemness and differentiation is critical for tissue functions. Some reports show that although this balance is achieved through asymmetric cell divisions, the maintenance of adult stem cell can also be determined by probabilistic loss and replacement of individual stem cells (Krieger T and Simons BD, 2015; Graf T and Stadtfeld M, 2008).

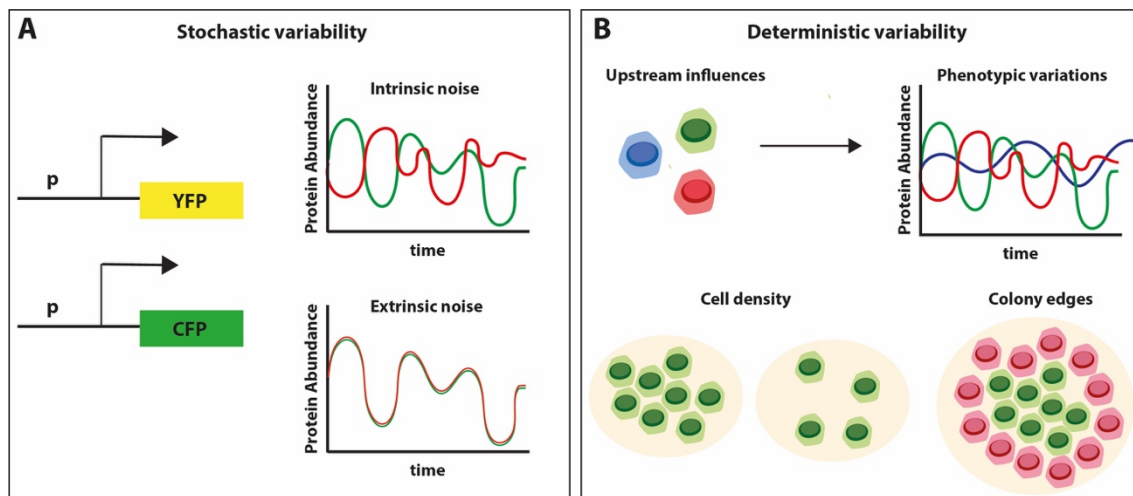


Figure 6. Stochastic vs. deterministic variability. A) Stochastic variability (noise) definition and characteristics. Intrinsic and extrinsic noise can be measured and distinguished by placing the gene encoding two fluorescent proteins under the control of the same promoter (YFP, shown in yellow; CFP, shown in green). Intrinsic noise results in differences between two reporters of the same gene in a single-cell (upper panel). Extrinsic noise affects two reporters of the same gene equally in a single-cell but causes differences from cell to cell over time (lower panel). **B)** The presence of upstream influences (deterministic variability) can be used to predict phenotypic variations in single-cells. Various cellular state parameters, such as cell size, growth speed, cell cycle state, and spatial cell population context parameters such as local cell density and location on cell colony edges (lower panel) can be source of deterministic cell-to-cell variability induced by external influences.

1.3 Cell-to-cell lipid variability

Single-cell biology aims at understanding cell-to-cell variability by studying genomes, transcriptomes, proteomes, and metabolomes at the single-cell level. However, cell-to-cell lipid variability has not yet been explored to the same extent. Indeed, although lipids, and in particular GSLs, are key regulatory molecules during development, differentiation events and in cancer, whether and how cell-to-cell lipids heterogeneity contributes to self-organization properties of cell populations or determines cell fate has not been systematically explored.

Recently, a few studies have uncovered an unsuspected degree of cell-to-cell variability for some lipids. According to these reports, lipid droplets (Herms A et al., 2013; Le TT and Cheng JX, 2009), cholesterol levels (Frenchin M et al., 2015), membrane ordering (Denz M et al., 2017), and glycosphingolipid composition (Russo D et al., 2018a,b) are subjected to high cell-to-cell variability. This variability results from microenvironmental cues, cell cycle or intrinsically bi-stable circuits, and influences cell signalling and gene transcription.

More specifically: **(i)** storage lipids (i.e., triglycerides and cholesterol esters) accumulation in hepatocytes displays a strong cell-to-cell heterogeneity with a minority of cells showing a ‘high fat storage’ phenotype due to fluctuations in fatty acid oxidation and lipolysis and possibly protecting the overall cell population from generalized lipotoxicity (Herms A et al., 2013); **(ii)** along similar lines, lipid droplets biogenesis in fibroblasts induced to differentiate to adipocytes happens heterogeneously at single-cell level and irrespective of the induction of adipogenic genes (Le TT and Cheng JX, 2009); **(iii)** the ordering of the plasma membrane varies among cells due to changes in lipid composition that depend on the cell cycle phase individual cells are in (Denz M et al., 2017); **(iv)** cholesterol and GSLs levels vary among cells depending on whether they are in a crowded or sparse cell environment (Frenchin M et al., 2015; Snijder B et al., 2009); **(v)** different cell types can show different lipids composition according to their function as in the case of astrocytes and neurons (Neumann EK et al., 2019).

An interesting case of cell-to-cell variability in lipid composition is that linked to GSLs belonging to the globo and ganglio series. Indeed, it has been reported that in several cell types globosides and gangliosides are produced by individual syngeneic cells in a mutual

exclusive fashion (Russo D et al. 2018a; Majoul I et al., 2002). This cell-to-cell heterogeneity can be explained by the operation of a self-contained bi-stable metabolic circuit (Russo et al., 2018a) by which globosides inhibit the production of the alternative GSL metabolic branch through the repression of a master regulator of neuronal genes expression AUTS2 (autism susceptibility gene 2) (Gao Z et al., 2014) that in turn binds and activates the promoter of the gene encoding GM3S (*ST3GAL5*). As a result, gangliosides and globosides are produced in a mutual exclusive fashion by single-cells depending on fluctuating AUTS2 levels. This process can be exploited during neuronal differentiation where globosides are highly produced in stem cells where they repress the expression of AUTS2, that is then induced when globosides expression decrease, resulting in gangliosides production and neuronal genes expression. These examples suggest that lipid metabolic reprogramming is an important contributor to (and not a mere consequence of) cell fate determination.

1.4 Single-cell techniques to investigate cellular heterogeneity

Technological improvements of single-cell techniques are now becoming crucial to investigate cell-to-cell variation. In the past indeed, one way to investigate single-cell phenotypes and their biological functions, has been the use of low-throughput approaches, such as immunofluorescence, fluorescent reporters (Elowitz MB et al., 2002), fluorescence in situ hybridization (FISH) (Raj et al., 2008; Femino AM et al., 1998) and single-cell polymerase chain reaction (PCR) (Maryanski JL et al., 1996; Taniguchi K et al., 2009; Citri A et al., 2012). However, in order to explain with sufficient detail the origin, the dynamics and the consequences of cell-to-cell heterogeneity we need technologies linking three essential elements: multiple simultaneous measurements (high-throughput), temporal resolution and spatial resolution. An all-inclusive tool is still unavailable, but we can rely on the combinations of high-resolution and high-throughput single-cell 'omics' techniques: genomics, transcriptomics, proteomics and metabolomics (Junker JP and van Oudenaarden A, 2014; Symmons O and Raj A, 2016; Ranzoni AM and Cvejic A, 2018) (**Figure 7**).

This depth of analysis has allowed to identify rare cell states or cell types (Schwalie PC et al., 2018; Jindal A et al., 2018; Cao J et al., 2017), to realize the contribution of multiple axes of variation to gene and protein expression, and to recognize differentiation trajectories (Tusi

BK et al., 2018). Here, I will briefly give an overview of the different single-cell omics techniques that have been developed in the past years.

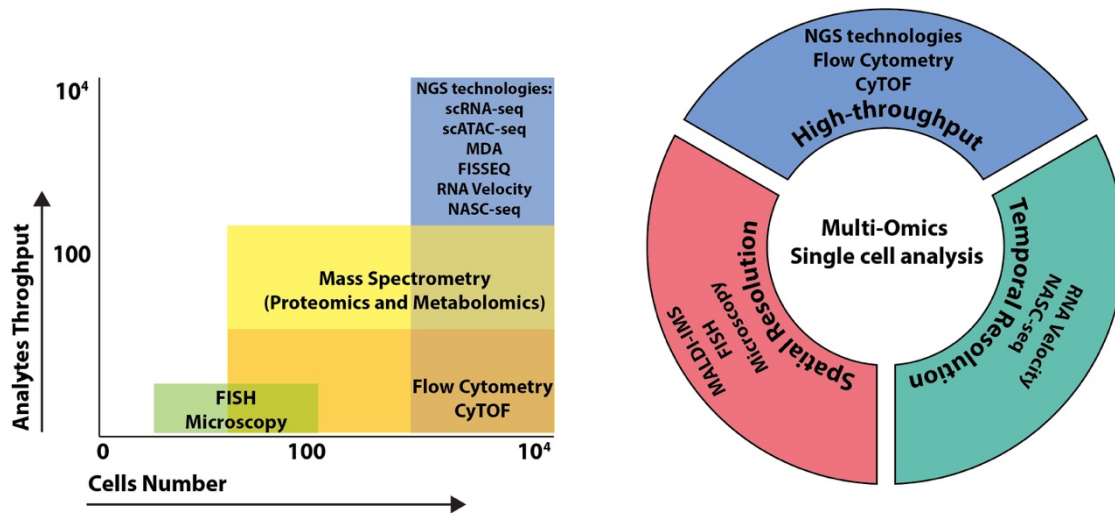


Figure 7. Main single-cell omics techniques. The throughput landscape of the latest single-cell analytical methods. On the x axis the number of cells that can be analysed in a single experiment is shown, while on the y axis, the number of analytes that can be identified. Different experimental approaches are required to quantitate and model single-cell properties of a complex organism. Multi-omics single-cell analysis that link functional, spatial and temporal scales in a high-throughput way will help to explain the multicellular dynamic interactions caused by cellular variability (right panel).

1.4.1 Single-cell sequencing

Quantitative polymerase chain reaction (qPCR) was one of the first genomic technologies to be used for measuring the expression of selected genes from single-cells. However, measuring multiple genes simultaneously from hundreds of individual cells was high time and cost consuming. This problem was overcome in the mid-2000's when, the first genomic sequencing of a single microorganism (Lasken RS, 2007), encouraged the birth of high-throughput single-cell next generation sequencing (NGS) analysis.

In less than a decade, improvements in NGS analysis provided reliable methods for high-quality measurement of DNA and RNA expression level, for a better understanding of the function of individual cells in multicellular context (Mardis ER, 2011; Metzker ML et al., 2010)

Single-cell sequencing technologies were developed to determine single-nucleotide variations (SNVs), copy number variations (CNVs), genomic structural variations of the single-cell genome, gene expression levels, gene fusion, alternative splicing of the single-cell transcriptome, and even the state of DNA methylation.

1.4.1.1 Single-cell genomics

In single-cell genomics one limiting step is the amplification of the single copy of a genome while minimizing the introduction of artefacts. Before the emergence of NGS technologies, whole genome amplification (WGA) methods such as ligation-anchored PCR (LA-PCR) (Troutt AB et al., 1992), primer extension pre-amplification PCR (PEP-PCR) (Zhang L et al., 1992) and degenerate oligonucleotide-primed PCR (DOP-PCR) (Telenius H et al., 1992), generated high amplification bias, leading to extremely low and uneven coverage of the genome and to the introduction of high number of mutations. Owing to these inherent drawbacks, PCR- based WGA methods are not appropriate for single-cell sequencing.

One possibility are isothermal methods such as multiple displacement amplification (MDA). MDA uses isothermal random priming and extension with Φ 29 polymerase, which has high processivity, a low error rate and strand displacement activity, resulting in a greater genome coverage, with lower error rates (Lasken RS, 2007). Thanks to technological improvements, single-cell genomics is now applied in diverse areas as microbial ecology, cancer, prenatal genetic diagnosis and the study of human genome structure and somatic variation and haplotype measurement (Marcy Y et al., 2007; Blainey PC, 2013; Shapiro E et al., 2013; Peters BA et al., 2013; McConnell MJ et al., 2013).

1.4.1.2 Single-cell epigenomics

In mammals, epigenetic regulation is crucial during development, cell differentiation, and proliferation (Bernstein BE et al., 2007). Epigenetic modifications include DNA methylation, chromatin remodelling, histone modification, and non-coding RNA (ncRNA) associated mechanisms (Egger G et al., 2014). Histones modifications are typically analysed using chromatin immunoprecipitation followed by sequencing (ChIP-seq). This method is highly

dependent on the specific binding of the antibody to histones and DNA-binding proteins, and requires a large number of cells as starting materials thus, not allowing single-cell high-throughput analysis (Zhou VW et al., 2011).

Another important topic in epigenomics is the understating of the spatial proximity and nuclear organization of specific genomic loci. Hi-C, first introduced in 2009, brings these analyses to the omic level by coupling proximity-based ligation with sequencing (Erez Lieberman-Aiden et al., 2009). Variations and optimizations have been performed to increase throughput and resolution to the single-cell level with a method referred to as single-cell Hi-C (scHi-C) (Flyamer IM et al., 2017; Nagano T et al., 2013; Ramani V et al., 2017). scHi-C has allowed visualization and reconstruction of the 3-dimensional organization of every chromosome in individual haploid cells and revealed how data from bulk analysis can obscure the dynamic reorganization of chromosome compartments during the cell cycle (Nagano T et al., 2017).

Another technique used to identify accessible DNA regions is Assay for Transposase-Accessible Chromatin (ATAC-seq), whose resolution has been improved with the development of single-cell ATAC-seq (scATAC-seq) (Buenrostro JD et al., 2013; Buenrostro JD, et al., 2015).

1.4.1.3 Single-cell transcriptomics

The first single-cell RNA sequencing (scRNA-seq) study was published in 2009 (Tang F et al. 2009) just a year after the first bulk RNA-seq publication (Mortazavi A et al. 2008). Although, they have been the first to combine whole transcriptome amplification (WTA) technology with NGS technologies, their method still required manual manipulation and was restricted to inspecting few cells. Further studies allowed the analysis of the limited mRNA transcripts from single-cells in a high-throughput manner with less sample manipulation (Lafzi A et al. 2018; Picelli S 2016; Svensson V et al. 2017). Among these methods, CEL-Seq (Hashimshony T et al. 2012), CEL-Seq2 (Hashimshony T et al. 2016), Drop-seq (Macosko EZ et al. 2015), Smart-seq (Ramskold D et al. 2012), Quartz-seq (Sasagawa Y et al. 2013), inDrop (Klein AM et al. 2015) and SPLiT-seq (Rosenberg AB et al. 2018) have been extensively used.

Typically, individual cells are isolated using microfluidics devices or droplet-based methods. In the first approach, single-cells are passively separated into individual wells of a microfluidic system, according to their size. Alternatively, in droplet-based cell isolations, cell mixture is fed into a microfluidic device, while beads coated in primers enter another input and capture up to thousands of cells at the time despite their size. Once isolated, individual cells are lysed, barcoded and reverse transcribed to cDNA using poly A tailing (Quartz-seq, Quartz-seq2), template-switching (Smart-seq, Smart-seq2, Chromium (10x Genomics)), or a combination of Ribonuclease (RNase H) with DNA pol I from *E. coli* (CEL-seq, CEL-seq2, MARS-seq, inDrop and sci-RNA-seq). Given the limited amount of material, the cDNA is amplified using standard PCR approaches, Rolling Cycle Amplification (RCA) or in vitro transcription (IVT) strategy. Finally, single-cells are sequenced and barcodes are used to assign sequencing reads to individual cells. Some of the available methods can collect reads from the entire transcript (full-length coverage), while others only capture the 3'- or 5'-ends.

Thanks to technological improvements, scRNA-seq has produced in the last years valuable insights on the dynamics of embryonic development and stem cell differentiation (Semrau S et al., 2017; Zeng C et al., 2017; Guo J et al., 2017), the composition of complex tissues (Hochane M et al., 2019; Wang P et al., 2018), expression differences and heterogeneity caused by cancer (Patel AP et al., 2014) and identification of rare cell subtypes (Xie T et al., 2018; Rodda LB et al., 2018; Aizarani N et al., 2019).

Other promising technologies are those allowing the study of individual cells in their natural microenvironment while maintaining the spatial information (Lee JH et al., 2014; Lee JH, 2017). Among them single-molecule fluorescence in situ hybridization (smFISH), Multiplexed error-robust FISH (MERFISH) or Fluorescent In Situ RNA Sequencing (FISSEQ) that allows highly multiplexed subcellular RNA sequencing are the most used.

1.4.2 Single-cell temporal omics approach

Single-cell omics technologies have helped in elucidating the role of cell-to-cell variability and revealed the complexity of developmental processes, gene regulatory networks, and cell fate commitment. High-throughput cell transcriptomics methods can provide snapshots of cell

and microenvironment states with an unprecedented depth of information, allowing the study of spectrums of cell types and their spatial organization within tissues. However, these methods cannot produce, can lost or hide, information about cell state transitions, the history of a cell and functional significance of putative aging-related heterogeneity (Isildak U et al., 2020).

The emergence of single-cell temporal omics approaches to profile dynamical processes, during tissue development, homeostasis and regeneration, has been crucial to characterize intermediate states (Mayr U et al., 2019; Lederer AR and La Manno G, 2020). In a recent study, La Manno et al. developed a method called “RNA velocity”. In this approach they use the ratio of unspliced mRNA to spliced mRNA of each gene, to deduce a probabilistic description of expression dynamics of future expression states (La Manno G et al., 2018). RNA velocity has been used in developmental studies (Lo Giudice Q et al., 2019; Xia B et al., 2019) and to describe pathological changes in human tissues (Zhang Q et al., 2019).

Other approaches are based on labelling newly synthesized RNA during transcription. A method called transcriptome alkylation-dependent single-cell RNA sequencing (NASC-seq) for example, is able to simultaneously sequence pre-existent and newly synthesized RNA providing high temporal resolution of short-term changes in gene expression even for the most unstable RNA (Hendriks GJ et al., 2019).

Lineage reconstruction is another challenge in biology. In 2017, Frieda et al. described a synthetic system that enables cells to record lineage information in the genome. This method, called memory by engineered mutagenesis with optical in situ readout (MEMOIR), is based on a set of barcoded recording elements termed scratchpads that can be altered by CRISPR/Cas9-based targeted mutagenesis, and later read out in single-cells through single-molecule RNA FISH (smFISH) (Frieda KL et al., 2017).

1.4.3 Single-cell proteomics and metabolomics

During the last 10-15 years, single-cell “omics” field has made substantial progress, especially in the area of genomics and transcriptomics. However, cells can differ in their proteomes and

metabolomes with significant functional consequences. Thus, single-cell proteomic and metabolomic studies can provide a wider picture of the heterogeneity among cancer cells in response to drugs, stem cells during differentiation and dynamics of immune cells (Wang YJ et al., 2019; Saadatpour A et al., 2015; Lu Y et al., 2017; Cohen AA et al., 2008). Proteomics and metabolomics are still challenging techniques due to the large dynamic range of the cellular proteome and metabolome, high complexity of the sample, rapid response to external stimuli, the difficulty of amplifying them and the absence of labelling methods for metabolites.

Mass Spectrometry (MS), a label free technique, with recently improved detection limit to the range of sub-attomole to zeptomole, in combination with the development of new metabolite and protein databases, is considered the best candidate for multiplexing, unlabelled and untargeted study of single-cell proteomics and metabolomics. However, there are still practical issues, such as the difficulty in interfacing single-cell samples with the MS instrument, high-throughput and sample handling (Zenobi R, 2013).

1.4.3.1 Proteomics

Measuring genomics and transcriptomics in single-cells can provide qualitative information on proteins as gene-products, but cannot provide information on their concentration and expression levels, localization, post-translational modification (PTMs) or protein-protein interactions. Conventional antibodies-based techniques such as flow cytometry and fluorescence microscopy have been powerful tool to study single-cell phenotypes but they are not comprehensive due to the limited amount of information and limited number of cells that can be analysed.

Flow cytometry is the most established method for both qualitative and quantitative multiparameter analysis of single-cells. With this method is possible to simultaneously measure 10–15 proteins in individual cells (De Rosa SC et al., 2001; Perez OD and Nolan GP, 2002). However, measurements beyond three fluorophores become more complex. Furthermore, sample preparation is still done manually and therefore requires a large number of cells that makes hard to analyse rare cell types.

A promising technology that combines flow cytometry and inductively coupled plasma MS (ICP-MS) is the mass cytometry, CyTOF (Cytometry by Time of Flight) (Bandura DR et al., 2009; Han G et al., 2018). CyTOF enables the simultaneous detections of signals with up to 50 parameters in millions of single-cells using antibodies that can be conjugated to metal isotopes instead of fluorophores. This method enabled the identification of rare cell types, new details on immune system regeneration and reprogramming regulators (Wang YJ et al., 2016; Lakshmikanth T et al., 2017; Lujan E et al., 2015).

Standard MS is also considered a powerful tool for label free and unbiased protein analysis, although is still limited to very abundant protein. To fill this gap, fractionation of the cell lysate by Capillary Electrophoresis (CE) prior to MS offers a good way to improve sensitivity (Mellors JS et al., 2010). Nemes et al. have developed a home-made microanalytical CE platforms for identifying proteins by high-resolution MS at ultrahigh sensitivity, identifying more than 1000 proteins from single *X. laevis* embryos (Lombard-Banek C et al., 2016). More recently the same group demonstrated the ability of CE-ESI-MS to analyze in situ more than 700 proteins in live embryos of *X. laevis* and zebrafish revealing previously unknown proteomic reorganization during embryo development (Lombard-Banek C et al., 2019).

Another platform dedicated to single-cell proteomics after fractionation is nano-LC-MS/MS that was used recently to identify specific markers for different cell type in lung primary cells (Zhu Y et al., 2018).

1.4.3.2 Metabolomics

Metabolomics provides the most immediate and dynamic picture of the functionality of a cell, linking its genotype, which describes its potential, and the phenotype, which describes its function. Thus, metabolites (amino acids, sugars, and lipids) could represent a “fingerprint” of each cell, having each one their role in cellular signaling cascades, epigenetics mechanisms and post-translational modifications (Johnson CH et al., 2016).

Single-cell metabolomics is not particularly new; in the late 1990s, Fung et al. profiled a handful of metabolites from single rat peritoneal mast cells using laser vaporization MS (Fung EN et al., 1998). In the following decade, a few more studies on single-cell metabolomics were reported, even though, these methods enabled the detection of only few cells and of a minor subset of abundant metabolites, due to sensitivity limitations and, extensively analyte loss during the preparation steps.

Recent progress in the field of MS, with the development of method with high mass resolution and high sensitivity, provides great hope for future successes in detecting and identifying metabolites in single-cells. Among the different ionization methods, the soft techniques (ESI, MALDI and DESI), that cause minimal fragmentation, are the favored method to identify both known and unknown metabolites.

Based on MALDI-MS (Matrix-Assisted Laser Desorption Ionization), Urban et al. developed a high-throughput platform to analyze thousands of individual cells in one experiment, called microarrays for mass spectrometry (MAMS). The MAMS chips are made of hydrophilic wells that enable automated isolation of single-cells. Using the platform, the authors monitored the metabolism of single yeast and algal cells and observed intrinsic variabilities that were not accessible by population-based metabolomics (Ibanez J et al., 2013; Urban et PL al., 2010). Since high-throughput analysis are always challenging, Ong et al. proposed a workflow in which cells are dispersed onto a microscope slide and then optical images are used to determine the cell coordinates to automatize MS measurements (Ong TH et al., 2015).

Based instead on nano-DESI-MS (Desorption ElectroSpray Ionization), Bergman and Lanekoff developed a method to measure 50 different lipids from single human cheek epithelial cells deposited on glass slides (Bergman HM and Lanekoff I, 2017). In a similar approach to nano-DESI, Pan et al. developed the single-probe electrospray (ESI). Their method allows direct sampling in live cells, enrichment of metabolites, which improved the sensitivity, subcellular detection with miniaturized probes, and simplified device with reusable probes (Pan N et al., 2014). With this approach it was possible to identify metabolites in Hela cells, in single marine dinoflagellate cells (*S. trochoidea*) and in single *Allium cepa* cells (Pan N et al., 2014; Gong X et al., 2014; Sun M et al., 2018).

Based on nano-ESI-MS, Mizuno et al., developed a method called “live single-cell mass spectrometry” (LSC-MS). In this method, an optical microscope is used to target an individual cell with a sharp metal coated nanospray microcapillary that penetrates the cell wall or membrane of live cells and withdraws a portion of the intracellular content that can be further analyzed by ESI-MS (Mizuno H et al., 2008; Fuji T et al., 2015).

The vast majority of the MS methodologies described above, directly introduce cellular contents into the mass spectrometer to facilitate analysis from small sample volumes. However, simultaneous ionization of all cellular contents, including phospholipids and salts, can introduce ionization suppression and hinder the observation of low abundance analytes. The added dimension of separation before MS analysis can reduce these limitations and improve detection limits for less abundant compounds. One example is capillary electrophoresis (CE) coupled to ESI-MS. CE-MS was used to detect hundreds of metabolites in single neurons from the sea slug *Aplysia californica* or during the development of a 16 cell *Xenopus laevis* embryo (Nemes P et al., 2011; Onjiko RM et al., 2015; Onjiko RM et al., 2017).

1.5 Imaging Mass Spectrometry (IMS)

While all the aforementioned metabolomics and proteomics techniques, have been reasonably successful in revealing cell-to-cell variability, the degree of manipulation required and the technical complexity associated, have limited their use to low multiplexing capacity. Moreover, the integration of spatial information is another frontier in the field that will be critical for linking single-cell phenomena to organismal behavior. To fill this gap, imaging studies seem to be a natural starting point, and among them, a rapidly emerging technique with a potential use in single-cell metabolomics and proteomics is imaging mass spectrometry (IMS).

IMS is a MS-based technique that enables the detection of molecules in situ, in a space-resolved fashion and generates distribution maps of a wide range of molecules, in the same specimen, without the need for invasive labelling and without altering the morphology of the tissue.

IMS was first introduced almost 50 years ago, using laser desorption ionization (LDI) and secondary ion mass spectrometry (SIMS) to study inorganic compounds and semiconductor surfaces respectively (Hillenkamp F et al., 1975; Castaing R and Slodzian G, 1981). However, it was the pioneering work of Bernhard Spengler first and Richard Caprioli then, in the late 1990s, to demonstrate how MALDI could be applied to analyse biomolecules (as proteins and lipids) in cells and tissue (Spengler B et al., 1994; Caprioli RM et al., 1997).

The principle of IMS is that to ionize the biological material present in a discrete spot of the sample and to collect the relative mass spectrum. The sample is then moved to reach another spot, until it is completely scanned. Each peak in the collected spectra can then be used to reconstruct an image that represents the distribution of that peak (and of the associated compound) in the sample. Nowadays, several ionization strategies are used in IMS: Desorption Electrospray Ionization (DESI), Secondary Ion Mass Spectrometry (SIMS) and Matrix-Assisted Laser Desorption/Ionization (MALDI), each of them with their pros and cons. Among them, SIMS and MALDI offer the highest lateral resolution enabling the visualization of metabolites at single-cell level (**Figure 8**).

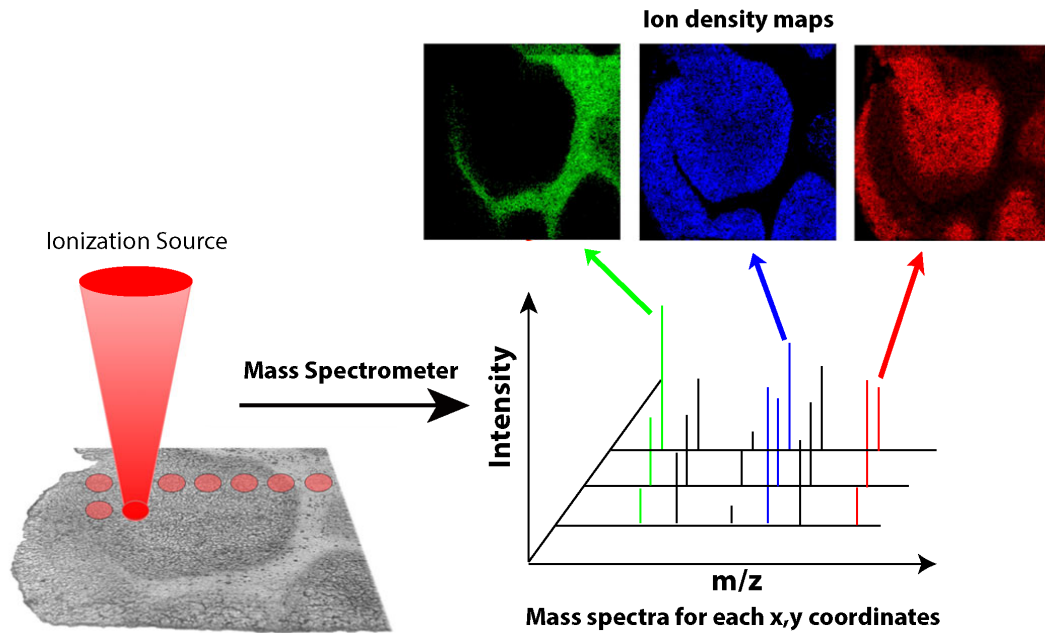
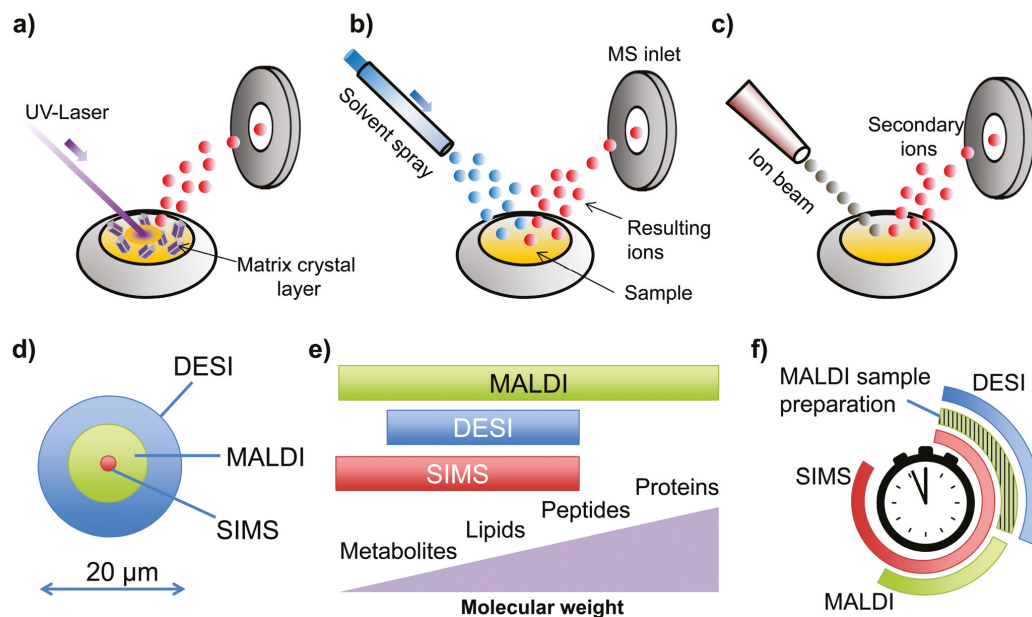
A**B**

Figure 8. Imaging mass spectrometry. A) Common IMS technologies. (a) MALDI-IMS requires applying an organic matrix across the sample in such a way that the analytes are locally extracted and incorporated into the matrix. (b) DESI-IMS requires a solvent spray directed towards the sample for desorption. (c) SIMS-IMS uses pulsed ion beams to locally desorb compounds from a certain position. (d) Spatial resolution reachable by the different ionization techniques. SIMS-IMS has the smaller laser diameter. (e) Mass range offered. MALDI-MSI, has the highest versatility in the mass range. (f) Sample preparation time. DESI is the fastest MSI method. (Figure B was adapted from Addie RD et al., 2015). **B)** In MALDI-IMS the tissue section is irradiated by a pulsed laser, an ion or a solvent spray beam that

raster the sample pixel by pixel. For each spot a mass spectrum is collected and then, mass images are reconstructed for each ion by plotting m/z intensity vs. x,y coordinates.

1.5.1 SIMS-IMS

In SIMS ionization, a focused primary ion beam is used to bombard a sample, ejecting secondary ions from the sample surface that are subsequently measured using a mass spectrometer. In imaging modality, Time-of-flight SIMS (TOF-SIMS) can reach submicron lateral resolution and is thus able to image the spatial distribution of metabolites in subcellular space. More and more researchers used TOF-SIMS for the detection of lipids and small molecules on single-cell surfaces (Kurczy ME et al., 2010; Colliver TL et al., 1997). One of its application for example, has been shown in 2013 when Leefmann and co-workers showed fatty acid cellular localization on cryosections of a phototropic microbial mat (Leefmann T et al., 2013).

SIMS-TOF has been also used to analyze 3D distribution of drugs in macrophages (Passarelli MK et al., 2015) or in HeLa cells (Huang L et al., 2016). Furthermore, the 3D depth profiling accuracy was validated by comparing the spatial distribution of polymeric nanoparticles measured by SIMS within HeLa cells with 3D optical data obtained by fluorescence labeling of polymeric nanoparticles (Graham DJ et al., 2016).

An improvement of TOF-SIMS is nanoscale SIMS (NanoSIMS), which combines high spatial resolution with simultaneous detection of both heavy and light elements. It was used to image and monitor the internalization of a new group of platinum-based chemotherapeutics in MCF7 breast cancer cells (Wedlock LE et al., 2013).

Despite its excellent lateral resolution, SIMS for single-cell analysis is typically limited in mass range to $m/z < 500$, and structural information is difficult to obtain. This is due to severe fragmentation of larger analyte ions and limited tandem mass spectrometry (MS/MS) capabilities in the imaging mode.

1.5.2 MALDI-IMS

Compared to SIMS-IMS, MALDI-IMS is considered a better technique to analyse small and large molecules while causing minimal fragmentation (Zimmerman TA et al., 2008). In a typical MALDI-IMS experiment, a sample is mounted on a target plate, coated with a homogenous layer of an organic matrix, placed in an ionization chamber and analyzed by a laser beam that 'scans' a specific area of the sample and collects a mass spectrum for each coordinate. MALDI-IMS is completely label-free and it has been optimized to work at atmospheric pressure with minimal sample manipulation.

The main disadvantages of MALDI-IMS in the past were the high vacuum in the ionization chamber and its low spatial resolution ($> 10\ \mu\text{m}$) that have limited studies of metabolites distribution among single-cells. Recent technological developments have led to the setup of atmospheric pressure instruments able to reach a spatial resolution of $< 2\ \mu\text{m}$, while maintaining good mass resolution and accuracy, thus allowing single-cell imaging. For example, atmospheric pressure scanning microprobe MALDI (SMALDI) or high vacuum transmission geometry, coupled with Orbitrap instruments, can allow higher spatial resolution, while keeping high sensitivity and mass accuracy (Spengler B and Hubert M et al., 2002; Zavalin A et al., 2012).

Several recent studies using MALDI imaging for single-cell metabolite profiling, used high spatial resolution to target cellular and sub-cellular lipids localizations. Indeed, lipids are particularly suited for MALDI-IMS analysis for two main reasons: first, lipids are abundant and second, the vast majority of them are already charged and this improves their ionization efficiency. One of the first example of MALDI-IMS analysis at single-cell level was reported in 2012. Shober et al. utilized atmospheric pressure SMALDI to image a number of metabolites and lipids of individual HeLa cells with $7\ \mu\text{m}$ resolution (Shober Y et al., 2012). Soon after, with the development of transmission geometry, Zavalin et al., performed direct imaging of lipids in single-cells at cellular and sub-cellular resolution with $1\ \mu\text{m}$ spatial resolution (Zavalin A et al., 2012). Kompauer et al. then, developed an atmospheric pressure SMALDI system with

1.4 μm lateral resolution, which was used to image *P. caudatum* single-cell organisms with subcellular resolution (Kompauer M et al., 2017).

MALDI-IMS has been applied also to the study of neurons by Setou's group, to analyze differences in intracellular PtdCho metabolism, by combining a microfluidic compartmentalized culture system with IMS (Sugiyama E et al., 2018). Another study employed 3D MALDI-IMS to map lipids distribution during the embryonic development of zebrafish (Duenas ME et al., 2017).

While sub-cellular imaging, as described, can reveal unique insights into metabolites localization, studying the cellular heterogeneity requires a large number of cells to be analysed and thus, analytical and computational workflow. For example, Yang et al. applied MALDI-IMS to monitor the metabolite heterogeneity from > 100 single-cells in culture upon external stimulation (Yang B et al., 2018). Another solution has been proposed by Alexandrov's group with the development of SpaceM, a method for spatial single-cell metabolomics of cell monolayers that integrates MALDI-imaging mass spectrometry with bright-field and fluorescence microscopy. With this method they analysed > 100 metabolites in > 10000 individual cells (Rappez L et al., Biorxiv).

All these pioneering works showed that MALDI-IMS is a good candidate to study metabolites, by keeping the spatial information, at cellular and sub-cellular resolution. However, when going to such high spatial resolution (< 2 μm), sensitivity and ion yield decrease dramatically, impeding sometimes to obtain interpretable mass spectra and reducing the number of recognizable compounds detected per ionization event. To this aim, post ionization approaches have been developed that increase the ionization yield of MALDI-IMS

One of the most promising methods is called MALDI-2 where the beam of a second UV laser intercepts the plume generated by the primary MALDI laser to initiate a second MALDI-like ionization process leading to an increase of the ionization yields by up to two orders of magnitude (Soltwish J et al., 2015; Ellis SR et al., 2017). It has been shown that coupling the use of transmission geometry with MALDI-2 ionization it is possible to achieve crucial sensitivity and spatial resolution to visualize even less abundant metabolites at single-cell and sub-cellular level in tissue sections and cultured cells (Niehaus M et al., 2019).

1.6 Goal of the project

Recent advances in single-cell biology have provided scientists with tools to study the variability associated with individual cells. Thanks to these approaches, cell-to-cell heterogeneity has emerged as a driver of self-organization, tissue development, differentiation events and multicellularity. While single-cell data are available for nucleic acids and by derivation for protein expression, they are still scarce for metabolic products (such as lipids), even though some studies have addressed and found that single-cell lipid variability plays a key role during development. Major reasons for this knowledge gap are the difficulties to visualise lipids in their biological context and to systematically analyse their amounts at the single-cell level.

The main goal of this research project was to systematically study single-cell lipid variability and to investigate whether and how lipids can influence cell states and contribute to cell identity.

Therefore, this project can be divided as follows:

- Developing a workflow to systematically visualize a consistent fraction of the lipidome in single-cells by using MALDI-IMS on dermal human fibroblasts (dHFs).
- Investigating cell-to-cell lipid variability.
- Understanding the origin of single-cell lipid variability and whether specific lipid compositions relate to cellular states.
- Evaluating how highly variable lipids participate in the maintenance of dHFs transcriptional states.

CHAPTER 2. SINGLE-CELL LIPIDOMICS OF DERMAL HUMAN FIBROBLASTS

Lipids are key components of eukaryotic cells since they contribute to several biological functions. Thanks to lipidomics, we now appreciate the lipid compositional dynamics of the cells and recent developments have provided MS with enough sensitivity to reveal molecules in a few hundred copies, making single-cell lipidomics possible. A technique with a potential use in single-cell lipidomics is Imaging Mass Spectrometry (IMS) and, in particular, MALDI-IMS. Indeed, latest MALDI-IMS instruments have reached a spatial resolution $< 10 \mu\text{m}$, thus allowing single-cell imaging. In this chapter, we aim to develop a workflow for single-cell lipidome analysis through MALDI-IMS.

2.1 Single-Cell Lipidomics by MALDI-IMS

In our workflow, we combined the use of high-resolution ($25\text{--}50 \mu\text{m}^2$ pixel size) MALDI-IMS [AP-SMALDI10/5, TransMIT GmbH] and of large cells (i.e., dermal human fibroblasts) to investigate the lipidome of hundreds of individual cells cultured in standard laboratory conditions. According to this pipeline, low passage dermal Human Fibroblasts (dHFs) were fixed, coated with a MALDI matrix (2,5-DHB) and analysed in positive ion mode with high resolution MALDI-IMS in the lipid mass range (**Figure 9**).

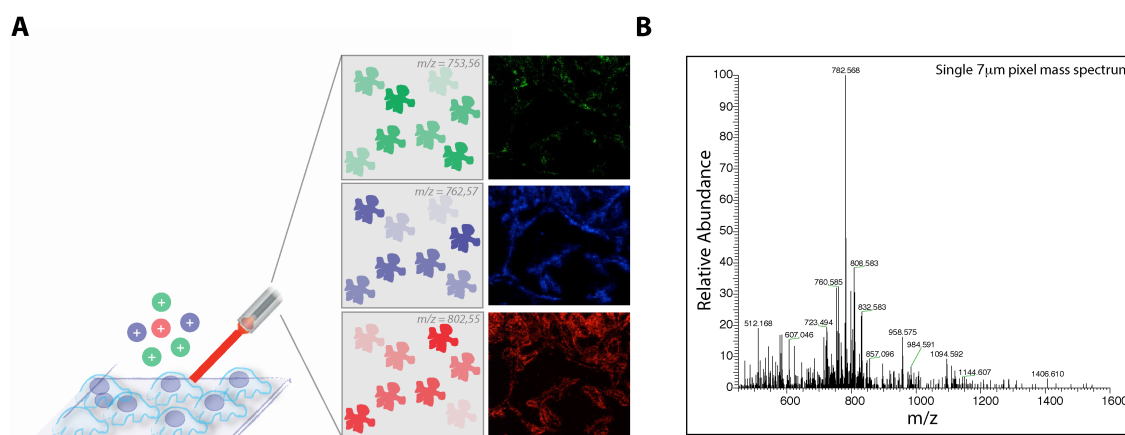


Figure 9. dHFs analysis workflow by MALDI-IMS. A) Schematic drawing of MALDI-IMS analysis. Cells were grown on coverslips, fixed and covered by a MALDI matrix. MALDI-IMS was performed on a small

area by rasterizing the laser across the field of the cells. Images of dHFs were reconstructed plotting the intensity of each m/z against the x,y coordinates. **B)** Mass spectrum acquired from a single $7\ \mu\text{m}$ /pixel mass spectrum in the lipid mass range (m/z 400-1600).

As a first step of data analysis, 296 mass images in the lipid range were extracted from raw data by either Mirion (Paschke C et al., 2013) or MSiReader software (Bokhart M et al., 2017). Subsequently, peak attribution and lipids identification were obtained by combining Alex123 (Husen P, 2013; <https://git.embl.de/ejsing/alex123>) and Metaspace metabolite annotation tool (Palmer A, 2017; <https://metaspace2020.eu>), and the LipidMaps database (Sud M, 2007; <https://www.lipidmaps.org>). As an independent validation of peak identity, lipid extracts from dHFs were analysed by Electrospray Ionization Liquid Chromatography Mass Spectrometry (ESI-LC/MS) and Multiple Reaction Monitoring (MRM) (**Table 1**). Specific peaks in the mass range of glycosphingolipids where their attribution was equivocal were further analysed by comparison with pure standards (**Figure 10**) or MS/MS fragmentation (**Figure 11**).

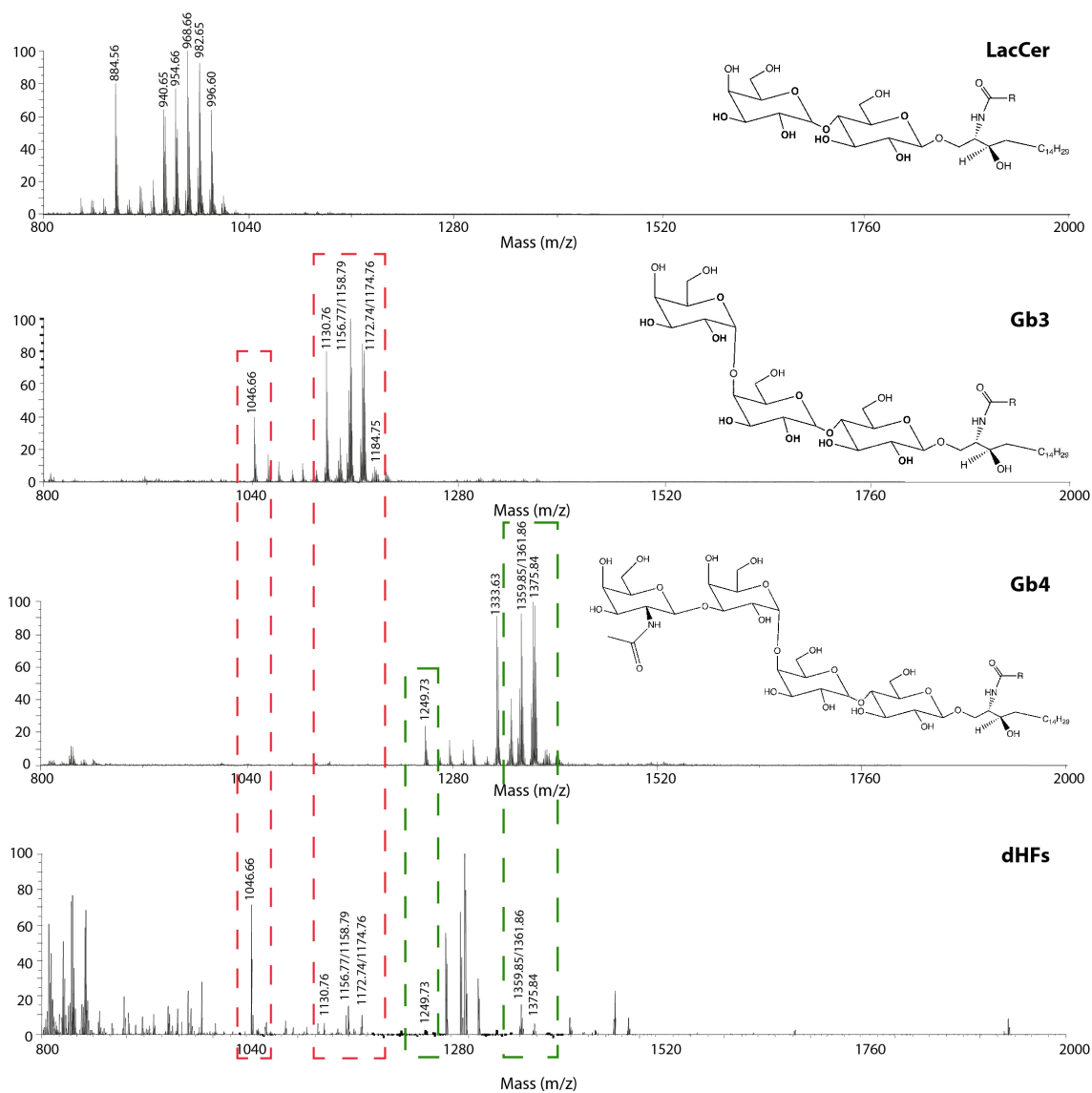


Figure 10. MALDI-TOF mass spectra of GSL standards. LactosylCeramide (LacCer), trihexosylceramide Gb3 and globosides Gb4 standards were analysed by MALDI-TOF in positive ion mode at 20 kV (upper panel) showing the presence of several species with different acyl chains. In the lower panel, lipids were extracted from dHFs and analysed by MALDI-TOF and compared to the mass spectra of GSL standards.

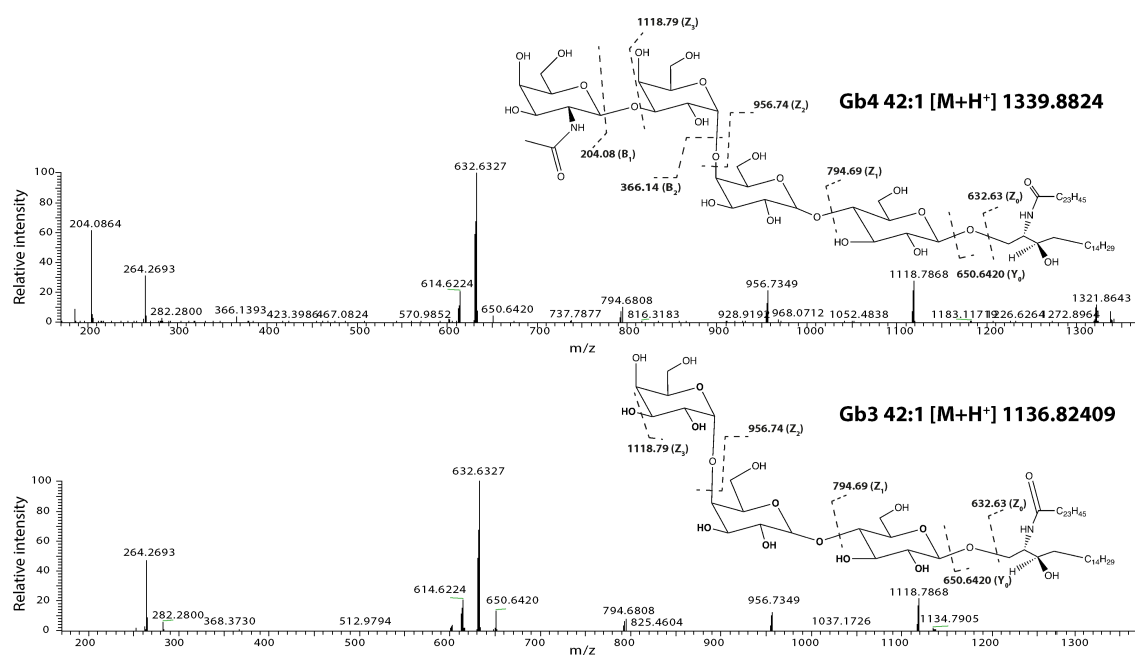
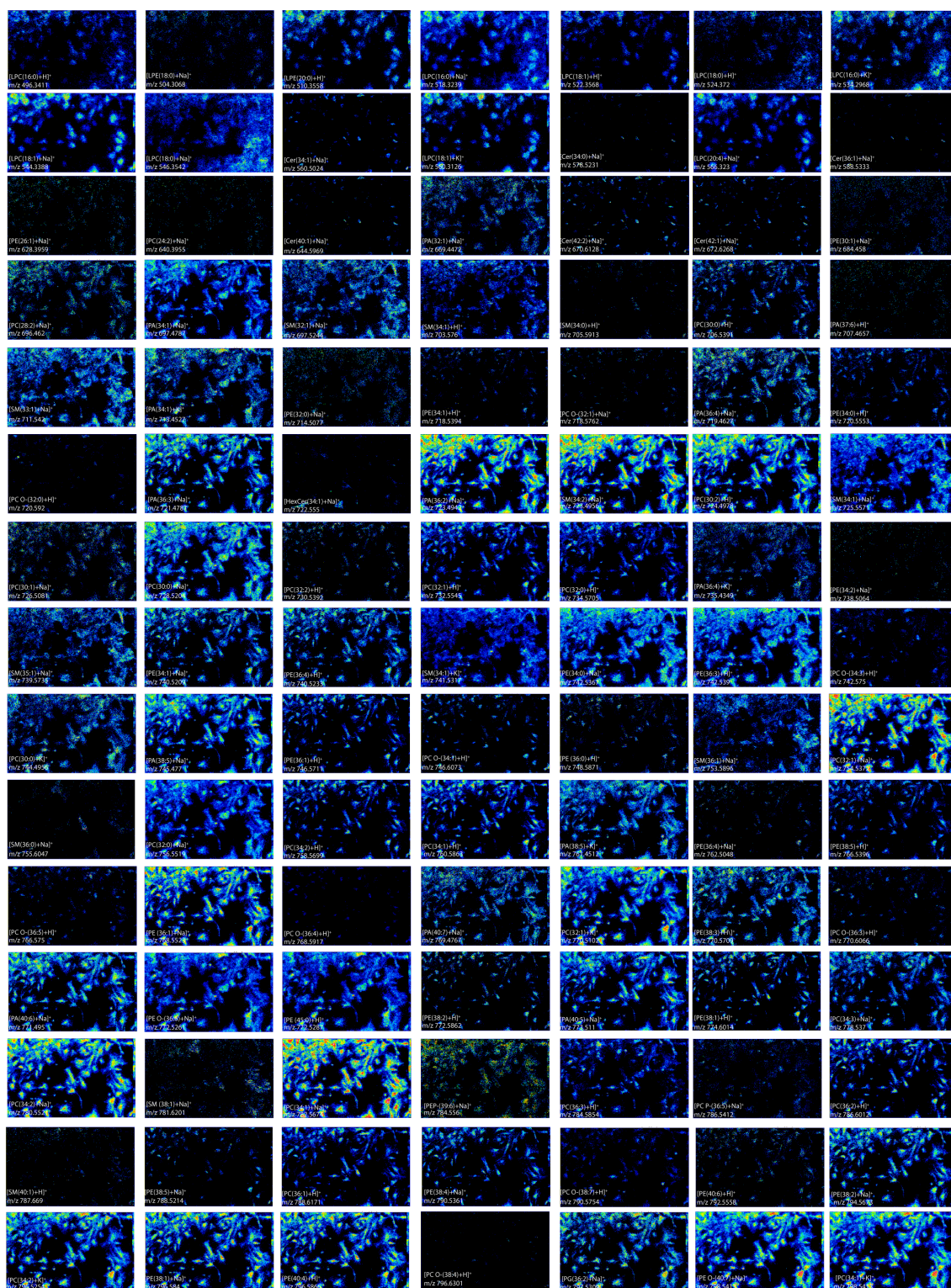


Figure 11. LC-MS/MS mass spectrum of Gb3 and Gb4. Lipids were extracted from dHFs and analysed by LC/MS analysis. Precursor ion species detected at m/z 1339.8824 and at m/z 1136.8240 were isolated and MS/MS fragmentations were obtained upon HCD fragmentation at 23 eV. Corresponding fragmentation scheme identified the precursor ion species as Gb4 (d18:1/C24:1) (upper panel) and Gb3 (d18:1/C24:1) (lower panel).

Based on the combination of these approaches, to each peak was associated an Attribution Confidence Score (ACS) obtained as detailed in methods. According to this procedure, 205 annotated peaks were obtained by MALDI-IMS (159 of which with high confidence; $ACS > 5$) (**Figure 12**) thus accounting for $\sim 12\%$ of the dHFs lipidome, as assessed by LC-MS (**Figure 13**). Therefore, by using MALDI-IMS we were among the first lab to accurately identify a good portion of the lipidome of a representative eukaryotic cell line with single-cell spatial resolution.



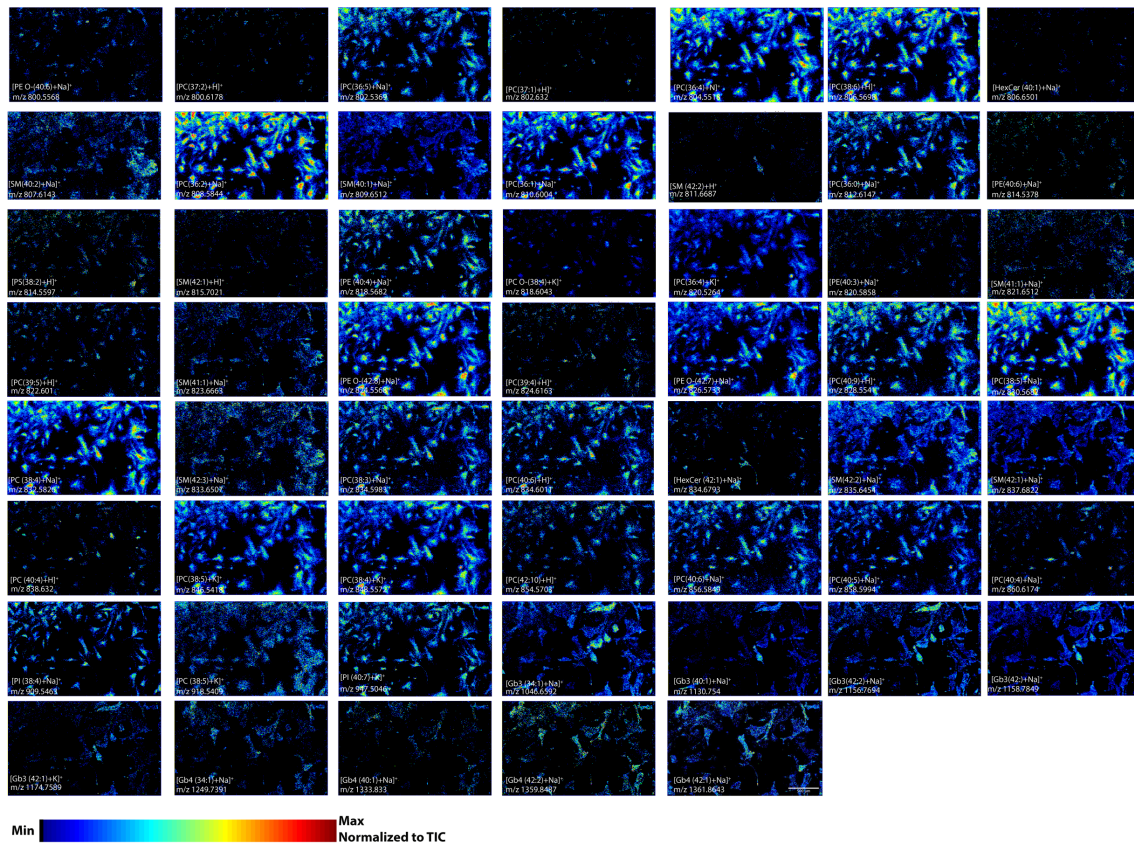


Figure 12. IMS images gallery of dHFs lipids identified with high accuracy. 7 μm ion images (354x218 pixels), extracted from MsiReader software, of 159 lipids identified with high ACS (>5). All signal intensities were normalized to the Total Ion Count (TIC). The maximum value for the ion intensities is found in the lower left corner. Scale bar is 500 μm.

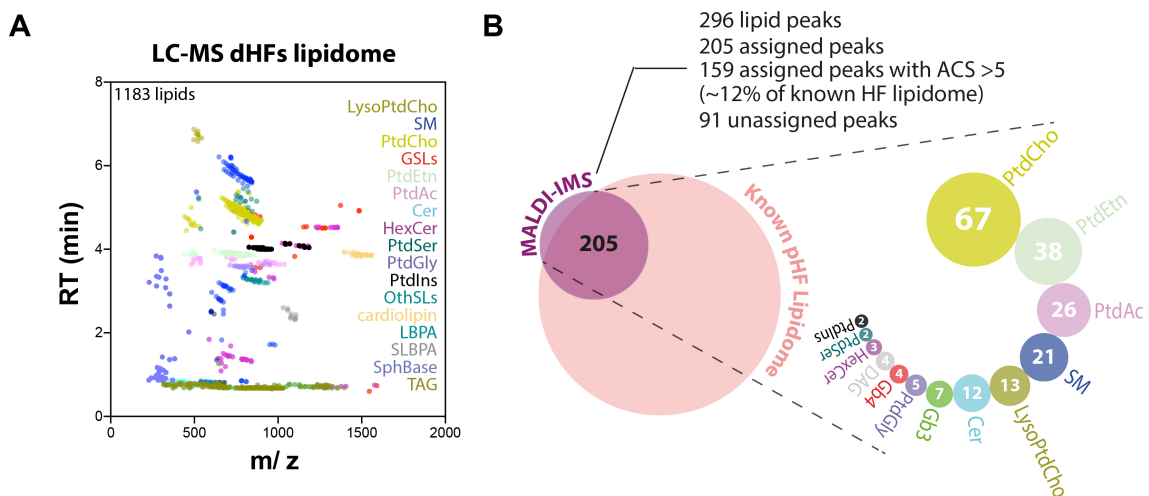


Figure 13. Comparison between LC/MS and MALDI-IMS lipidomics analysis of dHFs. **A)** Lipid extracts from dHFs, were separated on a HILIC column and analysed by ESI-LC/MS in positive ion mode. m/z

values for the whole dHF lipidome are plotted against their retention times. Each dot represents a lipid and colour code is according to the lipid species they belong to. 1183 lipids were identified from 17 different lipid classes. **B)** Positive ion mode MALDI-IMS analysis returned 296 ion images belonging to 13 lipid classes. By comparison with LC-ESI/MS, 205 lipids were identified, 159 of which with high confidence (ACS >5).

2.2 Single-pixel analysis on MALDI-IMS images

[The following analysis has been done in collaboration with Irina Khven]

On the mass images obtained by Mirion software, a single-pixel analysis was attempted. Here, intensity values in individual pixels of the 296 known and unknown lipids were considered. These values were used to build a multidimensional vector map, using Uniform Manifold Approximation and Projection (UMAP) analysis followed by clustering. Pixel clustering, based on the lipid composition of individual pixels, was able to discriminate between pixels belonging to cellular or intercellular space (**Figure 14A**). Randomly sampled pixels among those assigned to the cellular space were then used to generate a pixel similarity heatmap based on Pearson Correlation (PC) (**Figure 14B**). A few discrete pixels with similar lipid signatures could be recognized, suggesting that a finite number of lipid configurations exist in the sample.

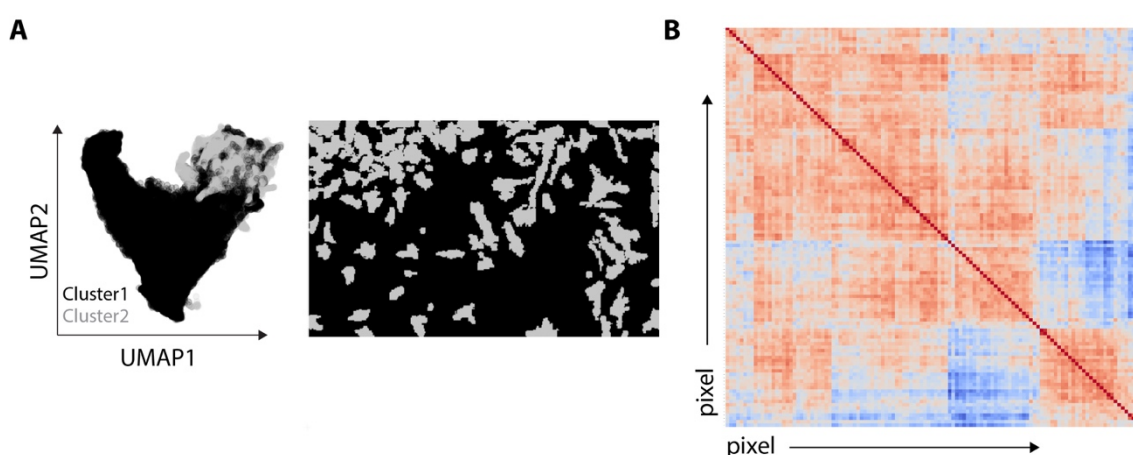


Figure 14. Single pixel analysis. A) UMAP analysis of single pixels lipid intensities, coloured by assigned cluster. Single pixels belonging to intercellular and intracellular space were discriminated into two clusters and mapped into the corresponding mass image. **B)** Pixel similarity heatmap based on Pearson

Correlation (PC). Log₁₀ normalized single pixel lipid values were used to calculate PC. Pixels with similar lipid composition were clustered together, both in vertical and horizontal axes, according to their PC and displayed as colour ranging from blue to red.

Thus, a Principal Component Analysis (PCA) was performed and the different Principal Components (PCs) were mapped into the corresponding mass image. In particular, when PC1 to 4 were mapped in the mass image, two interesting patterns emerged. PC1 and PC2 highlighted pixels populating inner and outer cell aspects, respectively, while PC3 and PC4 mapped to distinct cells (**Figure 15A**). This indicated that two major axis of lipid variation exist in dHFs: one deriving from the uneven intracellular distribution of lipids and another resulting from cell-to-cell heterogeneity. Major lipid contributors of the intracellular variability axis (PC1 and PC2) were sphingomyelins (SMs) (enriched in 'outer' cell pixels) and glycerolipids and ceramides (Cers) (enriched in 'inner' cell pixels) (**Figure 15B**). Lipids accounting for the cell-to-cell variation axis (PC3 and PC4) belonged instead to the glycosphingolipid (GSLs) series (i.e., trihexosylceramides [Gb3]; and globosides [Gb4]) (**Figure 15B**).

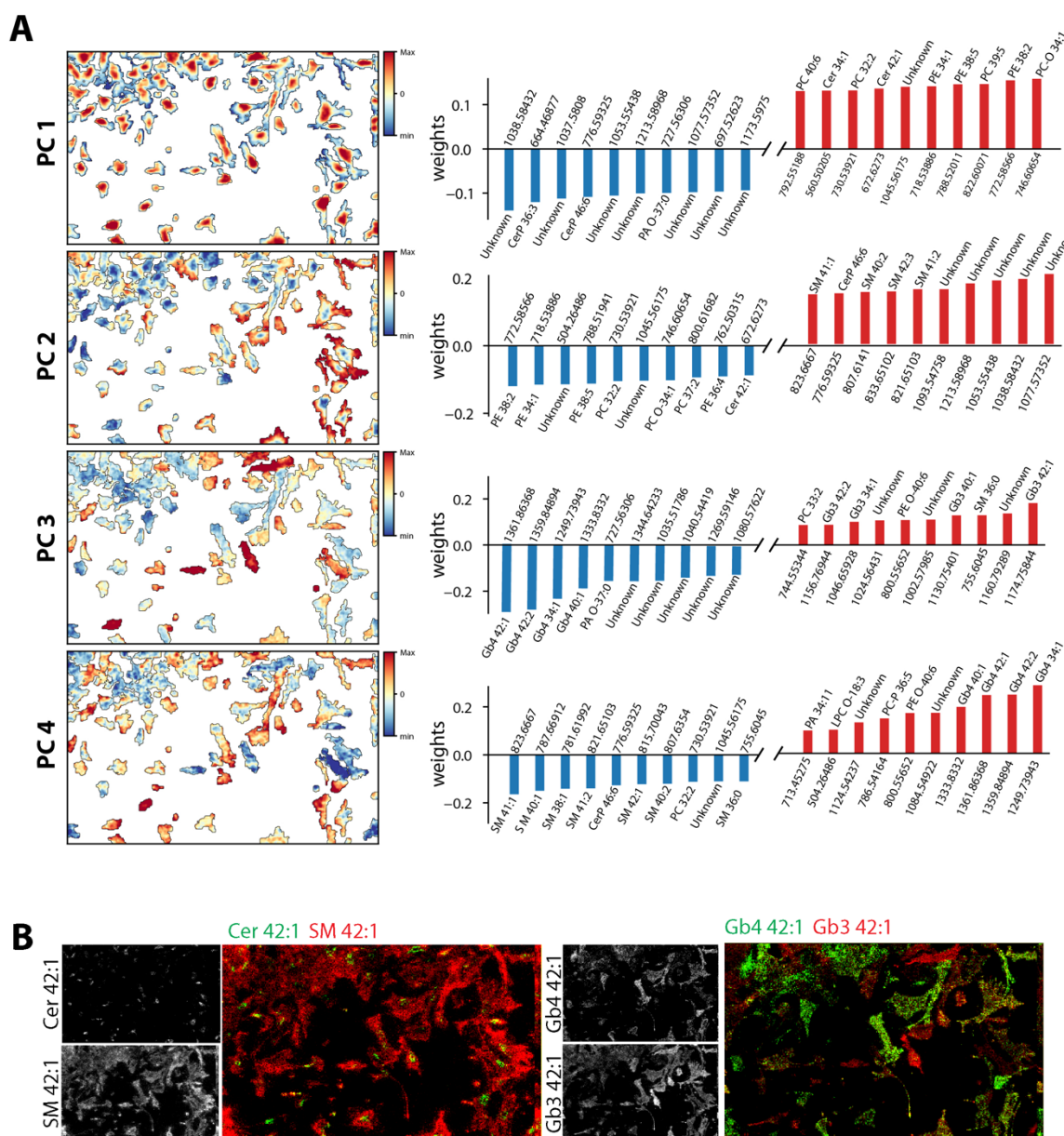


Figure 15. Principal Component Analysis of lipids based on single-pixel analysis. A) The intensity values for each non-background pixel were used for principal component analysis. PC1 to PC4 values are displayed on the correspondent mass image. Positive (red) and Negative (blue) contribution of variables to each principal component is shown. For every component, 10 loadings (lipids) that positively (red) or negatively (blue) contributed the most are shown. **B)** 7 μm ion images (354x218 pixels) showing the distribution of sphingolipids Cer 42:1 and SM 42:1 (left panel) or glycosphingolipids Gb3 42:1 and Gb4 42:1 (right panel).

2.3 Conclusions

This thesis is among the first report to use high spatial resolution MALDI-IMS to analyse dHF lipidome at cellular levels. With our approach we have measured 205 lipids (159 of which with high confidence), thus representing 12% of dHF lipidome. Moreover, by single-pixel MALDI-IMS analysis we revealed two major axes of variation in spatial lipid distribution: (i) an intracellular lipid inhomogeneity with complex sphingolipids preferentially populating peripheral cell areas and glycerolipids and sphingolipid precursors populating the perinuclear region; (ii) a marked cell-to-cell lipid variability whereby different sphingolipid species decorate the membranes of different cells in the population.

Firstly, the existence of discrete lipid environments (i.e., lipid territories) at different cell compartments is in agreement with the notion that the plasma membrane (represented by the 'outer' cell pixels) is enriched with SMs while glycerolipids are distributed to all cell membranes (Devaux FP, 1991; Op den Kamp JA, 1979; Sandra A and Pagano RE, 1978; Holthuis JCM and Menon AK, 2014) and major Cer pools are produced in intracellular (biosynthetic and degradative) compartments (Mullen TD et al., 2012) (represented here by the 'inner' cell pixels).

Secondly, these results align with previous reports where individual GSLs were found to vary in syngeneic cell populations (Russo D et al., 2018; Majoul I et al., 2002) and suggest that cell-to-cell variability is a conserved feature of GSL metabolism. Importantly, through this approach we were able for the first time to simultaneously evaluate the relative distributions of multiple GSLs and GSL precursors (>25 individual species) and to interpret them in the context of the overall local lipid composition.

CHAPTER 3. INVESTIGATION OF CELL-TO-CELL LIPID VARIABILITY

Lipids are key regulatory and bioactive molecules that have been shown to be cell-to-cell variable in syngeneic, homogeneous cell populations. However, cell-to-cell lipid variability has not been systematically explored so far, mainly due to technological barriers. We showed that MALDI-IMS is a good tool to study a large fraction of lipids in single-cell. Thus, in this chapter we studied cell-to-cell lipid variability deeper.

3.1 Cell-to-cell lipid variability

To investigate cell-to-cell variability we developed a dedicated MALDI-IMS workflow according to which, optical images were used to guide manual cell segmentation on MS images, and extract integrated count values for individual cells and for each of the MS peaks considered (**Figure 16**). Single-cells were therefore manually segmented to extract count values and the mass spectra were averaged for each Region of Interest (ROI). As shown in **Figure 17**, single-cells, defined as single ROI showed variable averaged mass spectra different from the one extracted from an area where only matrix is present.

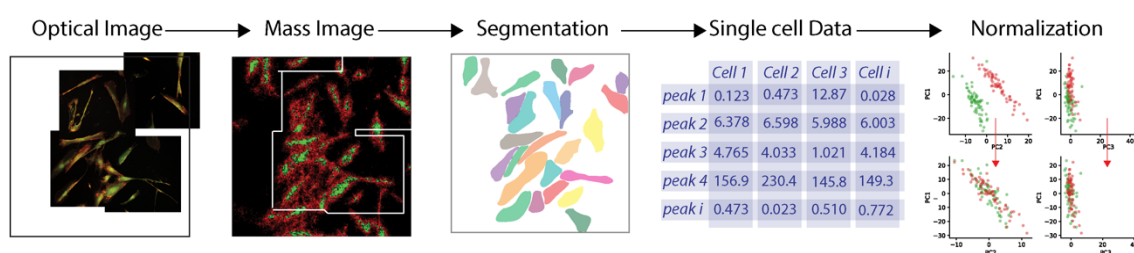


Figure 16. Single-cell IMS analysis workflow. Cells were grown on glass slides, fixed and processed for standard microscopy imaging. Microscopy images were then used as template to manually segment single-cells from 7 μm / pixel mass images reconstructed by MSiReader software. Single-cell ion abundance data were extracted with the Region of Interest (ROI) segmentation tool after normalization over total ion count (TIC) and batch corrected with ComBat algorithm.

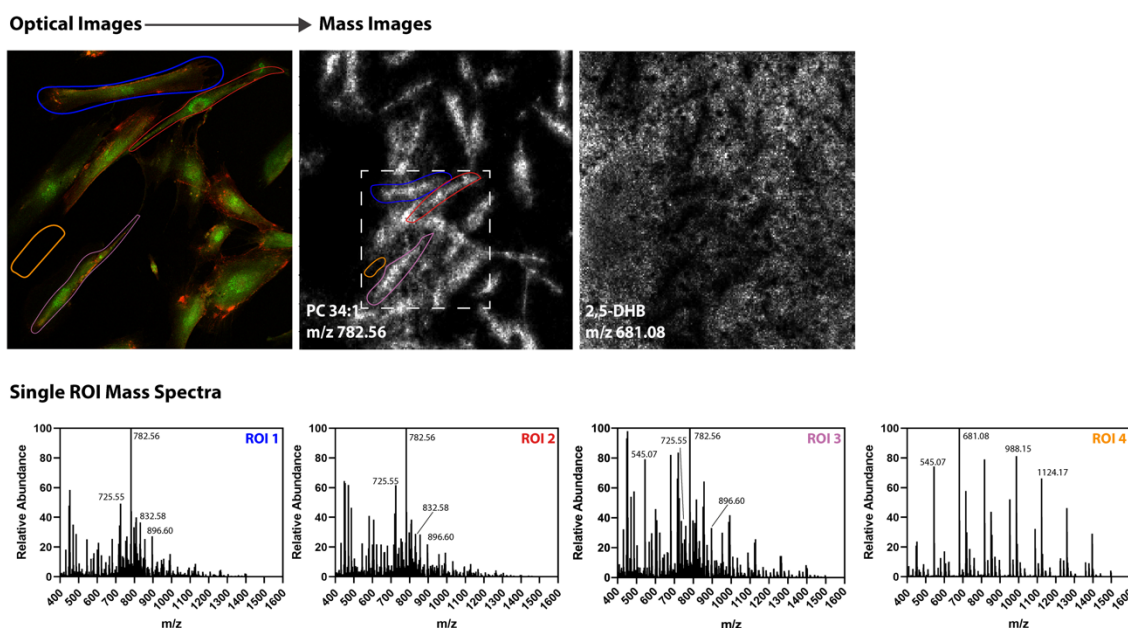


Figure 17. Single ROI mass spectra from individual cells. dHFs were fixed and stained for confocal microscopy with Phaseolus Vulgaris Lectins (red) and bodipy FL C5-Ceramide (green) to identify plasma membrane and intracellular compartments. Using microscopy images as template, cells were manually segmented to extract mass spectra from cells and from background (upper panel). In the bottom panel, single-cell averaged mass spectra in the lipid mass range (m/z 400-1600) are shown. Mass spectrum from the background shows peaks from 2,5-DHB MALDI matrix.

In order to increase the statistical power and the robustness of the results, IMS analysis were also performed with a higher spatial resolution system: AP-SMALDI5 (TransMIT GmbH).

Although the data coming from the two different instruments were processed using the python implementation ComBat (Johnson WE et al., 2007) to minimize batch effect, it was not possible to merge the two data set. Thus, the datasets were batch corrected separately (**Figure 18**) and kept separated for the following analyses. We analysed 160 cells with AP-SMALDI10 and 257 cells with AP-SMALDI5.

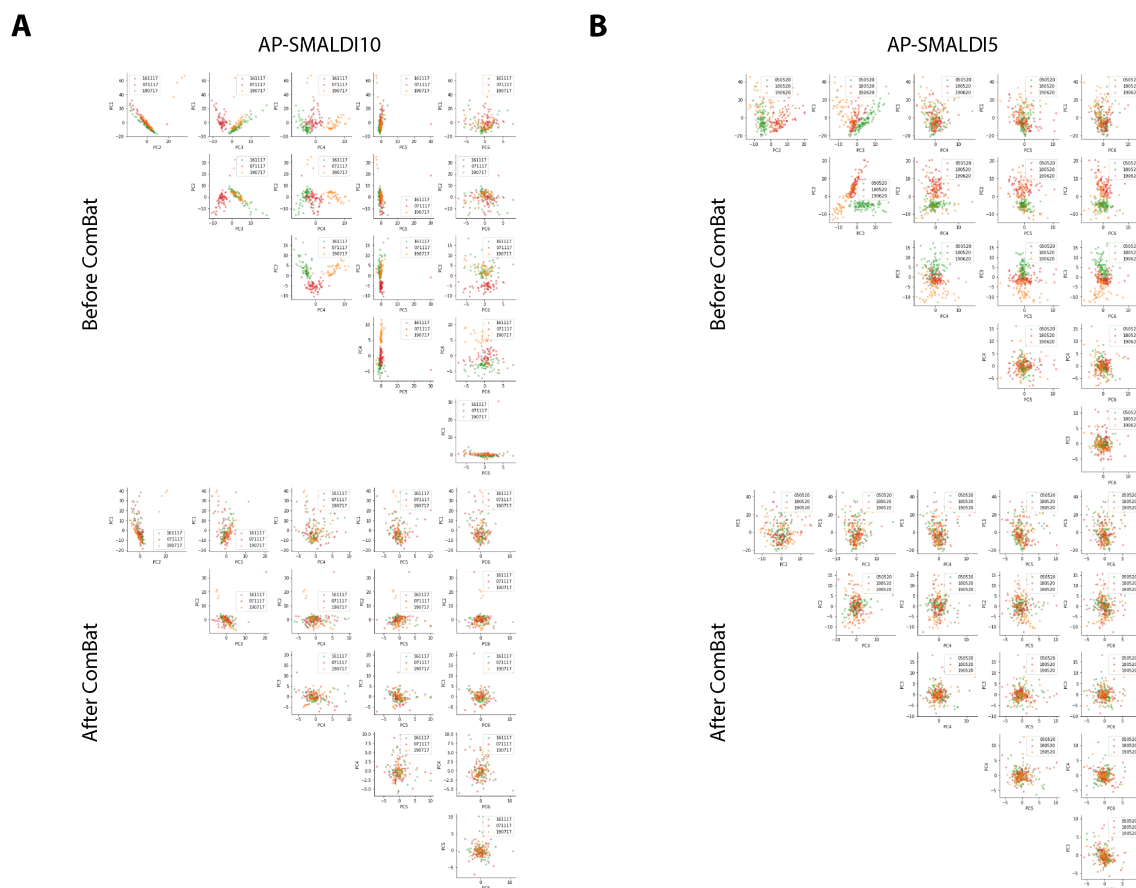


Figure 18. Batch correction analysis of single-cell lipid data. Batch correction of variability between three replicates of MALDI-IMS analyses on dHFs by using the ComBat algorithm. PCA plots of the single-cell lipid profiles with cells colour-coded according to the replicate before and after batch correction are shown. Data from AP-SMALDI10 and AP-SMALDI5 are shown in **A** and **B** respectively.

Batch corrected count values for individual cells and for each lipid were normalized according to their average values among individual cells and the obtained values were then used to cluster cells according to their lipid composition and lipids according to their co-variation among individual cells. In further details, the obtained single-cell lipidomics data were used to evaluate the cell-to-cell variability associated with individual lipid species expressed as Index of Dispersion (IoD; being the ratio of standard deviation over mean [σ/μ] of the normalized intensity values associated with a lipid across cell populations). The obtained values were used to rank lipids according to their decreasing IoD. As shown in **Figure 19**, lipid species annotated as sphingolipids (i.e., Cers, SMs, and GSLs) populated the top IoD ranking

positions. Thus, this suggests again that dHFs display a specific cell-to-cell variability in the sphingolipid synthetic pathway (**Figure 2**).

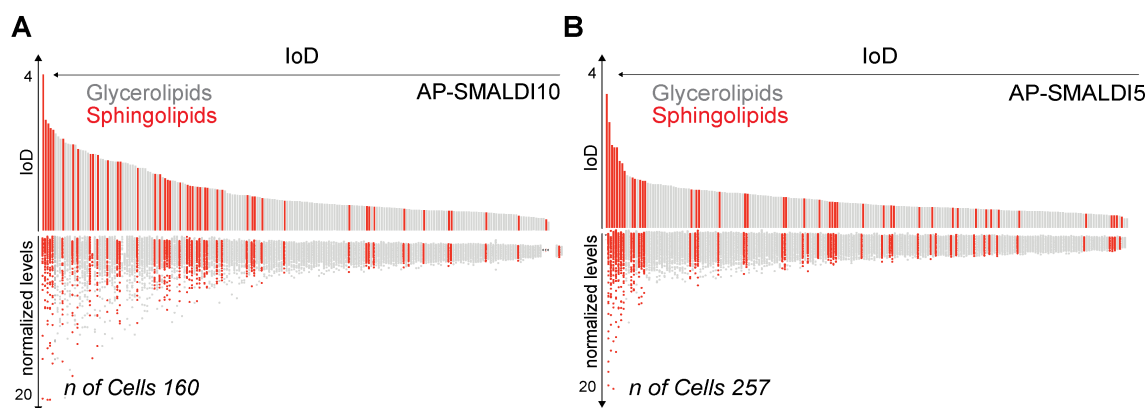


Figure 19. Lipid cell-to-cell variability. Batch corrected and normalized single-cell lipid values of 160 cells (**A**) and 257 cells (**B**) were used to determine cell-to-cell variability by using the Index of Dispersion (IoD). Lipids were ranked from the most to the least variable and colour coded according to the major lipid class they belong to (sphingolipids in red, glycerolipids in grey). Normalized lipid levels in each cell are shown in the bottom part of the plots. The same analysis was performed with two instruments: AP-SMALDI10 in **A** and AP-SMALDI5 in **B**.

To assess which lipid species co-vary across individual cells, lipid-to-lipid correlation (expressed as Pearson Correlation Coefficient [PCC]) was used to build a network where nodes are individual lipid species, node size represents IoD, node colour is according to lipid classes, node transparency depends on the Attribution Confidence Score (ACS; defined in Chapter 2 and detailed in Methods), and edges are drawn between lipid couples where their PCC is > 0.85 . As shown in **Figure 20**, highly variable sphingolipids form discrete co-variation groups that are not directly connected among them. Notably, these groups consisted of SLs bearing the same headgroup (i.e., OH with Cers; Hexose with HexosylCeramides [HexCers]; Trihexose with Gb3 species; and N-acetil-hexose-trihexose with Gb4 species) but different ceramide backbones.

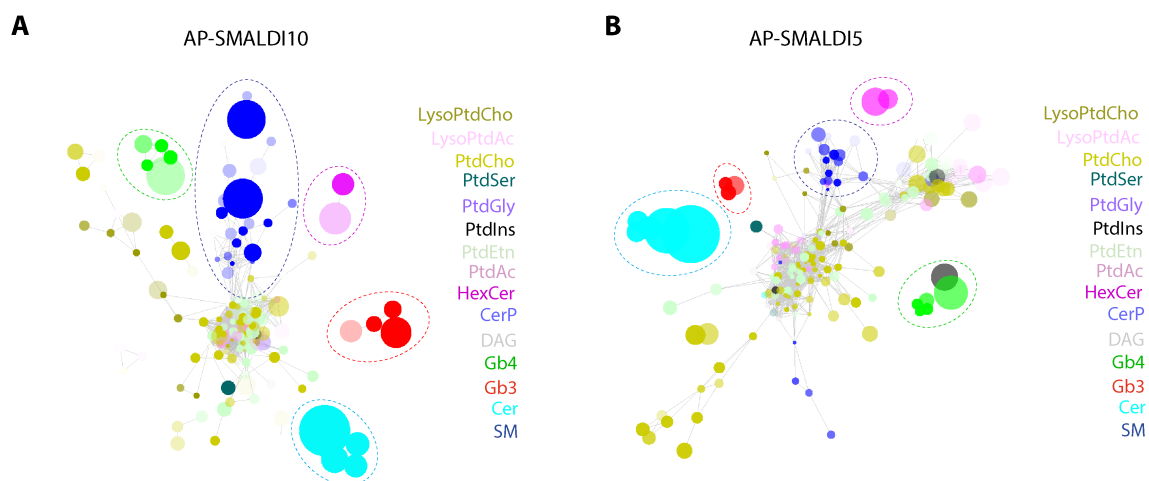


Figure 20. Single-cell lipid co-variation networks. Lipid networks were built using Cytoscape 3.8.0 with the extracted lipid count values from the analysis obtained by AP-SMALDI10 (A) or AP-SMALDI15 (B). Nodes are individual lipids, size represents $\log_{10}(D)$, colour is according to lipid class. Edges connect two lipids where the PCC of their values in the cell database is > 0.85 . Dotted circles highlight covariation groups composed of lipids belonging to the same class.

Accordingly, mass images showed that sphingolipids with different headgroups but same Cer backbone are differentially ‘expressed’ by individual dHFs (i.e., non-colocalized) while sphingolipids with same headgroup but different backbones are found to co-vary across the cell population (i.e., colocalized). When the relative abundance of couples of individual lipid species sharing either the same headgroup or backbone was plotted, lipids sharing the same headgroup were found to be more correlated than those sharing the same backbone, indicating that Cer processing is more cell-to-cell variable than Cer production (**Figure 21**).

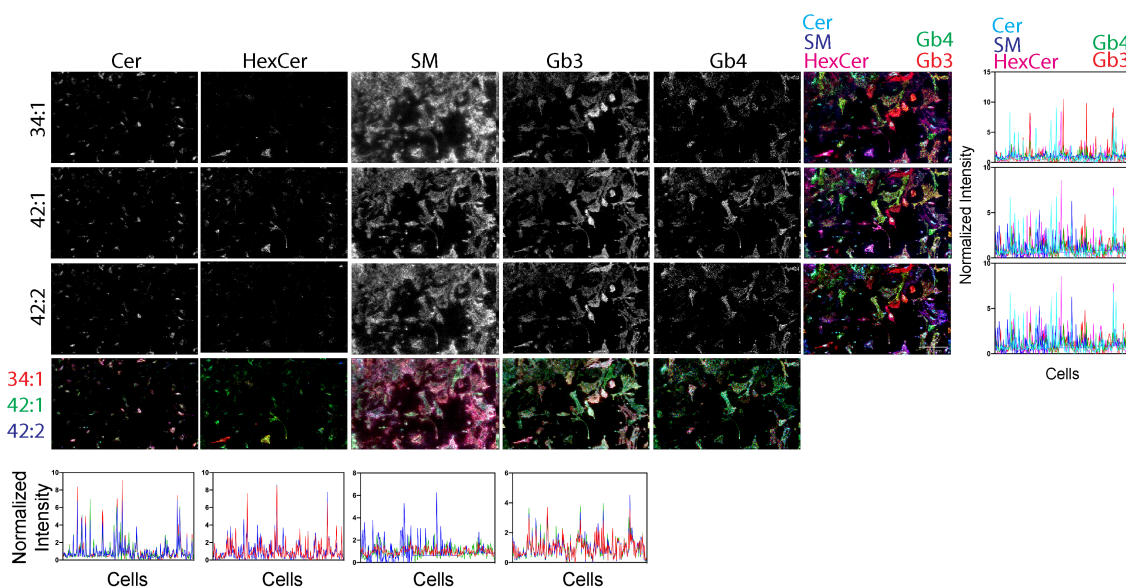


Figure 21. Mass Images of highly variable lipids. AP-SMALDI10 ion images (354x218 pixels) showing the spatial distribution of sphingolipid precursors (Cer) and complex sphingolipids (HexCer, Gb3 and Gb4). Overlay images show how sphingolipids with the same headgroup but different acyl chains are co-localized, while sphingolipids with different headgroups but same acyl chain do not co-localize in single-cells. Scale bar is 500 μm . Bottom down and right, relative abundances of individual lipid species in each cell sharing either the same headgroup or backbone are plotted.

In a parallel approach, single-cell lipidomes were also used to obtain graphs whereby cells were clustered according to their lipid content. As shown in **Figure 22A**, several cell clusters could be recognized. When the levels of prevalent sphingolipid species were considered for each cluster, we observed that given species (i.e., sharing the same headgroup and having different backbones) were enriched in specific cell clusters, suggesting that dHFs exist in lipid metabolic states characterized by discrete sphingolipid compositions (**Figure 22B**).

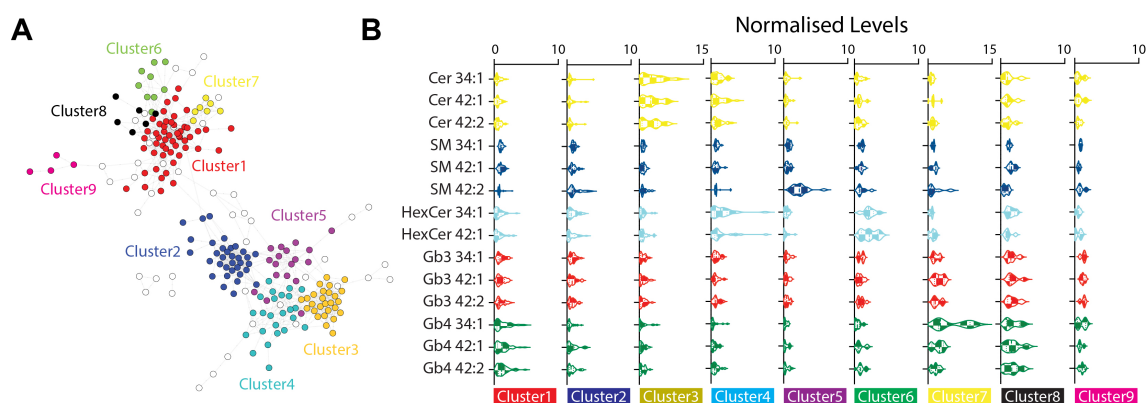


Figure 22. Cell-to-cell co-variation network. Cell network was built using Cytoscape 3.8.0 with the extracted lipid count values from the analysis obtained by AP-SMALDI5. **A)** Nodes are individual cell. Edges connect two cells where the PCC of their values in the lipid database is > 0.35 . **B)** Violin plots of normalised and batch corrected single-cell values for the most variable sphingolipids in the different cell clusters.

3.2 Conclusions

In this chapter, we used for the first time MALDI-IMS as tool to investigate cell-to-cell variability of a large portion of dHF lipidome. With our approach, we analysed single-cell heterogeneity of 296 molecules in the lipid mass range, in more than 400 cells and with two different instruments, obtaining reproducible results. We found that specific lipid metabolic segments, and in particular the sphingolipid pathway, are cell-to-cell variable and that sphingolipid variability is due to headgroup processing. Finally, we also found that cell-to-cell sphingolipid variability is sufficient to describe cell sub-populations with specific lipid compositions.

CHAPTER 4. CORRELATIVE VIDEO/ MASS MICROSCOPY OF SINGLE dHFs REVEALS THE EXISTENCE OF CELL ‘LIPOTYPES’.

[In this chapter, the lineage data analysis was done in collaboration with Gioele La Manno]

Different factors can contribute to cell-to-cell dHFs lipid heterogeneity including intrinsic stochasticity, local cell environment, cell cycle, or the existence of stable cell states through cell division. To assess which of these factors determine the observed lipid heterogeneity we developed a correlative video/mass microscopy experiment on dHFs.

4. 1 Development of correlative video/ mass microscopy of dHFs

Low passage dHFs were plated at low confluence and imaged by phase contrast microscopy for 68 hours. Cells were then fixed and coated with a MALDI matrix (2,5-DHB) and the same area imaged by phase contrast was analyzed in positive ion mode by high resolution MALDI-IMS (as detailed in methods). Individual cells were traced to reconstruct phylogeny and cell division times. Different cell parameters were considered including time elapsed since last cell division, number of cell divisions and phylogeny and correlated with relative levels of 254 known lipid species determined by MALDI-IMS (**Table 1**). In more detail, 50 cells at time point 0 were identified as progenitors. Tracking of progenitors and their progeny was carried out from time point 0 to time point 135 (68 h) by following cells manually and marking new daughter cells at each division with napari 0.3.8 (<https://napari.org>). Optical images were then used to guide automatic cell segmentation on mass images to extract single-cell lipid count values (**Figure 23**).

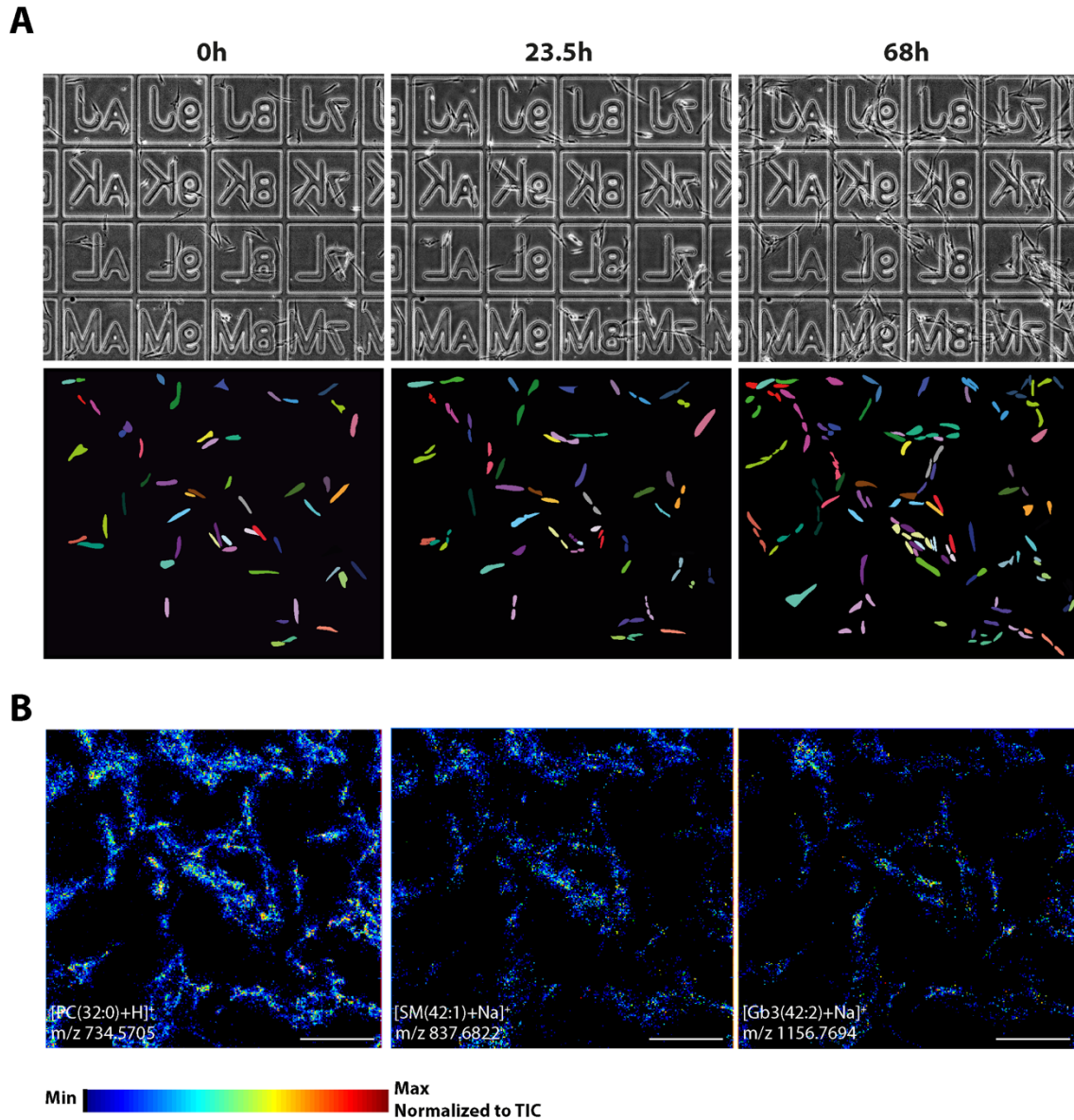


Figure 23. Correlative video/ mass microscopy of dHFs. dHFs were plated on gridded glass-bottomed tissue culture dish and imaged by phase contrast microscopy over 68h. After fixation, cells were processed for MALDI-IMS. **A)** Still images at different time point of the time-lapse are shown in the upper panel. Lower panel illustrate how individual cells were followed. 50 cells were identified as progenitors and by a different colour and manually tracked for 68h. Sister cells were identified with the same colour. **B)** 5 μ m AP-SMALDI5 ion images (314x314 pixels) showing the distribution of 3 know lipids. The maximum values for the ion intensities could be found in the lower left corner. Scale bar is 500 μ m

Single-cell lipid count values were used to build a t-distributed Stochastic Neighbour Embedding (t-SNE) dimensionality reduction map, where cells sharing similar lipid composition clustered together (**Figure 24**).

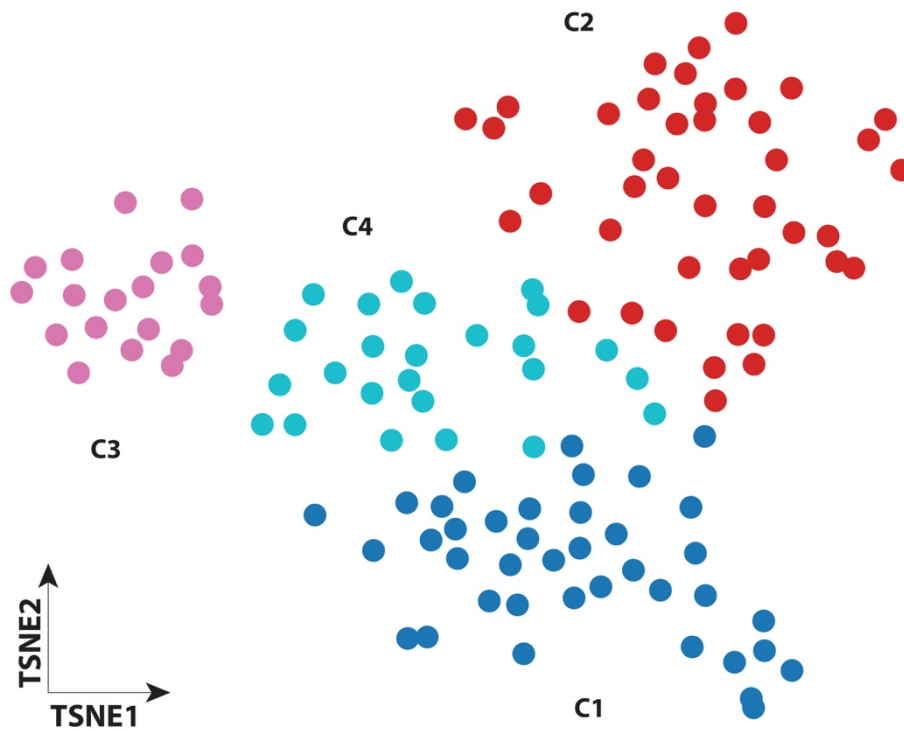


Figure 24. t-SNE dimensionality reduction analysis on dHFs based on single-cell lipid count values. Cells were clustered according to the values of 254 lipids extracted from the MALDI-IMS analysis by AP-SMALDI5. Lipid composition variances between cells ($n = 125$) are displayed as t-SNE, revealing the existence of 4 clusters.

We then analyzed the phylogeny of each cell (**Figure 25A**) and calculated the frequency by which phylogenetically related cells (i.e., sister, cousin, and aunt cells) belong to same or different lipidome-defined cell clusters. We found that phylogenetically related cells are more likely to belong to the same cell cluster (i.e., to share a similar lipid composition) with the exception of cluster 4 (**Figure 25B**). When we calculated the time elapsed since last cell division for each cell in the four clusters, we found no significant difference between the clusters (**Figure 25C**).

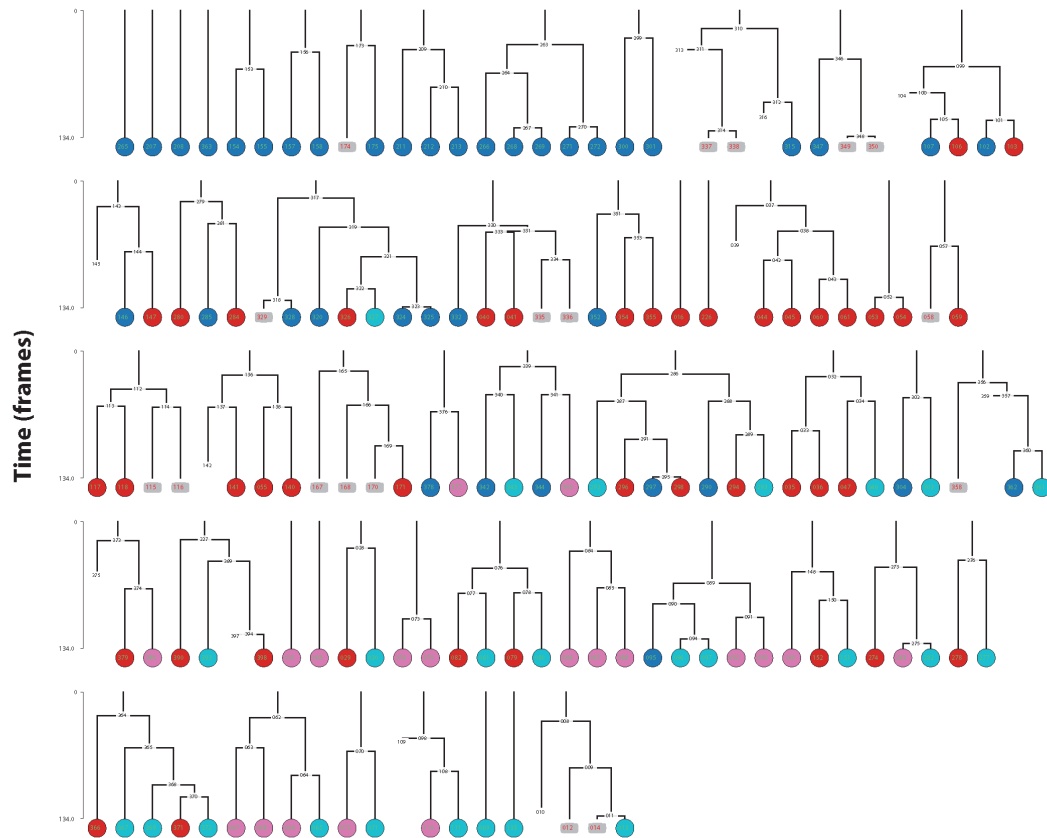
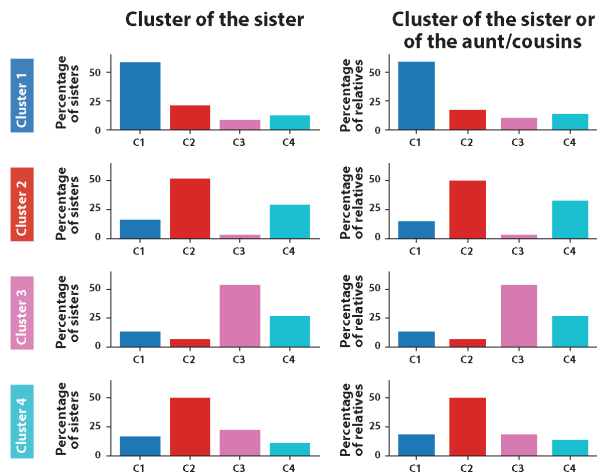
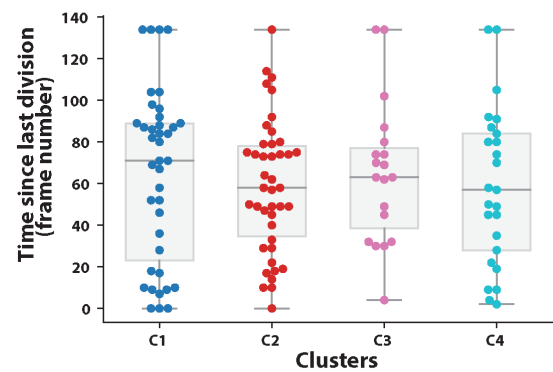
A**B****C**

Figure 25. Lineage analysis of dHFs. Each cell in the four clusters was manually tracked from time frame 0 to time frame 134. **A)** Cell hierarchy built on napari 0.3.8 is shown. Cells indicated with a grey box were not analyzed by MALDI-IMS. **B)** Probability analysis. **C)** Cell divisions were manually identified for each cell and reported here. For each cell, the frame number where we identified its last division, was manually identified.

These findings indicate that given lipidome configurations are stable across cell generations. To understand whether this holds true for the entire lipidome or whether few lipid species account for the existence of stable lipid states, we performed an analysis of lipid-based family separability for each lipid. To do this, we averaged the values of each lipid within a cell family and sorted the families from the one with the lowest average lipid level to the one with the highest without breaking any kinship link in the lineage (**Figure 26A**). As a statistical test, we plotted the trend of summing lipid levels across the sorted individual cells and compared it with the expected trend obtained by repeatedly (500 repetitions) permuting the lipid count values among cells but keeping the lineage structure constant (**Figure 26B,C**). By subtracting the observed from the expected trend, we obtained a value that we defined Area Under the Curve (AUC) and a corresponding p-value for each lipid (**Figure 26C**). When we considered the AUC along with the cell-to-cell variability associated with each lipid, we found that these two values were generally well correlated, and that lipids with a significant AUC difference (i.e., q-value <0.05) were frequently identified among those with high cell-to-cell variability levels (**Figure 26D**). This suggests that lipids whose levels vary (i.e., those that contribute the most to lipidome-defined cell clusters) are well-propagated across cell generations. Accordingly, when looking at the lipids with the highest q-value, we found them to belong to the sphingolipid and glycosphingolipid classes (**Figure 27**).

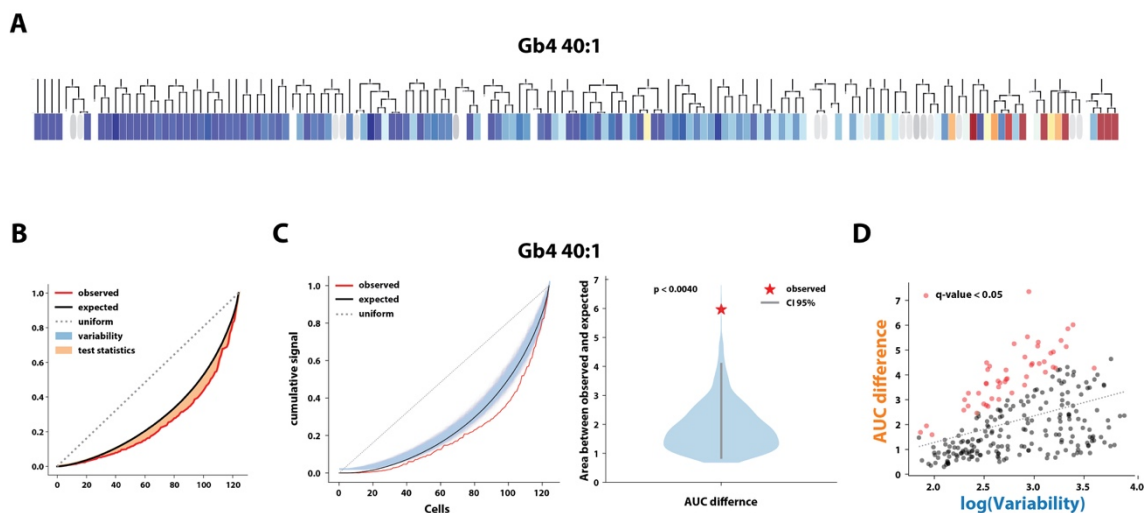


Figure 26. Lipid-based family separability analysis. Analysis was performed for each lipid using a family-constrained sorting. **A)** Lipid-based family analysis of lipid Gb4 40:1 is shown as an example. Families were ordered moving entire clades and pivoting daughter cells with a python custom script.

Colour scale is according to lipid level (blue represents low levels, red represents high lipid levels). **B)** A test statistic was performed considering the cumulative sum of values across the sorted families (red line) after this sorting was corrected by its expectation (black line). Dotted line represents a uniform situation where lipid intensities are equal in each cell. **C)** An empirical statistical test was performed 500 times, permuting the lipid values and keeping the lineage structure constant (blue shadow). In the right panel the AUC difference against the difference between the observed and expected curve is shown with the statistical significance (p-value) for lipid Gb4 40:1. **D)** AUC difference for each lipid is shown. Lipids with q-value < 0.05 (red dots) are considered significantly segregated from the others.

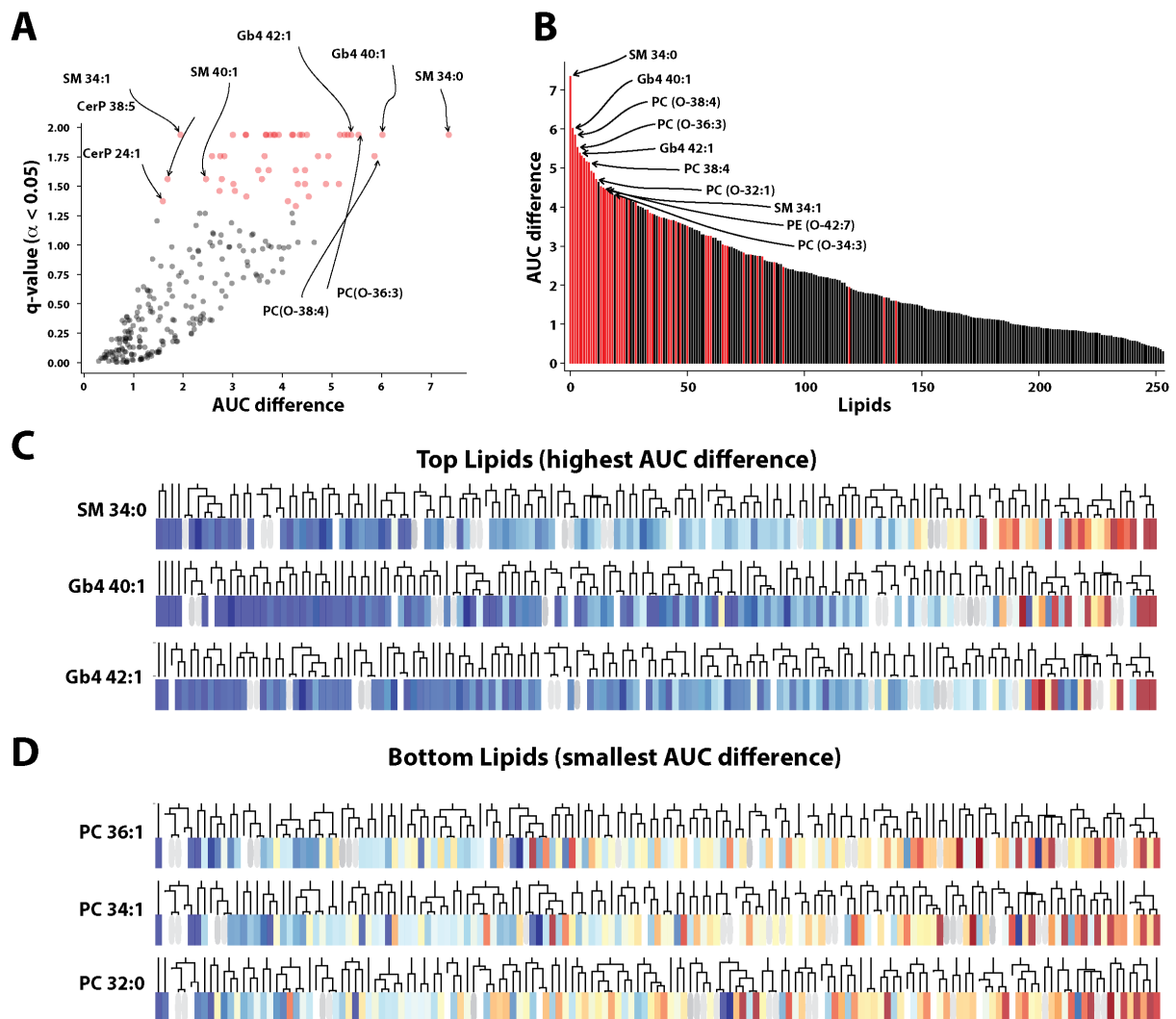


Figure 27. Lipid analyzed based on family separability analysis. A) Empirical non-parametric p-values for each lipid, analyzed based on AUC differences, were FDR-corrected with $[\alpha = 0.05]$ to calculate the q-value. Only lipids with q-value < 0.05 are considered significant (red dots). **B)** Lipids were ordered according to their AUC difference. **C, D)** Lipids with the highest and smallest AUC difference are

shown. Dendrograms showing lipids level calculated for each cell of the family. Colour scale is according to the lipid level (blue represents low levels, red represents high lipid levels).

4.2 Conclusions

Here we set up a correlative video/ mass microscopy approach to investigate the origin of cell-to-cell lipid variability. Our data indicate that a relevant fraction of cell-to-cell lipid variability is explained by phylogeny, with sister and related cells having higher chance to share a similar lipid composition. Lipids where their levels are similar within cell families are the same sphingolipids that account for the lipidome-defined cell clusters.

These data suggest that individual dHFs experience different lipid metabolic states that are largely determined by their sphingolipid composition and that are possibly relative stable states that are inherited through cell generations. For simplicity, hereafter we refer to these lipid metabolic states as *lipotypes*.

CHAPTER 5. MS-INDEPENDENT VALIDATION OF CELL-TO-CELL LIPID VARIABILITY

This report is among the first to investigate steady-state cell-to-cell lipid variability in a syngeneic cell population, based on single-cell lipidomics analysis by MALDI-IMS. Whether the obtained data faithfully reflect an actual difference in cell lipid composition is hard to conclude based on MALDI-IMS data only. In this chapter we independently validate our MALDI-IMS findings.

5.1 Validation of single-cell lipid heterogeneity by using bacterial toxins

To independently test lipid variability in dHFs we took advantage of the use of bacterial toxins fragments: ShigaToxinB1a (ShTxB1a), ShigaToxinB2e (ShTxB2e), and CholeraToxinB (ChTxB). These toxins recognize sphingolipid headgroups to intoxicate cells, with ShTxB1a binding to trihexosylceramide Gb3 (Jacewicz MARY, et al., 1986), ShTxB2e binding to Gb3 and globosides Gb4 (Muthing J et al., 2009), and ChTxB binding the ganglioside GM1 (van Heyningen S, 1974). Thus, we used ShTxB1a, ShTxB2e and ChTxB to reveal GSLs in single dHFs by standard fluorescence microscopy and found that they bind dHFs with different patterns of cell-to-cell variability reminiscent of what observed by MALDI-IMS (**Figure 28**).

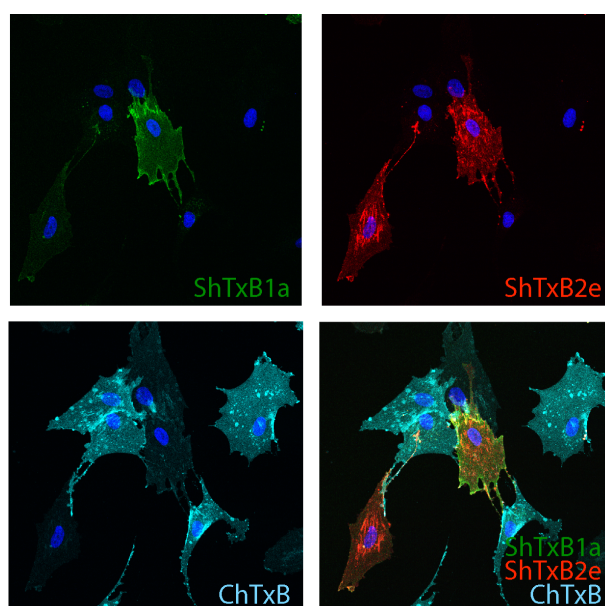


Figure 28. Bacterial toxin staining of dHFs. dHFs were fixed and processed for fluorescence microscopy. Cells were stained with bacterial toxins ShTxB1a (green), ShTxB2e (red), ChTxB (blue) and Hoechst (grey) for nuclei and images acquired by confocal microscopy. Scale bar is 50 μ m.

Along similar lines, cytofluorimetric assessment of toxin binding to dHFs membranes returned a heterogeneous picture with ShTxB1a, ShTxB2e and ChTxB identifying different cell populations (**Figure 29**).

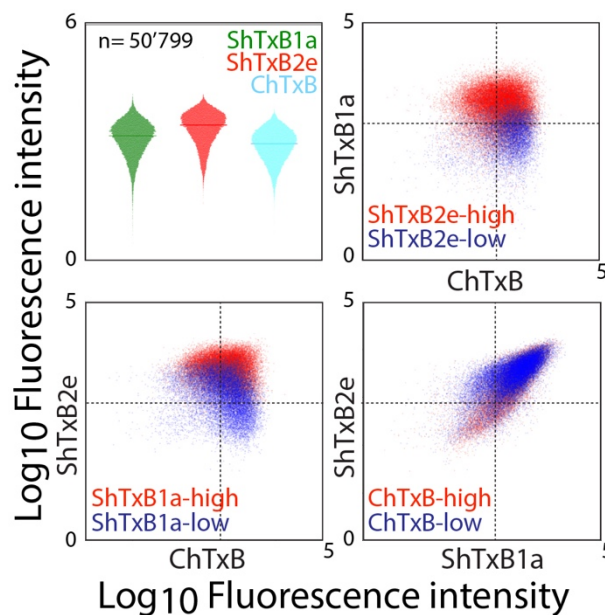


Figure 29. Cytofluorometric analysis of dHFs using bacterial toxins. Cells were fixed and stained with toxins recognizing lipid Gb3 (ShTxB1a/ShTxB2e), Gb4 (ShTxB2e) and GM1 (ChTxB). Side scatter plots and violin plots of \log_{10} fluorescence intensity value for each toxin are shown for each toxin. Unstained cells were used as negative control. Cells were gated on the singlet population.

Importantly, chemical inhibitors of three different reactions involved in SLs production (i.e., myriocin, Fumonisin B1 (FB1), and D-threo-1-phenyl-2-decanoylamino-3-morpholino-1-propanol [D-threo-PDMP]) (**Figure 30A**) affected toxin binding in a predictable manner (**Figure 30B**) indicating that toxin binding is a faithful proxy for dHF membranes SL composition in our setting. Similar results were obtained by silencing of key enzymes involved in GSLs production (i.e., *ST3GAL5*, encoding GM3 synthase [GM3S]; *A4GALT*, encoding Gb3 synthase [Gb3S]; and *B3GALNT1*, encoding Gb4 synthase [Gb4S]) (**Figure 31**).

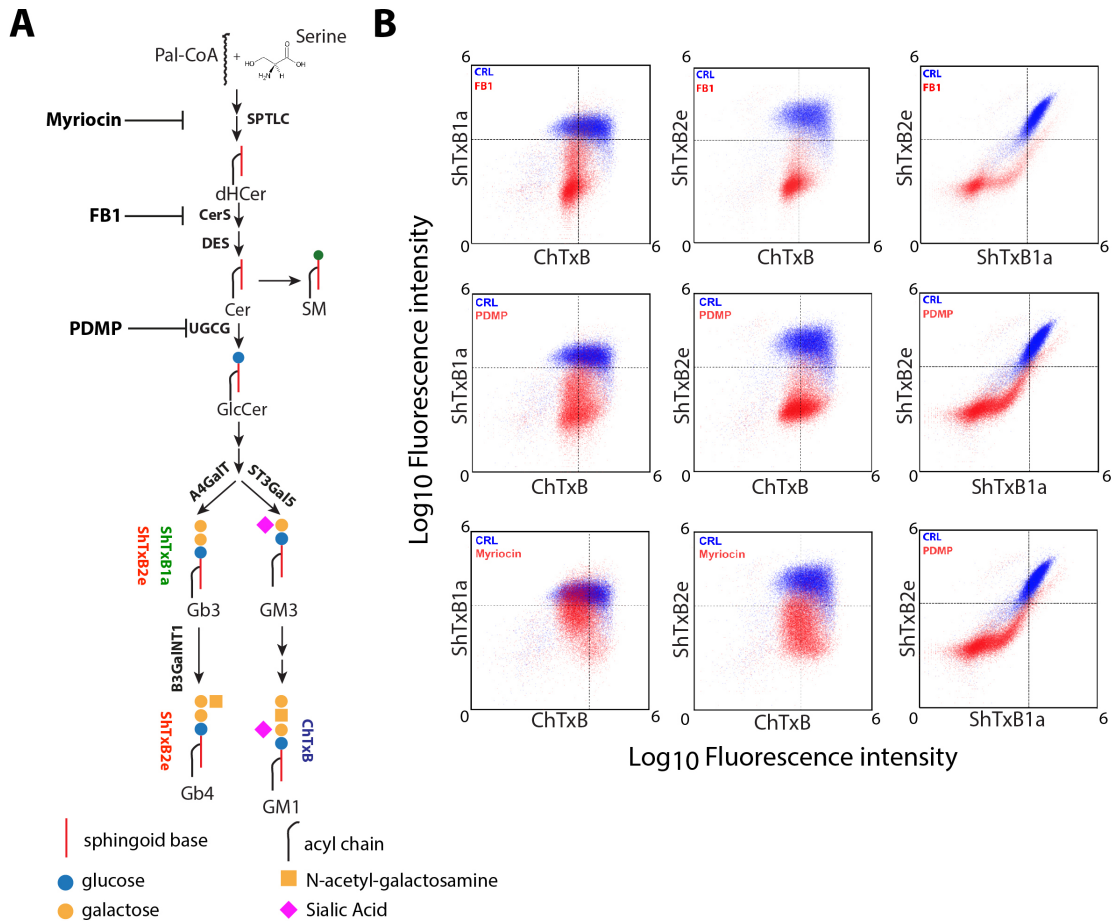


Figure 30. Chemical inhibition of sphingolipid biosynthetic pathway. A) Schematic and simplified representation of the de novo sphingolipid biosynthetic pathway with the enzymes affected by drug inhibition. As shown in the figure, myriocin inhibits SPTLC, FB1 inhibits CerS and PDMP inhibits UGCG. SPTLC, Serine palmitoyltransferase; CerS, Ceramide Synthase; UGCG, UDP-Glucose Ceramide Glucosyltransferase. **B)** Cytofluorometric analysis of dHFs. Cells were treated with SL inhibitors (2.5 μ M myriocin, 25 μ M FB1 or 10 μ M PDMP) for 6 days and stained with ShTxB1a, ShTxB2e and ChTxB. Side scatter plots of \log_{10} fluorescence intensity values for each toxin are shown. Unstained cells were used as negative control. Cells were gated on the singlet population. Control cells are shown in blue; treated cells in red. CTRL, n= 23'806; FB1, n= 23'007; myriocin, n= 22'470; PDMP, n= 25'308.

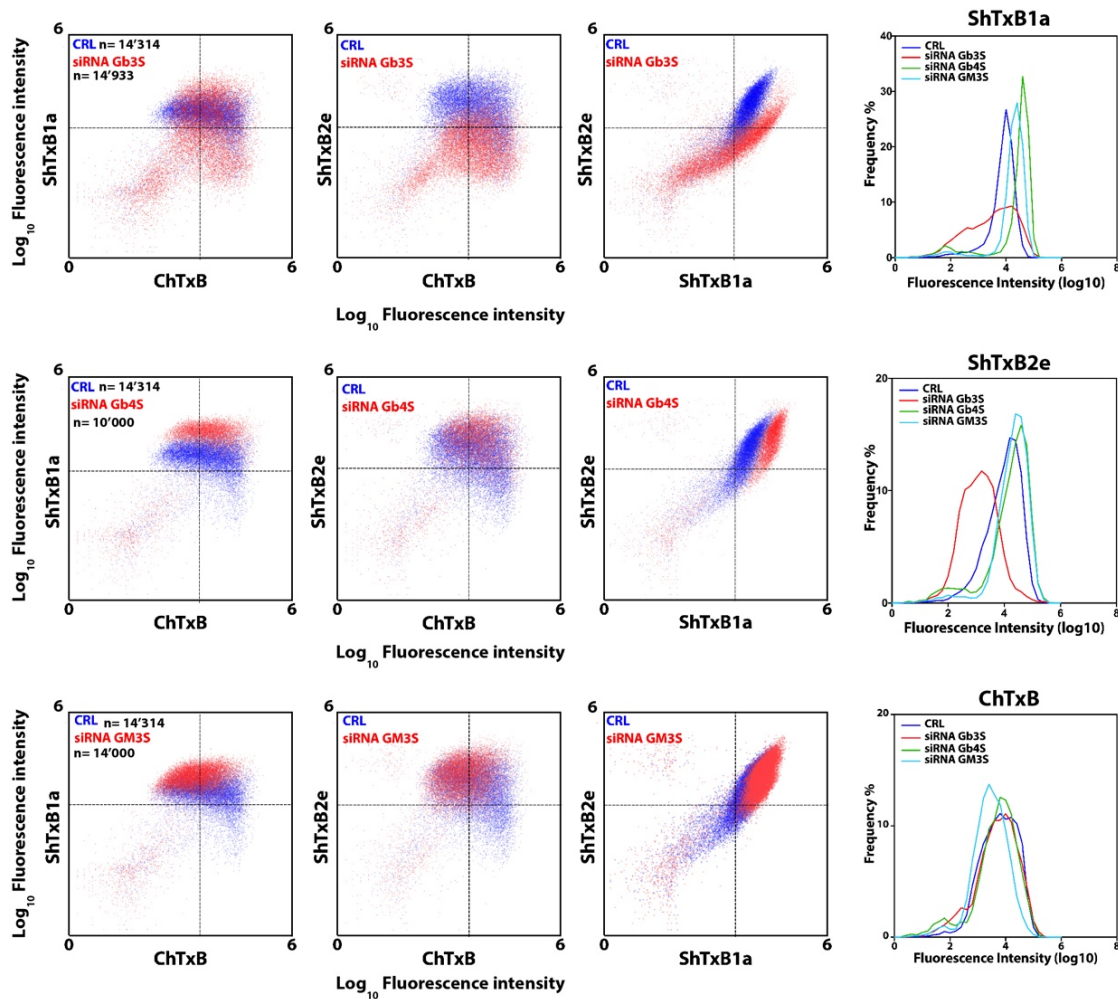


Figure 31. Cytofluorometric analysis of dHFs after siRNA-KD of the main GSL synthesizing enzymes. Cells were silenced for Gb3S (*A4GALT*), Gb4S (*B3GALNT1*) and GM3S (*ST3GAL5*) for 96h and then processed for flow cytometry. Cells were stained with ShTxB1a, ShTxB2e and ChTxB. Side scatter plots of \log_{10} fluorescence intensity values for each toxin are shown. Unstained cells were used as negative control. Cells were gated on the singlet population. Control cells are shown in blue, treated cells in red (left panel). Histograms of the frequency distribution are shown for each condition and for each toxin binding (right panel).

As a further validation test, we decided to directly correlate toxin staining and MALDI-IMS. To this aim, dHFs were first stained with ShTxB1a, ShTxB2e and ChTxB and subsequently imaged by MALDI-IMS. As shown in **Figure 32A** a close correspondence was found between the two imaging methods. In fact, cells stained by only ShTxB2e have a prevalent Gb4 positive profile in MALDI-IMS, those stained by both ShTxB1a and ShTxB2e have a prevalent Gb3 positive profile in MALDI-IMS, and those stained by ChTxB have a Gb3 and Gb4 negative

profile in MALDI-IMS (note that GM1 is not revealed by positive ion mode MALDI-IMS under the conditions used). Cells were then manually segmented to analyse both toxins fluorescence intensity in confocal images and lipids intensity in mass images, to analyse the correspondence between toxins and lipid for each cell. As shown in **Figure 32B**, a very strong correlation was found between ShTxB staining (both ShTxB1a and ShTxB2e) and the lipids they recognize (Gb3 and Gb4, independently on the acyl chain) while anti-correlation was found between ChTxB and lipids Gb3 and Gb4.

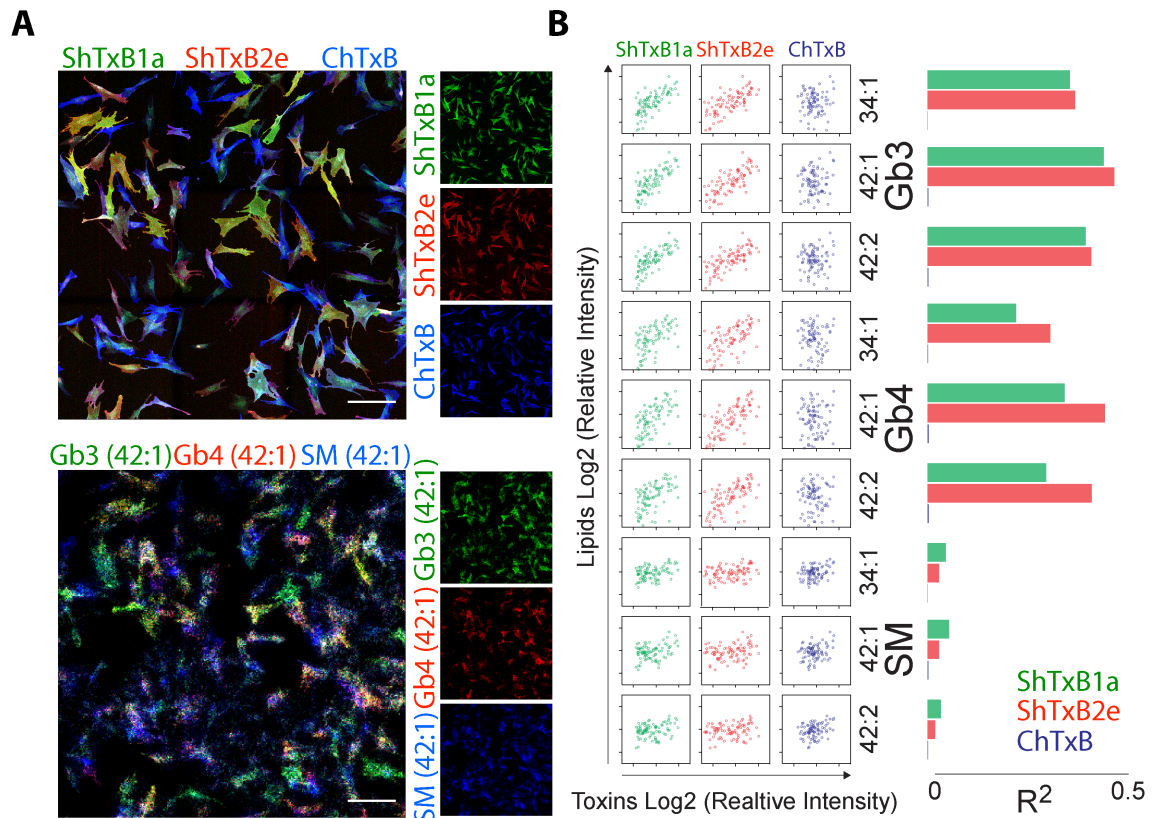


Figure 32. Correlative IMS-confocal analysis of dHFs. A) Cells were fixed and stained with bacterial toxins ShTxB1a (green), ShTxB2e (red) and ChTxB (blue) and images acquired by confocal microscopy (upper panel). Cells were then covered by a MALDI matrix and analysed by MALDI-IMS at high spatial resolution (5 μ m) (lower panel). Overlay ion image (320x320 pixels) of complex sphingolipids [SM (42:1), Gb3 (42:1) and Gb4 (42:1)] showed good correspondence with the confocal image. Scale bar is 200 μ m. **B)** Confocal images were manually segmented by Fiji software to calculate integrated intensities, while mass images were manually segmented by MSiReader software to obtain single cell lipids intensity. Data were plotted as log₂ relative intensity in each cell. Correlation was evaluated calculating R² for each toxin-lipid couple; n = 88.

We then asked whether the observed cell-to-cell lipid variability was specific to the dHF line and to the *in vitro* conditions used in this study. Thus, 4 independent dHF lines collected from healthy individuals were analysed by toxin staining coupled with cytofluorimetry. As reported in **Figure 33** all the tested fibroblast lines showed a cell to-cell variable GSL pattern, though with differences in the size of the different GSL-defined populations. Furthermore, in a similar way described in chapter 4, dHFs were imaged by phase contrast microscopy for 72 hours, fixed and processed for confocal microscopy, in order to confirm with toxin staining that phylogeny determine the observed lipid heterogeneity (**Figure 34**).

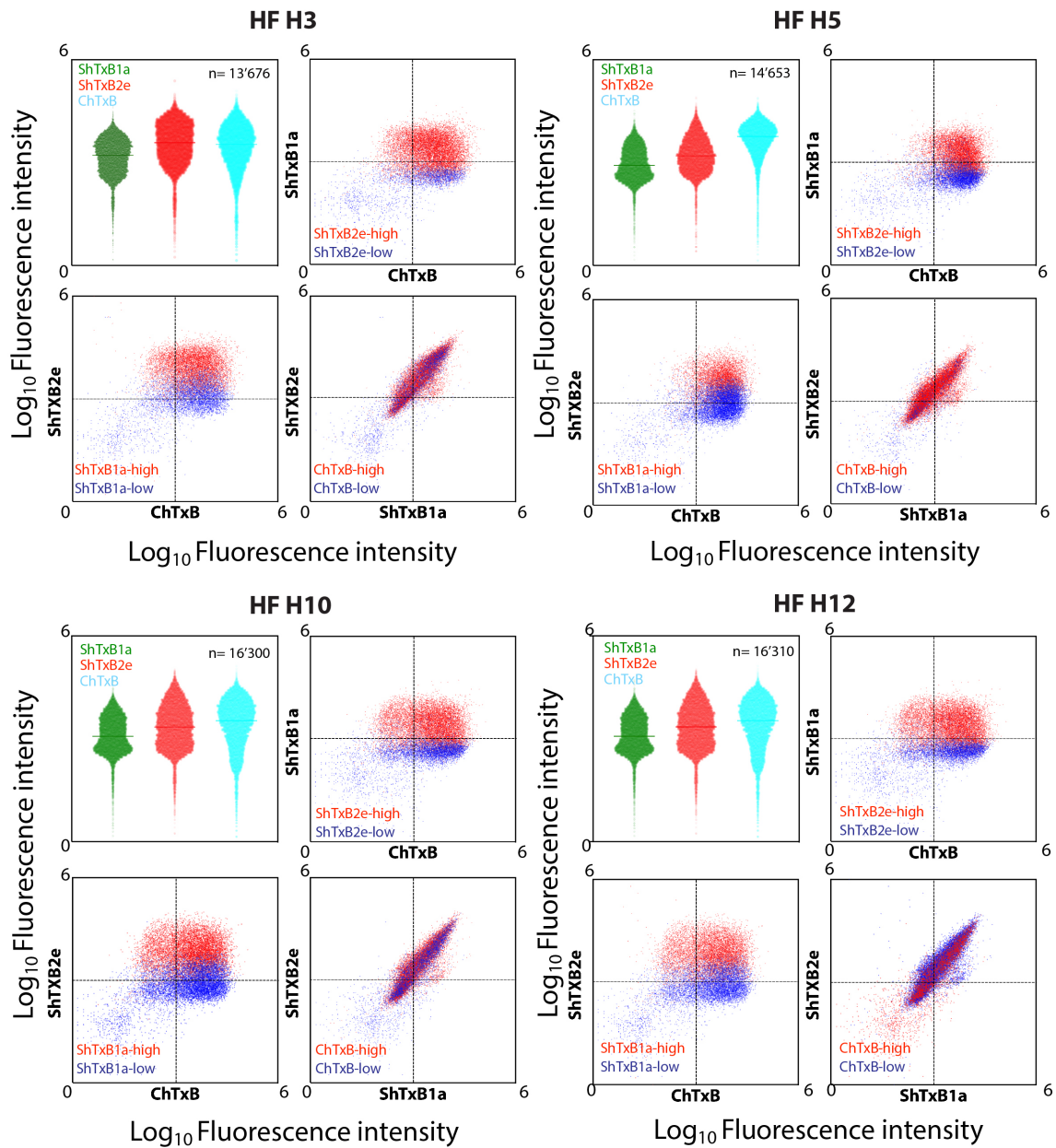


Figure 33. Cytofluorometric assessment of lipid heterogeneity in dHFs from healthy donors. Cytofluorometric analysis of 4 dHFs lines from healthy donors. Cells were stained with toxins recognizing lipid Gb3 (ShTxB1a/ShTxB2e), Gb4 (ShTxB2e) and GM1 (ChTxB). Side scatter plots and violin plots of \log_{10} fluorescence intensity values for each toxin are shown. Unstained cells were used as negative control. Cells were gated on the singlet population; n is indicated in the graph.

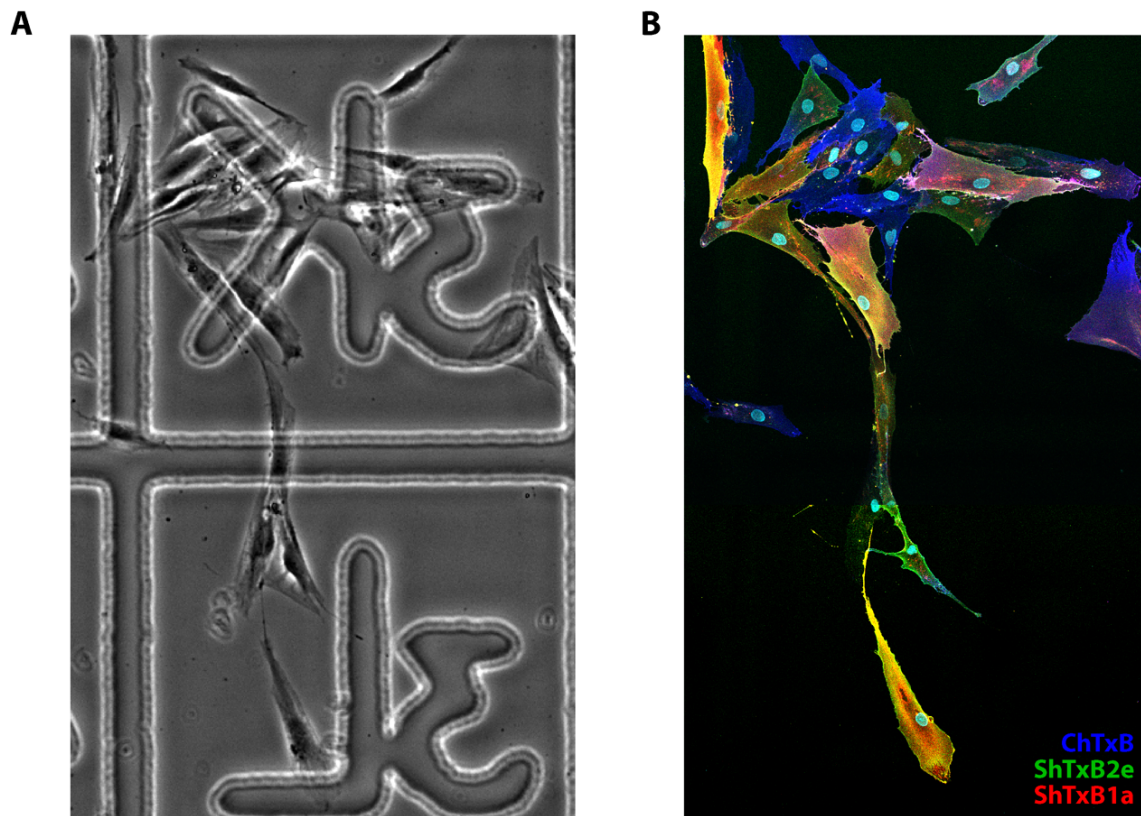


Figure 34. Correlative video/ confocal microscopy of dHFs. **A)** dHFs were plated on gridded glass-bottomed tissue culture dish and imaged by phase contrast microscopy over 72 h. Here a small part of one field is shown as example. **B)** After fixation, cells were stained with ShTxB1a (red), ShTxB2e (green) and ChTxB (blue). Confocal images were acquired in the same fields imaged by video microscopy. Here two field are grouped together and showed as example for confocal images.

After toxin staining, each cell was segmented to analyse their lipid composition by quantifying fluorescence intensities of each toxin. When analysed for lineage tracking, we found that cells sharing the same lipid composition were found to derive in most cases from a single progenitor indicating that, once established, a specific GSL state (i.e. ChTxB⁺, ShTxB2e⁺,

ShTxB1a⁺ShTxB2e⁺ or ChTxB⁺ShTxB2e⁺ShTxB1a⁺) can be maintained through cell generations (Figure 35).

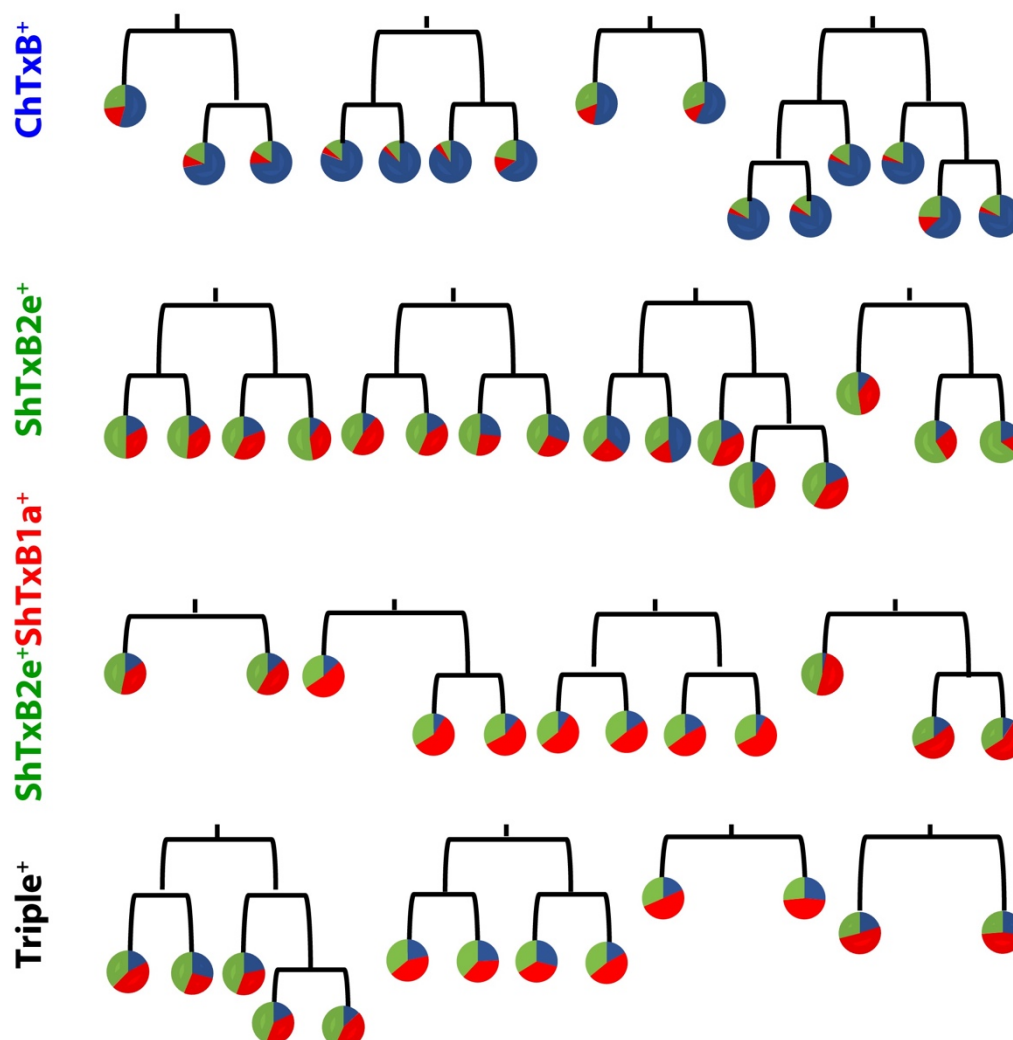


Figure 35. Dendrograms of single-cell lipid composition across cell generation. 56 daughter cells were manually segmented to analyse fluorescence intensities (represented as percentage) and tracked back to identify their common progenitor.

Heterogeneous cell-to-cell GSL composition could be also accounted by the single-cell expression of involved metabolic enzymes. To test this, mRNA fluorescence *in situ* hybridization (FISH) experiments were performed to simultaneously detect *ST3GAL5* (GM3S), *A4GALT* (Gb3S), and *B3GALNT1* (Gb4S) mRNAs in individual dHFs (Figure 36). By evaluating

the FISH signals in >750 individual cells we found that *A4GALT* and *B3GALNT1* expression largely correlated. *A4GALT* expression predominate while a discrete cell population showed high *B3GALNT1* mRNA expression. On the contrary *ST3GAL5* showed an overall tendency to anti-correlate with both *A4GALT* and *B3GALNT1* which was reminiscent of the relationship among the lipids produced by these enzymes (compare with **Figure 29**).

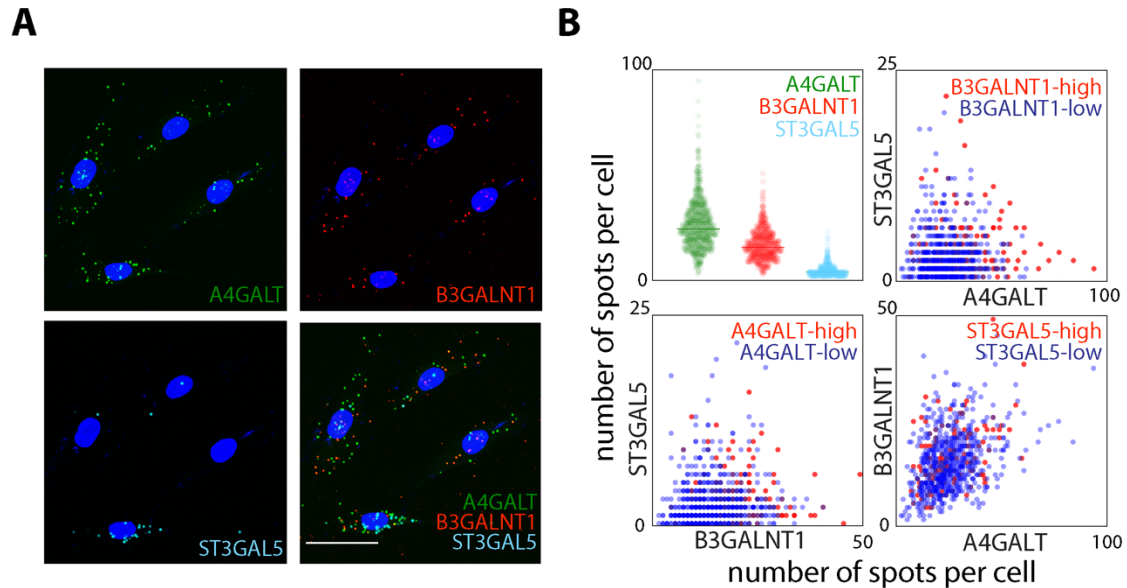


Figure 36. Fluorescence in situ hybridization (FISH) analysis of GSL synthesizing enzymes. A) Representative confocal microscopy images of mRNA-FISH using *A4GALT* (Gb3S) (green), *B3GALNT1* (Gb4S) (red) and *ST3GAL5* (GM3S) (cyan) probes. Nuclei were labelled with Hoechst (blue). Scale bar is 50 μ m. **B)** Quantification of mRNA-FISH analysis in 758 individual cells. Number of spots per cells is shown as violin plot or side scatter plot for each gene.

Since previous results were obtained in cultured dHFs, we wanted to know whether these phenotypes would hold in a more physiological condition. Therefore, we tested the GSL profile in the context of skin biopsies. We found that in their physiological context, *bona fide* dHFs also display remarkable cell-to-cell GSLs heterogeneity (**Figure 37**).

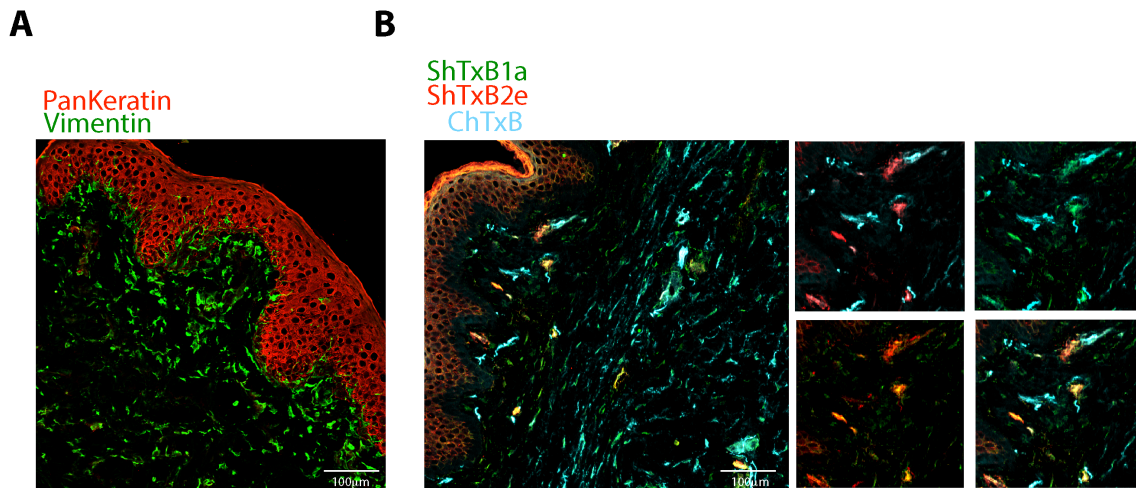


Figure 37. Characterization of skin tissue sections by bacterial toxins. Skin tissue sections embedded in Optimal Cutting Temperature (OCT) compound were processed for immunohistochemistry (IHC). **A)** Tissue section was stained with Pan-Keratin (red) and vimentin (green) to identify keratinocyte and fibroblasts, respectively. **B)** Tissue section was stained with bacterial toxins ShTxB1a (green), ShTxB2e (red) and ChTxB (cyan). Scale bar is 100 μm.

5.2 Conclusions

In this chapter we validated the existence of distinct SL *lipotypes* in dHFs with independent methods thanks to the use of bacterial toxins that recognize GSLs. We confirm the idea that a relevant fraction of cell-to-cell lipid variability is explained by phylogeny, with sister and related cells having higher chances to share a similar lipid composition. Finally, we found cell-to-cell lipid heterogeneity to exist under physiological conditions, in skin biopsies from healthy individuals, and to possibly derive from distinct cell transcriptional configurations that in turn influence GSL synthesizing enzymes.

CHAPTER 6. THE ORIGIN OF CELL-TO-CELL LIPID VARIABILITY: LIPOTYPES MARK SPECIFIC CELL STATES

[In this chapter, scRNAseq experiment and data analysis for both scRNAseq and bulk RNAseq has been done in collaboration with Irina Khven and Gioele La Manno]

As shown in the previous chapters, our results suggest that cell-to-cell lipid variability in dHFs is a consequence of discrete single-cell transcriptional states. It is increasingly appreciated that fibroblasts, are heterogeneous cells that, exhibit functional specialization due to the existence of multiple cell subtypes (i.e., *cytotypes*) (Lynch MD and Watt F, 2018; Rognoni E and Watt F, 2018). In this chapter, we thus asked whether specific *lipotypes* relate to discrete fibroblast cell states.

6.1 Transcriptomic analysis of dHFs

To study what global transcriptional configurations are associated with the different *lipotypes*, scRNAseq for a total of 5652 dHFs was performed. UMAP dimensionality reduction analysis was applied on global patterns of gene expression for each individual cell and automated clustering identified 17 cell groups (**Figure 38A**). When the relationship among these 17 groups was investigated we found them to converge into 6 recognizable super-clusters (**Figure 38B**). Genes enriched in the clusters were identified and mapped in the UMAP space highlighting six major variation axes linked to proliferation; pro-inflammatory cytokine secretion (inflammatory), pro-fibrotic secretion (fibrogenic), extracellular matrix remodelling (fibrolytic) and angiogenic secretion (vascular). A further group represented bona fide basal-state fibroblasts (basal) (**Figure 38C**).

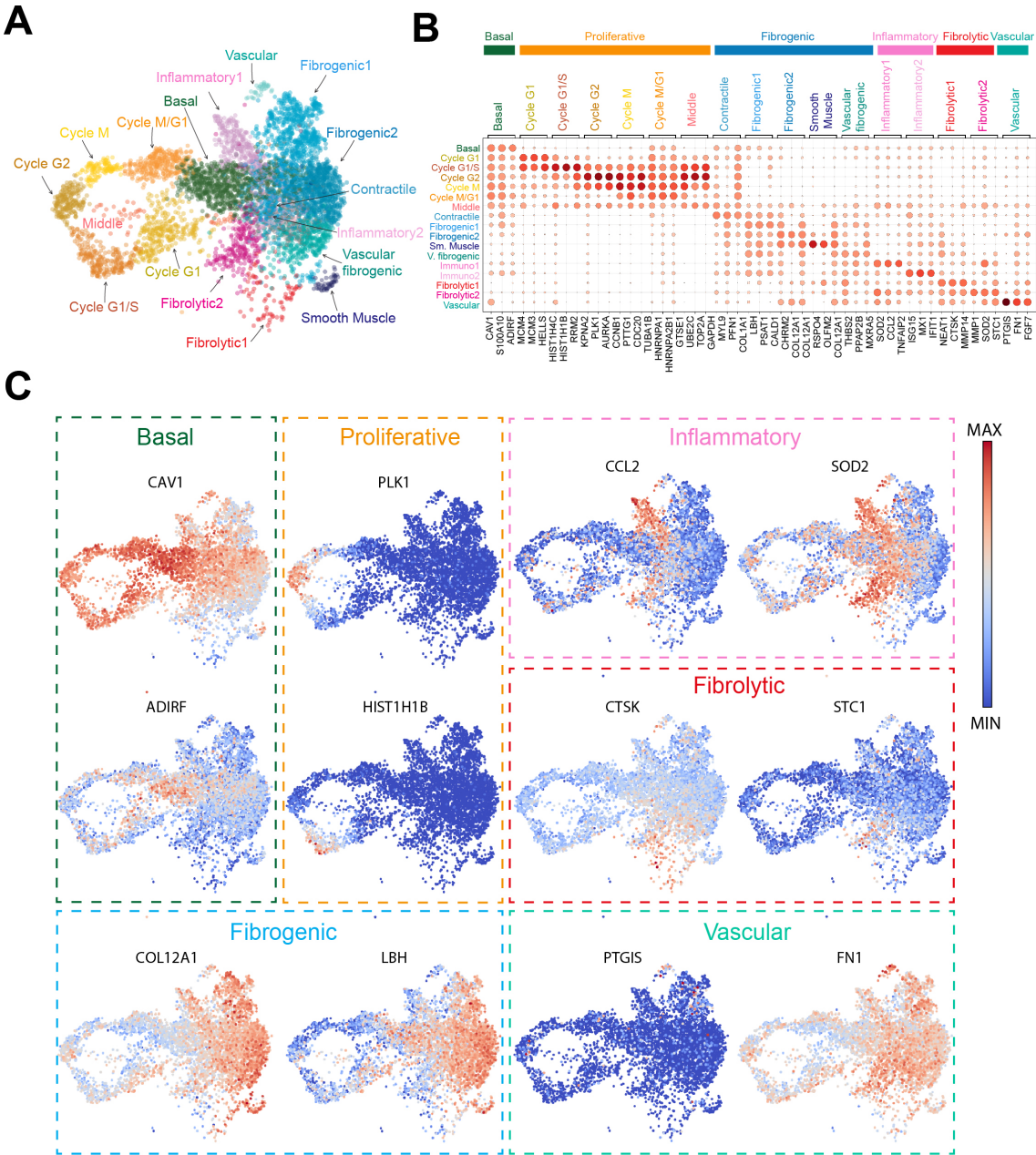


Figure 38. UMAP analysis after scRNAseq analysis. A) UMAP analysis of 10x Genomics Chromium based scRNAseq of 5652 individual dHFs coloured by assigned cluster. Louvain clustering algorithm returned 17 cell clusters. **B)** Top marker genes were identified with the Wilcoxon test for each cluster. Expression dot plots of these genes were used to cluster subgroups. **C)** UMAP projections of canonical markers for basal, proliferative, fibrogenic, inflammatory, fibrolytic and vascular cell states. Colour scale is according to gene expression level.

Next, dHFs were stained with bacterial toxins and isolated according to their *lipotype* by fluorescence activated cell sorting (FACS) to perform RNA bulk sequencing analysis (**Figure 39A,B**).

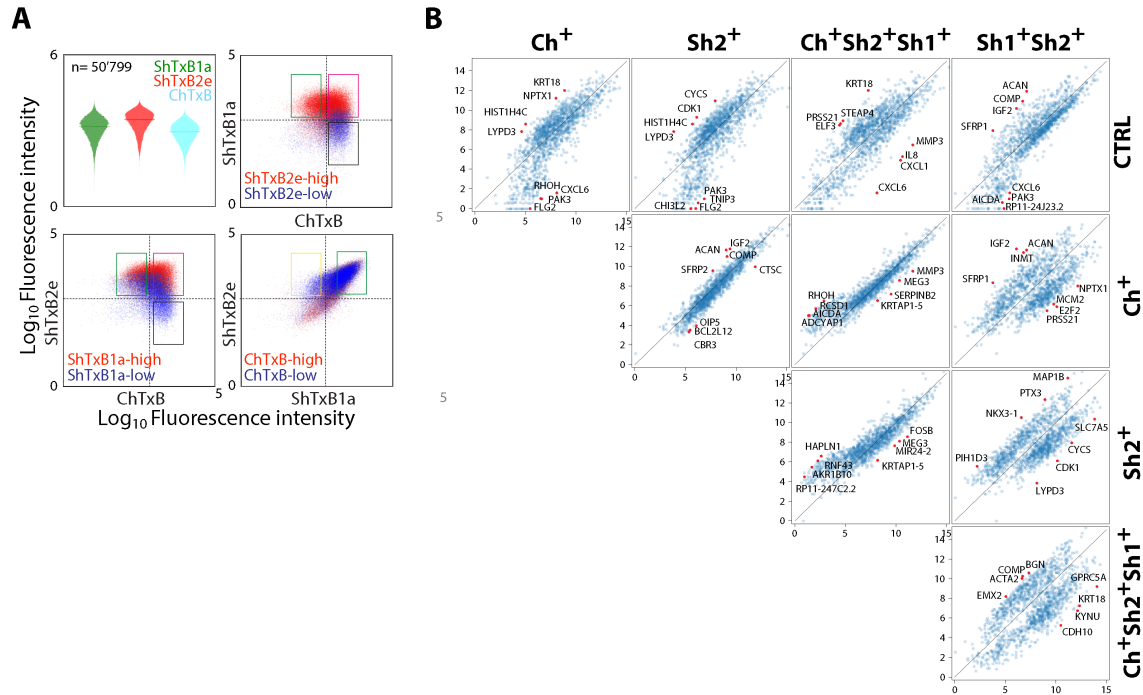


Figure 39. Bulk RNAseq analysis of dHFs FACS sorted according to their *lipotypes*. **A)** FACS sorting of dHFs. Cells were stained with toxins recognizing lipid Gb3 (ShTxB1a/ ShTxB2e), Gb4 (ShTxB2e) and GM1 (ChTxB). Unstained cells were used as negative control. Cells were gated on the singlet population. Violin plots and side scatter plots of \log_{10} fluorescence intensity values for each toxin with the sorting gates are shown. Four population ($ChTxB^+$, $ShTxB2e^+$, $ShTxB1a^+ShTxB2e^+$ and $ChTxB^+ShTxB2e^+ShTxB1a^+$) were isolated and processed for RNA extraction and bulk RNA-seq. **B)** Scatterplot matrices comparing the total gene expression in each *lipotype*. Top differentially expressed genes are shown for each comparison.

The averaged expression level of the 250 top genes found to be differentially expressed between the different *lipotypes* after bulk RNAseq were used to build *lipotype* signatures (**Table 2**). *Lipotype* gene signatures were used to calculate enrichment in functional categories. $ChTxB^+$ showed high expression of genes involved in extracellular matrix organization. $ShTxB2e^+$ showed high expression of genes involved in differentiation. $ShTxB1a/2e^+$ showed high expression of genes involved in cell proliferation and triple positive

cells of genes involved in cytokine mediated pathways (**Figure 40**), indicating a good degree of specialization among dHF bearing different *lipotypes*.

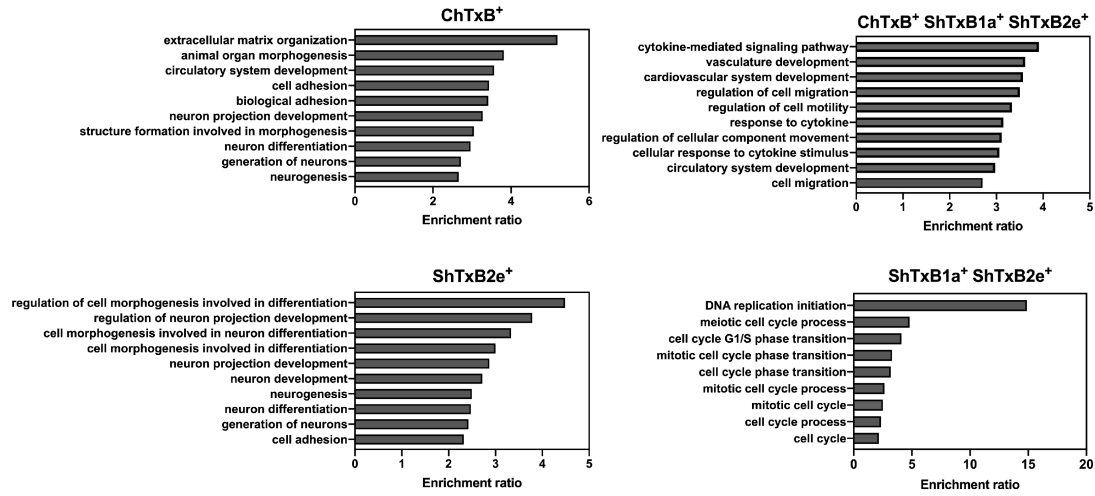


Figure 40. Over-Represented gene ontology Analysis (ORA). GO analysis were performed on 354 genes found to be unambiguous and annotated to belong to functional categories. Each panel represents the enrichment ratio of the over-represented genes for each lipotype and the biological process they belong to.

Lipotype gene signatures were then mapped into the UMAP space showing that they belong to discrete UMAP areas corresponding to the major transcriptional cluster (i.e., triple positive cells corresponded to inflammatory, fibrolytic and vascular fibroblasts, ShTxB1a/2e⁺ corresponded to proliferating cells, ShTxB2e⁺ corresponded to basal state fibroblasts, and ChTxB⁺ corresponded to fibrogenic fibroblasts) suggesting that specific membrane lipid compositions are associated with specific cell states (**Figure 41**).

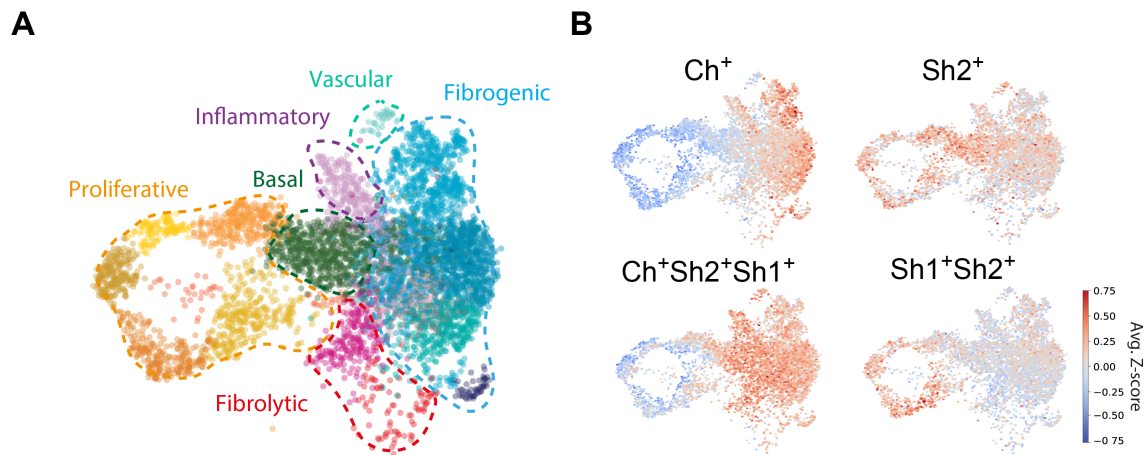


Figure 41. *Lipotype* signatures mapped in the UMAP space. A) UMAP analysis of scRNAseq of 5652 single dHFs coloured by assigned cluster. **B)** UMAP projections of *lipotypes* gene signatures. 250 top differentially expressed genes were used to calculate the average Z-score that was plotted into the UMAP space. Colour scale is according to Z-score level.

As even further validation, dHFs were stained with toxins and counterstained with markers of given *cytotypes*. As shown in **Figure 42**, a good correlation was found between *lipotypes* and markers of different cell states. In particular, a marker for fibrogenic cells, smooth muscle actin (encoded by the gene ACTA2) was found to have a good correlation with ChTxB, while a marker for cell cycle and basal state dHFs laminin A (encoded by the gene LMNA) had a good correlation with ShTxB2e.

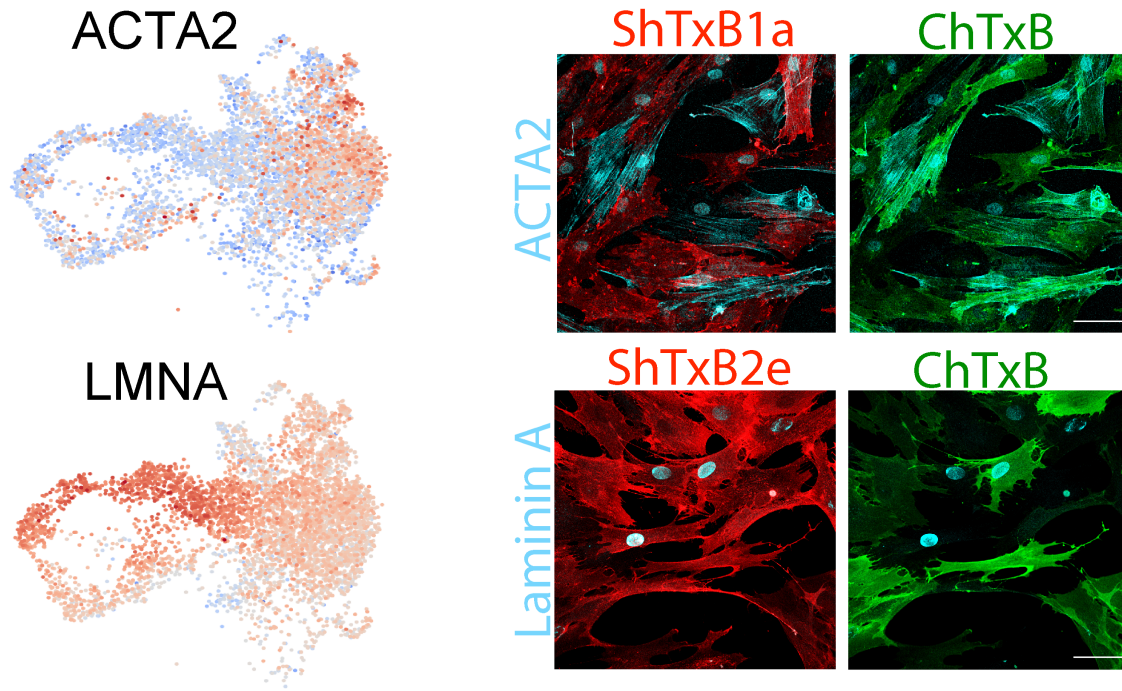


Figure 42. IF staining of dHFs with specific markers belonging to distinct transcriptional state. ACTA2 and LMNA were chosen as key markers for fibrogenic or basal dHFs states and plotted in the UMAP space (left panel). dHFs were then fixed and processed for IF. Cells were stained with bacterial toxins ShTxB1a/B2e (red) and ChTxB (green) and images acquired by confocal microscopy. In the right panel, merge images show how fibrogenic genes overlap with ChTxB⁺ cells while basal dHFs genes overlap with ShTxB2e⁺ cells. Scale bar is 100 μm.

6. 2 Conclusions

This chapter was dedicated to the understanding of the transcriptional configurations associated to dHFs in culture by using combination of toxins staining, which represent a way to visualize our *lipotypes*, and RNAseq analysis, to visualize the different transcriptional state (i.e. *cytotypes*). We could confirm that our dHFs in culture are associated with multiple transcriptional states. Importantly, we found that specific lipid configurations correspond to specific fibroblast states, with triple positive cells being pro-inflammatory fibroblasts, ShTxB1a/2e⁺ being proliferating cells, ShTxB2e⁺ being basal-state fibroblasts, and ChTxB⁺ being fibrogenic cells. These data trigger the question of whether lipid heterogeneity contributes to cell fate specification that we investigated in the following chapter.

CHAPTER 7. HIGHLY VARIABLE LIPIDS PARTICIPATE IN THE MAINTENANCE OF FIBROBLASTS TRANSCRIPTIONAL STATES

[In this chapter, the scRNA-seq experiment and data analysis has been done in collaboration with Irina Khven and Gioele La Manno]

GSL remodelling has been reported during cell differentiation to the point that GSLs have been used as differentiation stage and cell-type specific markers. It has also been shown that GSL-synthesis does not prevent cells growth in culture but stops embryonic development at an early stage. This suggests that GSLs are necessary for tissue patterning and multicellularity. Our results showed that given GSLs configurations (*lipotypes*) are associated with precise dHF states. In this chapter, we asked whether GSL metabolism influences transcriptional programs involved in the establishment of these dHFs states.

7.1 Transcriptomic analysis of dHFs after sphingolipids depletion

To study whether lipids participate in the maintenance of fibroblast transcriptional states, scRNAseq for a total of 6546 dHFs was performed in absence of SLs. In particular, SL biosynthetic pathway was blocked using a CerS inhibitor, FB1, as it showed a strong effect in decreasing SL synthesis (as shown in **Figure 30**). The scRNAseq experiment was performed in duplicate in two different days to ensure reproducibility. UMAP dimensionality reduction analysis was applied on global patterns of gene expression for each cell showing a global change in the transcriptional landscape (**Figure 43**).

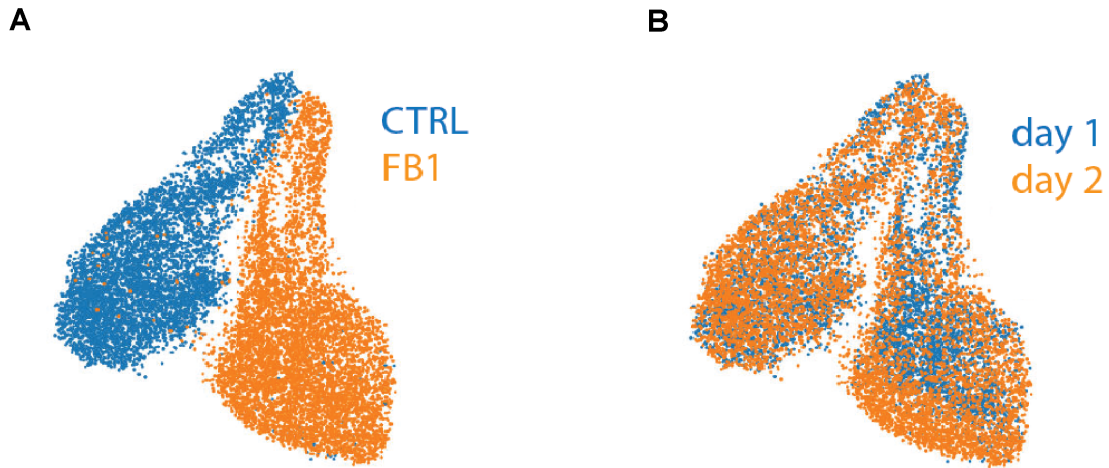


Figure 43. UMAP analysis of control and FB1 treated dHFs after scRNAseq analysis. UMAP analysis of 10x Genomics Chromium based single-cell RNAseq of 5652 single dHF for CTRL sample and 6546 single dHFs for FB1 treated sample. A) UMAP space of CTRL and FB1 treated. B) UMAP space of the two replicates for CTRL and treated sample show the high reproducibility of the analysis.

Data from control and treated samples were then integrated to identify the most significant transcriptional changes induced by sphingolipid depletion. When mapped in the transcriptional space along with control cells, FB1 treated dHFs displayed a different distribution (**Figure 44A**). FB1 treated cells were more frequently associated with fibrolytic (from 6% in CTRL to 23% in FB1 treated) and vascular (from 0.6% in CTRL to 1.3% in FB1 treated) states and less with the fibrogenic (from 48% in CTRL to 40% in FB1 treated) or inflammatory (from 9% in CTRL to 6% in FB1 treated) states (**Figure 44B**). When looking at the density map, it appeared even more clearly that SL inhibition by FB1 shifted cells from a fibrogenic state, associated with ECM organization, to a more fibrolytic state, associated with ECM degrading proteins (**Figure 44C**).

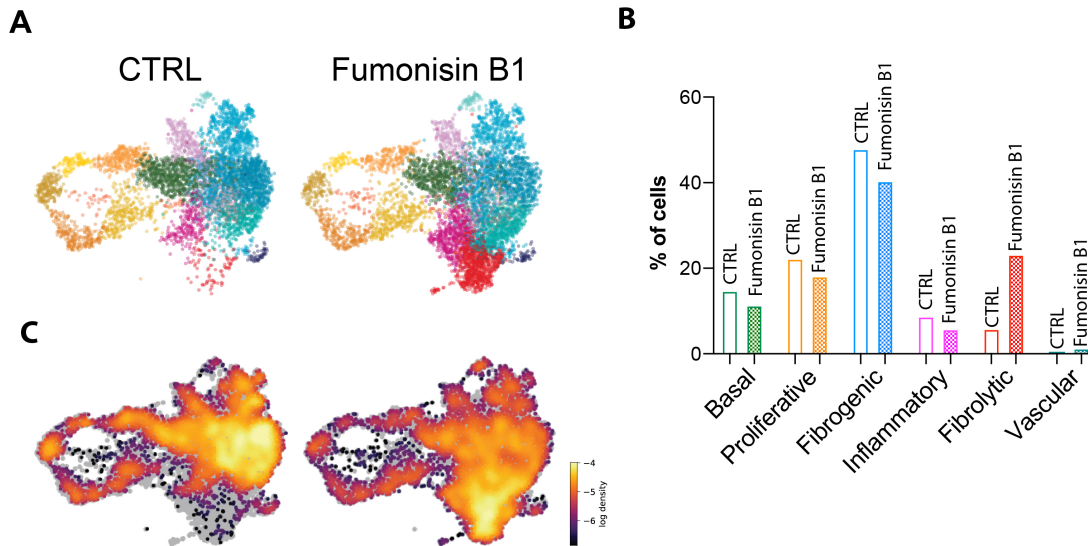


Figure 44. UMAP and cell density map of control and FB1 treated dHFs after scRNAseq. A) Integrated UMAP projections of CTRL (5652 individual dHFs) and FB1 treated cells (6546 individual dHFs) coloured by assigned cluster. **B)** Quantification of cell distribution across basal, proliferative, fibrogenic, inflammatory, fibrolytic and vascular cell clusters in CTRL and FB1 treated cells expressed as percentage of total cells. **C)** Density maps of CTRL and FB1 treated cells mapped in the integrated UMAP space. High relative cell density is shown as yellow.

When marker genes for fibrogenic cells, such as ACTA2 (i.e. smooth muscle actin SMA), or for fibrolytic cells, such as MMP1 (i.e. metalloprotease 1), were mapped into the integrated UMAP space, we found that fibrolytic proteins populated in FB1 treated sample, the area that was poorly populated in CTRL cells (**Figure 45**).

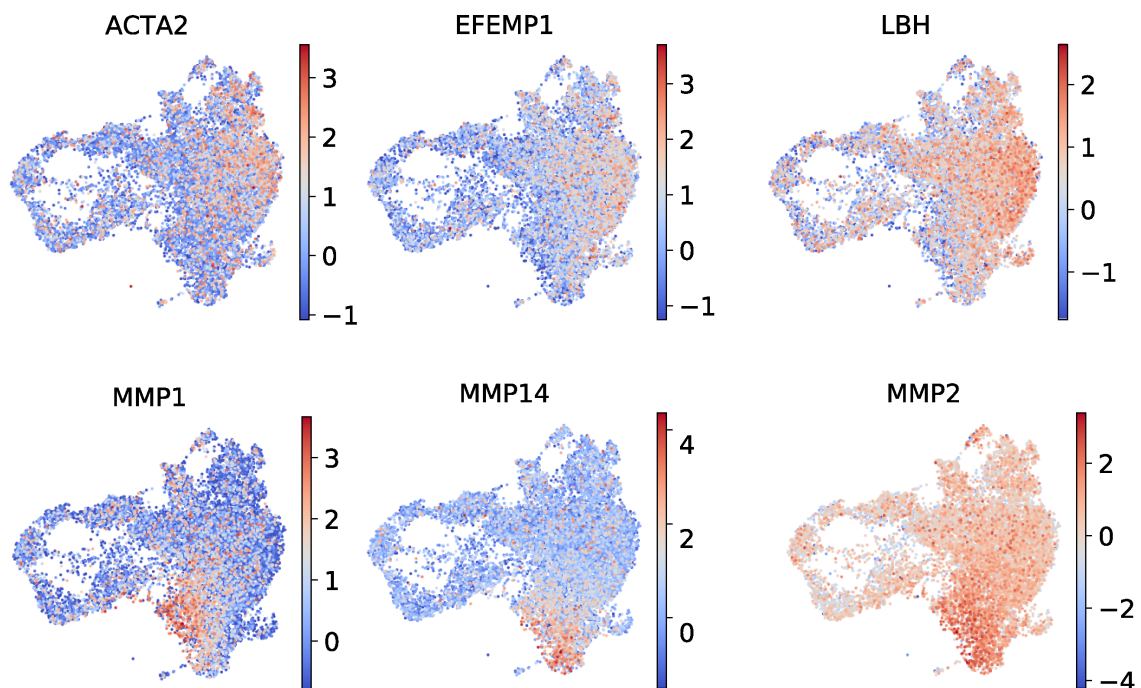


Figure 45. Integrated UMAP map of key marker genes for fibrogenic or fibrolytic genes. UMAP projections of genes encoding ECM depositing proteins (upper panel) or metalloproteases and (lower panel). Colour scale is according to gene expression level.

7.2 GSLs participate in the activation of FGF and TGF- β signalling pathways

It has been shown that both in physiological and pathological conditions, such as fibrosis, dHFs can exit their quiescent state and become “activated”. This process is driven by the activation of specific signalling pathways. Among these pathways, major contributors are Fibroblast Growth Factor (FGF) and Transforming Growth Factor Beta (TGF- β) signalling. They act through a reciprocal-negative regulation inducing fibrolytic or fibrotic states, respectively (David CJ and Massague' J, 2018; Calon A et al., 2014; Bishen KA et al., 2008; Inoue Y et al., 2002; Bordinon P et al., 2019). Thus, we evaluated the expression of FGF or TGF- β transcriptional signatures in dHFs (listed in **Table 3** and obtained as detailed in Bordinon P et al., 2019) and found that genes upregulated in TGF- β and downregulated in FGF pathways map the region where fibrogenic genes are, while genes downregulated in TGF- β and upregulated in FGF fall in the region of the UMAP highly populated after FB1 treatment (**Figure 46**). Going further, we mapped some of the marker genes for the FGF or TGF- β signalling pathways onto the UMAP space (**Figure 47**).

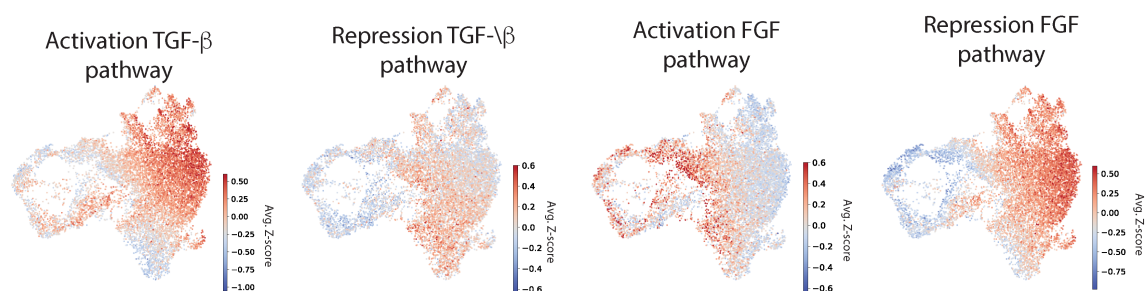
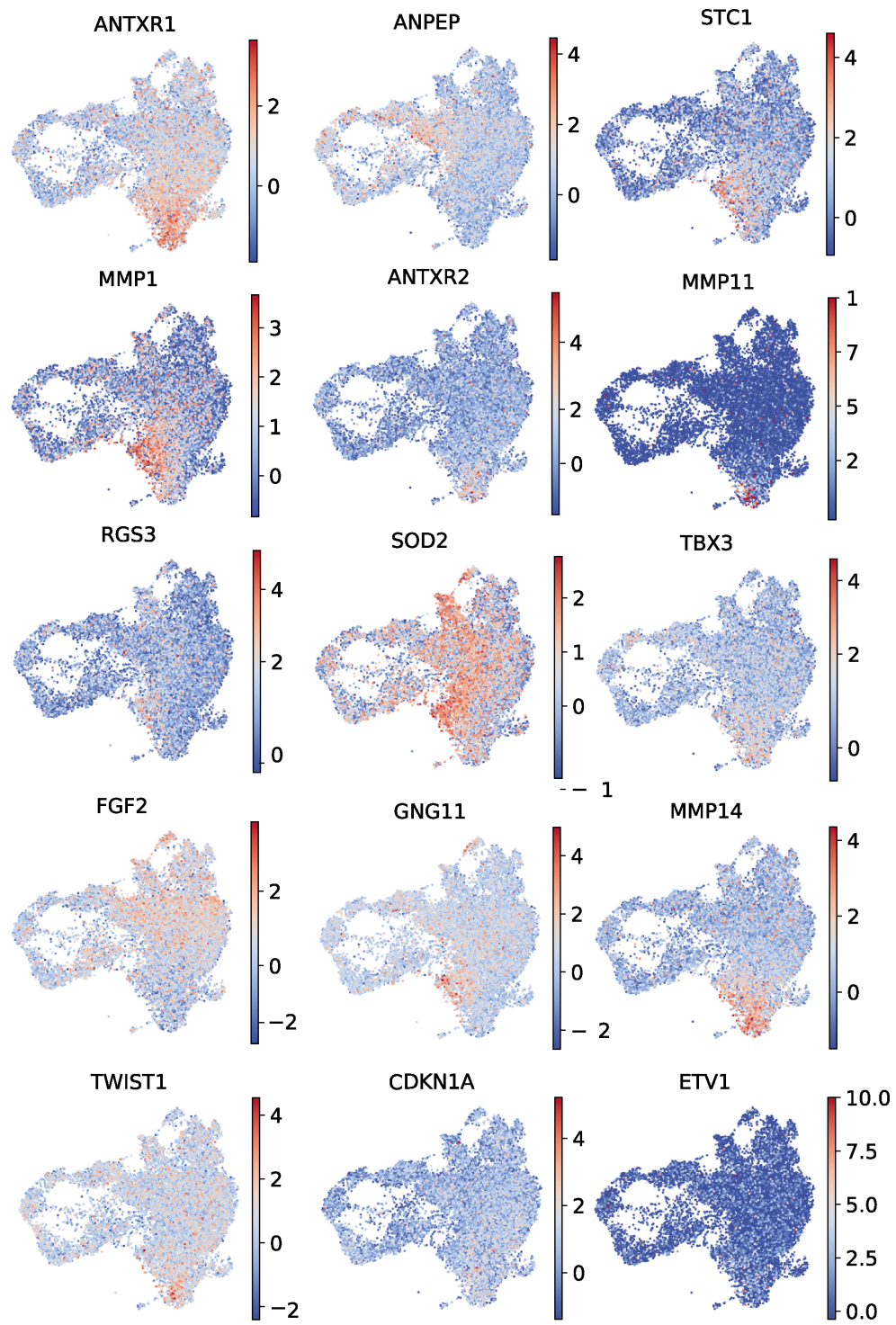


Figure 46. Integrated UMAP projections of FGF and TGF- β gene signatures. Signature genes were used to calculate the average Z-scores that were plotted into the UMAP space. Colour scale is according to Z-scores.

A**FGF Signatures**

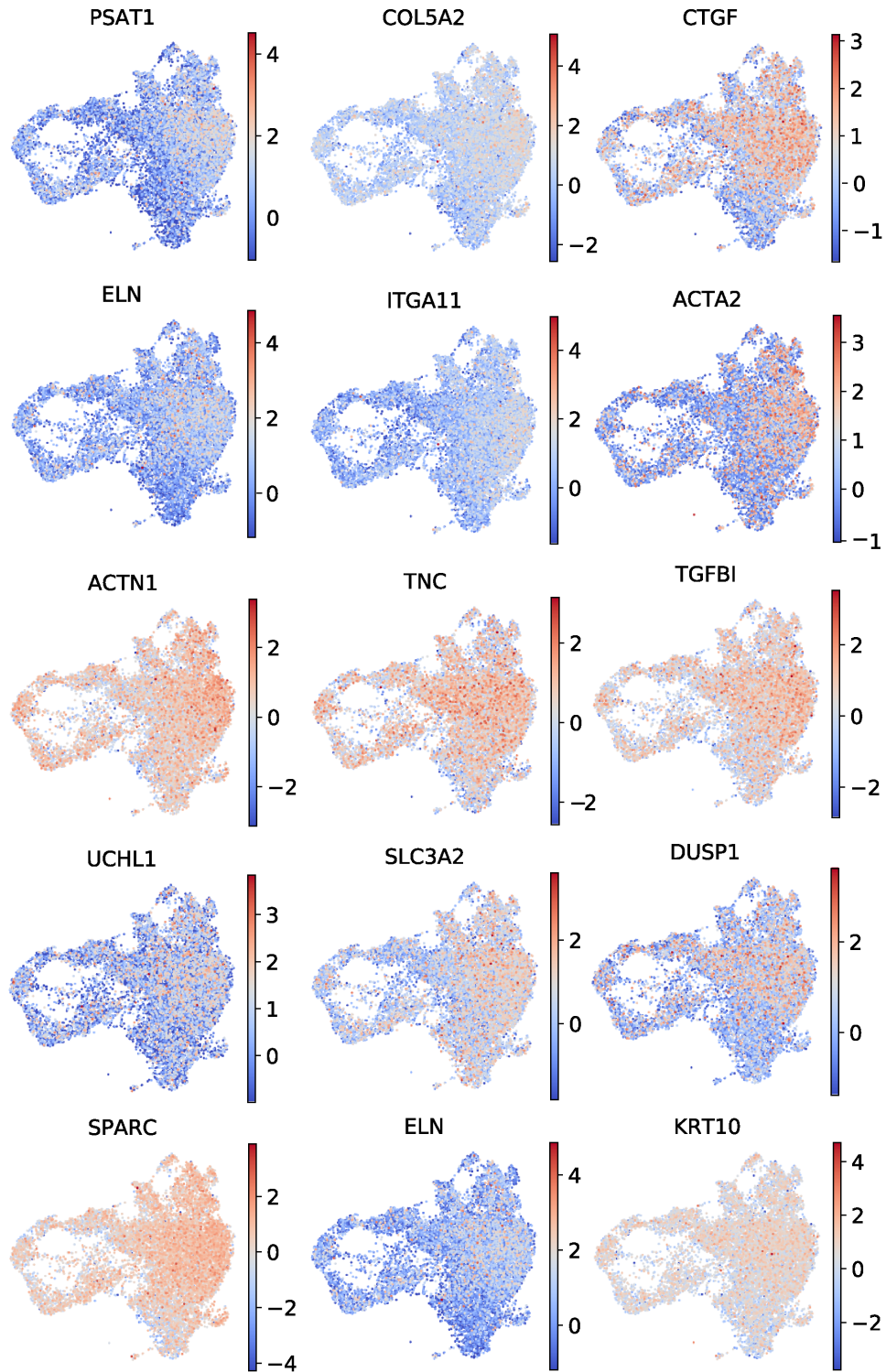
B**TGF- β Signatures**

Figure 47. UMAP projections of key marker genes up-regulated in FGF or TGF- β signalling pathways. Genes signatures were obtained as described in Bordignon et al., 2019. Colour scale is according to gene expression level.

Western blot (WB), quantitative real-time PCR (qRT-PCR) and immunofluorescence (IF) analysis on selected markers confirmed that there is a shift from TGF- β to FGF signatures when we treated dHFs with FB1, and extended this result to other SL synthetic inhibitors D-threo-PDMP and myriocin (**Figure 48**).

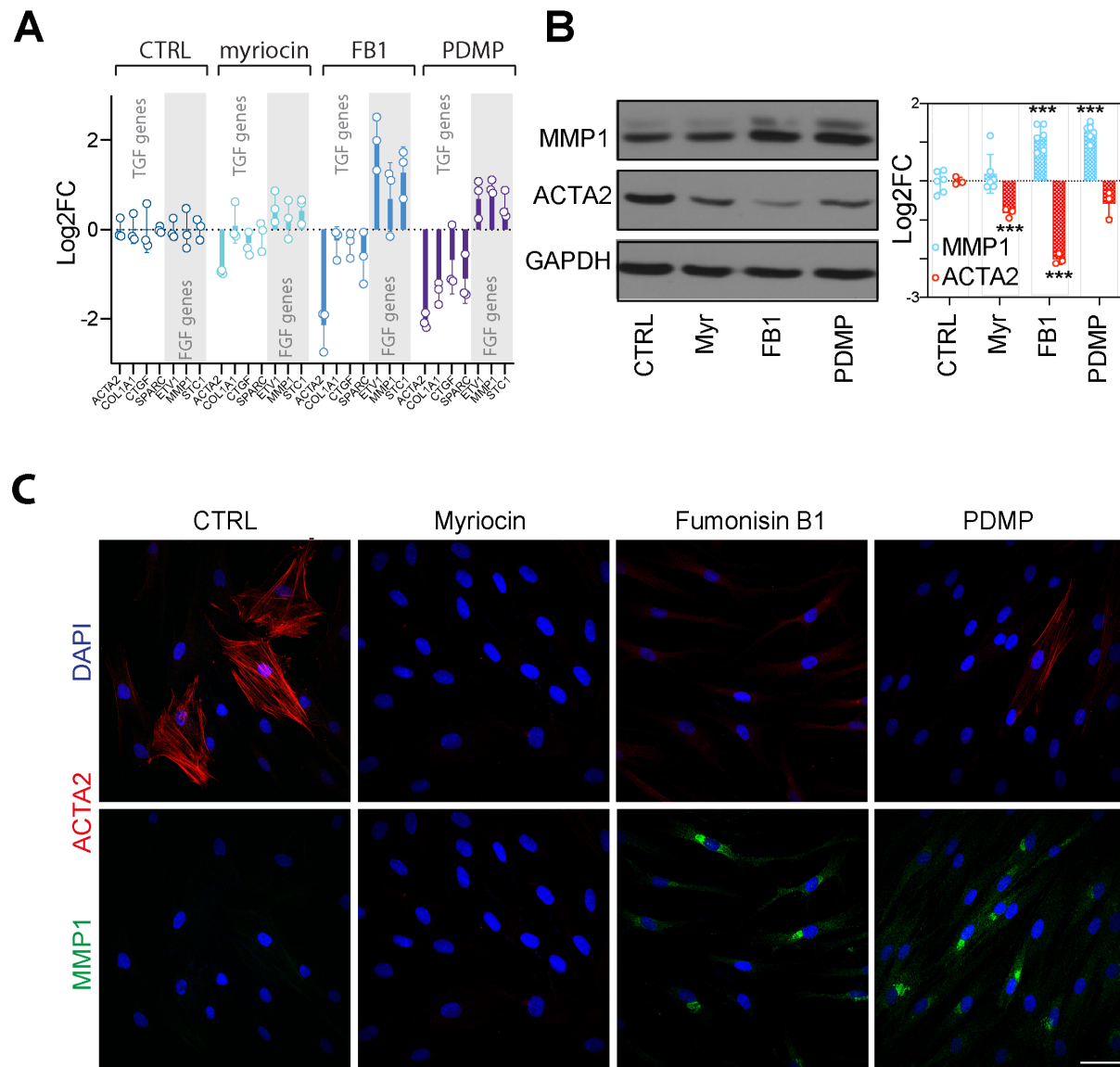


Figure 48. qRT-PCR, WB and IF analysis of FGF and TGF- β genes after SLs depletion. dHFs were treated with SL inhibitors (2.5 μ M myriocin, 25 μ M FB1 or 10 μ M PDMP) for 6 days and processed for qRT-PCR, IF or WB. **A**) mRNA levels of TGF- β and FGF genes were evaluated in CTRL and FB1 treated cells. qPCR data are shown as log₂ fold change over control. (n=3; data are means \pm StDev). **B**) Cells were lysed and processed for SDS-PAGE and western blotting analysis with antibodies recognizing ACTA2 and MMP1. Data were normalized against GAPDH and shown as log₂ fold change over control. (n=3; data are means \pm StDev; ***p < 0.001 [Student's t-test]). **C**) Cells were fixed and stained with ACTA2 (red) or MMP1 (green) antibodies. Scale bar is 50 μ m.

The effect of the SLs inhibition could be consequence of two opposite response: an inhibition of the TGF- β or an activation of the FGF signalling pathways. When we challenged dHFs with increasing amounts of TGF- β 1 we found that sphingolipid depletion does not inhibit TGF- β signalling, since the effect of TGF- β 1 on ACTA2 and MMP1 levels was amplified in FB1 treated cells. On the other side when we treated cells with increasing amounts of FGF2, we found that FB1 treated cells are sensitized to FGF signalling, since ACTA2 and MMP1 levels were lower and higher compared to CTRL cells, respectively. This suggested that SLs depletion is influencing FGF signalling, possibly activating the FGF receptor (**Figure 49**).

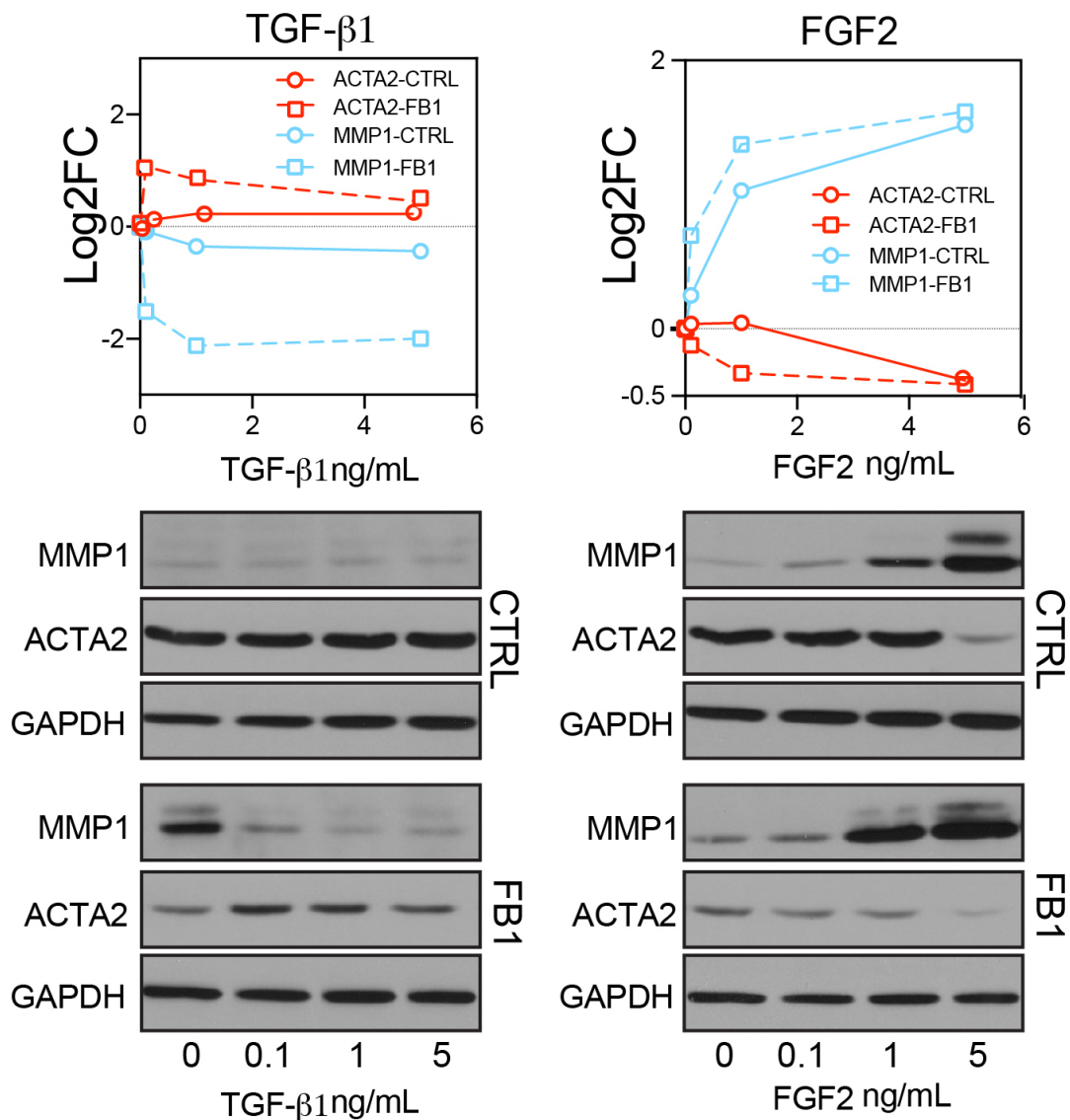


Figure 49. FGF2 and TGF- β 1 dose response analysis after SLs depletion by FB1. Cells were treated for 6 days with 25 μ M FB1 and then serum starved for 8h and fed with increasing concentration of FGF2 or TGF- β 1 for 72h. Cells were then lysed and processed for SDS-PAGE and western blotting analysis

with antibodies recognizing ACTA2 and MMP1. Quantification is shown in the upper panels. Data were normalized against GAPDH and shown as log₂ fold change over control; n=4.

To understand how these two axes are impacted by sphingolipid depletion we took advantage of dHFs where FGF or TGF- β signalling pathways were inactivated due to the expression of dominant negative versions of the TGF- β Receptor 2 (i.e., DNTGFR2) or of FGF Receptor 1 (i.e., DNFGFR1). These cell lines were treated with FB1 and their transcriptional response was analysed by qRT-PCR and WB (**Figure 50**). We observed that FB1 was ineffective in inducing its transcriptional changes in DNFGFR1-dHFs, indicating that sphingolipids influence FGF transcriptional program possibly modulating FGF receptor activity at the plasma membrane.

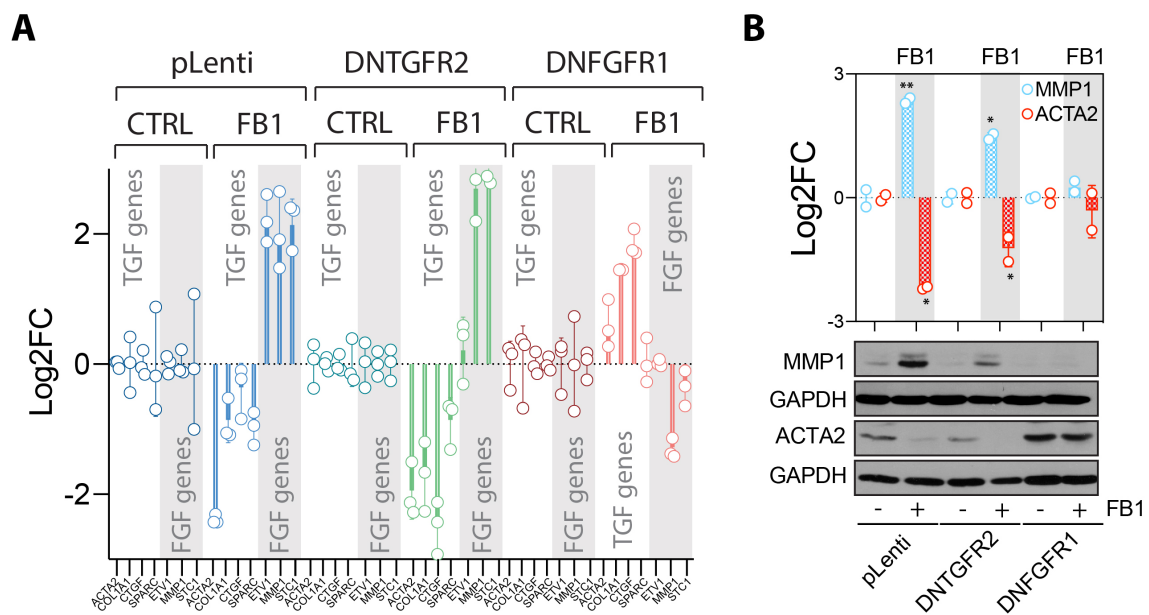


Figure 50. qRT-PCR and WB analysis of FGF and TGF- β key markers after FB1 treatment on DNTGFR2 and DNFGFR1 dHFs. dHFs were treated with 25 μ M FB1 for 6 days and processed for qRT-PCR or SDS-PAGE and western blotting. **A)** mRNA levels of TGF- β and FGF genes were evaluated in CTRL and FB1 treated cells. qRT-PCR data are shown as log₂ fold change over control. (n=3; data are means \pm StDev). **B)** Cells were lysed and processed for SDS-PAGE and western blotting analysis with antibodies recognizing ACTA2 and MMP1. Data were normalized against GAPDH and shown as log₂ fold change over control; (n=2; data are means \pm StDev; *p < 0.05, **p < 0.01 [Student's t-test]).

7.3 Which lipid participates in the modulation of FGF signalling pathway?

Myriocin, FB1 and D-threo-PDMP treatments deprive cells from many sphingolipids and how individual sphingolipids associated with distinct cell states influence FGF signalling cannot be inferred by these treatments only. We thus generated dHFs overexpressing either *B3GALNT1* (Gb4S) or *ST3GAL5* (GM3S) by lentiviral infection. Transfection level and the right cellular localization (i.e. Golgi complex) of the enzymes were tested by IF as compared to CTRL cells (**Figure 51**). By using an antibody against V5, the tag used in the plasmids chosen, we observed a good transfection level of GSL enzymes compared to CTRL cell and the correct localization at the Golgi complex. Moreover, these over-expressing cells displayed the expected changes in sphingolipid composition with GM3S-OE dHFs being largely ChTxB⁺ and ShtxB1a/2e⁻ and Gb4S-OE dHFs being prevalently ShtxB1a/2e⁺ and ChTxB⁻ (**Figure 52**).

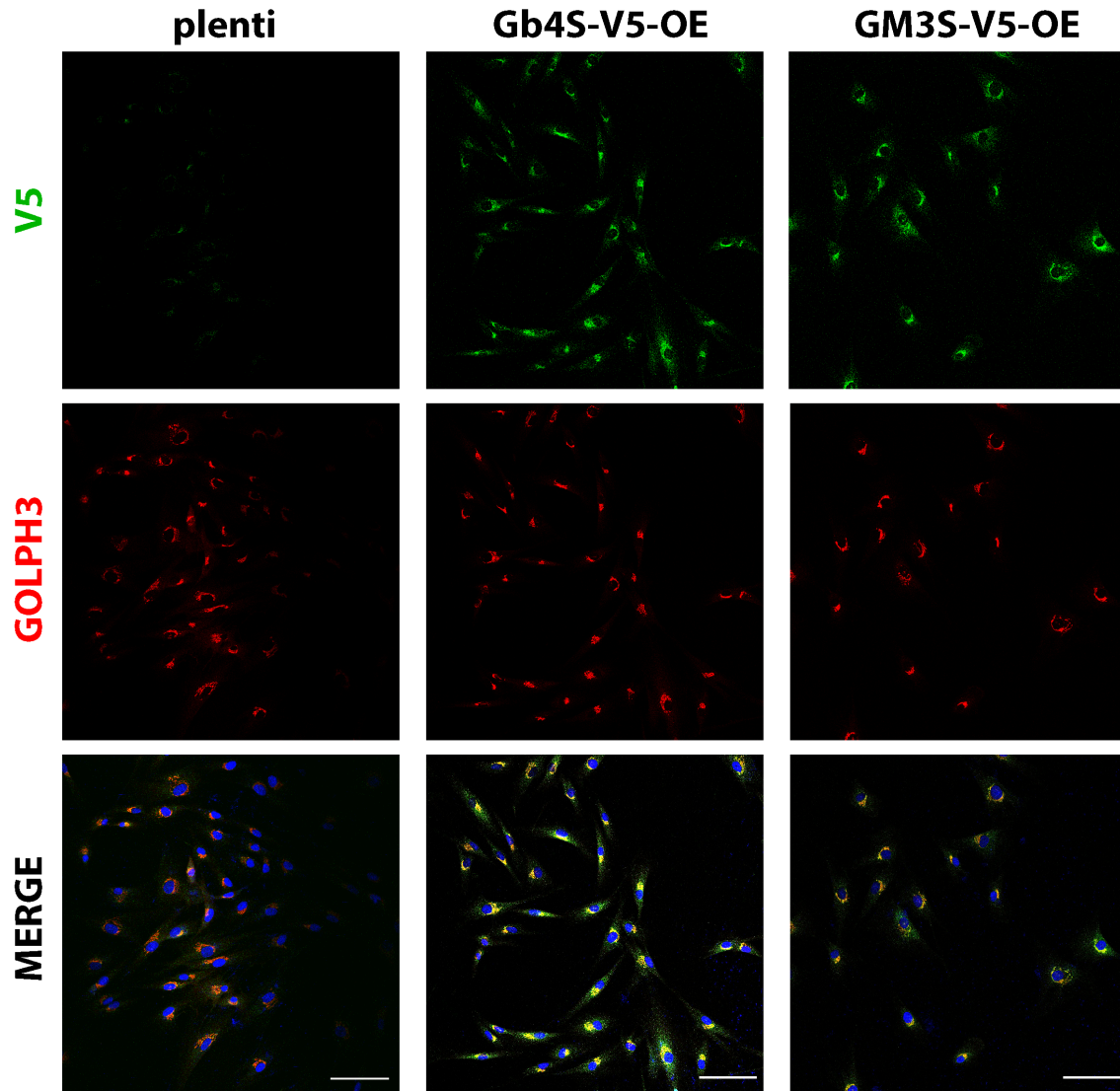


Figure 51. IF analysis of stable dHFs lines OE GSLs synthesizing enzymes. Cells were fixed and stained with V5 (green) antibody to detect the transfected enzymes or GOLPH3 (red) antibody to analyse GSL enzymes localization in the Golgi complex. Scale bar is 100 μm .

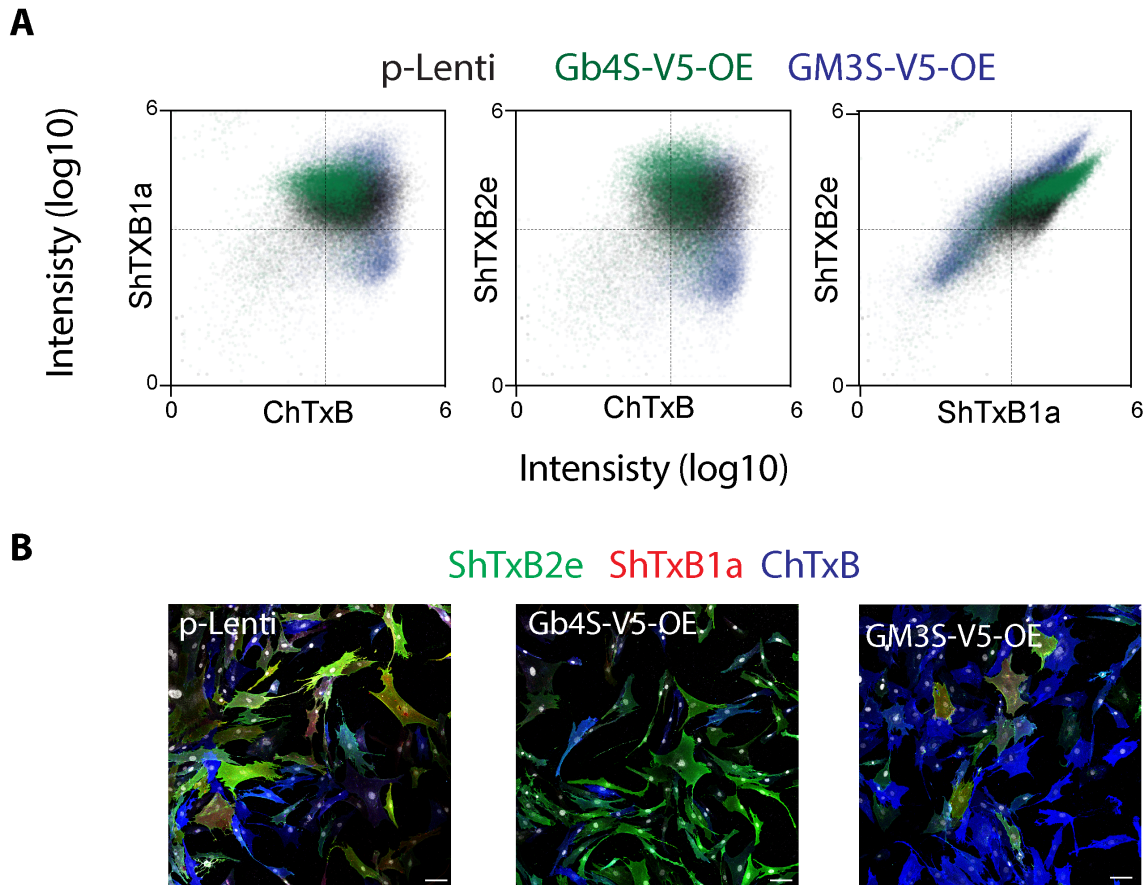


Figure 52. Cytofluorometric and fluorescence analysis of dHFs OE GSL synthesizing enzymes. A) Cells were stained with toxins recognizing lipid Gb3 (ShTxB1a/2e), Gb4 (ShTxB2e) and GM1 (ChTxB). Side scatter plots of \log_{10} fluorescence intensity values are shown for each toxin. Unstained cells were used as negative control. Cells were gated on the singlet population; CTRL $n=23'858$; GM3S-OE $n=24'007$; Gb4S-OE $n=21'358$. **B)** Cells were fixed and processed for fluorescence analysis. Cells were stained with bacterial toxins ShTxB1a (red), ShTxB2e (green) and ChTxB (blue) and images acquired by confocal microscopy. Scale bar is $100\mu\text{m}$.

Furthermore, western blot (WB) and immunofluorescence (IF) analysis on ACTA2 and MMP1 showed that the overexpression of *ST3GAL5* (GM3S) induces an increase in ACTA2 and a decrease in MMP1 levels, while opposite effect is shown by *B3GALNT1* (Gb4S) overexpressing dHFs (Figure 53).

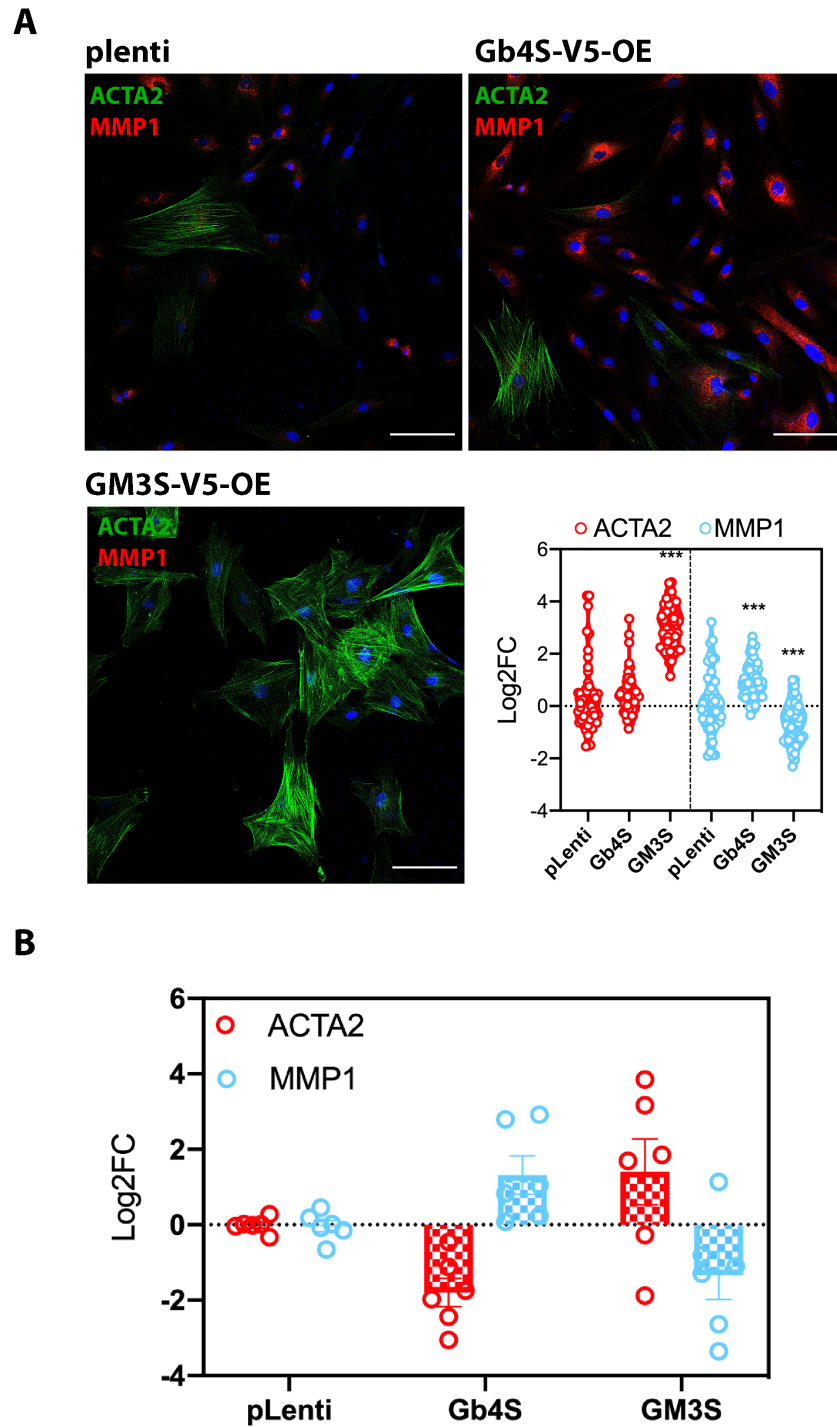


Figure 53. WB and IF analysis of FGF and TGF- β markers in dHFs OE GSL synthesizing enzymes. A) Cells were fixed and processed for IF. Cells were stained with ACTA2 (green) and MMP1 (red) and

images acquired by confocal microscopy. Scale bar is 100 μm . In the lower right panel, quantification of the immunofluorescence analysis is shown. Cells were segmented to calculate the integrated intensities of ACTA2 and MMP1. Data were normalized against the median and shown as \log_2 fold change over control in individual cell (CTRL n= 58; GM3S-OE n= 49; Gb4S-OE n= 81; ***p <0.001 [Student's t-test]). **B)** Cells were lysed and processed for SDS-page and western blotting analysis with antibodies recognizing ACTA2 and MMP1. Data were normalized over GAPDH and shown as \log_2 fold change over control (data are means \pm StDev; n=6).

7.4 Conclusions

In this chapter we show that highly variable lipids (i.e. Gb3, Gb4 and GM1) participate in the maintenance of dHFs transcriptional states. Specifically, we found that cells treated with sphingolipid synthesis inhibitor FB1 display a shift from a transcriptional state bearing fibrogenic properties to one expressing pro-inflammatory cytokines and more fibrolytic properties. We also found that this shift is largely due to a diversion in the FGF signalling induced by SLs deprivation. Interestingly, we found that, the overexpression of anti-regulated GSL synthesizing enzymes, have opposite effect on FGF and TGF- β signalling. This indicates that given lipid configurations (*lipotypes*) participate in dHFs fate determination by integrating transcriptional programmes endowed with key roles in skin homeostasis.

CHAPTER 8. CROSSTALKING BETWEEN dHFs AND LIPOTYPES

Specific lipid configurations (*lipotypes*), as shown in the previous chapter, participate in dHFs fate determination by integrating into the circuits that influence transcriptional programmes endowed with key roles in skin homeostasis: FGF and TGF- β signalling pathways. Whether FGF and TGF- β signalling in turn influence the balance among the different *lipotypes* in dHFs is not clear.

8.1 Do lipotypes and fibroblast signalling pathways crosstalk?

In order to answer this question, we again took advantage of dHFs expressing dominant negative versions of the TGF- β Receptor 2 (i.e., DNTGFR2) or of FGF Receptor 1 (i.e., DNFGFR1). Cells were stained by bacterial toxins and analysed by fluorescence and cytofluorimetry. As shown in **Figure 54**, DNTGFR2 expression is associated with a slight reduction in ChTxB staining while DNFGFR1 expression caused a substantial increase in ChTxB staining and an almost complete abrogation of ShTxB1a and ShTxB2e staining. This indicates that perturbations in major transcriptional programs accounting for fibroblast heterogeneity are reflected in cell-specific *lipotypes*.

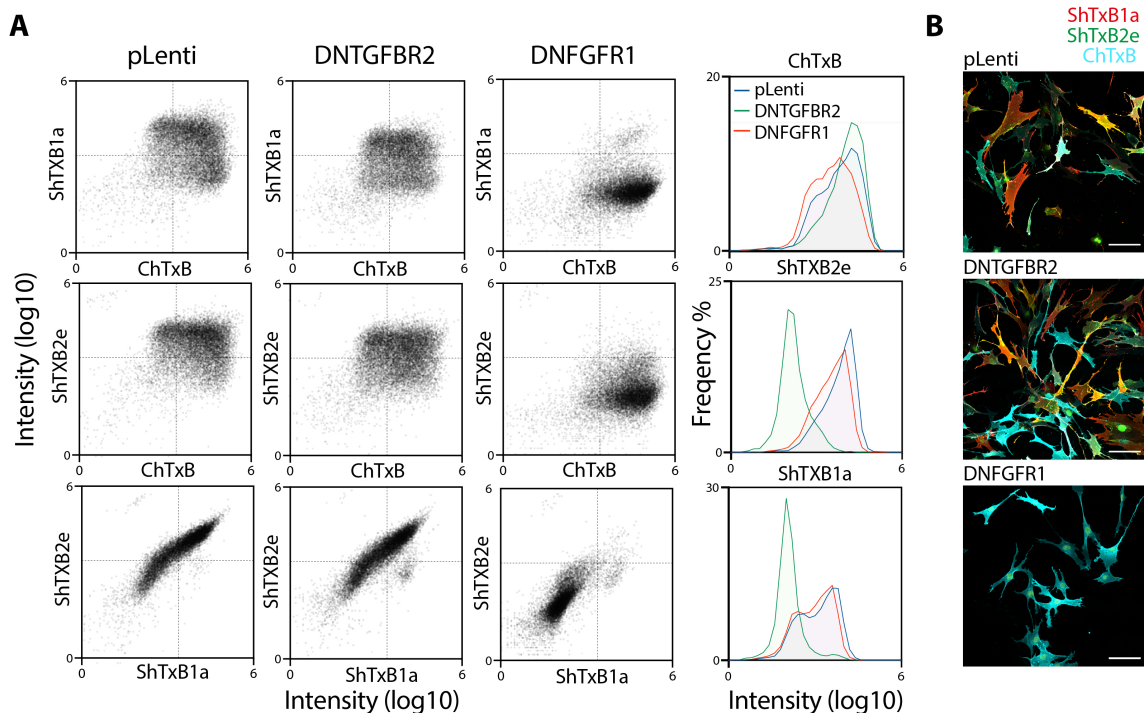


Figure 54. Cytofluorimetric and fluorescence analysis of dHFs expressing dominant negative form of TGFBR and FGFR. A) Cells were stained with toxins recognizing lipid Gb3 (ShTxB1a/2e), Gb4 (ShTxB2e) and GM1 (ChTxB). Side scatter plots of \log_{10} fluorescence intensity values are shown for each toxin. Histograms of the frequency distribution are shown for each condition and for each toxin binding (right panel). Unstained cells were used as negative control. Cells were gated on the singlet population (pLenti n=12'214; DNFGFR1 n=12'855; DNTGFR2 n=12'357. **B)** Cells were stained with bacterial toxins ShTxB1a (red), ShTxB2e (green) and ChTxB (cyan) and images acquired by confocal microscopy. Scale bar is 100 μm .

To confirm the changes in lipid composition in these cells, $[\text{H}^3]$ -sphingosine pulse experiment aimed at evaluating sphingolipid biosynthesis, was performed. As shown in **Figure 55**, DNTGFR2 expression has minimal impact on sphingolipid synthesis, while DNFGFR1 expression caused a substantial decrease in Gb3 production. This suggests that there is a crosstalk between FGF receptor and GSLs with a specific impact on globosides levels.

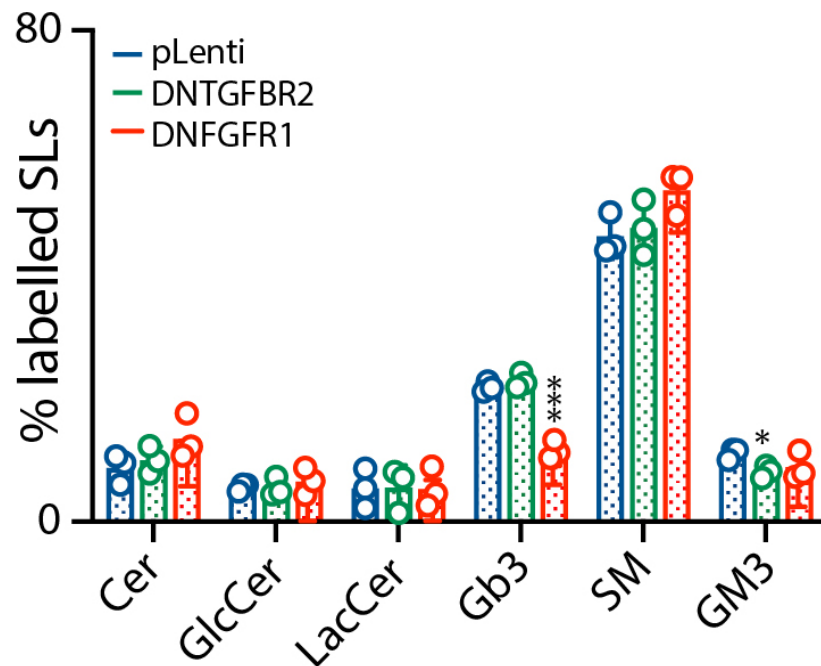


Figure 55. *De novo* sphingolipid synthesis in DNTGFR2 and DNFGFR1 dHFs. dHFs expressing dominant negative form of FGFR1 and TGFBR2 receptor were pulse labelled for 2 hours with $[\text{H}^3]$ -sphingosine for SLs synthesis assessment. The percentage of total radioactivity associated with SM, Cer and GSLs (i.e., GlcCer, LacCer, Gb3, and GM3) in the different cell lines was quantified after lipid extraction and HPTLC separation. (n=3; data are means \pm StDev; *p < 0.05, ***p < 0.001 [Student's t-test]).

Heterogeneous cell-to-cell GSL composition was found to correlate with the single-cell expression of the relevant GSL synthetic enzymes as shown by mRNA FISH experiments in **Figure 36**. Thus, mRNA FISH experiment was performed to simultaneously detect *ST3GAL5* (GM3S), *A4GALT* (Gb3S), and *B3GALNT1* (Gb4S) mRNA levels in individual dHFs expressing the dominant negative version of the TGF- β Receptor 2 (i.e., DNTGFR2) or of FGF Receptor 1 (i.e., DNFGFR1). By evaluating the FISH signals in >400 individual cells for each cell line, we found that *A4GALT* expression is slightly reduced in DNTGFR2 and DNFGFR1 dHFs, while *ST3GAL5* mRNA expression is significantly increased in DNFGFR1 expressing cells (**Figure 56**).

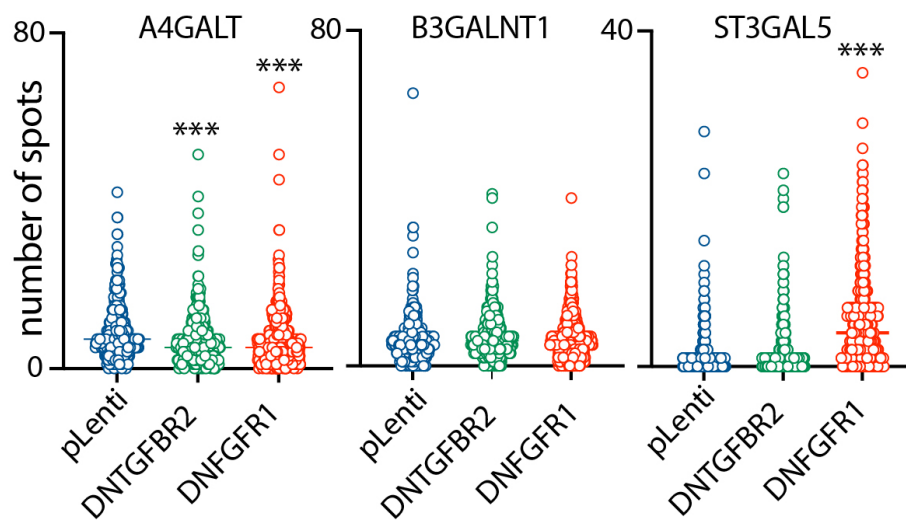


Figure 56. Fluorescence in situ hybridization (FISH) analysis of GSL synthesizing enzymes in DNTGFR2 and DNFGFR1 dHFs. Quantification of mRNA-FISH analysis in 356, 586 or 427 individual cells (pLenti, DNFGFR1 and DNTGFR2 respectively) is shown. mRNA levels of *A4GALT* (Gb3S), *B3GALNT1* (Gb4S) and *ST3GAL5* (GM3S) are represented as number of spots per individual cells in a violin plot (* $p < 0.05$, *** $p < 0.001$ [Student's t-test]).

Following a similar experimental setup, we decided to look at the mRNA level of the GSL synthesizing enzymes *ST3GAL5* (GM3S), *A4GALT* (Gb3S), and *B3GALNT1* (Gb4S) in individual dHFs after stimulation with FGF2 or TGF- β 1. By evaluating the FISH signals in >400 individual cells for each condition, we found that *ST3GAL5* mRNA expression is significantly decreased

in FGF2 treated cells, which is in good correlation with the fact that *ST3GAL5* mRNA level significantly increased in DNFGFR1 expressing cells (**Figure 57**).

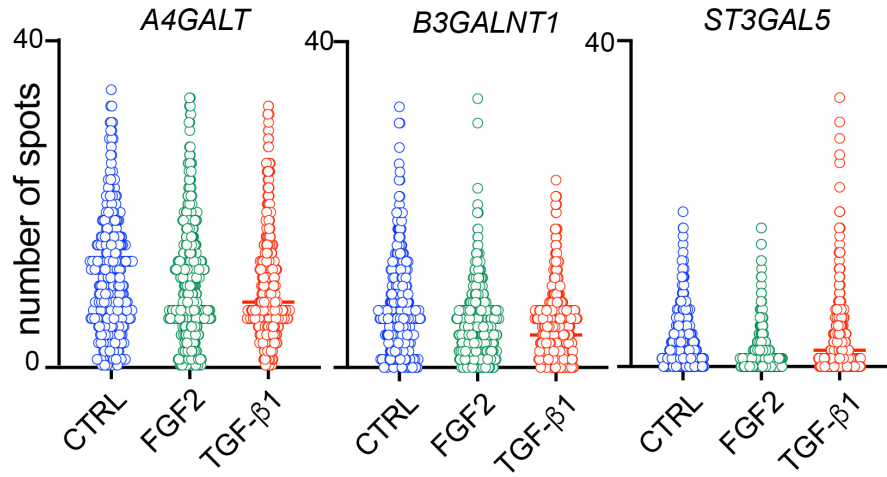


Figure 57. Fluorescence in situ hybridization (FISH) analysis of GSL synthesizing enzymes in dHFs treated with FGF2 or TGF- β 1. Cells were treated for 72 h with 10 ng/mL of FGF2 or TGF- β 1, then fixed and processed for FISH experiment. Quantification of mRNA-FISH analysis in 363, 564 or 496 individual cells (CTRL, FGF2 treated and TGF- β treated, respectively) is shown. mRNA levels of *A4GALT* (Gb3S), *B3GALNT1* (Gb4S) and *ST3GAL5* (GM3S) are represented as number of spots per individual cells in a violin plot (** $p < 0.001$ [Student's t-test]).

8.2 Conclusions

We observed that FGF signalling controls the expression of genes encoding key GSL synthetic enzymes and, as a consequence the cellular lipid composition. This regulatory wiring leads to a feedback loop circuit where its operation lead to multistability and to cell-to-cell heterogeneity, depending on a crosstalk between lipids and PM receptors (see discussion).

CHAPTER 9. DISCUSSION

Fibroblasts play an essential role in mammalian physiology by synthesizing the ECM that is necessary to maintain the structural integrity and the architecture of tissues and organs (Driskell RR and Watt FM, 2015; Thulabandu V et al., 2017). Although fibroblasts were long thought to be a homogeneous cell population, recent research has uncovered an unforeseen degree of complexity for this cell type (Sorrell JM and Caplan AI, 2004; Lynch MD and Watt FM, 2018). Individual fibroblast, indeed, exhibit discrete gene expression patterns, leading to different biological functions that depend on their anatomical location, embryonic origin, stage of development or tissue microenvironment (Lynch MD and Watt FM, 2018; Sriram G et al., 2015). Fibroblasts can show high heterogeneity even within the same tissue or when kept in culture under controlled conditions. One such example is constituted by fibroblasts of the skin or dermal fibroblasts (Ghetti M et al., 2018; Harper RA and Grove G, 1979; Wang JF et al., 2008). Multipotent progenitors differentiate into several dermal fibroblast lineages, which are primarily different due to their location in the dermis: papillary and reticular fibroblasts and dermal papilla (Driskell RR et al., 2013). Papillary and reticular fibroblasts exhibit differences in the expression of collagen subtypes, rate of cell division and contraction, and have different role in wound repair (Schoop VM et al., 1999; Philippeos C et al., 2018; Lynch MD and Watt FM, 2018; Sriram G et al., 2015; Griffin MF et al., 2020; Woodley DT, 2017; Janson DG et al., 2012; Rinn JL et al., 2006; Varkey M et al., 2011).

In addition to this first layer of heterogeneity, analysis based on scRNAseq, distinguished numerous mesenchymal populations in human skin, including pericytes, preadipocytes, and myofibroblasts and other uncharacterized cell types. According to this approach, dermal fibroblasts can be subdivided into four major populations with functionally distinct transcriptomic signatures and spatial distribution: secretory-reticular, secretory-papillary, pro-inflammatory and mesenchymal fibroblasts (Vorstandlechner V et al., 2019; Tabib T et al., 2018; Philippeos C et al., 2018; Solé-Boldo L et al., 2020).

dHFs heterogeneity, has profound implications for the understanding of pathological states, including diseases characterized by excessive fibrosis, aging (Maier AB et al., 2009; Haydont V et al., 2019; Solé-Boldo L et al., 2020), and cancer (Kalluri R and Zeisberg M, 2006). Among

them, skin fibrosis is the common outcome of many forms of tissue damage during the process of wound healing. It can manifest locally in response to dermal injury following burn, surgery, trauma, infection or radiation, or in association with systemic diseases such as scleroderma and graft-versus-host disease (Pedroza M et al., 2018; Song J et al., 2018).

Wound healing involves a dynamic series of cellular and biochemical events including immune response, local proliferation of cells, EMC deposition, and tissue regeneration. Wound repair, thus, requires the coordinated efforts of several cell types including keratinocytes, fibroblasts, smooth muscle cells, endothelial cells, immune cells, macrophages, and platelets. Following skin damage, fibroblasts, in particular, exit their quiescent state and become “activated”. However, fibroblast subpopulations differ in their wound healing response. For example, lineage-tracing studies demonstrated that reticular fibroblasts are the first to repopulate the damaged tissue and mediate the ECM deposition, whereas papillary fibroblasts move in later and may have a role in remodelling and/or regeneration (Rognoni E et al., 2018). Thus, during the process of skin repair, dHFs ‘differentiate’ into inflammatory cells involved in cytokine secretion and in ECM degradation and remodelling (production of matrix metalloproteases MMPs) or into myofibroblasts that produce ECM proteins (collagens and fibronectins). After some days, the inflammation is resolved and both inflammatory cells and myofibroblasts are removed. When the injury is more severe or persistent, regeneration is not possible and the organism will respond with fibrosis, producing scars full of inflammatory cells and myofibroblasts (Adler M et al., 2020). Hence, a balanced activity of the different fibroblast types is key to repair scars and avoid fibrosis (Darby IA and Tim DE, 2007; Klingberg F et al., 2013; Coentro JQ et al., 2018; Eming SA et al., 2014). Several transcriptional programs and signalling pathways involving growth factors, cytokines, and chemokines regulate the process of wound healing (Eming SA et al., 2014; Rossio-Pasquier P, et al., 1999; Gabbiani G., 2003). These include epidermal growth factor (EGF), fibroblast growth factor (FGF), insulin-like growth factor, keratinocyte growth factor, platelet-derived growth factor (PDGF) and transforming growth factor (TGF- β) pathways (Barrientos S et al., 2008). FGF and TGF- β are the two main pathways linked to fibroblasts activation and they work through a reciprocal-negative regulation (David CJ and Massague’ J, 2018; Calon A et al., 2014; Bishen KA et al., 2008; Inoue Y et al., 2002; Bordignon P et al., 2019).

TGF- β signalling in particular enhances invasive properties and epithelial-to-mesenchymal transition (EMT) with induction of a battery of genes encoding proteins connected with the fibrotic and wound-healing reaction (David and Massagué, 2018) and endowed with cancer-invasive properties (Calon A et al., 2014). On the other side, FGF has been implicated in multiple fibrotic disorders (Bishen KA et al., 2008; Inoue Y et al., 2002; Strutz F et al., 2000), in promoting macrophage infiltration, and it has also been reported to suppress myofibroblast activation in skin wounds (Ishiguro S et al., 2009), with a potentially favourable impact on hypertrophic scars. Thus, these two signalling pathways play key roles also in epithelial tumours, activating skin fibroblasts to cancer associated fibroblasts (CAFs).

CAFs as skin fibroblasts are highly heterogeneous and can be classified as inflammatory, immune or myofibroblast-like CAFs, each of which influence tumour growth and metastatization differently (Gascard P and Tlsty TD, 2016; Kalluri R and Zeisberg M, 2006).

Given the diversity of dHFs and CAFs, it is then necessary to define the role their heterogeneity has to define the circuit that induce cells to choose a particular fate that can lead to different physiological outcomes: i.e., fibrosis vs fibrolysis or cancer metastatization vs chronic inflammation (**Figure 58**).

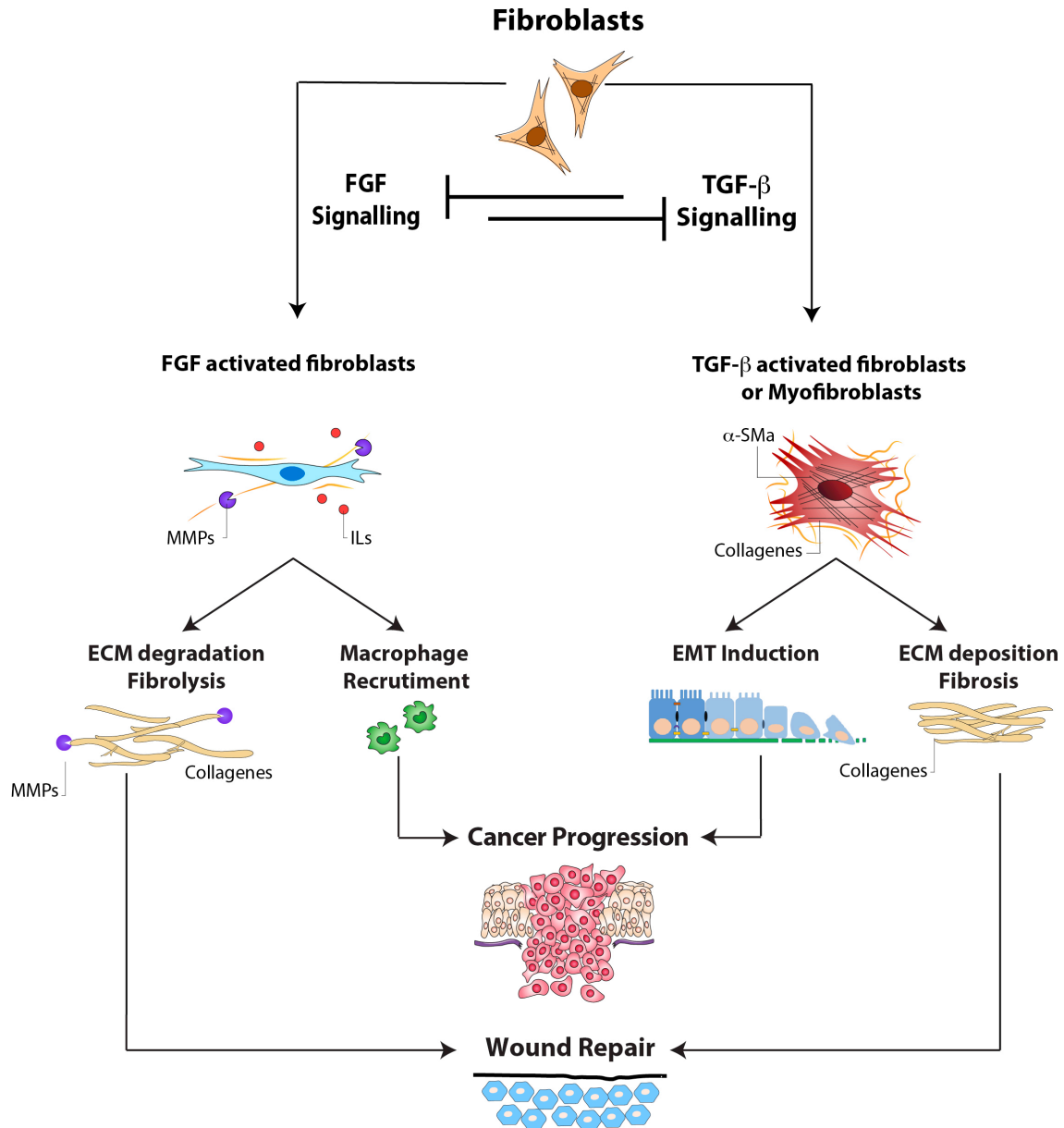


Figure 58. Simplified scheme of dHFs activation for tissue repair and cancer progression. Normal dHFs can be activated by two distinct signalling pathways. FGF and TGF- β control dHFs activation through a reciprocal-negative regulation. FGF-activated dHFs produce metalloproteases and cytokines while TGF- β -activated dHFs produce ECM proteins. Suppression of one pathway leads to activation of the other and vice-versa. This reciprocal regulation can lead to tumour-promoting CAF populations that favour metastasis through EMT or macrophage recruitment. On the other side it can lead to wound repair though the reciprocal action of ECM depositing cells (process of fibrosis) and ECM degrading proteins (process of fibrolysis).

In this thesis we have used high resolution MALDI-IMS to evaluate the lipid composition of individual dHFs in culture and found that individual dHFs vary in the sphingolipid composition of their membranes. Among sphingolipids, we focused our attention on GSLs Gb3, Gb4 and GM1 and found that these lipids define fibroblast sub-populations (*lipotypes*), that propagate across cell generation. By combining single-cell lipidomics with other existing and well established single-cell omics approaches, we also found that these *lipotypes* parallel the existence of dHFs cytotypes, with proliferative, inflammatory or fibrogenic properties, and that specific lipids where their expression is cell-to-cell variable participate in regulatory networks responsible for cell-to-cell heterogeneity. Finally, we have found that individual dHFs express specific GSL configurations depending on whether they are on resting or different activated states.

Our results indicate that different SL metabolic branches can modulate dHFs response to instructive stimuli. In particular, GSLs Gb4 and GM1 integrate into the circuits above mentioned that drive the activation of dHFs through TGF- β or FGF signalling (**Figure 59**). This suggests that pharmacological modulation of the sphingolipid metabolism may allow targeting of specific fibroblast populations and cell signalling pathways to prevent fibrotic lesions and to influence skin tumour microenvironment.

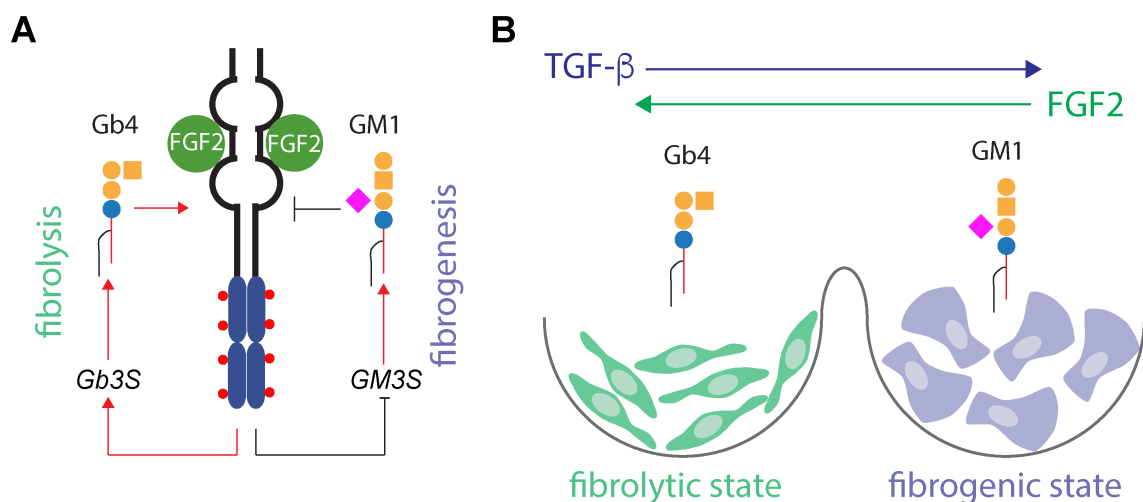


Figure 59. Hypothetical molecular model. **A)** Schematic representation of the FGF/sphingolipid circuit. FGF2 binds FGFR leading to the induction of A4GALT/Gb3S and to the repression of ST3GAL5/GM3S. This in turn will result in the prevalent production of Gb3/Gb4 over GM1. To close

the circuit GM1 negatively regulates FGFR, while Gb3/Gb4 activate FGFR in a positive feedback loop. **B)** The circuit described in **(A)** generates a bistable system where cells can be either Gb3/Gb4⁺ leading to a more fibrolytic state or GM1⁺ leading to a more fibrogenic state. Instructive signals (i.e., TGF- β and FGF) and lipid remodelling cooperate to assist cell state switches.

Interestingly, it has already been shown that GSL reprogramming has a role in the epithelial-to-mesenchymal transition (EMT). During TGF- β induced EMT, the production of GSLs is switched from the asialo to ganglio series owing to the induction of *ST3GAL5* and *ST8SIA1* (encoding GD3 synthase) and to the repression of *B3GALT4* (encoding GA1/GM1 synthase) (Mathow D et al., 2015) (**Figure 60**). Accordingly, Ghiroldi et al. found that an induced up-regulation of sialidase Neu3, a GM3 degrading enzyme, can significantly reduce cardiac fibrosis in primary cultures of human cardiac fibroblasts by inhibiting the TGF- β signalling pathway, ultimately decreasing collagen deposition (Ghiroldi A et al., 2020).

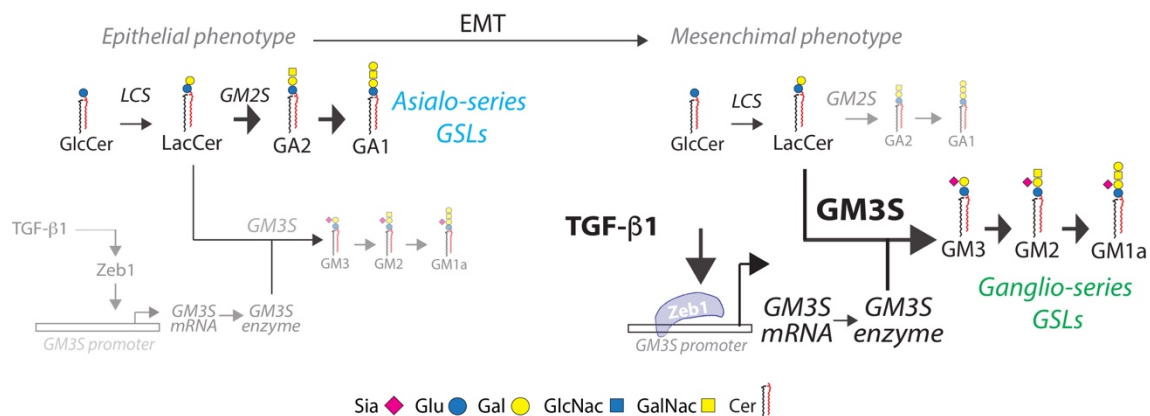


Figure 60. The asialo- to ganglio-GSL switch during EMT. During the acquisition of the mesenchymal phenotype, which is induced by TGF- β 1, the transcription factor Zeb1 binds the GM3S (*ST3GAL5*) promoter and activates its transcription. (Adapted from Russo et al., 2018).

Moreover, a set of GSLs have also been found to interact with PM located signalling receptors and to modulate their activation (Coskun U et al., 2011; Park SY et al., 2012; Rusnati M et al., 2002). Although some examples come from gangliosides which have been described to interact with platelet-derived growth factor receptor (PDGFR) and epidermal growth factor

receptor (EGFR), or with the ligands, such as FGF2, these reports are sometimes confusing since they point to opposing mechanisms (Miljan EA and Bremer EG, 2002). Thus, whether and how GSLs interact with PM receptors and how they influence their downstream effects is still to be investigated. Furthermore, these studies have been produced using bulk cell extracts and manipulating the level of few selected lipids, hence, which is exactly the role of GSLs in cell fate determination remains unclear.

Here, we were able to study hundreds of lipids at the same time in individual cells and we found that their heterogeneity at the level of single-cells is sufficient to modulate dHFs fate. Cell-to-cell variability (either stochastic or deterministic) indeed provides otherwise identical cells with the capability to break symmetry and change their differentiation potential (Huang, 2009). According to this concept, progenitor cells can follow alternative differentiation trajectories to achieve one of multiple stable states depending on the variable expression of a key factor, eventually leading to cell fate decisions (Huang, 2009). Besides proteins and nucleic acids, it has been shown that lipids also can influence these cell fate decisions during differentiation programs (Liang YJ et al., 2010, 2011; Russo D et al., 2018a; Breimer ME et al., 2017). Lipids are, indeed, the main components of biological membranes but they also participate in energy metabolism, mediate signalling pathways, act as precursor of bioactive molecules, and interact with proteins to influence their activity and intracellular distribution.

Among PM lipids, GSLs are particularly suited to influence signalling, receptor trafficking, cell-cell contacts and adhesion, and, thus, ultimately gene expression. This is due to their glycan moieties that facilitate interactions with glycans and proteins of the same PM or with adjacent cells. It is their structural diversity and GSLs tissue specific production (Ngamukote S et al., 2007) to suggest that, although they are dispensable for cell survival and basic cell functions, they can have a role in multicellularity by influencing cell fate decisions towards precise differentiation trajectories. It has been described that GSLs remodelling has a crucial role during embryonic development (Cochran FB et al., 1982; Handa K and Hakomori S, 2017; Kannagi R et al., 1983; Yamashita T et al., 1999) and neuronal differentiation (Liang YJ et al., 2010, 2011; Russo D et al., 2018a; Breimer ME et al., 2017) as defects in GSL metabolism in model animals often leads to neurodevelopmental phenotypes or to embryonic death (Yamashita T et al., 2002; Nishie T et al., 2010; Allende ML and Proia RL, 2014). Moreover, GSL

composition varies among cells in a syngeneic cell population owing to cell cycle phase (Majoul et al., 2002), the local microenvironment (Snijder et al., 2009) or to metabolic circuits (Russo et al., 2018). How extensive cell-to-cell GSL variability is and how it participates in cell fate decisions and tissue patterning it's still an open question.

Our work is the first to systematically analyse single-cell lipid variability in dHFs and to describe how their heterogeneity can influence cell fate decisions. This highlights how new technologies to analyse single-cell lipidomes can be used to characterize biological phenomena in situ and to reveal lipid roles in intracellular processes, molecular microenvironment, cell-cell interactions, cell fate decisions and differentiation trajectories.

In general, the discovery that single-cell lipidomes describe and determine cell states rises a whole set of new questions about the involvement of lipid metabolism in cell fate determination. What exact cell-to-cell variable lipid species influence signalling events involved in self-organisation and how mechanistically they do that? What regulatory networks dictate cell-to-cell lipid variability? What are the physiological contexts where cell-to-cell lipid variability plays a role? What are the pathological consequences of inappropriate cell-to-cell variable lipid expression? Answering these questions will provide a new dimension in our understanding of cell fate determination and tissue patterning.

CHAPTER 10. MATERIALS AND METHODS

All chemicals and reagents used are listed in **Annex 1. Table of chemicals and materials**. Working concentrations and time of treatment are indicated within the corresponding experiment.

10.1 Cell lines and cell growth conditions

Dermal skin human fibroblasts (dHFs) were kindly provided by the laboratory of Alberto Luini (IBP-CNR, Naples, Italy) and by the laboratory of Prof. Thorsten Hornemann (IKC-USZ, Zurich, Switzerland). For further validation and analysis 4 other dHF cell lines were kindly provided by the laboratory of Dr. Charna Dibner (iGE3-UNIGE, Geneva, Switzerland). Primary foreskin HF expressing dominant-negative FGFR1 (DNFGFR1) or dominant-negative TGFR2 (DNTGFR2) were kindly provided by the laboratory of Prof. Paolo Dotto (DB-UNIL, Lausanne, Switzerland).

Cells were grown in DMEM supplemented with 10% (v/v) foetal bovine serum (FBS), 4.5 g/l glucose, 2 mM L-glutamine, 1 U/ml penicillin/streptomycin. The cell lines were grown under a controlled atmosphere in the presence of 5% CO₂ at 37 °C. Cells were grown in a flask until 90% confluence. The medium was removed and trypsin-EDTA solution (0.05% trypsin, 0.02% EDTA) was added for 3-5 min. Then, the medium was added back to block the protease action, and the cells were collected into a plastic tube. After centrifugation for 5 min at 1000 rpm, the cell pellet was resuspended in fresh medium, gently mixed, and placed in a new plastic flask with fresh growth medium.

10.2 Generation of stable cell line over-expressing GSLs synthesizing enzymes

[Generation of stable cell lines was done with the help of Galina Glousker from Prof. Lingner's lab].

For lentiviral production 293T cells were transfected in 10 cm dishes with 4 µg of the corresponding lentiviral vectors (empty vector or transgene listed in **Annex 4**) and packaging vectors pMD2.G (1 µg) and pCMVR8.74 (3 µg) using Lipofectamine 2000 (1:400 in OPTIMEM). The next day, the medium was changed for DMEM with 10% FCS and penicillin/streptomycin. The first harvest of viral particles was done 40 hours after transfection and fresh medium was added to the cells. Virus-containing medium was filtered through 0.45 µm filters and 10 ml of filtrate was applied to 1 million cells in 15 cm dishes. The second harvest was done 24 hours after the first harvest and the transduction repeated as described. The next day, transduced cells were split and selected with Blasticidin (10 µg/mL) for at least one week.

10.3 Single-cell MALDI Imaging Mass Spectrometry (MALDI-IMS) workflow

10.3.1 Sample preparation

dHFs, were directly grown on glass bottom culture dish (Mattek) in complete media to roughly 60% confluence. After aspiration of media, cells were washed twice with PBS, followed by fixation in 0.25% glutaraldehyde for 15 min. Following fixation and washing, cells were stained, when required, with fluorescent dyes or with bacterial toxins (as described below). Pen marks were manually drawn on the glass slide, on the back side of the sample, for image registration and then, confocal images (as described below) were acquired from an area of interest.

For MALDI-IMS analyses, 150 µL of 2,5-dihydroxybenzoic acid (DHB), (30 mg/mL in 50:50 acetonitrile/water/0.1% TFA), were deposited on the surface of the samples using the automatic SMALDIprep (TransMIT GmbH).

10.3.2 MALDI-IMS analysis

IMS experiments were performed using the AP-SMALDI10 or AP-SMALDI5 mass spectrometer that couples a QExactive (Thermo Fisher) with an atmospheric-pressure scanning-microprobe MALDI imaging source (AP-SMALDI, TransMIT GmbH).

The MALDI laser focus was optimized manually using the source cameras with the focused beam diameter estimated to be around 5 µm. For each pixel, the spectrum was accumulated

from 50 laser shots at 60 Hz. MS parameters in the Tune software (ThermoFisher Scientific) were set to the spray voltage of 4 kV, S-Lens 100 eV, capillary temperature to 250°C. The step size of the sample stage was set to 7µm for AP-SMALDI10 or 5µm for AP-SMALDI5. Positive ion mode measurements were performed in full scan mode in the mass range m/z 400-1600 with a resolving power set to $R = 240000$ at $m/z = 200$. Mass spectra were internally calibrated using the lock mass feature of the instrument.

10.3.3 MALDI-IMS images reconstruction and annotation

The data obtained were converted from the RAW format into the imzML format containing only centroided data using the RAW2IMZML software (TransMit GmbH).

Mass images (296) were generated by MSiReader software (Bokhart et al., 2017; <https://msireader.wordpress.ncsu.edu>) after TIC normalization with a m/z tolerance of 3 ppm.

Metabolite annotation was performed in two steps: annotation with public databases and software and then ESI-LC/MS and MRM confirmation (as described below).

imzML files were uploaded on METASPACE (Palmer et al., 2016; <http://metaspace2020.eu>) for a preliminary lipids annotation, with the m/z tolerance of 3 ppm and FDR of 5%, 10%, 20%, and 50% against the SwissLipids metabolite database.

For further confirmation RAW data were analyzed with the software Alex123 (Analysis of Lipids Experiments) (Ejsing Lab, <https://git.embl.de/ejsing/alex123>) using a library with curated lipid ionization information with a m/z mass tolerance of 0.005 (Pauling et al., 2017). After peak identification based on the combination of two step approaches, to each lipid was associated an attribution confidence score (ACS) as detailed. 1 point was attributed when a lipid was identified by Alex123 software, while 1,2,3 or 4 points were attributed when a lipid was identified on MetaSpace with FDR 50, 20, 10 or 5% respectively. Finally, 5 points were given to a lipid that was identified by ESI-LC/MS with 1 extra point if the lipid identity was confirmed by MRM. Only lipids with an ACS > 5 were considered identified with high confidence.

10.3.4 Single pixel analysis

Single-pixel analysis was performed using Fiji software (Schindelin J et al., 2012; <https://imagej.net/Fiji>) on the 296 mass images collected at 7 μ m spatial resolution by AP-SMALDI10 (TransMit GmbH) and reconstructed by Mirion software (Paschke et al., 2013). Pixels corresponding to area where no cells were present displayed an extremely low total lipid intensity. These areas were identified using the evenly distributed lipid PtdAc 38:4 (m/z = 747.4937) and removed from further analysis. Lipid intensities in each pixel belonging to cell areas were then log-transformed and standardized across the entire image. PCA analysis was performed and the coordinate of each component was displayed with a different colour. The absolute values of the PCA loadings were then used to identify the lipids with most of the variance of each single component.

10.3.5 Image Processing and Batch Correction

Single dHFs were manually segmented on MsiReader with the free hand tool for ROI selection, after TIC normalization. Raw abundance data for each scan and each pixel in a ROI were exported with the MSiExport tool for the 296 m/z in the lipid mass range.

Normalized lipid count values for biological replicates were integrated using ComBat (Johnson et al., 2007) to correct batch effect. PCA dimensionality reduction was performed and the top PCs were retained.

10.3.6 Single-cell lipids data analysis (lipid and cell network)

Batch corrected count values were used to calculate average against which each value was then normalized. For each lipid, standard deviation was calculated on normalized values to obtain the Index of Dispersion (IoD). Lipids were ranked for the most variable to the least variable according to their IoD.

Single lipid values in each cell were used to determine their co-variation using the Pearson Correlation Coefficient (PCC). PCC was calculated using an in-house made R script (made by Francesco Russo, IBP, Napoli). Lipids with PCC >0.85 were connected to build a lipid correlation network using Cytoscape 3.8.0. Node size was calculated using the IoD (bigger is the node bigger is the IoD and vice versa) while nodes transparency was calculated according to the ACS (as detailed above).

Similarly, single-cell lipidomes values were used to determine their co-variation using the Pearson Correlation Coefficient (PCC). Cells with PCC >0.35 were connected to build a cell correlation network using Cytoscape 3.8.0.

10.4 Lipid analysis

10.4.1 Lipid extraction

Total lipid extracts were prepared using a standard MTBE protocol followed by a methylamine treatment for total lipid analysis by mass spectrometry. Briefly, cell pellet was resuspended in 100 μ L H₂O. 360 μ L methanol and 1.2 mL of MTBE were added and samples were placed for 10 min on a vortex at 4 °C followed by incubation for 1 h at room temperature on a shaker. Phase separation was induced by addition of 200 μ L of H₂O. After 10 min at room temperature, samples were centrifuged at 1000 g for 10 min. The upper (organic) phase was transferred into a glass tube and the lower phase was re-extracted with 400 μ L artificial upper phase [MTBE/methanol/H₂O (10:3:1.5, v/v/v)]. The combined organic phases were dried in a vacuum concentrator. Lipids were then resuspended in 500 μ L of CHCl₃ and divided in two aliquots for a further methylamine treatment for sphingo- and glycosphingolipids analysis. In details, 500 μ L of freshly prepared monomethylamine reagent [methylamine/H₂O/n-butanol/methanol (5:3:1:4, (v/v/v/v))] was added to the dried lipid extract and then incubated at 53 °C for 1 h in a water bath. Lipids were cooled to room temperature and then dried. The dried lipid extract was then extracted by n-butanol extraction using 300 μ L water-saturated n-butanol and 150 μ L H₂O. The organic phase was collected, and the aqueous phase was re-extracted twice with 300 μ L water-saturated n-butanol. The organic phases were pooled and dried in a vacuum concentrator.

10.4.2 MALDI-TOF untargeted lipidomics

Extracted lipids were resuspended in 500 μ L of CHCl₃ and analyzed by MALDI-MS. 30 mg/mL 2,5-DHB was freshly prepared in acetonitrile/water solution (50:50 v/v) with 0.1% TFA. An equivalent volume of sample solution (50 μ L) was then mixed with matrix before deposition on the MALDI target. All mass spectrometry analysis for the identification of lipids (m/z 400-

1800) were obtained using an Applied Biosystems 4800 MALDI-TOF/TOF mass spectrometer equipped with a 200 Hz tripled-frequency Nd:YAG pulsed laser with 355 nm wavelength. Measurements were performed in positive ion reflection mode at an accelerating potential of 20 kV. Each mass spectra were obtained by applying a laser energy of 4600 watts/cm², averaging 4000 single laser shots/spectrum.

10.4.3 LC-MS untargeted lipidomics

For phospholipid analysis, lipid extracts (2 µL injection volume in CHCl₃:MeOH 2:1) were separated over an 8 minute gradient at a flow rate of 200 µL/min on a HILIC Kinetex Column (2.6µm, 2.1 × 50 mm²) on a Shimadzu Prominence UFPLC xr system (Tokyo, Japan). Mobile phase A was acetonitrile:methanol 10:1 (v/v) containing 10 mM ammonium formate and 0.5% formic acid while mobile phase B was deionized water containing 10 mM ammonium formate and 0.5% formic acid. The elution of the gradient began with 5% B at a 200 µL/min flow and increased linearly to 50% B over 7 min, then the elution continued at 50% B for 1.5 min and finally, the column was re-equilibrated for 2.5 min. MS data were acquired in full-scan mode at high resolution on a hybrid Orbitrap Elite (Thermo Fisher Scientific, Bremen, Germany). The system was operated at 240,000 resolution (m/z 400) with an AGC set at 1.0E6 and one microscan set at 10-ms maximum injection time. The heated electrospray source HESI II was operated in positive mode at a temperature of 90 °C and a source voltage at 4.0KV. Sheath gas and auxiliary gas were set at 20 and 5 arbitrary units, respectively, while the transfer capillary temperature was set to 275 °C.

Mass spectrometry data were acquired with LTQ Tuneplus2.7SP2 and treated with Xcalibur 4.0QF2 (Thermo Fisher Scientific). Lipid identification was carried out with Lipid Data Analyzer II (LDA v. 2.6.3, IGB-TUG Graz University) (Hartler et al., 2011). The LDA algorithm identifies peaks by their respective retention time, m/z and intensity. Care was taken to calibrate the instrument regularly to ensure a mass accuracy consistently lower than 3 ppm thereby leaving only few theoretical possibilities for elemental assignment.

Data visualization was improved with LCMSEXplorer in a homemade web tool hosted at EPFL (<https://gecftools.epfl.ch/lcmsexplorer>).

MS/MS spectrum were acquired using a hybrid Velos pro dual cell differential pressure linear ion trap mass spectrometer with a high field Orbitrap Elite instrument. The fragment spectra were generated using parallel MS and MS_n analysis with 23eV in the HCD cell.

10.4.4 TSQ ANALYSIS (*Multi Reaction Monitoring*)

The lipid extracts were normalized against total phosphate content before analysis. Dried samples were re-suspended in 100uL chloroform/methanol (1:2) containing 5mM ammonium acetate and transferred to a 96well plate.

The sphingolipids species were quantified using multiple reaction monitoring MRM on a TSQ vantage Extended mass range Mass spectrometer (Thermo Fisher Scientific) equipped with a robotic nanoflow ion source (Triversa Nanomate, Advion Biosciences). Auto-tuned collision energies and s-lens values were used on standards lipids covering the analyzed subclasses to improve MRM transitions. Mass spectrometry data were acquired with TSQ Tune 2.6 SP1 and Xcalibur 4.0QF2 (Thermo Fisher Scientific).

The mass spectrometry results were treated with an automatic MRM lipid quantification platform, developed and hosted at EPFL Lausanne Switzerland (<http://lipidomes.epfl.ch>). Areas under the curve of MRM transitions were quantified relative to the internal standard.

10.4.5 HPTLC

dHFs were pulse-labelled in serum-free DMEM, supplemented with 1% BSA fatty acid free, with 0.1 μ Ci/mL ³H-sphingosine for 2 h. After labelling, the cells were further incubated in DMEM + 10% FCS for 24h. Cells were then harvested and lipids extracted with the standard Bligh and Dyer protocol (Bligh EG and Dyer WJ, 1959). Dried lipids were resuspended in 150 μ L of CHCl₃ and spotted on silica gel high-performance-TLC (HPTLC) plates (Merck, Germany) and resolved with a mixture of chloroform, methanol and water (65:25:4 v/v/v). To visualize and analyse radiolabelled sphingolipids (i.e. Cer, GlcCer, LacCer Gb3, GM3 and SM), the TLC plates were placed in the RITA TLC Analyser (Raytest, Germany) and quantified using GINA (Raytest, Germany) software analysis. The percentage of total C.P.M. associated with Cer, GlcCer, LacCer, Gb3, GM3 and SM peaks for each of the lipids is reported.

10.5 Immunofluorescence analysis

For IF analysis, dHFs were grown to approximately 80% confluency on glass coverslips, fixed with 4% paraformaldehyde for 10 minutes at RT and then washed three times with PBS. For tissues, samples were embedded in OCT compound and frozen, to be subsequently cryosectioned with a cryotome into 7-8 μm sections. Before staining, sections were dried at room temperature and then fixed with 4% paraformaldehyde for 20 minutes. After fixation, cells and tissues were blocked with 5% BSA and permeabilized when required with 0.5% saponin for 20 minutes at RT, followed by a 1 h incubation with selected antibodies (listed in **Annex 2**) against the antigen of interest in blocking reagent. Cells and tissues were then washed three times with PBS and incubated with appropriate isotype-matched, AlexaFluor-conjugated secondary antibodies (Invitrogen, USA) diluted in blocking solution for 30 min. After immuno-staining, they were washed three times in PBS and once in water, to remove salts. After Hoechst staining for nuclei, the samples were mounted with Fluoromount-G and analyzed under a confocal microscope Zeiss LSM700 with 20x air objective (0.8 NA) or Leica SP8 with 10x air objective (0.3 NA) or 20x air objective (0.75 NA).

Optical confocal sections were taken at 1 Airy unit under non-saturated conditions with a resolution of 1024x1024 or 2048x2048 pixels and frame average 4. Images were then processed using Fiji software (Schindelin J et al., 2012; <https://imagej.net/Fiji>). Adobe Photoshop CS3 was used to adjust the contrast of the images, whereas Adobe Illustrator 2020 was used to illustrate figures.

10.5.1 Immunofluorescence staining with toxins

For ShTxB1a-Cy3 and ChTxB-AlexaFluor488 or ChTxB-AlexaFluor647 staining, the cells were fixed with 4% PFA, blocked in PBS containing 5% bovine serum albumin (BSA) without detergent, incubated with fluorescent B-subunit toxins for 1h, and then mounted with Fluoromount-G.

In the case of ShTxB2e, after fixation and blocking, cells were incubated with the bacterial toxin for 30 min at RT, followed by conjugation with primary antibody for 1 hour and fluorescently-labelled secondary antibodies for 30 minutes. Cells were analysed by confocal microscopy as described above.

10.6 Flow cytometry analysis

dHFs were subjected to trypsin digestion (0.05% Trypsin/EDTA) and washed twice with PBS. For cell-surface GSLs staining, resuspended cells were blocked with 2% BSA for 30 minutes at 4°. Then, cells were extensively washed with PBS and incubated with optimal concentrations of the toxins for 1h at 4° and after washing with primary antibody. Cells were then washed again and incubated with fluorescently-labelled secondary antibodies when required for 30 minutes.

Cells resuspended in 2% BSA were analyzed by BD LSR Fortessa or LSRII SORP. (Becton Dickinson). Unlabeled cells were used as negative control. Viable cells were gated, and GSLs expressions were further analyzed in the gated region. Antibodies used are described in **Annex 2**.

Data were exported with an in-house built R script and analysed with GraphPad Prism 8 software.

10.6.1 Isolation of lipids population by FACS

A triplicate of primary human fibroblasts (5×10^6) in suspension were collected and stained as described above. Cells were resuspended in 2% BSA and sorted using a flow cytometer (FACSARIAII). After gating, four populations (ChTxB⁺, ShTxB1a/ShTxB2e⁺, triple positive and ShTxB2e⁺) were directly sorted through a 100 µm nozzle at 4° in 5 mL tubes filled with 1 mL lysis buffer or complete media. Cells were sorted in continuous in order to get the maximum amount from each population. Unlabeled cells were used as negative control.

10.7 siRNA treatment and transfection

The siRNAs for human *ST3GAL5/GM3S*, *A4GALT/Gb3S* and *B3GALNT1/Gb4S* (**Annex 3**) were obtained from Microsynth.

dHFs were plated at 30% confluence in 6-well plates and transfected with 50 nM of siRNAs mix with Oligofectamine, according to the manufacturer instructions. At 72 h after the initial treatment with the siRNAs, the cells were treated with siRNAs mix again for 24 hours. After 96 total hours of treatment the cells were processed for the different experiments.

10.8 Cell manipulation

10.8.1 Drug treatments

dHFs were treated by adding inhibitors of SLs synthesis, Fumonisin B1 25 μ M, PDMP 10 μ M or Myriocin 2.5 μ M, in complete media for six days. Stock solutions of the drugs were prepared dissolving powders in DMSO following providers instructions.

10.8.2 FGF2/TGF- β 1 treatment

dHFs were serum starved for 24h and then treated with different concentration (0, 0.1, 1 or 5 ng/mL) of growth factors FGF2 and TGF- β 1 by adding them in complete media for 72 hours. TGF- β 1 stock solution at 50 μ g/mL was prepared by dissolving it in water with citric acid 10mM pH3 and 0.1% BSA. FGF2 stock solution at 10 μ g/mL in PBS with 0.5% BSA.

10.9 Fluorescence In Situ Hybridization (FISH)

RNAscope Multiplex Fluorescent V2 assay (Bio-technique, Cat. No. 323110) was performed according to manufacturer's protocol on cells cultured in chamber slides, hybridized with the probes Hs 3plex positive control (Bio-technique, Cat. No. 320861) or 3Plex negative control (Bio-technique, Cat. No. 320751) or Hs-A4GALT-C1 (Bio-technique, Cat. No. 486601), Hs-ST3GAL5-C2 (Bio-technique, Cat. No. 816191-C2) and Hs-B3GALNT1-C3 (Bio-technique, Cat. No. 816181-C3) simultaneously at 40°C for 2 hours. The different channels were revealed with TSA Opal520 (Akoya Biosciences, Cat. No. FP1487001KT) for C1, TSA Opal650 (Akoya Biosciences, Cat. No. FP1488001KT) for C2 and TSA Opal570 (Akoya Biosciences, Cat. No. FP1488001KT) for C3. Tissues were counterstained with DAPI and mounted with Prolong Diamond Antifade Mountant (Thermo Fisher, P36965).

Data were analysed using an in-house Fiji script (made by Romain Guiet, EPFL, BIOP). Specifically, single-cells were automatically segmented based on nucleus staining (DAPI) to define a cell area where the number of spots per each cell and each probe were calculated

based on find local maxima. Statistical evaluations were reported as Student's t test * $p < 0.05$, ** $p < 0.01$, and *** $p < 0.001$.

10.10 Correlative video-confocal microscopy

dHFs, were directly seed the day before on gridded glass bottom culture dish (Mattek) in complete media to reach the day after roughly 30% confluence. Cells were then mounted on an Olympus Cell[^]R widefield microscope for transmission imaging under controlled temperature and CO₂ and followed for 72h. The images were acquired every 30 minutes with 40 ms exposure time with a 4x (0.13 NA) air objective.

After 72h, cells were fixed with 4% PFA and processed for toxin staining as described above. The same areas acquired by brightfield microscopy were analysed by confocal microscope Zeiss LSM700 with 20x air objective (0.8 NA) as described above.

Alternatively, after 72h, cells were fixed with 4% PFA and processed for MALDI-IMS (as detailed above) to couple phylogeny and single-cell lipidomics analysis.

10.10.1 Time-lapse and lineage analysis

Cells were tracked and each frame of the time lapse experiment annotated and the progeny of each cell was assigned. Time of division was annotated as the moment of visible cell contraction corresponding to the mitosis instead of at the moment cytokinesis (that was more difficult to determine accurately). We used a custom python script to build the mitotic lineage from the time lapse annotation and to perform the visualization and statistical analyses using. Cells were clustered using a subset of highly variable genes. To select the lipids we computed a bimodality score and selected the lipids with scores higher than 40 (43% of the lipids were retained). A score was computed for each lipid as the difference of the Bayesian information criterion (BIC) of two models: a simple gaussian distribution and a 2-gaussians mixture.

After feature selection we performed dimensionality reduction on the log transformed lipid intensities, we considered the first 5 PCs, explaining 73% of the variance and discarded the first component as it captured the trivial variation explained by total signal change. We performed a t-SNE embedding to display the data in a two-dimensional space and then we

obtained 4 clusters using a Gaussian mixture model with diagonal covariance (scikit-learn implementation).

Analysis of lipid-based family separability was performed for each lipid independently. We first found a family-constrained ordering of the cell based on the intensity of each lipid, then, we used the ordering to compute a test statistic for observed data and compared it to random realizations from the null distribution.

The ordering was obtained considering the lineage tree as a constraint, that is by sorting the leaves by level of expression to the extent allowed without breaking any kinship link of the tree (i.e. only moving entire clades and pivoting daughter cells is allowed). As test statistics we considered the difference cumulative sum of values along the ordering, corrected by the expectation. We performed an empirical statistical test permuting the lipid values and keeping the lineage structure constant. We sampled the null-distribution and computed the expected value by performing 500 random permutations of the lipid intensities. Empirical non-parametric p-values were FDR-corrected with $\alpha = 0.05$, we considered a lipid significantly segregated with respect to the structure of the lineage if $q\text{-value} < 0.01$.

10.11 Bulk RNA-sequencing of FACS sorted dHFs population

Bulk RNA sequencing was performed on the following FACS sorted populations of dHFs: Cholera Toxin positive (n=2), ChTxB/ShTxB1a/ShTxB2e positive (n=2), ShTxB1a/ShTxB2e positive (n=3) and ShTxB2e positive (n=1) and to a control unsorted population (n=2). Total RNA was isolated from FACS sorted dHFs populations using RNeasy Mini kits (Qiagen, Germany) according to the manufacturer instructions. The yield and the integrity of the RNA were determined using a spectrophotometer (NanoDrop ND-1000; Thermo Scientific, USA). Total RNA (10ng-1 μ g, depending on the different population) were submitted for RNA-seq with GENEWIZ, NJ.

Libraries were prepared using Illumina HiSeq platform with ultra-low input configuration and sequenced with 2 \times 150 bp sequencing configuration to a depth of 350 million reads (GENEWIZ, NJ).

Sequence reads were trimmed to remove possible adapter sequences and nucleotides with poor quality using Trimmomatic v.0.36. The trimmed reads were mapped to the Homo sapiens GRCh38 reference genome available on ENSEMBL using the STAR aligner v.2.5.2b.

Unique gene hit counts were calculated by using featureCounts from the Subread package v.1.5.2. The hit counts were summarized and reported using the gene_id feature in the annotation file. Only unique reads that fell within exon regions were counted (GENEWIZ, NJ). These bulk quantifications were used to extract, for each of the subpopulations, a set of enriched genes. First, we filtered the data tables from the genes that were lowly expressed along most of the samples: genes detected at average depth of less than 1.5 reads and that were at 8 reads in at least 15% of the samples were discarded. Samples were depth-normalized to reads per million (RPM) and log transformed. Then the average level of expression of a gene each condition was compared with the average of the rest of the samples. Genes were, then, sorted by the fold increase, excluding genes for which log2RPM was less than 4. For each of the subpopulations the top 200 genes were used to compute the population signature on the single-cell data (described below).

The signatures for TGF- β and FGF were computed with the same procedure starting from a list of the top 200 genes extracted from a previous bulk RNA-seq experiment (Bordignon P et al., 2019).

A gene ontology analysis was performed on the statistically significant set of genes by implementing the software GeneSCF v.1.1-p2. The goa_human GO list was used to cluster the set of genes based on their biological processes and determine their statistical significance. A list of genes clustered based on their gene ontologies was generated.

10.12 scRNA-seq experiment

scRNA-seq experiments were performed using 10X Genomics Chromium scRNA-seq kit v3.1. 3500 cells were loaded for each of the reaction following provider instructions. Libraries were sequenced at the depth of 300 million reads corresponding to an average of 80k reads per cell. Data were pre-processed using cellranger and velocity v0.17.

Single-cell data was analyzed using scanpy, velocity and a set of custom procedures. We selected most variable genes using a CV-mean modeling-based feature selection with minimal dispersion 0.5, maximal mean 3 and minimal mean 0.0125 as previously described (La Manno G et al., 2016). Single-cell profiles were normalized by the total UMI count, counts were log-normalized and PCA performed retaining the top 50 of components.

Clustering was performed using the Louvain clustering algorithm, with default parameters. Clusters were annotated consulting the literature relative to the differential expressed features.

Signature enrichment scores for the toxin-marked subpopulations and for TGF- β and FGF pathways were both computed as average Z-scores across the 200-genes lists described above. We used a procedure analogous to the one used Seurat CellCycleScoring function (Stuart T et al., 2019). Briefly, the log-transformed depth-corrected counts of genes in the list were zero-centered and standardized and the obtained Z-scores were averaged along each cell. To avoid capturing sequencing depth bias the score was corrected for the expectation estimated computing the average Z score of a random sample of genes stratified by average expression level.

10.12.1 scRNA-seq: Treatment-Control comparison

The two datasets were first analyzed together analogously to the way described above for the control dataset.

The integration analysis between the Treatment and control datasets was performed using Seurat integration algorithm with [default] parameters. Clustering and embedding were computed using Louvain and UMAP algorithm respectively. Density estimation on the embedding was performed using the kernel density estimator implemented in scikit-learn. Gene expression analysis was performed using the original counts (not integrated.)

10.13 Real Time PCR

Total RNA was extracted and DNase treated from a 10-cm dish with RNeasy Kit (Qiagen, Germany), according to manufacture instruction. The yield and the integrity of the RNA were determined using a spectrophotometer (NanoDrop ND-1000; Thermo Scientific, USA). Reverse transcription was performed using 250ng of RNA using random primers and SuperScript II (Invitrogen). Real-time PCR was performed with 7900HT Fast Real-Time PCR système (Applied Biosystems) using PowerUp SYBR Green reagent for detection (Applied Biosystems). All primer sequences are listed in **Annex 5**. mRNA levels were normalized to three housekeeping genes: Hypoxanthine-guanine phosphoribosyltransferase (HPRT), b-

microglobulin (bM2), TATA-binding protein (TBP). Data were average of three replicates from independent experiments.

10.14 SDS-PAGE and western blotting

10.14.1 SDS-PAGE

Two 16 x 18 cm plates were used for assembling standard gels. The plates were assembled to form a chamber using two 1.5 mm plastic spacers aligned along the lateral edges of the plates. The plates were then fixed using two clamps and mounted on a plastic base, which sealed the bottom. All of the materials were from Hoefer Scientific Instruments. The running gel was prepared by mixing H₂O, 30% (w/v) acrylamide-bisacrylamide solution, 1.5M Tris-HCl (pH 8.8), 10% (w/v) SDS, 10% ammonium persulfate (APS) and N,N,N',N'-tetramethylethylene diamine (TEMED) in different amount according to gel percentage. Soon after pouring, the gel was covered with a layer of water and left at RT for about 1 h. The water layer was removed. The stacking gel was prepared by mixing H₂O, 30% (w/v) acrylamide-bisacrylamide solution, 0.5 M Tris-HCl (pH 6.8), 10% (w/v) SDS, 10% (w/v) APS and TEMED, and the solution was pipetted and poured onto the running gel. Immediately, a 15-well comb was inserted between the glass plates and it was left 1 hour at RT.

For sample preparation, after treatment, the cells were washed three times with PBS and lysed in RIPA buffer (150 mM NaCl, 1% Triton X-100, 0.5% sodium deoxycholate, 0.1% SDS, 25 mM Tris-HCl, pH 7.4), supplemented with protease cocktail inhibitor. The lysates were clarified by centrifugation, and quantified using a commercially available BCA kit (Pierce™ BCA Protein Assay Kit, ThermoFisher) according to the manufacturer instructions.

Samples were prepared by adding an equal volume of 2x SDS sample buffer, incubating at 95 °C for 5 min, briefly centrifuging and then loading onto the gel. The gel was then transferred into the electrophoresis apparatus and the electrophoresis was carried out under a constant current of 7 mA overnight.

10.14.2 Western blotting

The polyacrylamide gel was soaked for 15 min in transfer buffer, placed on a sheet of 3MM paper (Whatman, NJ, USA) and covered with a nitrocellulose filter. The filter was covered with a second sheet of 3MM paper, to form a "sandwich" which was subsequently assembled into the blotting apparatus. Protein transfer occurred at 400 mA for 4 hours. At the end of the run, the sandwich was disassembled and the nitrocellulose filter was soaked in 0.2% Ponceau red and 5% (v/v) acetic acid, to visualize the protein bands, and then rinsed. The strips containing the proteins of interest were blocked in TBS-T/5% BSA for 45 min at RT, and then with the primary antibody diluted at its working concentration in the blocking solution buffer overnight at 4 °C. After Washing with TBS-T, the strips were next incubated for 1 h with the appropriate HRP-conjugated secondary antibody, diluted in antibody dilution buffer and washed twice in TTBS, for 10 min each. After washing, the strips were incubated with the ECL solution for 3 minutes and exposed to x-ray films, which were then scanned. The intensity of the bands and preparation of images was done using ImageJ and Adobe Illustrator 2020.

Annex 1. Table of chemicals and materials

Material	Provider	Catalogue number
DMEM	Life Technologies	31966021
Fetal Bovine Serum (FBS)	Life Technologies	10270106
L-glutamine	Life Technologies	25030024
Pen/Strep	Life Technologies	15140122
0.05% Trypsin/EDTA	Life Technologies	25300062
Fumonisin B1	Enzo	BML-SL220-0005
Myriocin	Enzo	BML-SL226-0005
DL-threo-PDMP	Enzo	BML-SL210-0010
FGF2	Bio-Techne	233-FB-025/CF
TGF- β 1	PeproTech EC Ltd	100-21
Square coverglasses	Gloor instruments	AGL46S10-15
Paraformaldehyde	EMS	50-259-96
Saponin	Sigma-Aldrich	47036
Fluoromount-G, 25 ml	Sigma-Aldrich	0100-01
Bovin Serum Albumin (BSA)	Sigma-Aldrich	A2153
PBS	Life Technologies	14190169
Oligofectamine	Life Technologies	12252011
Optimem	Life Technologies	31985070
Acrylamide/Bis-acrylamide, 30% solution	Sigma-Aldrich	A3699
Ammonium Persulfate (APS)	Sigma-Aldrich	A3678
N,N,N',N'-tetramethylethylenediamine	Sigma-Aldrich	T22500
Pierce Fast Western Blot Kit, ECL Substrat	Life Technologies	35050
Lipofectamine 2000	Life Technologies	11668027
Glutaraldehyde	EMS Electron	16120
Acetonitrile	Sigma-Aldrich	34851-1L
Trifluoroacetic acid	Sigma-Aldrich	302031-100ML
2,5-dihydroxybenzoic acid	Sigma-Aldrich	85707-1G-F

tert-Butyl methyl ether (MTBE)	Sigma-Aldrich	34875-1L
Methylamine	Sigma-Aldrich	534102-1L
Methanol	Sigma-Aldrich	34860-2.5L
Chloroform	Sigma-Aldrich	650498-1L
³ H-sphingosine	Anawa	ART 0490-50 µCi
BSA fatty acid free	Sigma-Aldrich	A-6003-10g
DMSO	LabForce	sc-359032
8 well chamber, removable	Vitaris	80841-IBI
35 mm Dish No. 1.5 Coverslip	Mattek	P35G-1.5-14-C
HPTLC plates	Sigma-Aldrich	1055480001
Prolong Diamond Antifade Mountant	Thermo Fisher	P36965
RNAscope Multiplex Fluorescent V2 assay	Bio-technie	323110
Chromium Next GEM Single-cell 3' GEM, Library & Gel Bead Kit v3.1, 4 rxns	10x-Genomics	1000128
Chromium Next GEM Chip G Single-cell Kit, 16 rxns	10x-Genomics	1000127

Annex 2. List of the antibodies used in this study for flow cytometry (FACS), Immunofluorescence (IF) and Western Blotting (WB)

Antibody/Toxins	Usage			Provider
	Flow Cytometry	IF	WB	
ChTxB-Alexa Fluor 488	1:1000	1:1000		Life Technologies C34775
ChTxB-Alexa Fluor 647	1:1000	1:1000		Life Technologies C34778
ShTxB1a-Cy3	1:1000	1:800		Prof. Johannes Lab; In-house prepared

ShTxB2e	1:300	1:300		Prof. Müthing lab
Mouse anti-ShTxB2e	1:300	1:300		Sifin TS2103
Mouse anti-SMa		1:300	1:500	Abcam Ab7817
Mouse anti-LMNA		1:100		CST #477
Rabbit anti-MMP1		1:300	1:1000	Lubioscience GTX100534
Rabbit anti-Vimentin		1:100		CST 5741S
Mouse anti-Pankeratin		1:500		BMA Biomedicals T-1302
Mouse anti-GAPDH			1:2000	Abcam ab9485
Mouse and Rabbit Anti-HRP			1:10000	Jackson Immunosearch 711-035-152 715-035-150
Mouse anti-V5		1:200		Thermo Fisher R96025

Annex 3. List of siRNAs used in this work

Human gene	Accession number	siRNA sequence
<i>A4GALT</i> /Gb3S	NM_017436	1# 5'-AGA AAG GGC AGC UCU AUA ATT -3' 2# 5'-GGA CAC GGA CUU CAU UGU UTT -3' 3# 5'-UGA AAG GGC UUC CGG GUG GTT -3' 4# 5'-GCA CUC AUG UGG AAG UUC GTT -3'
<i>ST3GAL5</i> /GM3S	NM_003896	1# 5'-CAA UGG CGC UGU UAU UUG ATT -3'

		2# 5'-GUG CAC CAG UUG AGG GAU ATT -3' 3# 5'-GAC CAU GCA UAA UGU GAC ATT -3' 4# 5'-CGG AAG UUC UCC AGU AAA GTT -3'
<i>B3GALNT1</i> /Gb4S	NM_003781	1# 5'-GAU AUG AGG UUC UUA CAU UTT -3' 2# 5'-CAG GUU AUC CUC UAA UUG ATT -3' 3# 5'-GUC GGG AUC UGU UUG AAU UTT -3' 4# 5'-GUG CCA AGG AUC UAU GAA ATT -3'

Annex 4. List of vectors used for lentiviral transduction of dHFs

Gene	Vector	Provider
Packaging vectors	pCMVR8.74	Addgene Cat # 22036
Packaging vectors	pMD2.G	Addgene Cat # 12259
plenti	pLX304, V5 (C-ter)	Gene Expression Core Facility (GECF, EPFL)
<i>B3GALNT1</i>	pLX304, V5 (C-ter)	Gene Expression Core Facility (GECF, EPFL)
<i>ST3GAL5</i>	pLX304, V5 (C-ter)	Gene Expression Core Facility (GECF, EPFL)

Annex 5. List of Real-time primers used in this work

Human qPCR Primers		
Gene	Primer Sequences (5'– 3')	
ACTA2	Forward	GAGTTACGAGTTGCCTGATG
	Reverse	GGTTTCATGGATGCCAGC
COL1A1	Forward	CATGGAGACTGGTGAGACCT
	Reverse	GCCATACTCGAACTGGAATC

COL5A2	Forward	GGATACATGGACGATCAAGC
	Reverse	GACAGTCTTGCCCACATTTTC
CTGF	Forward	GTCCAGACCACAGAGTGGAG
	Reverse	AGTACGGATGCACTTTTTGC
ETV1	Forward	CCAGCTTTCTGAACCCTGTA
	Reverse	TGTTCATACACTGGGTCGTG
MMP1	Forward	ACACCTCTGACATTCACCAAG
	Reverse	ATGAGCCGCAACACGATG
SPARC	Forward	CCTGTACACTGGCAGTTCG
	Reverse	TGTCATTGTCCAGGTCACAG
STC1	Forward	AAAGGATGATTGCTGAGGTG
	Reverse	GGCTTCGGACAAGTCTGTTA
HPRT	Forward	AGCTTGCTGGTGAAAAGGAC
	Reverse	GTCAAGGGCATATCCAACA
bM2	Forward	TGCTCGCGCTACTCTCTCTTT
	Reverse	TCTGCTGGATGACGTGAGTAAAC
TBP	Forward	GCCCGAAACGCCGAATATA
	Reverse	CGTGGCTCTCTTATCCTCATGA

TABLES

Table 1. List of identified compounds. Putative lipid features (296 total) recorded in positive ion mode with their experimental m/z values. Lipid confirmed by LC/MS and MRM are annotated. Data refer to four separate IMS measurements. Analysis were obtained with mass resolving powers of 240,000 (@m/z 200).

m/z experimental	m/z theoretical	Δ ppm	Tentative Lipids identification Alex123	Alex123 Adduct	Tentative Lipids identification Metaspacer	Metaspacer adduct	LC-MS confirmed	MRM confirmed
478.3306	478.3292	0.0014	LPC O-16:2	H	CerP 24:1	H		
485.2649	485.2638	0.0011	LPA 20:2	Na	LPA 20:2	Na		
496.3411	496.3397	0.0014	LPC 16:0	H	LPC 16:0	H	yes	yes
504.3068	504.306	0.0008	LPE 18:0	Na	LPE 18:0	Na	yes	yes
504.3461	504.3448	0.0013	LPC O-18:3	H	PC P-18:2	H		
506.3611	506.3605	0.0006	LPC O-18:2	H	PC O-18:2	H		
510.3558	510.3554	0.0004	LPE 20:0 ; LPC 17:0	H	LPE 20:0 ; LPC 17:0	H	yes	
516.3072	516.306	0.0012	LPC 16:1	Na	LPC 16:1	Na		
518.3239	518.3217	0.0022	LPC 16:0	Na	LPC 16:0	Na	yes	yes
522.3568	522.3554	0.0014	LPC 18:1	H	LPC 18:1	H	yes	yes
524.372	524.371	0.001	LPC 18:0	H	LPC 18:0	H	yes	yes
534.2968	534.2956	0.0012	LPE O-22:6	Na	LPC 16:0 / LPE 19:0	K		yes
535.29501	unknown	unknown	unknown	unknown	unknown	unknown	unknown	
542.4917	542.4907	0.001	Cer 34:2	Na				
544.3388	544.3373	0.0015	LPC 18:1	Na	LPC 18:1	Na	yes	yes
546.3542	546.353	0.0012	LPC 18:0	Na	LPC 18:0	Na	yes	yes
560.3121	560.3113	0.0008			LPC 18:1	K	yes	
560.5024	560.5013	0.0011	Cer 34:1	Na	Cer 34:1	Na	yes	yes
566.323	566.3217	0.0013	LPC 20:4	Na	LPC 20:4	Na	yes	
577.519	577.5197	-0.0007			DG P-34:1	H		
578.5231	578.5119	0.0112	Cer 34:0	Na			yes	
582.27369	unknown	unknown		unknown	unknown	unknown	unknown	
588.5333	588.5326	0.0007	Cer 36:1	Na	Cer 36:1	Na	yes	yes
590.5025	599.5033	-0.0008			DG P-36:5	H		
604.25558	unknown	unknown	unknown	unknown	DG O-36:3	unknown	unknown	
605.551	605.5503	0.0007			DG O-36:3	H		
613.3485	613.3476	0.0009			PG P-24:2	Na		
627.5352	627.5346	0.0006			DG O-38:6	H		
628.3959	628.3948	0.0011	PE 26:1	Na	PE 26:1	Na	yes	
632.6351	unknown	unknown	unknown	unknown	unknown	unknown	unknown	
640.3955	640.3948	0.0007			PC 24:2	Na	yes	
644.5969	644.5952	0.0017	Cer 40:1	Na	Cer 40:1	Na	yes	yes
654.411	654.4105	0.0005	PE 28:2	Na	PE 28:2	Na		
664.4687	664.4676	0.0011			CerP 36:3	Na		
666.4839	666.48395	-5E-05			CerP 38:5	Na		
669.4472	669.4466	0.0006	PA 32:1	Na	PA 32:1	Na	yes	
670.6128	670.6108	0.002	Cer 42:2	Na	Cer 42:2	Na	yes	yes
672.6268	672.6265	0.0003	Cer 42:1	Na	Cer 42:1	Na	yes	yes
682.458	682.4572	0.0008			CerP 36:2	K		
684.458	684.4574	0.0006	PE 30:1	Na	PE 30:1	Na	yes	yes
685.28285	unknown	unknown	unknown	unknown	unknown	unknown	unknown	
695.4627	695.4622	0.0005	PA 34:2	Na	PA 34:2	Na		
696.462	696.4599	0.0021	PC 28:2	Na			yes	
697.4787	697.4778	0.0009	PA 34:1	Na	PA 34:1	Na	yes	
697.52442	unknown	unknown	unknown	unknown	unknown	unknown	unknown	
697.5263	697.5255	0.0008	SM 32:1	Na	SM 32:1	Na	yes	yes
703.576	703.5748	0.0012	SM 34:1	H	SM 34:1	H	yes	yes
705.5913	705.5905	0.0008	SM 34:0	H	SM 34:0	H	yes	yes
706.5391	706.5381	0.001	PC 30:0	H	PC 30:0	H	yes	yes
707.4657	707.4646	0.0011			PA 37:6	H	yes	
709.4786	709.4778	0.0008			PA 35:2	Na		
711.4369	711.4361	0.0008			PA 34:2	K		
711.542	711.5411	0.0009			SM 33:1	Na	yes	
713.4527	713.4518	0.0009			PA 34:1	K	yes	
714.5077	714.5068	0.0009	PE 32:0	Na	PE 32:0	Na	yes	yes
718.5394	718.5381	0.0013	PE 34:1	H	PE 34:1	H	yes	yes
718.5762	718.5745	0.0017	PC O-32:1	H	PC O-32:1	H	yes	yes
719.4627	719.4622	0.0005	PA 36:4	Na	PA 36:4	Na	yes	
720.5553	720.5537	0.0016	PE 34:0	H	PE 34:0	H	yes	yes
720.592	720.5901	0.0019	PC O-32:0	H	PC O-32:0	H	yes	yes
721.4787	721.4778	0.0009			PA 36:3	Na	yes	
722.555	722.5541	0.0009	HexCer 34:1	Na	HexCer 34:1	Na	yes	yes
723.4942	723.4939	-0.0017	PA 36:2	Na	PA 36:2	Na		
723.4956	723.5411	-0.0455			SM34:2	Na	yes	
724.4978	724.48774	0.01006	PC 30:2	H			yes	
725.5571	725.5568	0.0003	SM 34:1	Na	SM 34:1	Na	yes	yes
726.5081	726.5068	0.0013	PC 30:1	Na	PC 30:1	Na	yes	yes
727.5631	727.5612	0.0019			PA O-37:0	Na		
728.5204	728.5201	0.0003	PC 30:0	Na	PC 30:0	Na	yes	yes
730.5392	730.5381	0.0011	PC 32:2	H	PC 32:2	H	yes	yes
732.5545	732.5537	0.0008			PC 32:1 / PE 34:1	H	yes	
733.5579	unknown	unknown	unknown	unknown	unknown	unknown	unknown	
734.5705	734.5694	0.0011	PC 32:0	H	PC 32:0	H	yes	yes
735.4349	735.4361	-0.0012			PA 36:4	K	yes	
735.57377	unknown	unknown	unknown	unknown	unknown	unknown	unknown	
737.4526	737.4518	0.0008			PA 36:3	K		
738.5064	738.5044	0.002	PE 34:2	Na	PE 34:2	Na	yes	yes
739.4682	739.4674	0.0008			PA 36:2	K		
739.5735	739.5724	0.0011			SM 35:1	Na	yes	
740.47166	unknown	unknown	unknown	unknown	unknown	unknown	unknown	
740.5209	740.5201	0.0008	PE 34:1	Na	PE 34:1	Na	yes	yes
740.5233	740.5224	0.0009	PE 36:4	H	PE 36:4	H	yes	yes
741.5317	741.5307	0.001			SM 34:1	K	yes	
742.5367	742.5357	0.001	PE 34:0	Na	PC 31:0 / PE 34:0 / PA 36:1	Na	yes	yes
742.539	742.5381	0.0009	PE 36:3	H	PE 36:3 / PC 33:3 / PA 38:4	H	yes	yes PE 36:3
742.575	742.5745	0.0005	PC O-34:3	H	PC O-34:3	H	yes	yes
744.4956	744.4938	0.0018	PC 30:0	K	PC 30:0 / PE 32:0	K	yes	yes
744.4956	744.4938	0.0018	PE O-36:6	Na	PE O-36:6 / PA 38:6	Na	yes	
744.5545	744.5537	0.0008			PC 33:2 / PE 36:2	H	yes	
745.4779	745.4778	1E-04	PA 38:5	Na	PA 38:5	Na	yes	
745.4791	745.4802	-0.0011			PA 40:8	H	yes	
746.5711	746.5694	0.0017	PE 36:1	H	PE 36:1 / PC 33:1	H	yes	yes PE 36:1
746.6073	746.6058	0.0015	PC O-34:1	H	PC O-34:1	H	yes	
747.4937	747.4959	-0.0022			PA 38:4	H	yes	
748.5871	748.585	0.0021	PE 36:0	H	PC 33:0 / PE 36:0	H	yes	

m/z experimental	m/z theoretical	Δ ppm	Tentative Lipids identification Alex123	Alex123 Adduct	Tentative Lipids identification Metaspace	Metaspace adduct	LC-MS confirmed	MRM confirmed
749.5107	749.5091	0.0016	PA 38:3	Na	PA 38:3	Na		
752.5225	752.5224	0.0001		Na	PC 34:5 / PE 37:5	H	yes	
753.5896	753.5881	0.0015	SM 36:1	Na	SM 36:1	Na	yes	yes
753.58865	unknown	unknown	unknown	unknown	unknown	unknown	unknown	
754.5372	754.5357	0.0015	PC 32:1	Na	PC 32:1	Na	yes	yes
755.6047	755.6037	0.001	SM 36:0	Na	SM 36:0	Na	yes	yes
756.5519	756.5513	0.0006	PC 32:0	Na	PC 32:0	Na	yes	yes
757.50864	unknown	unknown	unknown	unknown	unknown	unknown	unknown	
758.5699	758.5694	0.0005	PC 34:2	H	PC 34:2 / PE 36:2	H	yes	yes PC 34:2
760.5863	760.585	0.0013	PC 34:1	H	PC 34:1 / PE 37:1	H	yes	yes PC 34:1
761.4512	761.4518	-0.0006			PA 38:5	K	yes	
762.5048	762.5044	0.0004	PE 36:4	Na	PE 36:4	Na	yes	yes
765.4836	765.4831	0.0005			PA 38:3	K		
766.5396	766.5381	0.0015	PE 38:5	H	PE 38:5	H	yes	yes
766.575	766.5745	0.0005	PC O-36:5	H	PC 36:5 / PE 39:4	H	yes	yes PC O-36:5
767.4991	767.4987	0.0004			PA 38:2	K		
768.5523	768.5513	0.001			PE 36:1 / PC 33:1	Na	yes	
768.5917	768.5901	0.0016	PC O-36:4	H	PC O-36:4 / PE 39:3	H	yes	yes PC O-36:4
769.4767	769.4778	-0.0011			PA 40:7	Na	yes	
770.5102	770.5095	0.0007			PE O-38:7 / PC 32:1	Na or K	yes	yes PC 32:1
770.51014	unknown	unknown	PE O-38:7 / PC 32:1	Na or K	unknown	unknown	unknown	
770.5709	770.5694	0.0015	PE 38:3	H	PE 38:3 / PC 35:3	H	yes	yes
770.6066	770.6058	0.0008	PC O-36:3	H	PC O-36:3	H	yes	yes
771.495	771.4935	0.0015	PA 40:6	Na	PA 40:6	Na	yes	
771.50907	unknown	unknown	unknown	unknown	unknown	unknown	unknown	
772.49706	unknown	unknown	unknown	unknown	unknown	unknown	unknown	
772.5261	772.5251	0.001			PE O-36:6	Na	yes	
772.5287	772.5275	0.0012			PE 45:0	H	yes	
772.5862	772.585	0.0012	PE 38:2	H	PE 38:2 / PC 35:2	H	yes	yes PE 38:2
773.511	773.5091	0.0019	PA 40:5	Na	PA 40:5	Na	yes	
773.52911	unknown	unknown	unknown	unknown	unknown	unknown	unknown	
774.51274	unknown	unknown	unknown	unknown	unknown	unknown	unknown	
774.6014	774.6007	0.0007	PE 38:1	H	PE 38:1 / PC 35:1	H	yes	yes PE 38:1
776.5932	776.5952	-0.002			CerP 46:6	H		
778.537	778.5357	0.0013	PC 34:3	Na	PC 34:3	Na	yes	yes
780.5521	780.5513	0.0008	PC 34:2	Na	PC 34:2 / PE 36:2	Na	yes	yes PC 34:2
781.6201	781.6194	0.0007			SM 38:1	Na	yes	
782.5674	782.567	0.0004	PC 34:1	Na	PC 34:1 / PE 37:1	Na	yes	yes PC 34:1
783.57091	unknown	unknown	unknown	unknown	unknown	unknown	unknown	
784.556	784.5251	0.0309	PC O-36:7 / PE P-39:6	Na	PE P-39:6	Na	yes	
784.57396	unknown	unknown	unknown	unknown	unknown	unknown	unknown	
784.5854	784.585	0.0004	PC 36:3	H	PC 36:3 / PE 39:3	H	yes	yes PC 36:3
785.5292	785.5303	-0.0011			PG 35:1	Na		
786.5412	786.5408	0.0004			PC P-36:5 / PE P-39:5	Na	yes	
786.6012	786.6007	0.0005	PC 36:2	H	PC 36:2	H	yes	yes
787.4676	787.4674	0.0002			PA 40:6	K		
787.669	787.6687	0.0003	SM 40:1	H	SM 40:2	H	yes	yes
788.5214	788.5201	0.0013	PE 38:5	Na	PE 38:5	Na	yes	yes
788.6171	788.6163	0.0008			PC 36:1	H	yes	yes
789.4835	789.48348	2E-05			PA 40:5	K		
790.5361	790.5357	0.0004	PE 38:4	Na	PE 38:4 / PC 35:4	Na	yes	yes PE 38:4
790.5754	790.5745	0.0009	PC O-38:7	H	PC O-38:7 / PE P-41:6	H	yes	
792.5558	792.5537	0.0021	PE 40:6	H	PE 40:6 / PC 37:6	H	yes	yes PE 40:6
794.5673	794.567	0.0003	PE 38:2	Na	PE 38:2 / PC 35:2	Na	yes	yes PE 38:2
796.5254	796.5253	1E-04	PC 34:2	K	PC 34:2	K	yes	yes
796.584	796.5826	0.0014	PE 38:1	Na	PE 38:1 / PC 35:1	Na	yes	yes PE 38:1
796.5866	796.5851	0.0015	PE 40:4	H	PE 40:4 / PC 37:4	H	yes	yes PE 40:4
796.6301	796.6214	0.0087			PC O-38:4	H	yes	
797.5309	797.5303	0.0006	PG 36:2	Na	PG 36:2	Na	yes	
797.58672	unknown	unknown	unknown	unknown	unknown	unknown	unknown	
798.5413	798.5408	0.0005	PE O-40:7	Na	PE O-40:7	Na	yes	
798.5413	798.5409	0.0004	PC 34:1	K	PC 34:1 / PE 37:1	K	yes	yes PC 34:1
798.6102	798.6007	0.0095			PC 37:3 / PE 40:3	H	yes	
800.5568	800.5564	0.0004	PE O-40:6	Na	PC O-37:6 / PE O-40:6	Na	yes	yes PE O-40:6
800.6178	800.6163	0.0015			PC 37:2 / PE 40:2	H	yes	
802.5369	802.5357	0.0012	PC 36:5	Na	PC 36:5 / PE 39:5	Na	yes	yes PC 36:5
802.6331	802.632	0.0011			PC 37:1	H	yes	
804.5518	804.5513	0.0005			PC 36:4 / PE 39:4	Na	yes	
806.5698	806.5694	0.0004	PC 38:6	H	PC 38:6 / PE 41:6	H	yes	yes PC 38:6
806.6501	806.648	0.0021			HexCer 40:1	Na	yes	
807.6143	807.6141	0.0002	SM 40:2	Na	SM 40:2	Na	yes	yes
808.5844	808.5826	0.0018	PC 36:2	Na	PC 36:2	Na	yes	yes
809.58679	unknown	unknown	unknown	unknown	unknown	unknown	unknown	
809.6512	809.6507	0.0005	SM 40:1:2	Na	SM40:1	Na	yes	yes
810.6004	810.5983	0.0021	PC 36:1	Na	PC 36:1	Na	yes	yes
811.6687	811.6687	0			SM 42:3	H	yes	
812.5433	812.5412	0.0021	PS 36:1	Na	PS 36:1	Na		
812.6147	812.6139	0.0008	PC 36:0	Na	PC 36:0	Na	yes	yes
814.5378	814.5357	0.0021	PE 40:6	Na	PE 40:6 / PC 37:6	Na	yes	yes PE 40:6
814.5597	814.5592	0.0005	PS 38:2	H	PS 38:2	H	yes	yes
815.7021	815.7001	0.002	SM 42:1	H	SM42:1	H	yes	yes
816.592	816.5901	0.0019	PC O-40:8	H	PC O-40:8	H		
818.5682	818.567	0.0012	PE 40:4	Na	PE 40:4 / PC 37:4	Na		
818.6043	818.6034	0.0009	PC O-38:4	Na	PC O-38:4	Na	yes	yes
820.5264	820.5253	0.0011	PC 36:4	K	PC 36:4 / PE 39:4	K	yes	yes PC 36:4
820.5858	820.5826	0.0032	PE 40:3	Na	PE 40:3 / PC 37:3	Na	yes	yes PE 40:3
821.5289	821.5303	-0.0014			PG 38:4	Na		
821.6512	821.6507	0.0005			SM 41:2	Na	yes	
822.5417	822.5409	0.0008			PE P-42:8	Na		
822.601	822.6007	0.0003			PC 39:5 / PE 42:5	H	yes	
823.6676	823.6663	0.0013			SM41:1	Na	yes	
824.5568	824.5564	0.0004	PE O-42:8	Na	PE O-42:8	Na	yes	
824.6175	824.6163	0.0012			PC 39:4 / PE42:4	H	yes	
826.5733	826.5721	0.0012	PE O-42:7	Na	PE O-42:7	Na	yes	
828.5541	828.5537	0.0004	PC 40:9	H	PC 40:9	H	yes	
830.5682	830.567	0.0012	PC 38:5	Na	PC 38:5	Na	yes	yes
832.5834	832.5826	0.0008			PC 38:4	Na	yes	

m/z experimental	m/z theoretical	Δ ppm	Tentative Lipids identification Alex123	Alex123 Adduct	Tentative Lipids identification Metaspace	Metaspace adduct	LC-MS confirmed	MRM confirmed
833.651	833.6507	0.0003			SM 42:3	Na	yes	
834.5984	834.5983	1E-04			PC 38:3	Na	yes	
834.6011	834.6007	0.0004		H	PC 40:6	H	yes	yes
834.6795	834.6793	0.0002			HexCer 42:1	Na	yes	
835.60275	unknown	unknown	unknown	unknown	unknown	unknown	unknown	
835.6459	835.6454	0.0005	SM 42:2	Na	SM 42:2	Na	yes	yes
837.6822	837.68239	-0.00019	SM 42:1	Na	SM 42:1	Na	yes	yes
838.641	838.632	0.009			PC 40:4	H	yes	
846.5418	846.5409	0.0009	PC 38:5	K	PC 38:5	K	yes	yes
848.5572	848.5566	0.0006	PC 38:4	K	PC 38:4	K	yes	yes
854.5703	854.5694	0.0009	PC 42:10	H	PC 42:10	H	yes	
856.5849	856.5826	0.0023	PC 40:6	Na	PC 40:6	Na	yes	yes
858.5994	858.5983	0.0011	PC 40:5	Na	PC 40:5	Na	yes	yes
860.6174	860.6163	0.0011	PC 40:4	Na	PC 40:4	Na	yes	yes
868.56977	unknown	unknown	unknown	unknown	unknown	unknown	unknown	
896.60118	unknown	unknown	unknown	unknown	unknown	unknown	unknown	
901.56515	unknown	unknown	unknown	unknown	unknown	unknown	unknown	
909.5461	909.5463	-0.0002			PI 38:4	Na	yes	
918.5431	918.5409	0.0022			PC 44:11	K	yes	
930.54367	unknown	unknown	unknown	unknown	unknown	unknown	unknown	
931.54872	unknown	unknown	unknown	unknown	unknown	unknown	unknown	
933.5632	933.5616	0.0016			PGP 42:5	H		
944.5592	944.5566	0.0026			PC 46:12	K		
947.5014	947.5046	-0.0032			PI 40:7	K	yes	
956.55927	unknown	unknown	unknown	unknown	unknown	unknown	unknown	
958.575	958.57502	-2E-05			PE 50:12	K		
960.583	960.5879	-0.0049			PE 50:11	K		
974.54888	unknown	unknown	unknown	unknown	unknown	unknown	unknown	
980.5592	unknown	unknown	unknown	unknown	unknown	unknown	unknown	
984.59066	unknown	unknown	unknown	unknown	unknown	unknown	unknown	
986.606	986.6035	0.0025			PE 52:12	K		
1000.56442	unknown	unknown	unknown	unknown	unknown	unknown	unknown	
1002.5798	unknown	unknown	unknown	unknown	unknown	unknown	unknown	
1004.55923	unknown	unknown	unknown	unknown	unknown	unknown	unknown	
1006.5749	1006.57489	1E-05			Gb3 30:1	K		
1008.59036	unknown	unknown	unknown	unknown	unknown	unknown	unknown	
1010.60196	unknown	unknown	unknown	unknown	unknown	unknown	unknown	
1022.54852	unknown	unknown	unknown	unknown	unknown	unknown	unknown	
1024.56426	unknown	unknown	unknown	unknown	unknown	unknown	unknown	
1032.6165	1032.5867	0.0298			Gb3 32:2	K		
1035.51785	unknown	unknown	unknown	unknown	unknown	unknown	unknown	
1037.5808	unknown	unknown	unknown	unknown	unknown	unknown	unknown	
1038.58432	unknown	unknown	unknown	unknown	unknown	unknown	unknown	
1040.54419	unknown	unknown	unknown	unknown	unknown	unknown	unknown	
1045.56175	unknown	unknown	unknown	unknown	unknown	unknown	unknown	
1046.6592	1046.6597	-0.0005			Gb3 34:1	Na	yes	
1048.68	unknown	unknown	unknown	unknown	unknown	unknown	unknown	
1053.55434	unknown	unknown	unknown	unknown	unknown	unknown	unknown	
1054.59923	unknown	unknown	Unknown	Unknown	Unknown	Unknown	Unknown	
1066.56033	unknown	unknown	Unknown	Unknown	Unknown	Unknown	Unknown	
1068.57545	unknown	unknown	Unknown	Unknown	Unknown	Unknown	Unknown	
1077.57351	unknown	unknown	Unknown	Unknown	Unknown	Unknown	Unknown	
1080.57623	unknown	unknown	Unknown	Unknown	Unknown	Unknown	Unknown	
1082.53432	unknown	unknown	Unknown	Unknown	Unknown	Unknown	Unknown	
1084.54918	unknown	unknown	Unknown	Unknown	Unknown	Unknown	Unknown	
1092.57598	unknown	unknown	Unknown	Unknown	Unknown	Unknown	Unknown	
1093.5475	unknown	unknown	Unknown	Unknown	Unknown	Unknown	Unknown	
1094.59174	unknown	unknown	Unknown	Unknown	Unknown	Unknown	Unknown	
1096.59992	unknown	unknown	Unknown	Unknown	Unknown	Unknown	Unknown	
1106.55349	unknown	unknown	Unknown	Unknown	Unknown	Unknown	Unknown	
1108.56889	unknown	unknown	Unknown	Unknown	Unknown	Unknown	Unknown	
1108.60699	unknown	unknown	Unknown	Unknown	Unknown	Unknown	Unknown	
1109.61089	unknown	unknown	Unknown	Unknown	Unknown	Unknown	Unknown	
1111.56911	unknown	unknown	Unknown	Unknown	Unknown	Unknown	Unknown	
1116.57553	unknown	unknown	Unknown	Unknown	Unknown	Unknown	Unknown	
1118.59013	unknown	unknown	Unknown	Unknown	Unknown	Unknown	Unknown	
1120.6072	unknown	unknown	Unknown	Unknown	Unknown	Unknown	Unknown	
1122.52718	unknown	unknown	Unknown	Unknown	Unknown	Unknown	Unknown	
1122.62233	unknown	unknown	Unknown	Unknown	Unknown	Unknown	Unknown	
1124.5423	unknown	unknown	Unknown	Unknown	Unknown	Unknown	Unknown	
1130.754	1130.7536	0.0004			Gb3 40:1	Na	yes	
1132.56938	unknown	unknown	Unknown	Unknown	Unknown	Unknown	Unknown	
1134.58445	unknown	unknown	Unknown	Unknown	Unknown	Unknown	Unknown	
1136.58568	unknown	unknown	Unknown	Unknown	Unknown	Unknown	Unknown	
1138.59619	unknown	unknown	Unknown	Unknown	Unknown	Unknown	Unknown	
1142.59139	unknown	unknown	Unknown	Unknown	Unknown	Unknown	Unknown	
1144.60666	unknown	unknown	Unknown	Unknown	Unknown	Unknown	Unknown	
1149.54913	unknown	unknown	Unknown	Unknown	Unknown	Unknown	Unknown	
1151.56169	unknown	unknown	Unknown	Unknown	Unknown	Unknown	Unknown	
1156.56865	unknown	unknown	Unknown	Unknown	Unknown	Unknown	Unknown	
1156.7694	1156.7693	1E-04	Hex3Cer 42:2	H	Gb3 42:2	Na	yes	
1158.7848	1158.7849	-0.0001			Gb3 42:1	Na	yes	
1160.7929	unknown	unknown	Unknown	Unknown	Unknown	Unknown	Unknown	
1162.61473	unknown	unknown	Unknown	Unknown	Unknown	Unknown	Unknown	
1173.59749	unknown	unknown	Unknown	Unknown	Unknown	Unknown	Unknown	
1174.7584	1174.7589	-0.0005			Gb3 42:1	K	yes	
1182.58331	unknown	unknown	Unknown	Unknown	Unknown	Unknown	Unknown	
1184.59889	unknown	unknown	Unknown	Unknown	Unknown	Unknown	Unknown	
1208.62618	unknown	unknown	Unknown	Unknown	Unknown	Unknown	Unknown	
1213.58965	unknown	unknown	Unknown	Unknown	Unknown	Unknown	Unknown	
1228.90777	unknown	unknown	Unknown	Unknown	Unknown	Unknown	Unknown	
1230.60795	unknown	unknown	Unknown	Unknown	Unknown	Unknown	Unknown	
1249.8003	1249.7391	0.0612			GA1 34:1	Na	Gb4 34:1	
1258.63908	unknown	unknown	Unknown	Unknown	Unknown	Unknown	Unknown	
1269.5914	unknown	unknown	Unknown	Unknown	Unknown	Unknown	Unknown	
1270.59978	unknown	unknown	Unknown	Unknown	Unknown	Unknown	Unknown	
1286.57406	unknown	unknown	Unknown	Unknown	Unknown	Unknown	Unknown	
1294.80038	unknown	unknown	Unknown	Unknown	Unknown	Unknown	Unknown	
1310.59248	unknown	unknown	Unknown	Unknown	Unknown	Unknown	Unknown	
1326.56635	unknown	unknown	Unknown	Unknown	Unknown	Unknown	Unknown	
1333.8401	1333.833	0.0071			GA1 40:1	Na	Gb4 40:1	
1344.64232	unknown	unknown	Unknown	Unknown	Unknown	Unknown	Unknown	
1359.8489	1359.8487	0.0002			GA1 42:2	Na	Gb4 42:0	
1361.8635	1361.8643	-0.0008			GA142:1	Na	Gb4 42:1	

Table 2. Lipotypes gene signatures. By comparing the expression of the top 350 genes in each FACS-sorted population with the average expression of the others, lists of enriched genes have been generated as lipotypes signatures.

ChTx8	ChTx8ShTx8B1aShTx8B2e	ShTx8B1aShTx8B2	ShTx8B2e
IGF2	MEG3	CP51	HAS2
ACAN	SERPINB2	EFNA1	CEL4
INMT	KRTAP15	DSG2	ENSG00000280356
HAPLN3	NEAT1	KRT17	GREB1
ACVR2A	ADAM33	CCAT1	CAPZA1
SFRP1	APP	SLC7A2	PEG3
IGFBP7	TWIST2	NPTX1	FAM76A
VCAM1	MMP14	FAM83A	CHIT1
CDH6	MMP3	C4BPA	B3GALT1
KCND3	HLAB	VTN	SEMA3A
AFF3	S100A4	ECEL1	RP1116E18.3
DHR53	HLAA	NUP210	BROX
ADRA2A	FRMD6	CTC575D19.1	TMCC3
AC005013.1	ANPEP	CDH10	ADAMTS9
COMP	FKBP10	AQP3	BAGE2
SFRP2	ENSG00000281383	RP3523K23.2	RGR
SHANK2	ECM1	PRSS21	RP1196K19.4
GCNT4	GPNMB	LYPD3	ADAM23
CES1	MASP1	SRGN	EFNA5
SCUBE3	PSGS	S100P	ST8SIA5
SAMD11	CRABP2	TRIP13	KCNJ6
FHL1	MMP1	RASIP1	HHIP
HS3ST3B1	ANGPTL2	MAL2	TRAM1L1
PCDHGA10	LOXL1	TM4SF1	ADCY2
BRINP1	ANKA1	MAGEA6	LSM12
MMP11	CD248	CTB119C2.1	RNF157
HTR2A	C1orf63	E2F2	NTNG1
CHRM2	LPXN	MTS4	ATP10B
TRIB2	SGCB	SIK1	CD34
ID4	SPOCD1	SLCO4A1	PAG1
SULF2	TGFB1	PRAME	SLC6A15
HIVEP3	CDKN1A	KYNU	RAB22A
COL8A2	CTSK	PRSS56	ADAM8
ARID5B	TPST1	PDE3A	CACNA1H
AKAP6	HIST2H2BE	MTUS1	SLC41A2
WNK3	TRIM22	SLC27A2	PRRG3
DPT	SPARC	SERPINB5	PCDHA4
FAM20A	IL8	BMP2	DPYSL2
FAT2	AKR1C1	SLC43A3	BDH1
PLCH2	UBC	ZIC5	KSR2
DCDC1	C6orf1	PDE2A	MAP1B
AKAP7	IGFBP3	MAGEA12	RP11378J18.8
PKD1P5	OAS2	FOUR1	MYO7B
WNT2B	LUM	DNER	SCN1A
TSPAN18	PRAF2	LINC00473	SEMA3E
PDGFD	MIR242	SLC7A5	BAALC
DYSF	ENSG00000276107	SERPINB3	VIPR1A51
FREM2	OAT	MSLN	POU6F2
EXPH5	CLEC11A	ENSG00000275993	ENSG00000280543
SEMA6A	FOSL1	ZIC2	NOVA1
COL15A1	ZNF83	GAL	SLC24A4
ERBB4	FAM195B	TFAP2A	BICC1
ZNF521	THY1	PTP4A1	SNAP91
ZNF717	H1FO	ENSG00000272398	APBA1
RAB11FIP2	GREM2	ABLIM1	MYH7B
TET1	CD81	RP11461A8.4	LINC00702
FAM188B	DTX3	CD55	MEGF11
ROR1	NFATC4	JUP	CAMK4
SVOP	MMP2	CDK1	KCNA2
TGM2	PAMR1	PVRIG	ENSG00000279278
FGF9	EHD3	PRKAA2	CTSC
HNMT	DNM1	KRT18	ENSG00000280156
PRICKLE2	MME	LXN	ADAMTS20
FLI1	RP11894P9.1	POK4	ABCA13
AXIN2	MFAP4	PITX1	MYH2
SNED1	SNORD3A	MCAM	CYP46A1
TNFAIP6	IFI27L2	KCNN4	LINC00476
C10orf11	CHAC1	STRIP2	IQGAP2
IGFBP5	AQP1	LONRF3	ATP2B2
LINC00598	ADM	IGF2BP1	PKHD1L1
LIPG	TRPV2	FSTL3	GDNFAS1
ST3GAL5	BGN	CHML	OTOG
COL22A1	ENSG00000279520	ALPP	UGT3A1
RP3399L15.3	FMOD	C4BPB	KIF1A
ABCA1	GALNT15	GDA	GDNF
NRCAM	LSS	ELF3	COL17A1
MEGF6	ARL4C	ETS2	FYB
CACNA1E	SSTR1	TSPAN12	PITCHD1
CYP27A1	TNFRSF14	MAGEA3	NPAP1
POU5F2	UCHL1	36951	CHD5
C1orf198	SLC16A2	MTATP6P1	RIN2
CH25H	AKR1C2	KRT80	C8orf34
RNF150	HERC6	BAG1	RP11449L23.2
ABCA12	38047	NPR3	NKX31
UNC5B	KLF6	PRG4	NDNF
ITGA11	FTLP3	FAAH2	MOV10L1
PRELP	IFITM1	L1CAM	SCIN
CDH11	CHIC1	LAMA5	ZNF385D
NOG	C15	MCTP2	ENSG00000277363
MUC5B	MIRS03HG	FOXA1	ATP6V0E2
MAB21L1	ANKRD13A	KLF5	MUC16
HSPA2	ARMCK1	NUP155	MGAT4C
PLCG2	KLF7	ORC1	PLGRKT
OTOG	PODN	CCT5	RASGRP3
DCC	PLCB4	MTATP6	RBFox1
CADPS	SERPINH1	CITED4	UBA6
MRV11	TAX1BP3	BRI3BP	ZNRD1A51
RBMS3	AP2M1	TNS4	SRGAP1
CNN1	ACTA2	MCM2	CD226

ChTxB	ChTxBShTxB1aShTxB2e	ShTxB1aShTxB2	ShTxB2e
RP1177403.3	IGFBP6	MANEAL	DNAJC3
ADCY10P1	TIMP2	CXCR4	MAGI2
TNC	EDA2R	CFI	GPATCH2
PCDH15	ALDH1A3	COBL	XKR4
PART1	CYP7B1	BARX1	TMTCS
CTD2619/13.19	OLFML3	FZD5	ENSG00000280011
EMX2OS	FCGRT	PPAP2C	TLK1
FAM179A	HLAC	SNHG17	TBC1D32
GAB3	CTGF	FAM83H	EPHB2
RAPGEF5	QPR1	LIFR	COL2A1
BCL11A	SCPEP1	OLR1	ENSG00000280007
TEX41	CCNL1	LRP8	UNC80
CLSTN2	MTMR9LP	DSC2	BSN
ZNF516	GSTP1	SGK1	FRK
HSD17B2	GLIPR2	MAGEA1	ENSG00000274775
EBF1	APLP2	SMOC1	GABRG3
ROBO2	MT1E	RAB26	ALPK3
ITGA8	MAPK3	CYCS	DGKB
FZD4	CXCL1	TFRC	C14orf182
PAPPA2	SNAI2	SOHLH2	PCDH9
RP11413E6.7	TMEM140	CTAG2	SLC7A14
PCL0	ATP8B2	PAGE1	CSMD3
CNTNAP2	COL1A2	PODXL2	LINC00938
COL11A1	ARSJ	RG52	ENSG00000267719
GULP1	IFI27	IMPA2	CCDC30
STAB1	EPDR1	COL4A5	MYEF2
ITGBL1	ALPK2	DUSP16	RG510
SDK1	MXRA8	KLHL23	PPP1CB
PHACTR3	STC2	GIPC3	LOXHD1
PKHD1	SOD2	SNORA71B	FAT3
SMAD9	MTMR11	SERPINB4	AXL
OLFM2	CSF1	BMP6	HHAT
STK17B	CRYAB	TPD52	OTUD7A
SSPN	PIK3R1	MYBL2	STAB2
PTK28	DYNLRB1	NDC1	DNAH11
NOTCH3	HEPH	CKB	NTRK3
PREX2	PEA15	SLFNL1	SRGAP2C
PLCB1	LAMB2	MCM10	PTPRQ
LIMS2	RP11345P4.7	LY6K	MYRF
USH2A	C1orf85	MTND1	ENSG00000279184
KALRN	KCNK2	MRPS30	ENSG00000279080
PEAR1	GADD45A	STEAP4	NOS1
KCNQ1OT1	TUBB2A	GPRC5A	KCNS3
RUNX1T1	LRRCL5	GAGE1	TTC40
EMX2	ABHD4	NSUN2	ENSG00000275395
PKD1L2	PSMB9	ENSG00000270816	RP11379K17.4
OXTR	SRPX2	SFN	EFCAB4B
TRPM3	C1orf68	JPH1	Cxorf22
INTS6AS1	NFKBIZ	CEP72	MUC12
FRAS1	NFE2L1	FAM60A	PGBD1
RHOBTB3	FTL	ENSG00000273604	KIF5C
PCDH18	ISG15	RHOV	GRIN2A
WFDL1	NID1	RP1276N6.2	LRP2
NRXN3	MAML2	ABCC2	ANKS1B
KIAA1199	CDIPT	KLHL13	CTD3088G3.8
RF33	TMEM204	ITPR1	SSPO
BICC1	RCN3	PLA2G4A	RP11492D6.3
IKZF2	NAGK	HPD	FAM83F
LBH	TMEM47	AVP11	LRP1B
AR	SULF1	ACVR2B	LINC00886
LMOD1	RNF146	ANKRD32	DNAH7
RFTN1	LINC00968	CDC6	DZANK1
RELN	SRPX	FAM83D	DUOX1
GPC4	RGMB	CXADR	FSIP2
PDE11A	COL3A1	RTN4RL2	DGCR5
CDH23	ID2	NOLC1	C1orf222
C12orf55	SOC55	EPGN	FBXO36
SLC8A1	B2M	GLCCI1	RP11119F7.5
PRKD1	RABAC1	ACO10761.8	MUC17
XDH	MIR143HG	LDHB	RP11212P7.2
BEND7	CXCL6	MISP	NHLH2
KAZN	IL20RB	NRARP	SH3TC2
SAMD5	CAV1	OSBP2	SHISA4
CXCL12	GSTA4	PDE4D	LAMTOR5A1
STC1	GPR68	LAMC3	LINC00910
DAPK2	FAM127A	GPR126	TG
C2orf27A	MYD88	SLC29A2	PLEKHG4B
FAT4	GALNT5	FZD10	NTRK2
ATP8A2	STAT1	S100A9	VSIG10
ITGA9	STAT2	TRABD2A	ADPRHL1
C11orf87	TMEM119	SALL4	TNR
ITGB8	ADHS	SLPI	KIAA1456
BMPR2	SRSF5	SLC20A1	RGMA
ANK3	YPEL5	MCM3	PTPN14
ILDR2	ARMCX3	DEPDC1	REEP3
NAALADL2	TRPC4	MYPN	CSNK1A1
POSTN	DNM3OS	TUBA4A	CHN2
RYR1	PJA1	ENSG00000276850	CACNA1B
PLEKH2	VAT1	FKBP4	ADAM22
ENSG00000274775	SERPINE2	NEFH	CDKN2D
MYBPC3	AKR1C3	LAMA1	SLC48A1
RP11417E7.1	LENG8	VAMP8	DCP1B
RAB11FIP4	FOSB	KRT16	RHPN1
TENM4	ENPP2	CBFA2T3	SARDH
ANGPT2	APBB1	KIF21A	FAM46A
KCNQ2	OLFML1	BRIX1	PAQR8
PTPRG	DCN	CHAF1A	RP111220K2.2
DPP6	XG	CDCA7	ARHGEF26
MLYCD	TPRGL	C19orf33	ITGAX
EBF3	SERINC1	AOC2	GPRIN2

ChTxB	ChTxBShTxB1aShTxB2e	ShTxB1aShTxB2	ShTxB2e
SLCSA3	NPC2	hsamir6723	C1orf233
MUC19	DAPK3	STOX2	TMEM54
SCN4A	DPYSL3	CBX2	PAK3
CD302	FIBIN	PDHA1	MYO7A
SOX2OT	CFH	PEG10	CASA
ZBTB88	ARF4	SCARB1	DNAH2
TNFSF13B	PSMB8	WNT7B	ABCA4
SAMD12	RRAS	LRFN1	KCNJ14
PLXDC2	FTH1	KRT8	MYT1L
MEF2C	GRIA3	HSPA4L	RP11416018.1
TRAPPC12A51	FGF7	POLR18	ABCA10
MUC6	NDRG1	OTUD1	SVOPL
STMN2	MALAT1	LGR4	USP6
C1orf132	GALNT10	NAT8L	RPS6KA5
NLR3	ISLR	HGN2	PAX5
NR2F1	DAB2	SAPCD2	ST18
ESRRG	IER3	SNHG1	SLC16A10
COL16A1	C11orf96	C10orf2	ADRBK2
SLIT3	WISP1	NUP160	SCUBE1
ZNF585B	EPS8	DAK	ARF6
KCNK6	MIRGPRF	MFSO12	ENSG00000279652
AMIGO2	EMP1	ZYG11A	CUBN
MYO15A	RCAN2	EIF4A3	KIAA1244
SEMA5A	SEC24D	EXO1	C6orf62
JAM2	STX12	DDX11	GABRB3
PRKAR2B	PTTG1IP	HPDL	CSMD2
ENSG00000279118	ACTC1	SOWAHC	RAP2B
DNAJC4	IFIH1	BTBD3	AK5
DGKI	TUBA1A	DSP	ENSG00000278920
ALDH1L1	ID3	RIMS1	ARSK
EPB41L3	SH3BGRL	UCP2	RP1
TSIX	ACTN4	CDKN2A	PPP3CA
TPRG1	TOM1L2	TRAP1	DNAH8
SLC9A3R2	DYNLT1	LAPTM4B	DTNA
FADS2	SCOC	CLUH	PTPRT
RASGRF1	CREB3L1	MTND2	VWF
JPH2	EHBP1	SLC29A1	DNAH12
WHAMMP2	PKIG	NUP205	IL7R
PARP8	WSB1	RP11314013.1	RP11111M22.2
SDK2	WARS	TAF1D	KLHL28
MXRA5	SGCD	NPR1	NRXN1
LRP1B	THOC6	DDX12P	A2ML1
ZNF567	FGF2	GLA	TSIX
CLMN	FLNC	CDC25A	ILDR2
F2R	SPON2	FAM107B	MAP3K4
ZNF827	SLC17A9	USP2	KIAA1324
EDNRA	RNF185	KIF2C	FOXO1
DPYSL2	ARHGAP29	LRPPRC	CA12
ATL3	SPATA18	CELSR1	MYH11
NRP2	YPEL3	MATK	DTNB
DCHS2	ACTN1	EIF4A1	FBN3
SORBS1	GRN	CEBPA	GMPR
TBC1D8B	EFS	LINC00958	SERINC5
SPOCK1	FTH1P7	TOP2A	SRGAP3
PTPN14	TMBIM1	CHD7	CACNA1A
HYDIN	RP11138A9.2	MLK4	MYO15B
TIAF1	MAGED2	RF3C	TRIM59
PDE5A	UBA7	FAM81A	RP11282O18.3
NEB	PRKCD8P	DUSP2	C3orf70
SMAD6	AASS	RASSF9	SDK1
PTX3	SQSTM1	POLE3	RP11359E3.4
HMCN2	ATP6V1B2	WDR3	MGAM
NEXN	SMPD1	GFOD1	ZAN
ST18	COP22	CKS2	ENSG00000276975
ZNF704	TNFSF4	ARHGAP4	ACOT11
ADAMTSL3	LOX	ENSG00000261150	ENSG00000280061
COL4A3	ETS1	CPM	DNM3
FZD7	LGALS1	MOSPD1	ENSG00000281344
RP11416018.1	PDGFRB	ESRP2	MTTK
KIF26B	PARP14	PPAT	KCNJ2
AKAP12	RSU1	RABGGTB	MVB12B
RP11379K17.4	RND3	FAM46C	EYS
VCAN	WNT2	MCM4	RELN
MAN2A1	LRR32	MPY7	TNXB
CCDC168	PPP4C	CCDC86	SOX2OT
DDAH1	ANTXR2	DPH2	SORL1
ADAMT51	RAB32	HSPD1	GPR98
ZNF585A	VAMP5	CCNB1	RNF144B
GAS7	ACKR3	AURKA	DOCK8
ELN	STARD13	TROAP	KIAA1217
FSIP2	STX4	ESPL1	RYR2
PKD1L1	MYO1D	MIRPL12	ERO1LB
RP1	LRRN4CL	EMG1	CCBE1
GCH1	RBFA	MITCO2	CDKL1
SOX6	DLST	B4GALNT4	ENSG00000280434
ADAMT55	ITM2C	KIAA0947	CTC359D24.3
ARL10	PGRCM1	FANCD2	CACNA1D
VLDLR	MDK	CDC20	ERBB3
UNCB0	RECK	DKC1	GABBR2
CRISPLD2	ELN	FAM83AAS1	ICA1L
NHSL2	SAMHD1	TMC5	FAM114A1
SRRM4	FTH1P2	FARSA	ATL3
DCP2	FAM198B	BUB1B	SLC13A4
PTGDS	PCOLCE	GOLGA8B	RASGRF1
PRICKLE1	TPP1	SDHA	RP11286N22.8
GRIA1	SNRPN	CENPV	CACNB4
CALD1	HSPB7	WWC1	PTPRB
ECM2	TNFRSF19	TLCD1	KLHL3
CLEC2B	PSAP	NCAPG	TSPYL1
PALLD	ZNF25	BLM	SHOC2

ChTx8	ChTx8ShTxB1aShTxB2e	ShTxB1aShTxB2	ShTxB2e
CYP2U1	KIAA1462	MOB3B	SRPK2
PTPRD	ORAI3	TEX15	RP11366L20.2
ATP9B	TUSC3	NKRF	DCC
NOV	NDN	FAM195A	PREX2
PTGIS	FAM180A	PHKA2	ZNF442
EFEMP1	TRIM16L	SPIRE2	PPP1R148
FER1L5	MAPRE2	WDR4	NAALADL2
ZSCAN18	PLXNA3	NOP2	RNASET2
FHAD1	GFRA1	RRP7B	WNT5B
TULP4	MAGED1	ECT2	HYDIN
PAN3	RP4635E18.8	GAS8	KCTD16
C15orf59	AGA	GNAL	HOMER2
GBP4	TCIRG1	RP4742J24.2	S1PR1
DCLK1	APCDD1L	KIF4A	ERAP2
ACSS3	TMEM230	XRCC2	ADAMTSL3
PLXNA4	ANKA6	SH3GL2	ZNF462
DNAH6	HSD3B7	PPT2	ANP32E
SOX9	GNIA2	HDHD3	CYFIP2
CASP10	LINC00856	ELAC2	MMS22L
ACAP1	GN2	ANKRD188	MCF2L2
FBN2	IFI6	MCM7	PTPRD
ACTC1	ARMCK2	MBNL3	PRLR
NINL	MYL6	CARD14	ELTD1
38596	APOL1	OXCT1	PKD1L1
DNAH14	UBL3	CCDC138	PIP4K2A
ETV6	HMOX1	SLC38A1	DUSP7
RFTN2	LMCD1	SYNGR2	MDM2
ZAN	IL6	MTND4	CDCP1
RNF217	UBE2L6	CKS1B	DNAH6
MYLK	EHD2	ENSG00000275216	SRRM4
ZNF677	MFAP2	ABCG2	ENSG00000280383
RYR2	HOXC6	NLGN4X	LINC01116
FN1	APCDD1	FASN	RAPGEF3
PPM1K	CNTN3	PRPF19	SYT14
DAB1	PLBD2	NETO2	EXO5
MAF	RRAGA	FOXRED2	ZNF585B
LRP2	PAX8AS1	DIO2	PLXNA4
ZNF506	FCHSD1	RP1118114.10	KCNQ2
FZD1	EPSTI1	CEP152	DOPEY2
SETBP1	PLEKHO2	C1QB	ABC89
AKNA	TIPARP	UBE2T	TPRG1
NTRK3	MIR22HG	FANCI	ST3GAL3
DAPK1	GLT8D2	CDC7	ESYT3
KRCC1	CMTM3	DDX21	S100A10
TNFRSF11B	TMEM50A	NEK2	LRRK2
MFGE8	PRR16	NOL6	LRRK7
NRXN1	MMP19	HEATR1	FAM210A
CACNB4	RTN4	CHAC2	KCNQ1
ARRDC3	FBLN5	SASS6	ABCA12
KLRD1	IFIT3	ERMP1	DOK5
IL15RA	ZNF211	MET	ENSG00000265808

Table 3. FGF and TGF- β gene signatures. FGF and TGF- β signalling pathways signatures were kindly provided by Prof. Paolo Dotto (DB-UNIL, Lausanne) and obtained as detailed in Bordignon P et al., 2019.

FGF2 Up-regulated				FGF2 Down-regulated				
SLC5A3	CDCP1	MAP4K4	WWTR1	LIMA1	CRIM1	HSPG2	FSTL1	DAB1
CNIH3	AK5	MGLL	MRPL15	TN33	CCNG2	CFB	KCND3	SIPA1L2
PLXNA4	ANTXR2	NCAM1	MCM4	SLC39A7	MEDAG	ENAH	BAMBI	FAM198B
STC1	GDNF	FJX1	MFSO1	SLC39A14	NPIPA7	ASS1	FAM20A	LINC00968
NTSR1	MYEOV	PBX3	TLE3	CARS	TRIB3	FN1	FAT4	PIEZO2
ESM1	SLC29A1	SEMA3A	MYO10	ITGAV	NABP1	WARS	SEMA5A	LMOD1
TMEM158	SNGG	CTSS	NET1	PCOLCE	HEG1	PSG5	FRMD6	ALPK2
PRKG2	ITGB3	GRAMD18	WLS	SMAD3	RP11-334E6.12	C1orf115	ATOH8	LUM
COL10A1	TMEM35	CD68	SYT11	CALCOCO1	MEIS2	TSHZ2	CXCL6	SFRP4
THBD	ZC3H12C	JUN	SH3BGR13	TSC22D2	FTH1	DAAM1	FBLN2	WISP1
ETV1	RGS17	CDKN2D	MMP14	MARCKS	RBMS3	CTHRC1	CYP7B1	GRIAI
ITGA10	VEPH1	MMP16	PRKCD	FADS3	CALD1	APOL6	GBP1	RNF150
SPRY2	EHD3	EPHB1	C2CD2	AFAP1	ALDH1A3	CNN2	RP11-253M7.1	MXK
PODXL	RP11-887P2.3	NR1D1	FAM129B	P4HA2	PLOD2	PHGDH	CRISPLD2	SVEP1
RF8X	PREX1	TSZH3	DNMBP	PDGFRB	ENPP2	AJUBA	ADA	GPR133
C14orf169	DHR513	SLC6A6	RPS6KA3	XPOT	ITGBL1	MAP2	ADAMTS2	EFEMP1
KPRP	SPHKAP	S100A4	SH3PXD2B	KDMSB	MALT1	FOXC1	THBS1	STC2
LCE1F	TNFAIP8L3	PLAU	FANCA	RP11-958N24.1	LOX	TRIO	OSR2	IGFBP3
PRLR	GEM	TRPV2	KLF6	ATXN1	CPA4	TSPAN18	KCNK15	COL5A1
HMGAI1	VAT1L	BCL2L1	SMTN	SEMA3C	ACTA2	PAPPA	LRIG3	ADM2
INA	ANKH	TMEM171	GREM2	MYO1B	ATP10A	LEPRE1	KIAA1199	DAPK1
ARHGAP22	IL4R	DENND3	IL4R	XBP1	PGRMC2	GALNT5	IL7R	CXCL12
SFRP1	ABLUM3	STRIP2	MCM5	TOM1	RUNX1	TNFRSF11B	PALM2-AKAP2	SULF1
TFPI2	SLC35E4	RAB38	BAGALT1	ST5	UGCG	P4HA1	LMCD1	LMCD1
SLC20A1	CSMD2	LAMA5	MARS	CCDC80	ABCA5	MUC1	PDGFD	PDGFD
RP11-1198D22.2	SPRED1	MAP1B	FLRT2	PRKAB2	CTGF	ANGPT1	DHR53	COL1A1
CORO2B	PITPNC1	ACVRL1	RAC2	PRPS1	NUPR1	S1PR3	COL1A1	WISP2
FGF5	TNFRSF25	PNP	SH3KBP1	STAT2	GDF15	C1QTNF5	ARRDC4	COL3A1
SCUBE3	ANGPTL4	MYOSA	NCEH1	PMP22	GPR124	ID1	GDF6	WISP2
PHLDA1	ETV4	SLK	DOT1L	MAGED2	IFRD1	LURAP1L	NTN1	ADAMTS5
NCALD	LIMD1-AS1	SSX2IP	CAPG	FOSL2	TNFRSF19	WNT5A	STAT1	ADH1B
FOXF1	RP1-79C4.4	MT2A	MT2A	IDH2	TXNIP	PYCR1	PI16	KIF26B
FAM180A	SIPA1L3	CPNE7	CAPN5	SH3PXD2A	FNDCC3B	PLCB4	IRS2	ELN
STX1A	LIMD1	NHS2	E1F1AX	RABGAP1	GALNT15	FNDCC1	GNA14	
IGFBP5	ACD10441.1	ERRFI1	DUSP3	KRT7	LOX3	MIR503HG	MIR503HG	
DUSP6	HBEGF	PHLP1	PHLP1	C6orf48	PCDH18	FMOD	RP11-244F12.3	
MMP1	ITPR3	RASA1	KLHL21	FAM101B	SLC7A5	DPP4	GPR37	
CCND1	DCBLD2	CTD-2541J13.2	S100A6	MIN1	MEG3	PLXNC1	ID3	
FZD8	BCAR3	SLIT2	ATP9A	FGF7	MASP1	PLK2	OXTR	
SPRY4	LINC00341	IRX1	SACS	LIPA	CLRF1	MBNL2	PODNL1	
SLC6A15	SERPINB2	PPFBP1	TJP2	DAAM2	SESN2	ACKR3	HSPB7	
KCNQ5	MIR31HG	MAPKB1	CD109	sept.11	SPOCK1	COL4A2	STAC	
NES	SYNE3	ARRB1	MIR29A	SOGA2	CDH2	IL16	ACT13025.8	
ITGA2	GLUL	GNG2	SYNE2	KLHDC3	GLS	NRCAM	MIR145	
PRRX1	ELK3	RASSF8	FMNL3	AHR	IL20RB	TMEM189-UBE2V1	SYNPO2	
HAS2	PID1	RNF24	FIP1L1	GARS	PPIC	GREM1	CYP1B1	
COL13A1	ADRA1D	CHST7	ABI3BP	C6orf132	DDIT4	WNT2	RP11-426C22.4	
KCTD12	LRRRC8	PHLDA2	TMEM131	RUNX1T1	FBN1	TPM1	ID2	
FMNL2	SLC9A7	UHRF1	UHRF1	OSTC	NEK7	ACVR2A	TGFB1	
RNF152	ARNTL2	CAPN2	ZCCHC6	CD248	PALLD	FGF2	FAM110B	
RG54	TBX3	PAG1	FRMD4A	SHMT2	SORCS2	ADAMTS1	ARID5B	
IL13RA2	SCFD2	FBXO33	MCM3	MYLK	DAB2	GPR17	LBH	
LTBP1	RASSF2	RG53	SPEG	HERPUD1	FAP	DKK2	SLC39A8	
CEP170	FAM84A	DENND2A	COPRS	BMP2K	FAM19A5	TENM3	EBF1	
NTSE	PLEKHG5	TNKB	ECE1	GPX8	AVIL	DGKI	SLC6A9	
PRDM8	MAPKAPK3	GPR56	CBFB	HIF1A	GCNT1	SLC1A5	THRB	
RBPJ	ELTD1	E2F1	TAOK3	ERBB2IP	BGN	RHOBTB3	ECM2	
NRG2	NPTX1	RAPGEF3	MRPS6	AARS	SGCD	POSTN	PTX3	
ADIRF	KIAA1217	CKB	TRIOBP	ARHGEF2	C1RL	RP11-215G15.5	MIR143HG	
GPR68	CTSK	TMOD2	CTSL	CBS	LIMS2	CPM	ITGA11	
WNT9A	LAPTM5	MOXD1	MCM2	NPIPA7	SNED1	GABRE	ITGB8	
NTNG1	NRP3	CHST2	LGALS1	ROBO1	ADAMTS7	GDF5	FBN2	
NTM	CPED1	ENC1	MYO1D	MYO1D	NUAK2	AMOTL2	COL12A1	
SYT7	SYNM	KCNMA1	YWHAQ	DLG1	StGALNAC5	ASNS	GADD45B	
HGF	FAM129A	USP53	TRERF1	MATN2	PLD1	DSE	GPRC5B	
TOX2	TBX2	SALL1	PXN	DSP	DDIT3	VIT	CHRM2	
MAP3K5	SPRED3	UBASH3B	ARL2	CTSC	ADARB1	DCN	SERPINH1	
CAMK2N1	GPRIN1	JADE2	AKAP2	MAGED1	VWCE	NEDD9	PIM1	
RP11-366L20.2	TENM4	ATP2B4	SFXN3	ANKRD13A	JDP2	NREP	PSAT1	
ANPEP	KIAA1549L	PLN2	UBALD2	YARS	SEMA3B	CACNA1C	CHAC1	
PLCXD3	HPICAL1	TNFRSF21	ECM1	C9orf3	SLC3A2	SFRP2	TENM2	
GNG11	PAMR1	AHNAK2	SYNJ2	LGMM	TIMP3	PEAR1	SEMA3D	
FOSL1	CPNE3	FYCO1	TRAM1	PKDCC	PKDCC	PTGIS	RP11-1151B14.4	
IRAK2	PHC2	ADAMTS1	MCM7	RNF41	CNN1	GABARAPL1	MAP3K8	
POU2F2	TMEM200A	MEI2	SVIL	CYR61	RP11-572C15.6	COL4A1	ALDH1L2	
RNF157	OSBP2	MAN1A1	FST	THBS2	REV3L	SH2D4A	PRSS53	
C5orf30	SATB2	H1FO	USP36	ANTXR1	WEE1	SDC2	OLFAM2	
DOCK4	LRRN4CL	PSD4	ELOVL1	MKRA5	PXK	RHOBTB1	COL1A2	
CIT	ELOVL6	MDGA1	MCL1	TMEM119	RNF144B	COL8A1	ADRA2A	
APBA1	PLAUR	TFPI	CARHSP1	UNC5B	PAWR	NPAS1	CFD	
SLCO4A1	TOR4A	FZD1	DYNC1H1	PXDC1	MYL9	COMP	SLC7A11	
RP11-290L1.3	CPXM2	OLFM28	APLP2	XAF1	SYTL2	CCL2	DPT	
GALNT12	RMRP	C3orf18	BZW1	JAG1	ITIH5	C1R	LOXL2	
PTGER3	TNFRSF6B	PLAT	PPP1R18	FHL1	EPSTI1	ZNF469	NNMT	
RP4-555D20.2	NAGS	RP6-99M1.2	IER2	LEPREL4	GRAMD3	ANKRD33B	CEBPD	
OPCML	HIVEP3	ARHGAP18	RASA3	KDELRA3	KLF7	SLIT3	VGLL3	
HMG2A	TNFRSF18	OLFM2A	ABHD2	MMP2	SLC1A4	GFR1A	C10orf54	
SH2B3	FAM210B	SMURF2	PARP4	PBX1	PKC2	PTGDS	PODN	
HAS2-AS1	PLCXD1	VEGFC	FAM126A	SLC43A2	ACAP1	SPCS2P4	COL5A2	
MYH15	H53ST3A1	SDCCAG8	MAT2A	ATF4	NID2	PDE1C	MFAF4	
C6orf1	TMPO-AS1	PAK1	DNMT1	SWAP70	IL15	ELL2	ADAM12	
EBF2	EZF7	CDYL2	CLIC1	CERCAM	BICC1	PXDN	CLEC3B	
ETV5	ENPP1	HIPK2	HSPA8	THY1	MFAP5	TAGLN	ADM	
ZNF536	GALNT6	FHOD3	ANXA1	NID1	CITED2	MTHFD2	SPARC	
NAV3	TFAP2C	RIN1	CD59	BMP1	F3	CREB3L1	HMCN1	
MLPH	STEAP3	LRIG1	CCDC85B	MAGED4B	IGFBP4	CHN1	DEPTOR	
DUSP5	HSD3B7	IFFO1	MYO1E	APOL1	SELM	MGARP	MRV11	
SMAGP	PLXNA2	SNN	SH3GLB2	ADAMTS10	VDR	CCDC85A	CPZ	
LPXN	ZNF385D	TGM2	EHBPI1L1	COL16A1	PTK7	GRIA3	COL5A3	

TGF- β Up-regulated			TGF- β Down-regulated		
ELN	TP1P2	TPR	CCDC74B	PEBP1	NTN4
INHBE	GCLM	DUSP1	PERP	C10orf54	OLFML1
PI16	COL11A1	DSP	CPXM2	RAC2	TYMS
NOX4	EZR	XPOT	SLC9A9	IGFBP4	RAB38
KRT7	BCAT1	LIMS1	ADAM15	RNASE4	OAF
TRIB3	PLS3	ACTA2	GLB1	RNF144A	TGFBF3
MGF	TGFB1	TRIB2	PPARG	PRC1	RG52
BHLHE40	ACLY	KCTD15	HEXB	LETMD1	APOD
CNN1	COL8A1	ALPK2	RILPL2	KRT19	COLEC12
LTBP2	OXTR	WDR1	FYCO1	RASSF2	PDGFRL
ASNS	NPW	ZSWIM4	ITM2B	C10orf105	LUM
ITGA11	SGCD	NTSDC2	EVA1B	MAP3K5	ACKR4
SLC7A5	CARD9	ULBP1	ADD3	LRPAP1	HSD17B2
HSD17B6	LOC644936	CNN3	MT1A	HLA-E	PDGFD
PSAT1	PRUNE2	FSTL3	CREBRF	TKT	SLC7A14
KCNH1	PDJIM3	FZD7	MAD2L1	KIAA0101	PCOLCE2
NUAK1	HSPA9	RBBP8	ARMCX1	C1GALT1C1	CLDN11
MTNFD2	SLC1A4	SLC9A1	PTGS2	CTXN1	MMP1
SLC2A5	TSC2D3	COL4A1	SOD2	PRELP	APCDD1
TNC	SH3PXD2A	EPRS	TMEM51	ZNF581	CLEC3B
KCNMB1	RAP1GDS1	C4orf32	CTSB	ADAMTS5	NOV
ACTG2	IER3	FAM129A	ANKRD10	ANPEP	NPTX1
SERPINE1	ACTN1	AARD	NUSAP1	TFPI	
PMEP1	NGF	CHAC1	MBNL3	IQCK	
TPM1	GLIPR2	VASP	PTGS1	MYN1RIN	
WDFC1	PDCL3	TMEM2	C19orf21	CREB5	
PDJIM7	KIF26B	AP4E1	IFTM1	RNASET2	
ALDH1B1	NMMT	PHH1	BIRC5	PTGFR	
CDH2	TUBB8	SGPL1	PTGIS	GRK5	
CTPS1	FKBP11	SERPINB7	NDRG3	SPRY1	
SEL1L3	TCEA1	DNAJB9	TLE1	PYCARD	
MICAL2	ATP2A2	EIF5	C16orf45	INTS8	
PKC2	IARS	PLN	NNT	PLAT	
RBP1	NUPR1	EIF4EBP1	KCNK2	ZNF503	
EFHD1	ITGA1	PLEKHO1	ZNF277	ADAMTS8	
GBP1	TNFRSF12A	ILK	GSTM2	IGBP1	
MEGF6	FLNB	NEK7	ACKR3	MGRPRF	
DDIT4	PPP1R13L	CAV2	KITLG	MBP	
DACT1	GOT1	LARS	DENND2A	HIST1H2BD	
MAMDC2	SERTAD4-AS1	MFAP4	GRP	PRDM8	
PSPH	LRRC32	ANKRD11	PLCD3	SELENBP1	
MYOZ1	HACD1	RCN3	DACH1	SNHG7	
LOC284023	SNX30	EHDM4	ANTXR1	TOP2A	
PPP1R14A	LDLR	MORF4L2	MBN1	SMPD3A	
AIMP2	SGK223	CNN2	NBL1	FAM46C	
COL8A2	UPP1	SYNM	PCYOX1	HMGAI1	
CSRP2	PLXDC2		LAMB1	AOX1	
FAM101B	FERMT2		CDH13	CCBE1	
CTGF	CDK7		GSTM1	RPS29	
MYL9	TNFSF4		OSR1	EGFL6	
KCNG1	RUNX1		NFIB	CLCC1	
GADD45B	PAWR		CFH	SEMASA	
CSRP1	TXNDC12		EYA1	LRRN4CL	
EGR2	SLC7A1		DUSP19	PID1	
IGF1	CRLF1		RPL34	SVIL	
TSPAN2	MYLK		EPB41L2	NLGN4X	
PTK7	LIMCH1		NOA1	CTQTNF1	
SRF	C9orf3		CD59	ALDH1A3	
ANXA2	TUBA1A		ABRACL	OSR2	
CYR61	TNSI		ADGRL2	CD302	
UCHL1	GLPR1		SIPA1L2	RARRES3	
SLC6A9	RG54		GIPC	CLEC11A	
SLC1A5	XYLT1		PTGES	CASP1	
VLDLR	ECI1		RCAN2	LY6E	
WARS	DUSP14		BORCS7	STC1	
COL7A1	SCHIP1		CHP1	CMBL	
NRG1	ANKLE2		LD82	TM4SF1	
SCRG1	FBLN5		GNPMB	PPL	
CALD1	SLAH2		TCEA3	AMOT	
TUBB2A	TYMP		TSHZ2	PHLDA1	
TAGLN	COL16A1		CTSF	DPYD	
PFKP	FN1		EML1	EPHB6	
PYCR1	TP1		IGFBP6	PTGFRN	
SORBS1	CAP1		SLC1A3	CEMIP	
TPD52L1	SGCG		ECM1	ENPP2	
ANOS1	CFL1		ABI3BP	SMARCC2	
GALNT16	DDIT3		SH3D19	SIPR3	
SLC3A2	POTEE		MYLIP	CD44	
ADAMT9	CILP		NAV2	AKR1C4	
GLS	ARF4		ABCA1	IGFBP2	
CADM1	ITSN1		GINM1	F10	
CBS	TP53I3		RPUSD4	SFRP2	
CH25H	TGIF1		MME	ZNF423	
CDK5RAP2	LONP1		AKR1C2	CCNG1	
TNFAIP6	CSPG4		WLS	TMEM158	
IL6	CEBPG		FMOD	FLRT3	
CCDC80	FGF2		FAM198B	SFRP1	
PLOD2	BT3L3L4		CTSC	PKD4	
P4HA2	DPT		NR1H3	MATN2	
TENM3	TUBB3		GPSM2	ERAP2	
MYADM	CLIC4		RBBP4	PLPP3	
BCAS4	C11orf96		DPP4	KLF4	
SMYD3	GRAMD3		C17orf58	RSP03	
ZNF365	ACOT2		CAMK2N1	NFIA	
EVA1A	IL11		INHBB	GPM6B	
VCAN	HES4		UBA7	OLFM2A	
GPT2	ABCC3		TAPBP	ADH1A	
NREP	BMP6		PLCB1	ANGPTL4	
MARS	NEXN		AKR1C3	TNFRSF19	

REFERENCES

- Adada, Mohamad M., et al. "Intracellular sphingosine kinase 2-derived sphingosine-1-phosphate mediates epidermal growth factor-induced ezrin-radixin-moesin phosphorylation and cancer cell invasion." *The FASEB Journal* 29.11 (2015): 4654-4669.
- Addie, Ruben D., et al. "Current state and future challenges of mass spectrometry imaging for clinical research." (2015): 6426-6433.
- Adler, Miri, et al. "Principles of Cell Circuits for Tissue Repair and Fibrosis." *Iscience* 23.2 (2020): 100841.
- Aizarani, Nadim, et al. "A human liver cell atlas reveals heterogeneity and epithelial progenitors." *Nature* 572.7768 (2019): 199-204.
- Allende, Maria Laura, and Richard L. Proia. "Simplifying complexity: genetically resculpting glycosphingolipid synthesis pathways in mice to reveal function." *Glycoconjugate journal* 31.9 (2014): 613-622.
- Altschuler, Steven J., and Lani F. Wu. "Cellular heterogeneity: do differences make a difference?." *Cell* 141.4 (2010): 559-563.
- Astudillo, Leonardo, et al. "Human genetic disorders of sphingolipid biosynthesis." *Journal of inherited metabolic disease* 38.1 (2015): 65-76.
- Balaban, Nathalie Q., et al. "Bacterial persistence as a phenotypic switch." *Science* 305.5690 (2004): 1622-1625.
- Balla, Tamas. "Phosphoinositides: tiny lipids with giant impact on cell regulation." *Physiological reviews* 93.3 (2013): 1019-1137
- Bandura, Dmitry R., et al. "Mass cytometry: technique for real time single-cell multitarget immunoassay based on inductively coupled plasma time-of-flight mass spectrometry." *Analytical chemistry* 81.16 (2009): 6813-6822.
- Barrientos, Stephan, et al. "Growth factors and cytokines in wound healing." *Wound repair and regeneration* 16.5 (2008): 585-601.
- Bartke, Nana, and Yusuf A. Hannun. "Bioactive sphingolipids: metabolism and function." *Journal of lipid research* 50.Supplement (2009): S91-S96.

- Bergman, Hilde-Marléne, and Ingela Lanekoff. "Profiling and quantifying endogenous molecules in single-cells using nano-DESI MS." *Analyst* 142.19 (2017): 3639-3647.
- Bernstein, Bradley E., Alexander Meissner, and Eric S. Lander. "The mammalian epigenome." *Cell* 128.4 (2007): 669-681.
- Biase, Fernando H., Xiaoyi Cao, and Sheng Zhong. "Cell fate inclination within 2-cell and 4-cell mouse embryos revealed by single-cell RNA sequencing." *Genome research* 24.11 (2014): 1787-1796.
- Bieberich, Erhard, et al. "Regulation of ganglioside biosynthesis by enzyme complex formation of glycosyltransferases." *Biochemistry* 41.38 (2002): 11479-11487.
- Biellmann, Franziska, et al. "The Lc3-synthase gene *B3gnt5* is essential to pre-implantation development of the murine embryo." *BMC developmental biology* 8.1 (2008): 109.
- Bishen, Kundendu Arya, Raghu Radhakrishnan, and Kapaettu Satyamoorthy. "The role of basic fibroblast growth factor in oral submucous fibrosis pathogenesis." *Journal of oral pathology & medicine* 37.7 (2008): 402-411.
- Blainey, Paul C. "The future is now: single-cell genomics of bacteria and archaea." *FEMS microbiology reviews* 37.3 (2013): 407-427.
- Bligh, E. Graham, and W. Justin Dyer. "A rapid method of total lipid extraction and purification." *Canadian journal of biochemistry and physiology* 37.8 (1959): 911-917
- Boccuto, Luigi, et al. "A mutation in a ganglioside biosynthetic enzyme, *ST3GAL5*, results in salt & pepper syndrome, a neurocutaneous disorder with altered glycolipid and glycoprotein glycosylation." *Human molecular genetics* 23.2 (2014): 418-433.
- Bokhart, Mark T., et al. "ImsReader v1. 0: evolving open-source mass spectrometry imaging software for targeted and untargeted analyses." *Journal of The American Society for Mass Spectrometry* 29.1 (2017): 8-16.
- Bordignon, Pino, et al. "Dualism of FGF and TGF- β signaling in heterogeneous cancer-associated fibroblast activation with ETV1 as a critical determinant." *Cell reports* 28.9 (2019): 2358-2372.
- Boukhris, Amir, et al. "Alteration of ganglioside biosynthesis responsible for complex hereditary spastic paraplegia." *The American Journal of Human Genetics* 93.1 (2013): 118-123.

- Breimer, Michael E., et al. "Glycosphingolipids of human embryonic stem cells." *Glycoconjugate journal* 34.6 (2017): 713-723.
- Brites, Pedro, Hans R. Waterham, and Ronald JA Wanders. "Functions and biosynthesis of plasmalogens in health and disease." *Biochimica et Biophysica Acta (BBA)-Molecular and Cell Biology of Lipids* 1636.2-3 (2004): 219-231.
- Buenrostro, Jason D., et al. "Single-cell chromatin accessibility reveals principles of regulatory variation." *Nature* 523.7561 (2015): 486-490.
- Buenrostro, Jason D., et al. "Transposition of native chromatin for fast and sensitive epigenomic profiling of open chromatin, DNA-binding proteins and nucleosome position." *Nature methods* 10.12 (2013): 1213.
- Calon, A., D. V. F. Tauriello, and E. Batlle. "TGF-beta in CAF-mediated tumor growth and metastasis." *Seminars in cancer biology*. Vol. 25. Academic Press, 2014.
- Cao, Junyue, et al. "Comprehensive single-cell transcriptional profiling of a multicellular organism." *Science* 357.6352 (2017): 661-667.
- Caprioli, Richard M., Terry B. Farmer, and Jocelyn Gile. "Molecular imaging of biological samples: localization of peptides and proteins using MALDI-TOF MS." *Analytical chemistry* 69.23 (1997): 4751-4760.
- Castaing, Raymond, and Georges Slodzian. "Analytical microscopy by secondary ion imaging techniques." *Journal of Physics E: Scientific Instruments* 14.10 (1981): 1119.
- Chambers, Ian, et al. "Nanog safeguards pluripotency and mediates germline development." *Nature* 450.7173 (2007): 1230-1234.
- Chang, Hannah H., et al. "Transcriptome-wide noise controls lineage choice in mammalian progenitor cells." *Nature* 453.7194 (2008): 544-547
- Citri, Ami, et al. "Comprehensive qPCR profiling of gene expression in single neuronal cells." *nature protocols* 7.1 (2012): 118
- Cochran, Frederick B., Robert W. Ledeen, and K. Yu Robert. "Gangliosides and proteins in developing chicken brain myelin." *Developmental Brain Research* 6.1 (1982): 27-32
- Coentro, João Q., et al. "Current and upcoming therapies to modulate skin scarring and fibrosis." *Advanced drug delivery reviews* 146 (2019): 37-59.
- Cohen, Ariel A., et al. "Dynamic proteomics of individual cancer cells in response to a drug." *science* 322.5907 (2008): 1511-1516.

- Colliver, Thomas L., et al. "Atomic and molecular imaging at the single-cell level with TOF-SIMS." *Analytical Chemistry* 69.13 (1997): 2225-2231.
- Coskun, Ünal, et al. "Regulation of human EGF receptor by lipids." *Proceedings of the National Academy of Sciences* 108.22 (2011): 9044-9048.
- D'Angelo, Giovanni, et al. "Glycosphingolipid synthesis requires FAPP2 transfer of glucosylceramide." *Nature* 449.7158 (2007): 62-67.
- D'Angelo, Giovanni, et al. "The multiple roles of PtdIns (4) P—not just the precursor of PtdIns (4, 5) P2." *Journal of cell science* 121.12 (2008): 1955-1963.
- D'Angelo, Giovanni, et al. "Vesicular and non-vesicular transport feed distinct glycosylation pathways in the Golgi." *Nature* 501.7465 (2013a): 116-120.
- D'Angelo, Giovanni, et al. "Glycosphingolipids: synthesis and functions." *The FEBS journal* 280.24 (2013b): 6338-6353.
- D'Arrigo, Paola, and Stefano Servi. "Synthesis of lysophospholipids." *Molecules* 15.3 (2010): 1354-1377.
- Darby, Ian A., and Tim D. Hewitson. "Fibroblast differentiation in wound healing and fibrosis." *International review of cytology* 257 (2007): 143-179.
- David, Charles J., and Joan Massagué. "Contextual determinants of TGF β action in development, immunity and cancer." *Nature reviews Molecular cell biology* 19.7 (2018): 419-435.
- De Matteis, Maria Antonietta, and Anna Godi. "PI-loting membrane traffic." *Nature cell biology* 6.6 (2004): 487-492.
- De Matteis, Maria Antonietta, Antonella Di Campli, and Anna Godi. "The role of the phosphoinositides at the Golgi complex." *Biochimica et Biophysica Acta (BBA)-Molecular Cell Research* 1744.3 (2005): 396-405.
- De Rosa, Stephen C., et al. "11-colours, 13-parameter flow cytometry: identification of human naive T cells by phenotype, function, and T-cell receptor diversity." *Nature medicine* 7.2 (2001): 245-248.
- Denz, Manuela, et al. "Cell cycle dependent changes in the plasma membrane organization of mammalian cells." *Biochimica et Biophysica Acta (BBA)-Biomembranes* 1859.3 (2017): 350-359.

- Dietrich, Jens-Erik, and Takashi Hiiragi. "Stochastic patterning in the mouse pre-implantation embryo." *Development* 134.23 (2007): 4219-4231
- Devaux, Philippe F. "Static and dynamic lipid asymmetry in cell membranes." *Biochemistry* 30.5 (1991): 1163-1173.
- Driskell, Ryan R., et al. "Distinct fibroblast lineages determine dermal architecture in skin development and repair." *Nature* 504.7479 (2013): 277-281.
- Driskell, Ryan R., and Fiona M. Watt. "Understanding fibroblast heterogeneity in the skin." *Trends in cell biology* 25.2 (2015): 92-99.
- Dueñas, Maria Emilia, Jeffrey J. Essner, and Young Jin Lee. "3D MALDI mass spectrometry imaging of a single-cell: spatial mapping of lipids in the embryonic development of zebrafish." *Scientific reports* 7.1 (2017): 1-10
- Egger, Gerda, et al. "Epigenetics in human disease and prospects for epigenetic therapy." *Nature* 429.6990 (2004): 457-463
- Eldar, Avigdor, and Michael B. Elowitz. "Functional roles for noise in genetic circuits." *Nature* 467.7312 (2010): 167-173
- Ellis, S. R., et al. "Laser post-ionisation combined with a high resolving power orbitrap mass spectrometer for enhanced MALDI-MS imaging of lipids." *Chemical Communications* 53.53 (2017): 7246-7249.
- Elowitz, Michael B., et al. "Stochastic gene expression in a single-cell." *Science* 297.5584 (2002): 1183-1186
- Eming, Sabine A., et al. "Wound repair and regeneration: mechanisms, signaling, and translation". *Sci. Transl. Med.* 6 (2014) 265sr6.
- Eyster, Kathleen M. "The membrane and lipids as integral participants in signal transduction: lipid signal transduction for the non-lipid biochemist." *Advances in physiology education* 31.1 (2007): 5-16
- Femino, Andrea M., et al. "Visualization of single RNA transcripts in situ." *Science* 280.5363 (1998): 585-590
- Flyamer, Ilya M., et al. "Single-nucleus Hi-C reveals unique chromatin reorganization at oocyte-to-zygote transition." *Nature* 544.7648 (2017): 110-114
- Fragaki, Konstantina, et al. "Refractory epilepsy and mitochondrial dysfunction due to GM3 synthase deficiency." *European Journal of Human Genetics* 21.5 (2013): 528-534.

- Frenchin, Mathieu, et al. "Cell-intrinsic adaptation of lipid composition to local crowding drives social behaviour." *Nature* 523.7558 (2015): 88-91.
- Frieda, Kirsten L., et al. "Synthetic recording and in situ readout of lineage information in single-cells." *Nature* 541.7635 (2017): 107-111
- Fu, Audrey Qiuyan, and Lior Pachter. "Estimating intrinsic and extrinsic noise from single-cell gene expression measurements." *Statistical applications in genetics and molecular biology* 15.6 (2016): 447-471.
- Fujii, Takashi, et al. "Direct metabolomics for plant cells by live single-cell mass spectrometry." *Nature protocols* 10.9 (2015): 1445.
- Funakoshi, Tomoko, et al. "Reconstitution of ATP-and cytosol-dependent transport of de novo synthesized ceramide to the site of sphingomyelin synthesis in semi-intact cells." *Journal of Biological Chemistry* 275.39 (2000): 29938-29945.
- Fung, Eliza N., and Edward S. Yeung. "Direct analysis of single rat peritoneal mast cells with laser vaporization/ionization mass spectrometry." *Analytical chemistry* 70.15 (1998): 3206-3212.
- Gabbiani, G. "The myofibroblast in wound healing and fibrocontractive diseases." *The Journal of Pathology: A Journal of the Pathological Society of Great Britain and Ireland* 200.4 (2003): 500-503.
- Gao, Zhonghua, et al. "An AUTS2–Polycomb complex activates gene expression in the CNS." *Nature* 516.7531 (2014): 349-354
- Gascard, Philippe, and Thea D. Tlsty. "Carcinoma-associated fibroblasts: orchestrating the composition of malignancy." *Genes & development* 30.9 (2016): 1002-1019.
- Gault, Christopher R., Lina M. Obeid, and Yusuf A. Hannun. "An overview of sphingolipid metabolism: from synthesis to breakdown." *Sphingolipids as signaling and regulatory molecules*. Springer, New York, NY, 2010. 1-23.
- Geyer, Philipp Emanuel, et al. "Gastric adenocarcinomas express the glycosphingolipid Gb3/CD77: Targeting of gastric cancer cells with Shiga toxin B-subunit." *Molecular cancer therapeutics* 15.5 (2016): 1008-1017
- Ghetti, M., et al. "Subpopulations of dermal skin fibroblasts secrete distinct extracellular matrix: implications for using skin substitutes in the clinic." *British Journal of Dermatology* 179.2 (2018): 381-393.

- Ghiroldi, Andrea, et al. "Role of sialidase Neu3 and ganglioside GM3 in cardiac fibroblasts activation." *Biochemical Journal* 477.17 (2020): 3401-3415.
- Giraudo, Claudio G., and Hugo JF Maccioni. "Ganglioside glycosyltransferases organize in distinct multienzyme complexes in CHO-K1 cells." *Journal of Biological Chemistry* 278.41 (2003): 40262-40271
- Goldman, James E., et al. "GD3 ganglioside is a glycolipid characteristic of immature neuroectodermal cells." *Journal of neuroimmunology* 7 (1984): 179-192
- Gomez-Muñoz, Antonio, et al. "Caged ceramide 1-phosphate (C1P) analogs: Novel tools for studying C1P biology." *Chemistry and physics of lipids* 194 (2016): 79-84.
- Gong, Xiaoyun, et al. "Single-cell analysis with probe ESI-mass spectrometry: detection of metabolites at cellular and subcellular levels." *Analytical chemistry* 86.8 (2014): 3809-3816.
- Gouaze-Andersson, Valerie, and Myles C. Cabot. "Glycosphingolipids and drug resistance." *Biochimica et Biophysica Acta (BBA)-Biomembranes* 1758.12 (2006): 2096-2103
- Graf, Thomas, and Matthias Stadtfeld. "Heterogeneity of embryonic and adult stem cells." *Cell stem cell* 3.5 (2008): 480-483
- Graham, Daniel J., et al. "Three-dimensional localization of polymer nanoparticles in cells using ToF-SIMS." *Biointerphases* 11.2 (2016): 02A304.
- Griffin, Michelle F., et al. "Understanding the impact of fibroblast heterogeneity on skin fibrosis." *Disease Models & Mechanisms* 13.6 (2020).
- Guo, Jingtao, et al. "Chromatin and single-cell RNA-seq profiling reveal dynamic signaling and metabolic transitions during human spermatogonial stem cell development." *Cell stem cell* 21.4 (2017): 533-546.
- Hammad, Samar M., et al. "Increased plasma levels of select deoxy-ceramide and ceramide species are associated with increased odds of diabetic neuropathy in type 1 diabetes: a pilot study." *Neuromolecular medicine* 19.1 (2017): 46-56.
- Han, Guojun, et al. "Metal-isotope-tagged monoclonal antibodies for high-dimensional mass cytometry." *Nature protocols* 13.10 (2018): 2121-2148.
- Hanada, Kentaro, et al. "Molecular machinery for non-vesicular trafficking of ceramide." *Nature* 426.6968 (2003): 803-809.

- Handa, Kazuko, and Sen-itiroh Hakomori. "Changes of glycoconjugate expression profiles during early development." *Glycoconjugate journal* 34.6 (2017): 693-699.
- Hannich, J. Thomas, et al. "1-Deoxydihydroceramide causes anoxic death by impairing chaperonin-mediated protein folding." *Nature Metabolism* 1.10 (2019): 996-1008.
- Hannun, Yusuf A., and Lina M. Obeid. "Principles of bioactive lipid signalling: lessons from sphingolipids." *Nature reviews Molecular cell biology* 9.2 (2008): 139-150.
- Hannun, Yusuf A., and Lina M. Obeid. "Sphingolipids and their metabolism in physiology and disease." *Nature reviews Molecular cell biology* 19.3 (2018): 175.
- Harlalka, Gaurav V., et al. "Mutations in B4GALNT1 (GM2 synthase) underlie a new disorder of ganglioside biosynthesis." *Brain* 136.12 (2013): 3618-3624.
- Harper, Robert A., and Gary Grove. "Human skin fibroblasts derived from papillary and reticular dermis: differences in growth potential in vitro." *Science* 204.4392 (1979): 526-527.
- Hartler, Jürgen, et al. "Lipid Data Analyser: unattended identification and quantitation of lipids in LC-MS data." *Bioinformatics* 27.4 (2011): 572-577.
- Hartmann, Daniela, et al. "Long chain ceramides and very long chain ceramides have opposite effects on human breast and colon cancer cell growth." *The international journal of biochemistry & cell biology* 44.4 (2012): 620-628.
- Hashimshony, Tamar, et al. "CEL-Seq: single-cell RNA-Seq by multiplexed linear amplification." *Cell reports* 2.3 (2012): 666-673.
- Hashimshony, Tamar, et al. "CEL-Seq2: sensitive highly-multiplexed single-cell RNA-Seq." *Genome biology* 17.1 (2016): 77.
- Haydont, Valérie, et al. "Genome-wide profiling of adult human papillary and reticular fibroblasts identifies ACAN, Col XI α 1, and PSG1 as general biomarkers of dermis ageing, and KANK4 as an exemplary effector of papillary fibroblast ageing, related to contractility." *Mechanisms of ageing and development* 177 (2019): 157-181.
- Hendriks, Gert-Jan, et al. "NASC-seq monitors RNA synthesis in single-cells." *Nature communications* 10.1 (2019): 1-9.
- Hermansson, Martin, Kati Hokynar, and Pentti Somerharju. "Mechanisms of glycerophospholipid homeostasis in mammalian cells." *Progress in lipid research* 50.3 (2011): 240-257.

- Herms, Albert, et al. "Cell-to-cell heterogeneity in lipid droplets suggests a mechanism to reduce lipotoxicity." *Current Biology* 23.15 (2013): 1489-1496.
- Hetz, Claudio A., et al. "Caspase-dependent initiation of apoptosis and necrosis by the Fas receptor in lymphoid cells: onset of necrosis is associated with delayed ceramide increase." *Journal of cell science* 115.23 (2002): 4671-4683.
- Hilfinger, Andreas, and Johan Paulsson. "Separating intrinsic from extrinsic fluctuations in dynamic biological systems." *Proceedings of the National Academy of Sciences* 108.29 (2011): 12167-12172.
- Hillenkamp, Franz, et al. "Laser microprobe mass analysis of organic materials." *Nature* 256.5513 (1975): 119-120.
- Hochane, Mazène, et al. "Single-cell transcriptomics reveals gene expression dynamics of human fetal kidney development." *PLoS biology* 17.2 (2019): e3000152.
- Holthuis, Joost CM, et al. "The organizing potential of sphingolipids in intracellular membrane transport." *Physiological reviews* 81.4 (2001): 1689-1723.
- Holthuis, Joost CM, and Anant K. Menon. "Lipid landscapes and pipelines in membrane homeostasis." *Nature* 510.7503 (2014): 48-57.
- Huang, Lu, et al. "Fast single-cell patterning for study of drug-induced phenotypic alterations of HeLa cells using time-of-flight secondary ion mass spectrometry." *Analytical chemistry* 88.24 (2016): 12196-12203.
- Husen, Peter, et al. "Analysis of lipid experiments (ALEX): a software framework for analysis of high-resolution shotgun lipidomics data." *PloS one* 8.11 (2013): e79736.
- Ibáñez, Alfredo J., et al. "Mass spectrometry-based metabolomics of single yeast cells." *Proceedings of the National Academy of Sciences* 110.22 (2013): 8790-8794.
- Ichikawa, Shinichi, and Yoshio Hirabayashi. "Glucosylceramide synthase and glycosphingolipid synthesis." *Trends in cell biology* 8.5 (1998): 198-202.
- Inoue, Yoshikazu, et al. "Basic fibroblast growth factor and its receptors in idiopathic pulmonary fibrosis and lymphangioleiomyomatosis." *American journal of respiratory and critical care medicine* 166.5 (2002): 765-773.
- Ishiguro, Shigeki, et al. "Basic fibroblast growth factor induces down-regulation of α -smooth muscle actin and reduction of myofibroblast areas in open skin wounds." *Wound repair and regeneration* 17.4 (2009): 617-625.

- Ishii, Atsushi, et al. "Expression cloning and functional characterization of human cDNA for ganglioside GM3 synthase." *Journal of Biological Chemistry* 273.48 (1998): 31652-31655.
- Jacewicz, M. A. R. Y., et al. "Pathogenesis of shigella diarrhea. XI. Isolation of a shigella toxin-binding glycolipid from rabbit jejunum and HeLa cells and its identification as globotriaosylceramide." *The Journal of experimental medicine* 163.6 (1986): 1391-1404.
- Jacob, F., et al. "The glycosphingolipid P 1 is an ovarian cancer-associated carbohydrate antigen involved in migration." *British journal of cancer* 111.8 (2014): 1634-1645
- Janson, David G., et al. "Different gene expression patterns in human papillary and reticular fibroblasts". *J. Invest. Dermatol.* 132 (2012): 2565-2572.
- Jindal, Aashi, Prashant Gupta, and Debarka Sengupta. "Discovery of rare cells from voluminous single-cell expression data." *Nature communications* 9.1 (2018): 1-9.
- Johnson, W. Evan, Cheng Li, and Ariel Rabinovic. "Adjusting batch effects in microarray expression data using empirical Bayes methods." *Biostatistics* 8.1 (2007): 118-127.
- Johnson, Caroline H., Julijana Ivanisevic, and Gary Siuzdak. "Metabolomics: beyond biomarkers and towards mechanisms." *Nature reviews Molecular cell biology* 17.7 (2016): 451-459.
- Junker, Jan Philipp, and Alexander van Oudenaarden. "Every cell is special: genome-wide studies add a new dimension to single-cell biology." *Cell* 157.1 (2014): 8-11.
- Kalluri, Raghu, and Michael Zeisberg. "Fibroblasts in cancer." *Nature Reviews Cancer* 6.5 (2006): 392-401.
- Kalmar, Tibor, et al. "Regulated fluctuations in nanog expression mediate cell fate decisions in embryonic stem cells." *PLoS biology* 7.7 (2009).
- Kannagi, Reiji, et al. "Stage-specific embryonic antigens (SSEA-3 and-4) are epitopes of a unique globo-series ganglioside isolated from human teratocarcinoma cells." *The embo journal* 2.12 (1983): 2355-2361
- Kitatani, Kazuyuki, Jolanta Idkowiak-Baldys, and Yusuf A. Hannun. "The sphingolipid salvage pathway in ceramide metabolism and signaling." *Cellular signalling* 20.6 (2008): 1010-1018.
- Kiviet, Daniel J., et al. "Stochasticity of metabolism and growth at the single-cell level." *Nature* 514.7522 (2014): 376-379.

- Klein, Allon M., et al. "Droplet barcoding for single-cell transcriptomics applied to embryonic stem cells." *Cell* 161.5 (2015): 1187-1201.
- Klingberg, Franco, Boris Hinz, and Eric S. White. "The myofibroblast matrix: implications for tissue repair and fibrosis." *The Journal of pathology* 229.2 (2013): 298-309.
- Kobayashi, Taeko, et al. "The cyclic gene Hes1 contributes to diverse differentiation responses of embryonic stem cells." *Genes & development* 23.16 (2009): 1870-1875
- Kojima, Yoshinao, et al. "Molecular cloning of globotriaosylceramide/CD77 synthase, a glycosyltransferase that initiates the synthesis of globo series glycosphingolipids." *Journal of Biological Chemistry* 275.20 (2000): 15152-15156
- Kompauer, Mario, Sven Heiles, and Bernhard Spengler. "Atmospheric pressure MALDI mass spectrometry imaging of tissues and cells at 1.4- μ m lateral resolution." *Nature methods* 14.1 (2017): 90.
- Kovbasnjuk, Olga, et al. "The glycosphingolipid globotriaosylceramide in the metastatic transformation of colon cancer." *Proceedings of the National Academy of Sciences* 102.52 (2005): 19087-19092.
- Kraveka, Jacqueline M., et al. "Involvement of dihydroceramide desaturase in cell cycle progression in human neuroblastoma cells." *Journal of Biological Chemistry* 282.23 (2007): 16718-16728.
- Krieger, Teresa, and Benjamin D. Simons. "Dynamic stem cell heterogeneity." *Development* 142.8 (2015): 1396-1406.
- Kroesen, Bart-Jan, et al. "Induction of apoptosis through B-cell receptor cross-linking occurs via de novo generated C16-ceramide and involves mitochondria." *Journal of Biological Chemistry* 276.17 (2001): 13606-13614.
- Kumagai, Tadahiro, et al. "Involvement of murine β -1, 4-galactosyltransferase V in lactosylceramide biosynthesis." *Glycoconjugate journal* 27.7-9 (2010): 685-695.
- Kurczy, Michael E., et al. "Mass spectrometry imaging of mating Tetrahymena show that changes in cell morphology regulate lipid domain formation." *Proceedings of the National Academy of Sciences* 107.7 (2010): 2751-2756.
- La Manno, Gioele, et al. "Molecular diversity of midbrain development in mouse, human, and stem cells." *Cell* 167.2 (2016): 566-580.
- La Manno, Gioele, et al. "RNA velocity of single-cells." *Nature* 560.7719 (2018): 494-498.

- Lafzi, Atefeh, et al. "Tutorial: guidelines for the experimental design of single-cell RNA sequencing studies." *Nature protocols* 13.12 (2018): 2742-2757
- Lakshmikanth, Tadepally, et al. "Mass cytometry and topological data analysis reveal immune parameters associated with complications after allogeneic stem cell transplantation." *Cell reports* 20.9 (2017): 2238-2250.
- Lasken, Roger S. "Single-cell genomic sequencing using multiple displacement amplification." *Current opinion in microbiology* 10.5 (2007): 510-516.
- Le, Thuc T., and Ji-Xin Cheng. "Single-cell profiling reveals the origin of phenotypic variability in adipogenesis." *PLoS One* 4.4 (2009).
- Lederer, Alex R., and Gioele La Manno. "The emergence and promise of single-cell temporal-omics approaches." *Current Opinion in Biotechnology* 63 (2020): 70-78.
- Lee, Je Hyuk, et al. "Highly multiplexed subcellular RNA sequencing in situ." *Science* 343.6177 (2014): 1360-1363.
- Lee, Je H. "Quantitative approaches for investigating the spatial context of gene expression." *Wiley Interdisciplinary Reviews: Systems Biology and Medicine* 9.2 (2017): e1369.
- Leefmann, Tim, et al. "Biomarker imaging of single diatom cells in a microbial mat using time-of-flight secondary ion mass spectrometry (ToF-SIMS)." *Organic geochemistry* 57 (2013): 23-33.
- Liang, Yuh-Jin, et al. "Switching of the core structures of glycosphingolipids from globo- and lacto- to ganglio-series upon human embryonic stem cell differentiation." *Proceedings of the National Academy of Sciences* 107.52 (2010): 22564-22569
- Liang, Yuh-Jin, et al. "Changes in glycosphingolipid composition during differentiation of human embryonic stem cells to ectodermal or endodermal lineages." *Stem cells* 29.12 (2011): 1995-2004.
- Lieberman-Aiden, Erez, et al. "Comprehensive mapping of long-range interactions reveals folding principles of the human genome." *science* 326.5950 (2009): 289-293.
- Liu, Pengda, et al. "Cell-cycle-regulated activation of Akt kinase by phosphorylation at its carboxyl terminus." *Nature* 508.7497 (2014): 541-545

- Liu, Yong-Yu, Ronald A. Hill, and Yu-Teh Li. "Ceramide glycosylation catalyzed by glucosylceramide synthase and cancer drug resistance." *Advances in cancer research*. Vol. 117. Academic Press, 2013. 59-89.
- Lo Giudice, Quentin, et al. "Single-cell transcriptional logic of cell-fate specification and axon guidance in early-born retinal neurons." *Development* 146.17 (2019): dev178103.
- Locke, James CW, and Michael B. Elowitz. "Using movies to analyse gene circuit dynamics in single-cells." *Nature Reviews Microbiology* 7.5 (2009): 383-392.
- Lombard-Banek, Camille, Sally A. Moody, and Peter Nemes. "Single-cell mass spectrometry for discovery proteomics: quantifying translational cell heterogeneity in the 16-cell frog (*Xenopus*) embryo." *Angewandte Chemie International Edition* 55.7 (2016): 2454-2458.
- Lombard-Banek, Camille, et al. "Microsampling capillary electrophoresis mass spectrometry enables single-cell proteomics in complex tissues: developing cell clones in live *Xenopus laevis* and zebrafish embryos." *Analytical chemistry* 91.7 (2019): 4797-4805.
- Losick, Richard, and Claude Desplan. "Stochasticity and cell fate." *science* 320.5872 (2008): 65-68
- Lu, Yao, et al. "Microchip-based single-cell functional proteomics for biomedical applications." *Lab on a Chip* 17.7 (2017): 1250-1263.
- Lujan, Ernesto, et al. "Early reprogramming regulators identified by prospective isolation and mass cytometry." *Nature* 521.7552 (2015): 352-356.
- Lynch, Magnus D., and Fiona M. Watt. "Fibroblast heterogeneity: implications for human disease." *The Journal of clinical investigation* 128.1 (2018): 26-35.
- Macosko, Evan Z., et al. "Highly parallel genome-wide expression profiling of individual cells using nanoliter droplets." *Cell* 161.5 (2015): 1202-1214.
- Maheshri, Narendra, and Erin K. O'Shea. "Living with noisy genes: how cells function reliably with inherent variability in gene expression." *Annu. Rev. Biophys. Biomol. Struct.* 36 (2007): 413-434.
- Majoul, Irina, et al. "Differential expression of receptors for Shiga and Cholera toxin is regulated by the cell cycle." *Journal of Cell Science* 115.4 (2002): 817-826.

- Marcy, Yann, et al. "Dissecting biological "dark matter" with single-cell genetic analysis of rare and uncultivated TM7 microbes from the human mouth." *Proceedings of the National Academy of Sciences* 104.29 (2007): 11889-11894.
- Mardis, Elaine R. "A decade's perspective on DNA sequencing technology." *Nature* 470.7333 (2011): 198-203.
- Maryanski, Janet L., et al. "Single-cell PCR analysis of TCR repertoires selected by antigen in vivo: a high magnitude CD8 response is comprised of very few clones." *Immunity* 4.1 (1996): 47-55.
- Mathow, Daniel, et al. "Zeb1 affects epithelial cell adhesion by diverting glycosphingolipid metabolism." *EMBO reports* 16.3 (2015): 321-331.
- Maier, Andrea B., and Rudi GJ Westendorp. "Relation between replicative senescence of human fibroblasts and life history characteristics." *Ageing research reviews* 8.3 (2009): 237-243.
- Mayr, Urs, Denise Serra, and Prisca Liberali. "Exploring single-cells in space and time during tissue development, homeostasis and regeneration." *Development* 146.12 (2019): dev176727.
- McConnell, Michael J., et al. "Mosaic copy number variation in human neurons." *Science* 342.6158 (2013): 632-637.
- Mellors, J. Scott, et al. "Integrated microfluidic device for automated single-cell analysis using electrophoretic separation and electrospray ionization mass spectrometry." *Analytical chemistry* 82.3 (2010): 967-973.
- Merrill Jr, Alfred H. "Sphingolipid and glycosphingolipid metabolic pathways in the era of sphingolipidomics." *Chemical reviews* 111.10 (2011): 6387-6422.
- Mesicek, Judith, et al. "Ceramide synthases 2, 5, and 6 confer distinct roles in radiation-induced apoptosis in HeLa cells." *Cellular signalling* 22.9 (2010): 1300-1307.
- Metzker, Michael L. "Sequencing technologies—the next generation." *Nature reviews genetics* 11.1 (2010): 31-46.
- Miljan, Erik A., and Eric G. Bremer. "Regulation of growth factor receptors by gangliosides." *Science Signaling* 2002.160 (2002): re15-re15.

- Mizuno, Hajime, et al. "Live single-cell video-mass spectrometry for cellular and subcellular molecular detection and cell classification." *Journal of mass spectrometry* 43.12 (2008): 1692-1700.
- Modrak, David E., et al. "Ceramide regulates gemcitabine-induced senescence and apoptosis in human pancreatic cancer cell lines." *Molecular Cancer Research* 7.6 (2009): 890-896.
- Morad, Samy AF, and Myles C. Cabot. "Ceramide-orchestrated signalling in cancer cells." *Nature Reviews Cancer* 13.1 (2013): 51-65.
- Mortazavi, Ali, et al. "Mapping and quantifying mammalian transcriptomes by RNA-Seq." *Nature methods* 5.7 (2008): 621
- Mullen, Thomas D., Yusuf A. Hannun, and Lina M. Obeid. "Ceramide synthases at the centre of sphingolipid metabolism and biology." *Biochemical Journal* 441.3 (2012): 789-802.
- Müthing, Johannes, et al. "Shiga toxins, glycosphingolipid diversity, and endothelial cell injury." *Thrombosis and haemostasis* 101.02 (2009): 252-264.
- Nagano, Takashi, et al. "Single-cell Hi-C reveals cell-to-cell variability in chromosome structure." *Nature* 502.7469 (2013): 59-64.
- Nagano, Takashi, et al. "Cell-cycle dynamics of chromosomal organization at single-cell resolution." *Nature* 547.7661 (2017): 61-67.
- Nagata, Y., et al. "Expression cloning of beta 1, 4 N-acetylgalactosaminyltransferase cDNAs that determine the expression of GM2 and GD2 gangliosides." *Journal of Biological Chemistry* 267.17 (1992): 12082-12089.
- Nemes, Peter, et al. "Metabolic differentiation of neuronal phenotypes by single-cell capillary electrophoresis–electrospray ionization-mass spectrometry." *Analytical chemistry* 83.17 (2011): 6810-6817.
- Neumann, Elizabeth K., et al. "Lipid Analysis of 30 000 Individual Rodent Cerebellar Cells Using High-Resolution Mass Spectrometry." *Analytical chemistry* 91.12 (2019): 7871-7878.
- Ngamukote, Sathaporn, et al. "Developmental changes of glycosphingolipids and expression of glycogenes in mouse brains." *Journal of neurochemistry* 103.6 (2007): 2327-2341.

- Niehaus, M., et al. "Transmission-mode MALDI-2 mass spectrometry imaging of cells and tissues at subcellular resolution." *Nature methods* 16.9 (2019): 925-931.
- Nishie, Toshikazu, et al. " β 4-Galactosyltransferase-5 is a lactosylceramide synthase essential for mouse extra-embryonic development." *Glycobiology* 20.10 (2010): 1311-1322.
- Novick, Aaron, and Milton Weiner. "Enzyme induction as an all-or-none phenomenon." *Proceedings of the National Academy of Sciences of the United States of America* 43.7 (1957): 553.
- Ogretmen, Besim. "Sphingolipid metabolism in cancer signalling and therapy." *Nature Reviews Cancer* 18.1 (2018): 33
- Ojima, Takuma, et al. "Glycolipid dynamics in generation and differentiation of induced pluripotent stem cells." *Scientific reports* 5.1 (2015): 1-13.
- Ong, Ta-Hsuan, et al. "Classification of large cellular populations and discovery of rare cells using single-cell matrix-assisted laser desorption/ionization time-of-flight mass spectrometry." *Analytical chemistry* 87.14 (2015): 7036-7042.
- Onjiko, Rosemary M., Sally A. Moody, and Peter Nemes. "Single-cell mass spectrometry reveals small molecules that affect cell fates in the 16-cell embryo." *Proceedings of the National Academy of Sciences* 112.21 (2015): 6545-6550.
- Onjiko, Rosemary M., et al. "In situ microprobe single-cell capillary electrophoresis mass spectrometry: metabolic reorganization in single differentiating cells in the live vertebrate (*Xenopus laevis*) embryo." *Analytical chemistry* 89.13 (2017): 7069-7076.
- Op den Kamp, Jos AF. "Lipid asymmetry in membranes." *Annual review of biochemistry* 48.1 (1979): 47-71.
- Osawa, Yosuke, et al. "Roles for C16-ceramide and sphingosine 1-phosphate in regulating hepatocyte apoptosis in response to tumor necrosis factor- α ." *Journal of Biological Chemistry* 280.30 (2005): 27879-27887.
- Palmer, Andrew, et al. "FDR-controlled metabolite annotation for high-resolution imaging mass spectrometry." *Nature methods* 14.1 (2017): 57-60.
- Pan, Ning, et al. "The single-probe: a miniaturized multifunctional device for single-cell mass spectrometry analysis." *Analytical chemistry* 86.19 (2014): 9376-9380.

- Park, Seung-Yeol, et al. "Globoside promotes activation of ERK by interaction with the epidermal growth factor receptor." *Biochimica et Biophysica Acta (BBA)-General Subjects* 1820.7 (2012): 1141-1148.
- Paschke, C., et al. "Mirion—a software package for automatic processing of mass spectrometric images." *Journal of The American Society for Mass Spectrometry* 24.8 (2013): 1296-1306.
- Passarelli, Melissa K., et al. "Single-cell analysis: visualizing pharmaceutical and metabolite uptake in cells with label-free 3D mass spectrometry imaging." *Analytical chemistry* 87.13 (2015): 6696-6702.
- Patel, Anoop P., et al. "Single-cell RNA-seq highlights intratumoral heterogeneity in primary glioblastoma." *Science* 344.6190 (2014): 1396-1401
- Pedroza, Mesias, et al. "Role of STAT3 in skin fibrosis and transforming growth factor beta signalling." *Rheumatology* 57.10 (2018): 1838-1850.
- Pelkmans, Lucas. "Using cell-to-cell variability—a new era in molecular biology." *Science* 336.6080 (2012): 425-426
- Penno, Anke, et al. "Hereditary sensory neuropathy type 1 is caused by the accumulation of two neurotoxic sphingolipids." *Journal of biological chemistry* 285.15 (2010): 11178-11187.
- Perez, Omar D., and Garry P. Nolan. "Simultaneous measurement of multiple active kinase states using polychromatic flow cytometry." *Nature biotechnology* 20.2 (2002): 155-162.
- Peters, Brock A., et al. "Accurate whole-genome sequencing and haplotyping from 10 to 20 human cells." *Nature* 487.7406 (2012): 190-195.
- Philippeos, Christina, et al. "Spatial and single-cell transcriptional profiling identifies functionally distinct human dermal fibroblast subpopulations." *Journal of Investigative Dermatology* 138.4 (2018): 811-825.
- Picelli, Simone. "Single-cell RNA-sequencing: the future of genome biology is now." *RNA biology* 14.5 (2017): 637-650
- Pyne, Susan, and Nigel Pyne. "Sphingosine 1-phosphate signalling via the endothelial differentiation gene family of G-protein-coupled receptors." *Pharmacology & therapeutics* 88.2 (2000): 115-131.

- Raj, Arjun, and Alexander van Oudenaarden. "Nature, nurture, or chance: stochastic gene expression and its consequences." *Cell* 135.2 (2008): 216-226.
- Raj, Arjun, et al. "Imaging individual mRNA molecules using multiple singly labeled probes." *Nature methods* 5.10 (2008): 877-879.
- Ramani, Vijay, et al. "Massively multiplex single-cell Hi-C." *Nature methods* 14.3 (2017): 263-266.
- Ramsköld, Daniel, et al. "Full-length mRNA-Seq from single-cell levels of RNA and individual circulating tumor cells." *Nature biotechnology* 30.8 (2012): 777.
- Ranzoni, Anna M., and Ana Cvejic. "Single-cell biology: resolving biological complexity, one cell at a time." *Development* 145.13 (2018).
- Rappez, Luca, et al. "Spatial single-cell profiling of intracellular metabolomes in situ." *BioRxiv* (2019): 510222.
- Resnick, Igor B., et al. "Treatment of severe steroid resistant acute GVHD with mesenchymal stromal cells (MSC)." *American journal of blood research* 3.3 (2013): 225.
- Rinn, John L., et al. "Anatomic demarcation by positional variation in fibroblast gene expression programs." *PLoS Genet* 2.7 (2006): e119.
- Rodda, Lauren B., et al. "Single-cell RNA sequencing of lymph node stromal cells reveals niche-associated heterogeneity." *Immunity* 48.5 (2018): 1014-1028.
- Roesch, Alexander, et al. "A temporarily distinct subpopulation of slow-cycling melanoma cells is required for continuous tumor growth." *Cell* 141.4 (2010): 583-594.
- Rognoni, Emanuel, and Fiona M. Watt. "Skin cell heterogeneity in development, wound healing, and cancer." *Trends in cell biology* 28.9 (2018): 709-722.
- Rosenberg, Alexander B., et al. "Single-cell profiling of the developing mouse brain and spinal cord with split-pool barcoding." *Science* 360.6385 (2018): 176-182.
- Rossio-Pasquier, Patricia, et al. "Wound healing of human skin transplanted onto the nude mouse after a superficial excisional injury: human dermal reconstruction is achieved in several steps by two different fibroblast subpopulations." *Archives of dermatological research* 291.11 (1999): 591-599.
- Rusnati, Marco, et al. "Cell membrane GM1 ganglioside is a functional coreceptor for fibroblast growth factor 2." *Proceedings of the National Academy of Sciences* 99.7 (2002): 4367-4372.

- Russo, Domenico, et al. "Glycosphingolipid metabolic reprogramming drives neural differentiation." *The EMBO journal* 37.7 (2018a).
- Russo, Domenico, et al. "Glycosphingolipid metabolism in cell fate specification." *J Cell Sci* 131.24 (2018b): jcs219204.
- Saadatpour, Assieh, et al. "Single-cell analysis in cancer genomics." *Trends in Genetics* 31.10 (2015): 576-586.
- Sandra, Alexander, and Richard E. Pagano. "Phospholipid asymmetry in LM cell plasma membrane derivatives: polar head group and acyl chain distributions." *Biochemistry* 17.2 (1978): 332-338.
- Sasagawa, Yohei, et al. "Quartz-Seq: a highly reproducible and sensitive single-cell RNA sequencing method, reveals non-genetic gene-expression heterogeneity." *Genome biology* 14.4 (2013): 3097.
- Sato, Ban, et al. "Preferential localization of SSEA-4 in interfaces between blastomeres of mouse preimplantation embryos." *Biochemical and biophysical research communications* 364.4 (2007): 838-843.
- Schindelin, Johannes, et al. "Fiji: an open-source platform for biological-image analysis." *Nature methods* 9.7 (2012): 676-682.
- Schober, Yvonne, et al. "Single-cell matrix-assisted laser desorption/ionization mass spectrometry imaging." *Analytical chemistry* 84.15 (2012): 6293-6297.
- Schroepfer Jr, George J. "Sterol biosynthesis." *Annual review of biochemistry* 50.1 (1981): 585-621.
- Schwalie, Petra C., et al. "A stromal cell population that inhibits adipogenesis in mammalian fat depots." *Nature* 559.7712 (2018): 103-108.
- Semrau, Stefan, et al. "Dynamics of lineage commitment revealed by single-cell transcriptomics of differentiating embryonic stem cells." *Nature communications* 8.1 (2017): 1-16
- Senkal, Can E., et al. "Alteration of ceramide synthase 6/C16-ceramide induces activating transcription factor 6-mediated endoplasmic reticulum (ER) stress and apoptosis via perturbation of cellular Ca²⁺ and ER/Golgi membrane network." *Journal of Biological Chemistry* 286.49 (2011): 42446-42458.

- Seumois, Grégory, et al. "De novo C16-and C24-ceramide generation contributes to spontaneous neutrophil apoptosis." *Journal of leukocyte biology* 81.6 (2007): 1477-1486.
- Shapiro, Ehud, Tamir Biezuner, and Sten Linnarsson. "Single-cell sequencing-based technologies will revolutionize whole-organism science." *Nature Reviews Genetics* 14.9 (2013): 618-630.
- Schoop, Veronika M., et al. "Epidermal organization and differentiation of HaCaT keratinocytes in organotypic coculture with human dermal fibroblasts." *J. Invest. Dermatol.* 112 (1999) 343-353.
- Simons, Kai, and Elina Ikonen. "Functional rafts in cell membranes." *nature* 387.6633 (1997): 569-572
- Singer, Zakary S., et al. "Dynamic heterogeneity and DNA methylation in embryonic stem cells." *Molecular cell* 55.2 (2014): 319-331
- Siwik, Deborah A., Donny L-F. Chang, and Wilson S. Colucci. "Interleukin-1 β and tumor necrosis factor- α decrease collagen synthesis and increase matrix metalloproteinase activity in cardiac fibroblasts in vitro." *Circulation research* 86.12 (2000): 1259-1265.
- Skwarek, Lara C., and Gabrielle L. Boulianne. "Great expectations for PIP: phosphoinositides as regulators of signaling during development and disease." *Developmental cell* 16.1 (2009): 12-20.
- Smith, E. R. "Effects of sphingosine and other sphingolipids on protein kinase." *Methods Enzymol.* 312 (2000): 361-373.
- Snijder, Berend, et al. "Population context determines cell-to-cell variability in endocytosis and virus infection." *Nature* 461.7263 (2009): 520-523.
- Solé-Boldo, Llorenç, et al. "Single-cell transcriptomes of the human skin reveal age-related loss of fibroblast priming." *Communications Biology* 3.1 (2020): 1-12.
- Soltwisch, Jens, et al. "Mass spectrometry imaging with laser-induced postionization." *Science* 348.6231 (2015): 211-215.
- Song, Jianyuan, et al. "The role of FABP5 in radiation-induced human skin fibrosis." *Radiation research* 189.2 (2018): 177-186.
- Sorrell, J. Michael, and Arnold I. Caplan. "Fibroblast heterogeneity: more than skin deep." *Journal of cell science* 117.5 (2004): 667-675.

- Spencer, Sabrina L., et al. "Non-genetic origins of cell-to-cell variability in TRAIL-induced apoptosis." *Nature* 459.7245 (2009): 428-432.
- Spengler, Bernhard, Hubert Martin, Kaufmann Raimund in *Proceedings of the 42nd Annual Conference on Mass Spectrometry and Allied Topics*, Chicago, Illinois, 1994, p. 1041
- Spengler, Bernhard, and Martin Hubert. "Scanning microprobe matrix-assisted laser desorption ionization (SMALDI) mass spectrometry: instrumentation for sub-micrometer resolved LDI and MALDI surface analysis." *Journal of the American Society for Mass Spectrometry* 13.6 (2002): 735-748.
- Spiegel, Sarah, and Sheldon Milstien. "The outs and the ins of sphingosine-1-phosphate in immunity." *Nature Reviews Immunology* 11.6 (2011): 403-415
- Spudich, John L., and Daniel E. Koshland. "Non-genetic individuality: chance in the single-cell." *Nature* 262.5568 (1976): 467-471.
- Sriram, Gopu, Paul Lorenz Bigliardi, and Mei Bigliardi-Qi. "Fibroblast heterogeneity and its implications for engineering organotypic skin models in vitro." *European journal of cell biology* 94.11 (2015): 483-512.
- St-Pierre, François, and Drew Endy. "Determination of cell fate selection during phage lambda infection." *Proceedings of the National Academy of Sciences* 105.52 (2008): 20705-20710
- Strutz, Frank, et al. "Basic fibroblast growth factor expression is increased in human renal fibrogenesis and may mediate autocrine fibroblast proliferation." *Kidney international* 57.4 (2000): 1521-1538.
- Stuart, Tim, et al. "Comprehensive integration of single-cell data." *Cell* 177.7 (2019): 1888-1902.
- Sud, Manish, et al. "Lmsd: Lipid maps structure database." *Nucleic acids research* 35.suppl_1 (2007): D527-D532.
- Sugiyama, Eiji, Ikuko Yao, and Mitsutoshi Setou. "Visualization of local phosphatidylcholine synthesis within hippocampal neurons using a compartmentalized culture system and imaging mass spectrometry." *Biochemical and biophysical research communications* 495.1 (2018): 1048-1054.

- Sun, Mei, Zhibo Yang, and Boris Wawrik. "Metabolomic fingerprints of individual algal cells using the single-probe mass spectrometry technique." *Frontiers in Plant Science* 9 (2018): 571.
- Suwara, M. I., et al. "IL-1 α released from damaged epithelial cells is sufficient and essential to trigger inflammatory responses in human lung fibroblasts." *Mucosal immunology* 7.3 (2014): 684-693.
- Svensson, Valentine, et al. "Power analysis of single-cell RNA-sequencing experiments." *Nature methods* 14.4 (2017): 381
- Symmons, Orsolya, and Arjun Raj. "What's luck got to do with it: single-cells, multiple fates, and biological nondeterminism." *Molecular cell* 62.5 (2016): 788-802
- Tabib, Tracy, et al. "SFRP2/DPP4 and FMO1/LSP1 define major fibroblast populations in human skin." *Journal of Investigative Dermatology* 138.4 (2018): 802-810.
- Takhaveev, Vakil, and Matthias Heinemann. "Metabolic heterogeneity in clonal microbial populations." *Current opinion in microbiology* 45 (2018): 30-38
- Tang, Fuchou, et al. "mRNA-Seq whole-transcriptome analysis of a single-cell." *Nature methods* 6.5 (2009): 377.
- Taniguchi, Kiyomi, Tomoharu Kajiyama, and Hideki Kambara. "Quantitative analysis of gene expression in a single-cell by qPCR." *Nature methods* 6.7 (2009): 503.
- Telenius, Hakan, Carter, Nigel P., et al. "Degenerate oligonucleotide-primed PCR: general amplification of target DNA by a single degenerate primer." *Genomics* 13.3 (1992): 718-725.
- Thulabandu, Venkata, Demeng Chen, and Radhika P. Atit. "Dermal fibroblast in cutaneous development and healing." *Wiley Interdisciplinary Reviews: Developmental Biology* 7.2 (2018): e307.
- Troutt, Anthony B., et al. "Ligation-anchored PCR: a simple amplification technique with single-sided specificity." *Proceedings of the National Academy of Sciences* 89.20 (1992): 9823-9825.
- Tusi, Betsabeh Khoramian, et al. "Population snapshots predict early haematopoietic and erythroid hierarchies." *Nature* 555.7694 (2018): 54-60.
- Ulaş, Işıldak, et al. "Temporal changes in the gene expression heterogeneity during brain development and aging." *Scientific Reports (Nature Publisher Group)* 10.1 (2020)

- Ungrin, Mark D., et al. "Reproducible, ultra high-throughput formation of multicellular organization from single-cell suspension-derived human embryonic stem cell aggregates." *PloS one* 3.2 (2008).
- Urban, Pawel L., et al. "High-density micro-arrays for mass spectrometry." *Lab on a chip* 10.23 (2010): 3206-3209.
- van Heyningen, Simon. "Cholera toxin: interaction of subunits with ganglioside GM1." (1974): 656-657.
- van Meer, Gerrit. "Cellular lipidomics." *The EMBO journal* 24.18 (2005): 3159-3165.
- Varkey, Mathew, Jie Ding, and Edward E. Tredget. "Differential collagen–glycosaminoglycan matrix remodeling by superficial and deep dermal fibroblasts: Potential therapeutic targets for hypertrophic scar." *Biomaterials* 32.30 (2011): 7581-7591.
- Vorstandlechner, Vera, et al. "Deciphering the functional heterogeneity of skin fibroblasts using single-cell RNA sequencing." *The FASEB Journal* 34.3 (2020): 3677-3692.
- Wang, Dao-Guang, et al. "Roles of cellular heterogeneity, intrinsic and extrinsic noise in variability of p53 oscillation." *Scientific reports* 9.1 (2019): 1-11.
- Wang, JianFei, et al. "Deep dermal fibroblasts contribute to hypertrophic scarring." *Laboratory investigation* 88.12 (2008): 1278-1290.
- Wang, Ping, et al. "Dissecting the global dynamic molecular profiles of human fetal kidney development by single-cell RNA sequencing." *Cell reports* 24.13 (2018): 3554-3567.
- Wang, Yue J., et al. "Single-cell mass cytometry analysis of the human endocrine pancreas." *Cell metabolism* 24.4 (2016): 616-626.
- Wedlock, Louise E., et al. "NanoSIMS multi-element imaging reveals internalisation and nucleolar targeting for a highly-charged polynuclear platinum compound." *Chemical Communications* 49.62 (2013): 6944-6946.
- White, Melanie D., et al. "Long-lived binding of Sox2 to DNA predicts cell fate in the four-cell mouse embryo." *Cell* 165.1 (2016): 75-87.
- Woodley, David T. "Distinct fibroblasts in the papillary and reticular dermis: implications for wound healing". *Dermatol. Clin.* 35 (2017): 95-100.

- Xenopoulos, Panagiotis, et al. "Heterogeneities in Nanog expression drive stable commitment to pluripotency in the mouse blastocyst." *Cell reports* 10.9 (2015): 1508-1520.
- Xia, Bo, et al. "Widespread transcriptional scanning in the testis modulates gene evolution rates." *Cell* 180.2 (2020): 248-262.
- Xie, Ting, et al. "Single-cell deconvolution of fibroblast heterogeneity in mouse pulmonary fibrosis." *Cell reports* 22.13 (2018): 3625-3640.
- Yamashita, Tadashi, et al. "A vital role for glycosphingolipid synthesis during development and differentiation." *Proceedings of the National Academy of Sciences* 96.16 (1999): 9142-9147
- Yamashita, Tadashi, Ryuichi Wada, and Richard L. Proia. "Early developmental expression of the gene encoding glucosylceramide synthase, the enzyme controlling the first committed step of glycosphingolipid synthesis." *Biochimica et Biophysica Acta (BBA)-General Subjects* 1573.3 (2002): 236-240
- Yang, Bo, et al. "Single-cell mass spectrometry reveals changes in lipid and metabolite expression in RAW 264.7 cells upon lipopolysaccharide stimulation." *Journal of The American Society for Mass Spectrometry* 29.5 (2018): 1012-1020.
- Zavalin, Andre, et al. "Direct imaging of single-cells and tissue at sub-cellular spatial resolution using transmission geometry MALDI MS." *Journal of Mass Spectrometry* 47.11 (2012): 1473-1481.
- Zeng, Chun, et al. "Pseudotemporal ordering of single-cells reveals metabolic control of postnatal β cell proliferation." *Cell metabolism* 25.5 (2017): 1160-1175.
- Zenobi, Renato. "Single-cell metabolomics: analytical and biological perspectives." *Science* 342.6163 (2013): 1243259.
- Zhang, Lin, et al. "Whole genome amplification from a single-cell: implications for genetic analysis." *Proceedings of the National Academy of Sciences* 89.13 (1992): 5847-5851
- Zhang, Qiming, et al. "Landscape and dynamics of single immune cells in hepatocellular carcinoma." *Cell* 179.4 (2019): 829-845.
- Zhang, Weifei, et al. "Concentrating Single-cells in Picoliter Droplets for Phospholipid Profiling on a Microfluidic System." *Small* 16.9 (2020): 1903402.

- Zhou, Vicky W., Alon Goren, and Bradley E. Bernstein. "Charting histone modifications and the functional organization of mammalian genomes." *Nature Reviews Genetics* 12.1 (2011): 7-18.
- Zhu, Ying, et al. "Proteomic analysis of single mammalian cells enabled by microfluidic nanodroplet sample preparation and ultrasensitive nanoLC-MS." *Angewandte Chemie* 130.38 (2018): 12550-12554
- Zimmerman, Tyler A., et al. "Imaging of cells and tissues with mass spectrometry: adding chemical information to imaging." *Methods in cell biology* 89 (2008): 361-390.

CURRICULUM VITAE

Laura Capolupo

Chemin des Diablerets 7A | 1012 Lausanne, Switzerland | +41767909628 | laura.capolupo@epfl.ch

Education

2016- present PhD in Bioengineering & Biotechnology

EDBB PhD programme at the École Polytechnique Fédérale de Lausanne (EPFL), Switzerland.
Thesis title: Single-Cell Lipidomics reveals a role for sphingolipids in fibroblast activation

2012 - 2014 MSc Chemical Science

University of Naples “Federico II”, Naples (Italy).
Thesis title: Structural study of lipopolysaccharide from *Psychrobacter arcticus* strain

2009 –2012 BSc Chemistry

University of Naples “Federico II”, Naples (Italy).
Thesis title: Isolation and analysis of chemical properties of Regiolone an α -tetralone from *Juglans regia*

Research Experience

October 2018 – present PhD student, with Prof. Giovanni D’Angelo

Laboratory of Lipid Cell Biology, Institute of Bioengineering, EPFL
Topic: Use of single-cell omics techniques with a focus on MALDI-IMS to reveal the role of lipids in fibroblasts cell fate decision.

October 2016 – October 2018 PhD student, with Prof. Giovanni D’Angelo

Institute of Protein Biochemistry, National Research Council, Naples (Italy).
Topic:

- Development of single-cell lipidomics workflow using MALDI-IMS
- Collaboration with Dr. Floriana Della Ragione and Dr. Maurizio D’Esposito to find perturbation of lipid metabolism in Rett syndrome mouse models by MALDI-IMS.

January 2016 – July 2016 Chemistry Fellowship, with Prof. Vincenza Faraco

Department of Chemistry, University of Naples “Federico II”, Naples (Italy).
Topic: Optimization of lignocellulose biomasses pretreatment for biorefinery development.

March 2015 – October 2015 Chemistry Fellowship, with Dr. Adriano Boni

IIT@NEST-Center for Nanotechnology Innovation, Pisa (Italy)

Topic: Synthesis and structural, magnetic and relaxometric characterization of new multifunctional magnetic nanoparticle for simultaneous imaging and therapy of diseases.

January 2014 – December 2014 Master Thesis Researcher, with Prof. Maria Michela Corsaro
Department of Chemistry, University of Naples “Federico II”, Naples (Italy).

Topic: Structural characterization by MS and NMR of a lipopolysaccharide from a *Psychrobacter arcticus* strain.

Teaching Experience

BIOENG-444 Advanced Bioengineering methods laboratory (2018/2019).

BIO-213 Biological Chemistry II (2019/2020).

Competences

Biochemistry and molecular biology:

- DNA/ RNA isolation, RT-PCR and quantitative PCR, cell culture, cell transfection, cell-based assays, western Blotting, flow cytometry

Chemistry:

- Inorganic and organic synthesis, chromatography, TLC, lipid extraction

Mass spectrometry:

- MALDI-IMS, ICP-MS, LC-MS, GC-MS
- Data analysis: Mirion, MSiReader, MSIQuant, MetaSpace, Excalibur, Tune, AMDIS

Microscopy

- Immunofluorescence microscopy, live-imaging. Image analysis (Fiji and ZenLite).
- Microscopes: Zeiss LSM 700 confocal, Leica SP8 confocal.

Digital skills

- Statistics and data analysis: R studio, Graph Pad prism, Fiji, Office suite
- Figure preparation: Adobe Illustrator, Adobe Photoshop

Personal competences

- Highly motivated, team player, extremely organized. Ability to work independently or in a team.

Publications

- Boni, A., et al. "Optimized PAMAM coated magnetic nanoparticles for simultaneous hyperthermic treatment and contrast enhanced MRI diagnosis." RSC advances 7.70 (2017): 44104-44111.
- Capolupo, Laura, and Vincenza Faraco. "Green methods of lignocellulose pretreatment for biorefinery development." Applied microbiology and biotechnology 100.22 (2016): 9451-9467.
- Pothukuchi, Prathyush, et al. "Regulated compartmentalization of enzymes in Golgi by GRASP55 controls cellular glycosphingolipid profile and function." bioRxiv (2020).
- Rizzo, Riccardo, et al. "Retrograde Transport of Golgi Enzymes by GOLPH3 Across Maturing Cisternae Regulates Glycan Assembly on Sphingolipids and Cell Growth." bioRxiv (2019): 870477.
- Russo, Domenico, et al. "Glycosphingolipid metabolism in cell fate specification." Journal of Cell Science 131.24 (2018).

Participation in scientific conferences

- Short talk (virtual) | 24h-IMSI. 19 November 2020.
- Short talk (virtual) | Emerging Technologies in Single-cell Research. 20 November 2020.
- Regular talk | OurCon VII. Saint-Malo, France. 28-31 October. 2019
- Short talk | Sphingolipid Biology: Sphingolipids in Physiology and Pathology. Cascais, Portugal. 6-10 May 2019
- Short talk & Poster | IMSS II & OurCon VI. Charleston, South Carolina. 11-14 November 2018.
- Poster | Bioengineering day. EPFL, Lausanne, Switzerland. 27 November 2019

Participation to scientific courses

- Attendance to "Advanced Training Course on Emerging Biotechnologies for Sustainable Waste Management and Biorefinery Development" - Napoli, 4 e 5 April 2016
- Attendance to "Advanced Imaging Mass Spectrometry Laboratory Course (AIMS.2018)" - Nashville, 23-27 April 2018

Professional membership

September 2018 – present Member of Imaging Mass Spectrometry society